



THE HONG KONG
POLYTECHNIC UNIVERSITY

香港理工大學

Pao Yue-kong Library

包玉剛圖書館

Copyright Undertaking

This thesis is protected by copyright, with all rights reserved.

By reading and using the thesis, the reader understands and agrees to the following terms:

1. The reader will abide by the rules and legal ordinances governing copyright regarding the use of the thesis.
2. The reader will use the thesis for the purpose of research or private study only and not for distribution or further reproduction or any other purpose.
3. The reader agrees to indemnify and hold the University harmless from and against any loss, damage, cost, liability or expenses arising from copyright infringement or unauthorized usage.

If you have reasons to believe that any materials in this thesis are deemed not suitable to be distributed in this form, or a copyright owner having difficulty with the material being included in our database, please contact lbsys@polyu.edu.hk providing details. The Library will look into your claim and consider taking remedial action upon receipt of the written requests.



The Hong Kong Polytechnic University

Department of Mechanical Engineering

**FORCED CONVECTION AND FLUID FRICTION
IN A HORIZONTAL TRIANGULAR DUCT
WITH UNIFORMLY RIBBED OR GROOVED
INTERNAL SURFACES**

By

LUO DAN DAN

A thesis submitted in partial fulfillment of the requirements for the
Degree of Doctor of Philosophy

July 2006



Pao Yue-kong Library
PolyU • Hong Kong

CERTIFICATE OF ORIGINALITY

I hereby declare that this thesis is my own work and that, to the best of my knowledge and belief, it reproduces no material previously published or written, nor material that has been accepted for the award of any other degree or diploma, except where due acknowledgement has been made in the text.

_____ (Signed)

Luo Dan Dan (Name of student)

ABSTRACT

Fully developed turbulent flows in equilateral-triangular ducts with or without internal roughened surfaces were investigated from both experimental and numerical approaches in the present study. Better understanding of the thermal performance as well as flow characteristics of the forced convective turbulent flow was achieved, which is of importance for nowadays engineering applications.

The inner surfaces of the triangular ducts were either plane or fabricated with uniformly spaced square-ribs or V-grooves. It was aimed to identify the effects of the duct geometry, fabricated ribs and V-grooves, as well as flow conditions on forced convection and fluid friction of the turbulent flow in the triangular duct. For the present investigation, the rib size to hydraulic diameter ratio (e/D) ranged from 0.11 to 0.21 and the rib-to-rib spacing to rib size ratio (S_r/e) ranged from 3.41 to 13.93. The apex angle (θ) of the V-groove varied from 30° to 150° , corresponding to a relative apex angle ($\vartheta = \frac{\theta}{180} \cdot \pi$) varying from 0.78 to 2.62, and the groove-to-groove spacing to hydraulic diameter ratio (S_v/D) varied from 0.54 to 1.23. The measurements were performed under steady-state turbulent conditions, with hydraulic-diameter-based Reynolds number (Re) ranging from 4,000 to 23,000. Enhancement in heat transfer efficiency of the triangular duct was observed with either ribbed or V-grooved internal surfaces, though the ribbed surface obtained a much better performance than the V-grooved surface. Optimum rib size, rib-to-rib spacing, V-groove apex angle and groove-to-groove spacing corresponding to maximum forced convections were proposed, respectively. Non-dimensional

expressions for the determinations of average Nusselt number (Nu) and average friction factor (f) in terms of (Re), (e/D), (\mathcal{G}), (S_r/e) and (S_v/D) were also deduced.

In addition, the turbulent flow characteristics of the rib-roughened triangular duct were particularly investigated through experimental visualization method by using Particle Image Velocimetry (PIV) technique. The aspect ratio of rib size to hydraulic diameter of the triangular duct was kept constant at $e/D = 0.2$ at a fixed Reynolds number of $Re = 10,800$. Development of the secondary flow, detachment and reattachment of the main flow, as well as formation of the vortex around the ribs and in the duct corners were studied, respectively.

In the numerical simulation studies, the assumptions of steady-flow of incompressible Newtonian fluid were taken into consideration under turbulent-flow conditions. There were three configurations considered: 1) a two-dimensional flow in a channel formed by two parallel plates with a uniformly heated and ribbed bottom plate; 2) a three-dimensional triangular duct with smooth internal surfaces; 3) a three-dimensional triangular duct with internal ribbed surfaces. A finite volume code, FLUENT 6.0, was applied to perform the calculations. The governing equations (i.e., *continuity*, *momentum* and *energy*) were solved by the pressure correction algorithm SIMPLE. Two semi-empirical turbulence models, namely, the Standard $k - \varepsilon$ Model and Reynolds Stress Model (RSM), were used for the present simulations. It was found that, in the prediction of a two-dimensional flow, the former model had superiority over the latter one. However, to predict a three-

dimensional channel flow, application of the RSM became necessary instead of the Standard $k - \varepsilon$ Model.

Comparisons between the numerical-predicted and experimental-measured turbulent flows in the triangular duct were also conducted. Good agreements were observed from both visual and metrical aspects. Moreover, it was proposed that a suitable two-dimensional numerical model could be applied more effectively instead of the complicated and expensive three-dimensional model in simulating the turbulent flow characteristics in a triangular duct with ribbed internal surfaces.

In conducting the present research project, I have made the following contributions towards this topic area:

1. Provide general summarizations of the thermal performance of the triangular duct with internal uniformly ribbed or grooved surfaces;
2. Explore the flow characteristics of the rib-interrupted turbulent flow in the triangular duct through visualization study;
3. Achieve a better understanding of the heat transfer mechanism of such a dynamic thermal system via numerical simulation approach;
4. Suggest the use of a suitable simple two-dimensional model to tackle a complicated three-dimensional problem;
5. Publish several journal papers and conference proceedings with the findings obtained, which are listed detailedly in Section: *PUBLICATIONS ARISING FROM THE THESIS*.

ACKNOWLEDGEMENTS

It is a pleasure to express my gratitude to many who have helped in this research project. I would like to thank Prof. C. W. Leung, Dr. T. L. Chan and Dr. W. O. Wong, for their guidance, comment and constructive criticism throughout my research study. My grateful acknowledgements also go to Dr. Jay C. S. Tse, Mr. Raymond H. T. Chan, and Mr. W. W. Lam, for their technical support.

The financial support from CERG of the Hong Kong Research Grant Council and CRG of the Hong Kong Polytechnic University is much appreciated. (Project No.: PolyU5165/01E)

Finally, I wish to thank my parents for their love, support and encouragement in the last four years.

TABLE OF CONTENTS

	PAGE NO.
ABSTRACT	i
ACKNOWLEDGEMENTS	iv
TABLE OF CONTENTS	v
LIST OF FIGURES	x
LIST OF TABLES	xv
NOMENCLATURE	xvi
1 INTRODUCTION	1
1.1 Scope and Background	1
1.2 Research Objectives	5
1.3 Layout of Present Thesis	9
2 LITERATURE REVIEW	11
2.1 Ducts with Smooth Internal Surfaces	12
2.1.1 Under Laminar Flow Conditions	12
2.1.2 Under Turbulent Flow Conditions	14
2.2 Application of Surface Roughness	16
2.2.1 Ribbed Internal Surface	16
2.2.2 Grooved Internal Surface	19
2.2.3 Other Types of Roughness	21
2.3 Secondary Flow	23
2.4 Triangular Sectional Ducts	24
2.5 Numerical Predictions of Internal Flow	27
2.5.1 Laminar Flow	27
2.5.2 Turbulent Flow	28
2.6 Visualization of Internal Flow	32
2.7 Summary of Literature Review	34

3	EXPERIMENTAL ARRANGEMENT	37
3.1	Design of the Test Rig	38
3.2	Measurement of Experimental Parameters	42
3.2.1	Temperatures	42
3.2.1.1	Wall Temperatures	42
3.2.1.2	Airflow Temperatures	43
3.2.2	Pressure Drop	44
3.2.3	Airflow Rate	46
3.3	Calibration of Instruments	47
3.3.1	Calibration of Thermocouple	47
3.3.2	Calibration of Manometer	49
3.3.3	Calibration of Wattmeter	49
3.4	Experimental Procedures	50
3.5	Handling of Experimental Data	52
3.6	Generalizations for Nusselt Number and Friction Factor	56
3.7	Experimental Reliability	57
4	THERMAL AND HYDRODYNAMIC PERFORMANCES OF THE RIBBED TRIANGULAR DUCT	59
4.1	Arrangement of Ribs	60
4.2	Average Nusselt Number	61
4.2.1	Effects of Rib Size	61
4.2.2	Effects of Rib-to-Rib Spacing	66
4.2.3	Effects of Reynolds Number	68
4.2.4	Generalization of Average Nusselt Number	72
4.3	Average Friction Factor	76
4.3.1	Effects of Rib Size	76
4.3.2	Effects of Rib-to-Rib Spacing	79
4.3.3	Effects of Reynolds Number	81
4.3.4	Generalization of Average Friction Factor	84
4.4	Volume Goodness Factor	88
4.5	Summary	90
5	THERMAL AND HYDRODYNAMIC PERFORMANCES OF THE V-GROOVED TRIANGULAR DUCT	92
5.1	Arrangement of V-Grooves	92

5.2	Average Nusselt Number	94
5.2.1	Effects of V-Groove Apex Angle	94
5.2.2	Effects of Groove-to-Groove Spacing	95
5.2.3	Effects of Reynolds Number	97
5.2.4	Generalization of Average Nusselt Number	98
5.3	Average Friction Factor	100
5.3.1	Effects of V-Groove Apex Angle	100
5.3.2	Effects of Groove-to-Groove Spacing	101
5.3.3	Effects of Reynolds Number	102
5.3.4	Generalization of Average Friction Factor	103
5.4	Comparison between Ribbed and Grooved Surfaces	105
5.4.1	Forced Convection Characteristics	107
5.4.2	Fluid Friction Characteristics	108
5.4.3	Volume Goodness Factor	109
5.5	Summary	111
6	VISUALIZATION OF THE TURBULENT FLOW IN THE RIBBED TRIANGULAR DUCT	112
6.1	Experimental Set-Up	113
6.2	Experimental Methodology	115
6.2.1	Particle Image Velocimetry (PIV)	116
6.2.2	Setting up of the Test Rig	118
6.2.3	Analysis of Experimental Data	120
6.3	Results and Discussions	121
6.3.1	Velocity Fields and Distributions of Plane I	122
6.3.1.1	Smooth Triangular Duct	122
6.3.1.2	Ribbed-Triangular Duct	123
6.3.2	Velocity Fields and Distributions of Plane II	124
6.3.2.1	Smooth Triangular Duct	124
6.3.2.2	Ribbed-Triangular Duct	125
6.3.3	Velocity Fields and Distributions of Plane III	127
6.3.3.1	Smooth Triangular Duct	127
6.3.3.2	Ribbed-Triangular Duct	127
6.4	Summary	130

7	FLOW PREDICTIONS BY TWO TURBULENCE MODELS	131
7.1	Problem Description and Analysis	132
7.2	Governing Equations	133
7.3	Turbulence Models	134
	7.3.1 Standard $k - \varepsilon$ Model	135
	7.3.2 Reynolds Stress Model (RSM)	136
	7.3.3 Standard Wall Functions	137
7.4	Assumptions	137
7.5	Boundary Conditions	138
7.6	Numerical Scheme	140
7.7	Solution Techniques	141
7.8	Results and Discussions	142
	7.8.1 Flow Patterns around the Ribs	143
	7.8.2 Distributions of Local Nusselt Number along the Ribbed-Surface	146
	7.8.3 Distributions of Local Nusselt Number at Different Reynolds Numbers	150
	7.8.4 Comparison between Two Models	153
7.9	Summary	153
8	SIMULATION OF EFFECTS OF GEOMETRY ON RIB-DISTURBED TURBULENT FLOW	155
8.1	Problem Description and Analysis	156
8.2	Assumptions	158
8.3	Boundary Conditions	159
	8.3.1 Uniformly Ribbed Parallel Plates	159
	8.3.2 Smooth Equilateral Triangular Duct	161
8.4	Numerical Schemes	162
	8.4.1 Uniformly Ribbed Parallel Plates	162
	8.4.2 Smooth Equilateral Triangular Duct	162
8.5	Solution Techniques	164
8.6	Results and Discussions	164
	8.6.1 Uniformly Ribbed Parallel Plates	164
	8.6.2 Smooth Equilateral Triangular Duct	166
	8.6.3 Comparison	169
8.7	Summary	171

9	SIMULATION OF TURBULENT FLOW IN THE RIBBED TRIANGULAR DUCT WITH 3-D MODELS	173
9.1	Three-Dimensional (3-D) Turbulence Model	174
9.1.1	Development of 3-D Model	174
9.1.2	Assumptions	176
9.1.3	Periodic Conditions	176
9.2	Solution Procedures	177
9.3	Results and Discussions	178
9.3.1	Velocity Fields and Distributions of Plane I	180
9.3.1.1	Smooth Triangular Duct	180
9.3.1.2	Ribbed-Triangular Duct	183
9.3.2	Velocity Fields and Distributions of Plane II	185
9.3.2.1	Smooth Triangular Duct	185
9.3.2.2	Ribbed-Triangular Duct	186
9.3.3	Velocity Fields and Distributions of Plane III	189
9.3.3.1	Smooth Triangular Duct	189
9.3.3.2	Ribbed-Triangular Duct	190
9.4	Summary	195
10	CONCLUSIONS AND SUGGESTIONS FOR FUTURE WORK	197
10.1	Conclusions	197
10.1.1	Experimental Measurement of Turbulent Flow in the Rib- or V-Groove- Roughened Triangular Duct	198
10.1.2	Numerical Prediction of Turbulent Flow in the Ribbed Triangular Duct	201
10.2	Suggestions for Future Work	203
	PUBLICATIONS ARISING FROM THE THESIS	205
	REFERENCES	206
APPENDICES:		
I.	Error Analysis and Estimation	I-1
II.	Determination of Mass Flow Rate	II-1
III.	Instruments Used in Experiments	III-1

LIST OF FIGURES

Figure 1-1.	Plate-pin compact heat exchanger with isosceles-triangular cross-sectional passages	3
Figure 1-2.	Roughened surfaces: (a). Rib-roughened surface; (b). V-groove-roughened surface.	6
Figure 3-1.	The schematic experimental set-up	38
Figure 3-2.	Cross view of the triangular duct	40
Figure 3-3.	Locations of temperature measurement along the triangular duct	43
Figure 3-4.	Locations of temperature measurement in a cross-sectional plane of the triangular duct	44
Figure 3-5.	Locations of pressure measurement in a cross-sectional plane of the triangular duct	45
Figure 3-6.	Thermocouple calibrator	48
Figure 3-7.	A digital multi-meter for wattmeter calibration	50
Figure 4-1.	Schematic representation of the ribbed surface	60
Figure 4-2.	Variation of Nu with Re for square ribs of different e 's	62
Figure 4-3.	Variation of Nu with H/D ($Re = 10,400$, $S_r/W = 7.22$)	64
Figure 4-4.	Variation of Nu with Re for square ribs of different S_r 's	66
Figure 4-5.	Variation of Nu with S_r/W ($Re = 10,400$, $H/D = 0.1795$)	67
Figure 4-6.	Plot of effect of Re on Nu	69
Figure 4-7.	Plot of effect of H/D on Nu	70
Figure 4-8.	Plot of effect of Re on Nu	71
Figure 4-9.	Plot of effect of S_r/W on Nu	72
Figure 4-10.	Plot of effect of Re on Nu	73
Figure 4-11.	Plot of effect of S_r/W on Nu	74
Figure 4-12.	Plot of effect of H/D on Nu	75
Figure 4-13.	Variation of f with Re for square ribs of different e 's	77
Figure 4-14.	Variation of f with H/D ($Re = 10,400$, $S_r/W = 7.22$)	78

<i>Figure 4-15.</i>	<i>Variation of f with Re for square ribs of different S_r's</i>	79
<i>Figure 4-16.</i>	<i>Variation of f with S_r/W ($Re = 10,400, H/D=0.1795$)</i>	80
<i>Figure 4-17.</i>	<i>Plot of effect of Re on f</i>	82
<i>Figure 4-18.</i>	<i>Plot of effect of H/D on f</i>	82
<i>Figure 4-19.</i>	<i>Plot of effect of Re on f</i>	83
<i>Figure 4-20.</i>	<i>Plot of effect of S_r/W on f</i>	83
<i>Figure 4-21.</i>	<i>Plot of effect of Re on f</i>	84
<i>Figure 4-22.</i>	<i>Plot of effect of S_r/W on f</i>	85
<i>Figure 4-23.</i>	<i>Plot of effect of H/D on f</i>	85
<i>Figure 4-24.</i>	<i>Plot of experimental and predicted values of Nu</i>	87
<i>Figure 4-25.</i>	<i>Plot of experimental and predicted values of f</i>	87
<i>Figure 4-26.</i>	<i>Variation of h with Es for different e's</i>	89
<i>Figure 4-27.</i>	<i>Variation of h with Es for different S_r's</i>	89
<i>Figure 5-1.</i>	<i>Schematic representation of the uniformly-spaced V-grooved surface</i>	94
<i>Figure 5-2.</i>	<i>Variation of Nu with Re for different θ's</i>	96
<i>Figure 5-3.</i>	<i>Variation of Nu with Re for different S_v's</i>	96
<i>Figure 5-4.</i>	<i>Plot of effect of Re on Nu</i>	98
<i>Figure 5-5.</i>	<i>Plot of effect of S_v/D on Nu</i>	99
<i>Figure 5-6.</i>	<i>Plot of effect of \mathcal{G} on Nu</i>	99
<i>Figure 5-7.</i>	<i>Variation of f with Re for different θ's</i>	101
<i>Figure 5-8.</i>	<i>Variation of f with Re for different S_v's</i>	102
<i>Figure 5-9.</i>	<i>Plot of effect of Re on f</i>	103
<i>Figure 5-10.</i>	<i>Plot of effect of S_v/D on f</i>	104
<i>Figure 5-11.</i>	<i>Plot of effect of \mathcal{G} on f</i>	104
<i>Figure 5-12.</i>	<i>Comparison of predicted and measured values of Nu</i>	106
<i>Figure 5-13.</i>	<i>Comparison of predicted and measured values of f</i>	106
<i>Figure 5-14.</i>	<i>Comparison of Nu for ribbed and grooved surfaces</i>	108

<i>Figure 5-15.</i>	<i>Comparison of f for ribbed and grooved surfaces</i>	<i>109</i>
<i>Figure 5-16.</i>	<i>Comparison of h for ribbed and grooved surfaces</i>	<i>110</i>
<i>Figure 6-1.</i>	<i>Equilateral triangular duct with internal ribbed surfaces</i>	<i>114</i>
<i>Figure 6-2.</i>	<i>Measurement planes for the triangular duct with internal ribbed-surfaces</i>	<i>115</i>
<i>Figure 6-3.</i>	<i>PIV experimental set-up</i>	<i>118</i>
<i>Figure 6-4.</i>	<i>A photo of the PIV experiment: the ribbed triangular duct in the wind tunnel</i>	<i>119</i>
<i>Figure 6-5.</i>	<i>A sample of the camera imagine recordings</i>	<i>122</i>
<i>Figure 6-6.</i>	<i>(a). Velocity field (b). Corresponding vorticity map in Plane I for the smooth triangular duct</i>	<i>123</i>
<i>Figure 6-7.</i>	<i>(a). Velocity field (b). Corresponding vorticity map in Plane I for the ribbed triangular duct</i>	<i>124</i>
<i>Figure 6-8.</i>	<i>Velocity profile in Plane II for the smooth triangular duct</i>	<i>125</i>
<i>Figure 6-9.</i>	<i>Velocity profile in Plane II for the ribbed triangular duct</i>	<i>126</i>
<i>Figure 6-10.</i>	<i>Velocity profile in Plane III for the smooth triangular duct</i>	<i>127</i>
<i>Figure 6-11.</i>	<i>Velocity profiles in Plane III for the ribbed triangular duct (a). the upper part; (b). the lower part.</i>	<i>128</i>
<i>Figure 7-1.</i>	<i>Geometry of the two-parallel-plate channel with eight identical ribs</i>	<i>133</i>
<i>Figure 7-2.</i>	<i>The mesh distribution of the typical computational domain</i>	<i>141</i>
<i>Figure 7-3.</i>	<i>Predicted streamlines of the turbulent flow in the channel at different Reynolds numbers by the Standard $k - \varepsilon$ Model (a). $Re = 22,000$; (b). $Re = 44,000$; (c). $Re = 63,000$; (d). $Re = 80,000$; (e). $Re = 94,000$.</i>	<i>144</i>
<i>Figure 7-4.</i>	<i>Predicted streamlines of the turbulent flow in the channel at different Reynolds numbers by the RSM (a). $Re = 22,000$; (b). $Re = 44,000$;</i>	<i>145</i>

	(c). $Re = 63,000$;	
	(d). $Re = 80,000$;	
	(e). $Re = 94,000$.	
Figure 7-5.	<i>Isotherms of the turbulent flow around the ribs as predicted by</i>	146
	(a). <i>the Standard $k - \varepsilon$ Model;</i>	
	(b). <i>the RSM.</i>	
Figure 7-6.	<i>Predicted distribution of local Nusselt number along the ribbed surface at $Re = 94,000$</i>	147
Figure 7-7.	<i>The distribution of Nusselt number above the seventh rib at $Re = 94,000$</i>	149
Figure 7-8.	<i>The distribution of Nussult number at different Reynolds numbers predicted with the Standard $k - \varepsilon$ Model</i>	151
Figure 7-9.	<i>The distribution of Nusselt number at different Reynolds numbers predicted with the RSM</i>	152
Figure 8-1.	<i>The geometry of</i>	157
	(a). <i>a parallel plate channel with three identical ribs;</i>	
	(b). <i>an equilateral triangular duct with smooth internal surface.</i>	
Figure 8-2.	<i>Mesh distribution of a typical computational domain of</i>	163
	(a). <i>the ribbed parallel plate channel;</i>	
	(b). <i>the equilateral triangular duct.</i>	
Figure 8-3.	<i>Streamlines around the ribs at $Re = 10,400$</i>	165
Figure 8-4.	<i>The local Nusselt number distribution around the rib at $Re = 10,400$</i>	166
Figure 8-5.	<i>The isotherms around the ribs at $Re = 10,400$</i>	167
Figure 8-6.	<i>Velocity vectors in the cross section of an equilateral triangular duct at $Re = 10,400$</i>	167
Figure 8-7.	<i>Normal stresses along the bisector lines of an equilateral triangular duct at $Re = 10,400$</i>	168
Figure 8-8.	<i>Comparisons of experimental and predicted Nu 's</i>	170
Figure 9-1.	<i>The mesh distribution of the ribbed triangular duct</i>	175
Figure 9-2.	<i>Schematic computational-cell with the nodal grid pattern</i>	177
Figure 9-3.	<i>Locations of planes (I, II, III) and lines (A, B, C) in the triangular duct with internal ribbed-surfaces</i>	179
Figure 9-4.	<i>Velocity profiles in Plane I of the smooth triangular duct</i>	181

	<i>as,</i>	
	<i>(a). measured by PIV in Chapter 6;</i>	
	<i>(b). predicted by RSM in Chapter 8,</i>	
	<i>and corresponding vorticity maps as,</i>	
	<i>(c). measured by PIV in Chapter 6;</i>	
	<i>(d). predicted by RSM in Chapter 8.</i>	
<i>Figure 9-5.</i>	<i>Velocity distribution on Plane I for the smooth triangular duct</i>	<i>182</i>
<i>Figure 9-6.</i>	<i>Velocity profiles in Plane I of the ribbed triangular duct as,</i>	<i>184</i>
	<i>(a). measured by PIV in Chapter 6;</i>	
	<i>(b). predicted by RSM in Chapter 8,</i>	
	<i>and corresponding vorticity maps as,</i>	
	<i>(c). measured by PIV in Chapter 6;</i>	
	<i>(d). predicted by RSM in Chapter 8.</i>	
<i>Figure 9-7.</i>	<i>Velocity distribution on Plane I for the ribbed triangular duct</i>	<i>185</i>
<i>Figure 9-8.</i>	<i>Velocity profile in Plane II of the smooth triangular duct</i>	<i>186</i>
<i>Figure 9-9.</i>	<i>Velocity distribution on Plane II for the smooth triangular duct</i>	<i>187</i>
<i>Figure 9-10.</i>	<i>Velocity profiles in Plane II of the ribbed triangular duct as,</i>	<i>188</i>
	<i>(a). measured by PIV;</i>	
	<i>(b). predicted by RSM.</i>	
<i>Figure 9-11.</i>	<i>Velocity distribution on Plane II for the ribbed triangular duct</i>	<i>189</i>
<i>Figure 9-12.</i>	<i>Velocity profile in Plane III for the smooth triangular duct</i>	<i>190</i>
<i>Figure 9-13.</i>	<i>Velocity profile in Plane III for the ribbed triangular duct</i>	<i>191</i>
<i>Figure 9-14.</i>	<i>Velocity distribution on Plane III for the smooth triangular duct</i>	<i>194</i>
<i>Figure 9-15.</i>	<i>Velocity distribution on Plane III for the ribbed triangular duct</i>	<i>194</i>

LIST OF TABLES

<i>Table 4-1.</i>	<i>Ranges of rib size and spacing ($D = 44\text{mm}$)</i>	<i>61</i>
<i>Table 5-1.</i>	<i>Ranges of V-groove's apex angle and spacing ($D = 44\text{mm}$, $d = 1\text{mm}$)</i>	<i>93</i>

NOMENCLATURE

A	Inner heat transfer surface area of the duct wall [m^2]
A_c	Cross-sectional area of the triangular duct [m^2]
A_0, A_1	Coefficients in Equation (4-11)
a	Side length of the triangular duct [m]
B_0, B_1, B_2	Coefficients in Equation (4-12)
b	Height of the triangular duct [m]
C_p	Specific heat at constant pressure [$\text{J}\cdot\text{kg}^{-1}\cdot\text{K}^{-1}$]
C_μ	Viscosity constant [$\text{N}\cdot\text{m}^{-2}\cdot\text{s}^{-1}\cdot\text{K}^{-1}$]
C_1, C_2	Modeling constant in Chapter 7
C_1, C_2, C_3	Coefficients in Equations (3-10, 12, 13) of Chapter 3; Coefficients in Equation (4-13) of Chapter 4
D	Hydraulic diameter of the triangular duct [m]
d	Depth of the V-groove [m]
E	Electric power supplied to heat the triangular duct [W]
E_s	Standard pumping power per unit heat transfer area, namely, Volume Goodness Factor [$\text{W}\cdot\text{m}^{-2}$]
e	Rib Size [m]
F	View factor for thermal radiation from the duct ends to its surroundings
f	Average fanning friction factor, dimensionless
g_c	Proportionality constant in Newton's second law of motion, $g_c = 1$
H	Rib height [m]
h^*	Dimensionless rib height, $h^* = H / L$
h	Convection heat transfer coefficient [$\text{W}\cdot\text{m}^{-2}\cdot\text{K}^{-1}$]
k	Thermal conductivity of air [$\text{W}\cdot\text{m}^{-1}\cdot\text{K}^{-1}$]
k_p	Thermal conductivity of the plywood [$\text{W}\cdot\text{m}^{-1}\cdot\text{K}^{-1}$]

k_w	Thermal conductivity of the duct wall [$\text{W}\cdot\text{m}^{-1}\cdot\text{K}^{-1}$]
L	Axial length of the triangular duct [m]
\tilde{L}	Periodic length of the triangular duct [m]
l	Thickness of the plywood [m]
M	Magnification factor
\dot{m}	Mass flow rate [$\text{kg}\cdot\text{s}^{-1}$]
n_1, n_2, n_3	Power indices in Equations (3-10, 12, 13)
Nu	Average Nusselt number based on the hydraulic diameter, dimensionless
Nu_x	Local Nusselt number at the location of x
P	Fluid pressure [Pa]
P_0	Periodic part of pressure in Chapter 8 [Pa]
Pr	Prandtl number of air, dimensionless
Q	Heat input per unit length of the channel [$\text{W}\cdot\text{m}^{-1}$]
Q_c	Steady-state heat transfer from the triangular duct to the fluid [W]
Q_l	Heat loss from the external surfaces of the triangular duct to the surroundings [W]
Q_r	Radiation heat loss from both ends of the triangular duct to the surroundings [W]
\dot{q}	Heat flux [$\text{W}\cdot\text{m}^{-2}$]
Ra	Rayleigh Number, dimensionless
Re	Reynolds number based on the hydraulic diameter, dimensionless
S	Spacing between two adjacent roughness elements [m]
S_r	Spacing between two adjacent ribs [m]
S_v	Spacing between two adjacent V-grooves [m]
T	Temperature for the fluid [K]
T_0	Inlet temperature of the fluid (ambient temperature);
T_a	Mean temperature of the airflow [K]
T_{ai}	Mean inlet temperature of the airflow [K]

T_∞	Mean outlet temperature of the airflow [K]
T_p	Wall temperature of the plywood [K]
T_w	Wall temperature of the triangular duct [K]
T_∞	Ambient temperature [K]
U	Mean air velocity in the triangular duct [$\text{m}\cdot\text{s}^{-1}$]
U_∞	Free stream (approach) velocity [$\text{m}\cdot\text{s}^{-1}$]
u	Velocity component in x direction [$\text{m}\cdot\text{s}^{-1}$]
u^*	Dimensionless velocity component in x direction, $u^* = u/U$
u_i	Velocity component in i direction [$\text{m}\cdot\text{s}^{-1}$]
u_j	Velocity component in j direction [$\text{m}\cdot\text{s}^{-1}$]
u_k	Velocity component in k direction [$\text{m}\cdot\text{s}^{-1}$]
$\overline{u_i u_j}$	Turbulent shear stress [$\text{m}^2\cdot\text{s}^{-2}$]
$\overline{u_i t}$	Turbulent heat flux [$\text{m}\cdot\text{s}^{-1}\cdot\text{K}$]
v	Velocity component in y direction [$\text{m}\cdot\text{s}^{-1}$]
v^*	Dimensionless velocity component in y direction, $v^* = v/U$
W	Rib width [m]
w	Velocity component in z direction [$\text{m}\cdot\text{s}^{-1}$]
w^*	Dimensionless velocity component in z direction, $w^* = w/U$
x	Coordinate in x direction [m]
x^*	Dimensionless x coordinate
x_i	Coordinate in i direction [m]
x_j	Coordinate in j direction [m]
x_k	Coordinate in k direction [m]
Δx	Measurement error in Chapter 6 [m]
y	Coordinate in y direction [m]
y^*	Dimensionless y coordinate
z	Coordinate in z direction [m]
z^*	Dimensionless z coordinate

Greek symbols

ε	Turbulent dissipation rate [$\text{m}^2 \cdot \text{s}^{-3}$]
ε_γ	Mean surface emissivity with respect to thermal radiation
κ	Turbulent kinetic energy [$\text{m}^2 \cdot \text{s}^{-2}$]
λ	Thermal conductivity of the fluid [$\text{W} \cdot \text{m}^{-1} \cdot \text{K}^{-1}$]
θ	Dimensionless temperature, $\theta = (T - T_0)/(Q/k_f)$
θ	Apex angle of the V-groove [degree]
ϑ	Apex angle of the V-groove [rad]
μ	Dynamic viscosity of the fluid [$\text{Kg} \cdot \text{m}^{-1} \cdot \text{s}^{-1}$]
μ_{eff}	Effective viscosity of the fluid [$\text{Kg} \cdot \text{m}^{-1} \cdot \text{s}^{-1}$]
μ_t	Turbulent viscosity of the fluid [$\text{Kg} \cdot \text{m}^{-1} \cdot \text{s}^{-1}$]
ν	Kinematic viscosity of the fluid [$\text{m}^2 \cdot \text{s}^{-1}$]
ρ	Density of the fluid [$\text{kg} \cdot \text{m}^{-3}$]
σ	Stefan-Boltzmann constant [$= 5.67 \times 10^{-8} \text{W} \cdot \text{m}^{-2} \cdot \text{K}^{-4}$]
α	Thermal diffusivity [$\text{m}^2 \cdot \text{s}^{-1}$]
β	Non-periodic pressure gradient [$\text{Pa} \cdot \text{m}^{-1}$]

Subscripts

a	Air
i	Inlet plane of the triangular duct
f	Fluid
L	Left
max	Maximum value
min	Minimum value
o	Outlet plane of the triangular duct
p	Plywood
R	Right
r	Rib
s	Solid
T	Top

t	Total
v	V-groove
w	Wall of the triangular duct
∞	Free stream

1 INTRODUCTION

1.1 Scope and Background

Heat exchangers are often used in many industrial applications, such as chemical process, cryogenic techniques, steam power engineering, air-conditioning and refrigeration, heat pumps and systems, as well as mobile power plants for automotive, marine and aerospace vehicles. As the most frequently applied and sophisticated component in engineering projects, the heat exchanger's importance has been increased greatly not only for the viewpoint of energy conservation, conversion, recovery and implementation of new energy sources, but also for environmental concerns such as thermal pollution, air/water pollution, and waste disposal. Proper functioning of the heat exchanger ensures effective and reliable operations of various kinds of installations. For example, heat exchangers are used widely on the board ship to transfer heat from hot fluid to seawater. In a motor ship, its main propulsion engine, engine jacket water, lubricating oil and charging air must be cooled as well as water and oil used in cooling the pistons. For a steam ship, apart from the heat yielded by the main condenser, the turbine and gearbox lubricating oil provide the main source of heat. Auxiliary prime movers and compressor inter-coolers and after-coolers also require cooling. Failing to transfer the heat rapidly to the environment will lead to malfunction and breakdown of the entire system. Therefore, there are many kinds of heat exchangers such as heavy fuel heaters, boiler air pre-heaters, and units to heat seawater for tank washing, evaporators, feed heaters as well as clarifiers.

Since the first industrial revolution, heat exchanger design has gone through several innovations. More and more industrial engineers focus on the investigation of the heat exchanger [Podhorsky et al. 1998; Roetzel et al. 1999; Ramesh et al. 2003]. Due to its wide use in practice, it is essential to design an effective and practical heat exchanger. An optimum thermal design of the heat exchanger can be obtained with a good understanding of the fundamental knowledge of its thermal characteristics, which include right flow conditions and suitable structure of the heat exchanger. For various service aspects, there are different kinds of heat exchangers with a variety of types, shapes, arrangements and combinations. Generally, heat exchangers used most in industrial applications can be classified into *tubular* and *plate* types according to the geometrical characteristics. Because of the geometrical advantage, the tubular exchanger, which can tolerate a higher temperature and pressure, is always adopted in a wider range of applications than the plate one. However, considering the limited space and manufacture cost in practical applications, more and more plate exchangers are used in various units or systems. A compact plate-pin heat exchanger with tightly packed triangular cross-sectional flow passage is shown in Fig. 1-1. Comparing to a traditional shell-and-tube type heat exchanger, it has advantages of compactness (i.e. a high ratio of heat-transfer surface area to core volume, usually in excess of $700\text{m}^2/\text{m}^3$), relative lightweight, low construction cost, easy operation, as well as convenient flow arrangement. Therefore, it gradually becomes a preferred choice of many industrial applications, especially in vehicles, aircrafts, space shuttles and electronic equipments.

However, the compact plate-pin heat exchanger has a disadvantage of a relatively poor thermal performance per unit surface area [Kays et al. 1984]. To overcome this

drawback and achieve a highest possible compactness, a variety of high-performance secondary surfaces are often produced along the flow passage to increase the heat transfer areas and promote turbulence in the flow, which helps to achieve high heat transfer coefficients even at low flow rates. Such effective secondary surfaces can be achieved by artificially roughening processes, such as machining (i.e. milling, shaping, casting and sand blasting), or fixing ribs or cutting grooves along the axial length of the flow passage.

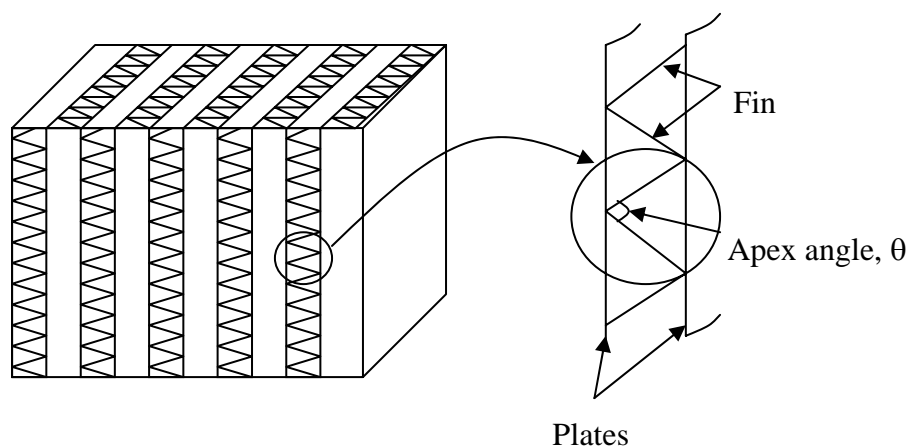


Fig. 1-1 Plate-pin compact heat exchanger with isosceles-triangular cross-sectional passages

Then, what will be the fluid flow characteristics in the heat exchanger after introduction of the additional roughness? Basically, fluid needs to be pumped through the compact plate-pin heat exchanger in most applications. On the one hand, the major heat transfer mechanism occurring in the flow passage of the heat exchanger is forced convection, which affects most, compared to heat conduction in

the plates or other components, the overall heat transfer rate. On the other hand, it is essential to determine the fluid pumping power required as part of system design and operating cost analysis. The fluid pumping power is proportional to the axial pressure drop, which is associated with fluid friction and other pressure drop contributions such as sudden contraction and expansion losses, bend losses, and branch losses, which are depending on the geometry along the fluid flow path. Many studies [Braaten et al. 1984, Hirota et al. 1998, Kim et al. 1995] have been conducted to investigate the channel flow with artificial roughness and it is recovered that though an enhanced forced convection is obtained consequently, a higher fluid friction ensues as well, which results in a higher pressure drop along the flow direction and thus a higher pumping power required for driving the fluids. How to get a highest effectiveness of a compact plate-pin heat exchanger becomes an interesting topic of many industrial engineers. As important factors to evaluate the effectiveness of a heat exchanger, its heat transfer and pressure drop performances need to be considered simultaneously.

In addition, fluid flows into and out of heat exchangers through passages such as pipes, ducts, or nozzles. Geometry of the flow passage as well as flow conditions in a heat exchanger affects its thermal and dynamic performances significantly. The situation is far more complicated when artificially roughness is fabricated on the flow passage's internal surfaces. In this case, shape, size and arrangement of the roughness should also affect the heat exchanger's overall performance. Liou et al. [1993] and Ahn [2001] studied the flow characteristics in a rectangular channel with internal ribbed surfaces. Several kinds of rib shapes were applied: square, triangle,

circle, semicircle and wire, and it was found that rib shape has a great influence on heat transfer and friction factor of the flow.

Consequently, forced convection and fluid friction of flows in pipes or ducts (i.e., internal flows) with a diversity of cross-sectional shapes and geometries need to be investigated in order to study the fluid's behaviors when it is flowing through various kinds of passages in compact heat exchangers.

1.2 Research Objectives

As shown in Fig. 1-1, flow passages of a compact plate-pin heat exchanger are usually of triangular cross-section. A duct with a flow passage of triangular cross-section is in preference to ducts of circular, rectangular, square or other cross-sections for its high compactness and convenience to fabricate. In addition, an equilateral triangle shape is suggested to give the best convective heat transfer performance among various kinds of triangular configurations [Leung et al. 1997], therefore, an equilateral triangular duct is selected for investigation in the present research study. To improve its thermal performance, internal surfaces of the triangular duct are roughened artificially, either by fixing square ribs or by cutting V-grooves as shown schematically in Fig. 1-2, since they achieve much better performances than machined roughness [Wong et al. 2002]. A rougher surface and thus a higher axial pressure drop along the triangular duct are expected to occur.

How does the particular geometry affect the thermal and dynamic characteristics of the flow in a triangular duct? To explore the heat transfer performance of a triangular duct fabricated with artificial roughness requires a simultaneously analysis

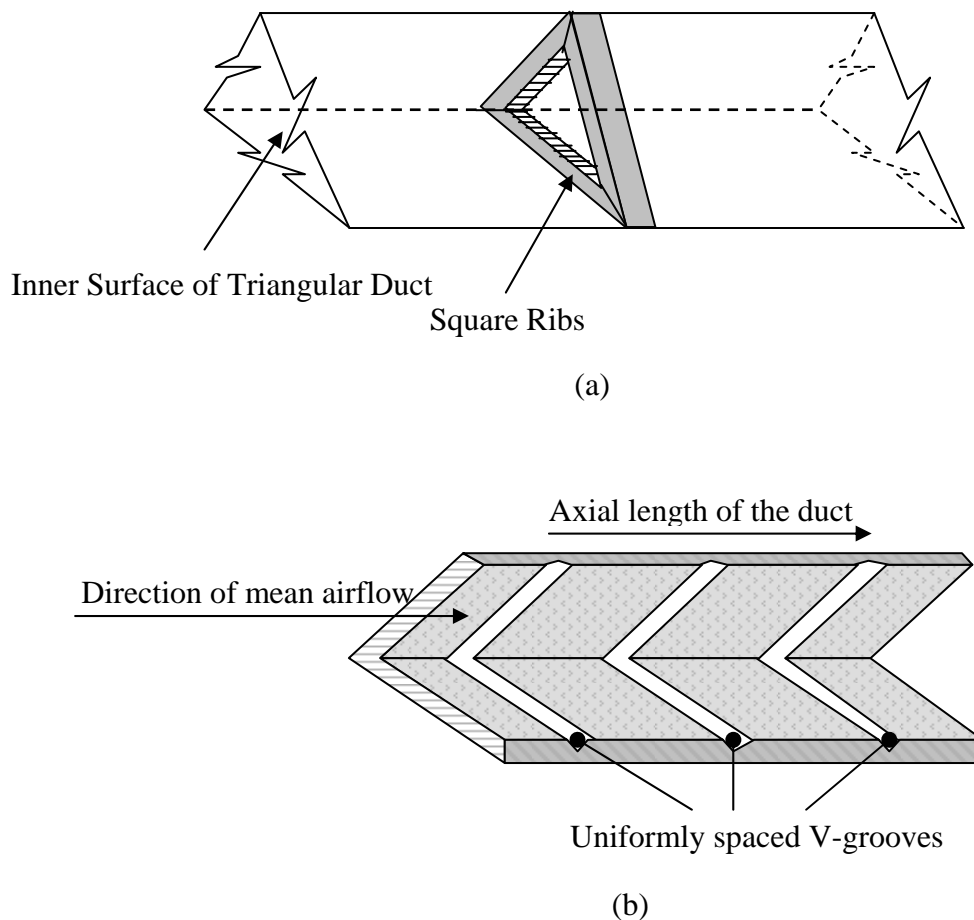


Fig. 1-2 Roughened surfaces: (a) Rib-roughened surface; (b) V-groove-roughened surface

of heat conduction within the duct wall, surface roughness on the internal surfaces, and forced convection and fluid friction along the flow passage. In addition, since compact heat exchangers are usually operated under turbulent flow conditions (i.e., for forced convection conditions, a turbulent flow is achieved by an internal flow with a hydraulic-diameter-based Reynolds number, $Re \geq 2,000$) because of the large cooling capacity required, especially when the working fluid has a high density (i.e. $1,000\text{kg/m}^3$ for water), a study on the behavior of the turbulent flow rather than the

laminar flow (i.e., for forced convection conditions, a laminar flow is achieved by an internal flow with a hydraulic-diameter-based Reynolds number, $Re \leq 2,000$) is more meaningful to heat-exchanger designers. However, quantitative knowledge of the forced convection characteristics concerning turbulent flow is relatively rare. A comprehensive and in-depth study on turbulent forced convection in the triangular duct fabricated with internal roughened surfaces is hence needed to achieve a better understanding of the thermal performance of the compact heat exchanger.

The present investigation will be performed with an air-cooled horizontal equilateral triangular duct with internal ribbed or grooved surfaces under various turbulent flow conditions. The following studies will be concentrated on essentially:

- 1) Experimental study to identify the effects of rib size, rib-to-rib spacing and Reynolds number on forced convection and fluid friction in the triangular duct attached with uniformly spaced square ribs on its internal surfaces.
- 2) Experimental study on the effects of V-groove angle, groove-to-groove spacing and Reynolds number on forced convection and fluid friction in the triangular duct fabricated with uniformly spaced V-grooves on its internal surfaces.
- 3) Developments of non-dimensional equations to predict the heat transfer coefficients and friction factors of the triangular ducts with ribbed or grooved internal surfaces.
- 4) Visualization of the turbulence-generated secondary flow in the near-wall regions of the triangular duct with uniformly ribbed internal surfaces.
- 5) Numerical simulation of the forced convection in a triangular duct with ribbed internal surfaces, based on both two-dimensional (2-D) and three-dimensional (3-D) models.

- 6) Comparison between the results of the experimental and numerical work to further study the effects of roughness, secondary flow, as well as Reynolds number on forced convective heat transfer in the triangular duct with internal ribbed surfaces.

This project has both academic value and practical significance to the industry. Valuable information will be obtained from this project to optimize the thermal and dynamic performances of a compact heat exchanger having a triangular cross-section, which is of importance in maintaining an effective and reliable operation of its associated industrial applications. Outcome of this investigation will be very useful for engineering systems, which require efficient cooling. When sufficient results have been obtained to provide a good fundamental knowledge, it is expected to achieve the following objectives:

- 1) Optimum rib size, V-groove angle, rib-to-rib spacing and groove-to-groove spacing can be identified, respectively, thus better utilization of the thermal performance of the compact heat exchanger becomes possible.
 - 2) Non-dimensional expressions for determinations of the steady-state heat transfer coefficients and fanning friction factors of the equilateral triangular duct with internal ribbed or grooved surfaces can be developed.
 - 3) The obtained experimental results can be used to provide qualified data for the evaluation of associated numerical results.
 - 4) The flow pattern of the secondary flow in the roughened triangular duct can be visually predicted from both experimental and numerical approaches. The mechanism of the secondary flow on affecting the performance of the turbulent flow can be further understood.
-
-

-
-
- 5) Appropriate numerical models can be proposed to simulate this kind of complicated thermal system.
 - 6) It is hoped that the numerical simulation method developed in the present study can also be applicable to ducts with multi-corner cross-sectional geometries.

1.3 Layout of Present Thesis

Present thesis includes both experimental and numerical study reports. Ten chapters are involved.

Chapter 1 offers an overview of the scope and background of the present project. Heat exchangers, as important parts in many industrial and engineering applications, have been being developed for several decades. To improve their thermal performances and thus obtain better utilizations, efforts are carried on by engineering designers. The objectives of this research work are proposed.

A lot of related studies have been conducted previously, which are summarized in Chapter 2. Because of the still insufficient information, further investigations need to be taken. How to fill up the research gaps and fulfill the present project? Basic ideas are presented.

Thermal performance of the artificially roughened triangular duct, which is either attached with square ribs or cut with V-grooves on its internal surfaces, is studied experimentally. Experimental arrangement and methodology are described in Chapter 3, while experimental results for either ribbed or V-grooved triangular duct can be found in Chapters 4 and 5, respectively. Non-dimensional expressions for

predictions of Nusselt number and friction factor are also proposed for industrial reference. In addition, comparisons between these two kinds of roughened surfaces are conducted as well.

Turbulence-generated secondary flow in the triangular duct with internal ribbed surface, which is chosen as a typical and efficient roughened surface, are analyzed particularly through flow visualization method, see in Chapter 6. Particle Image Velocimetry (PIV) method is applied. Three-dimensional motion of the disturbed turbulent flow is detected. Velocity fields as well as velocity distributions in the triangular duct with or without ribbed surface are provided, which reasonably well explain the flow characteristics in this kind of complicated triangular duct.

Chapters 7 and 8 report some numerical studies of the turbulent flows in the rib-roughened triangular duct. The prediction abilities of two turbulence models, in the present study, namely, the Standard $k-\varepsilon$ Model and Reynolds Stress Model (RSM), are verified. A comparison between these two models is also performed, which provides a basic application background on channel flow simulations.

To further understand the turbulent flow in such a complicated flow system, a three-dimensional Reynolds Stress Model, which is stated in Chapter 9, is introduced. Secondary flows in the near-wall regions are predicted successfully, which are further validated through detailed comparisons with experimentally measured results.

Findings from the present project work are summed up in Chapter 10. Future work is also recommended and proposed, which is of importance and needs to be conducted further.

2 LITERATURE REVIEW

Nowadays, the heat exchanger plays a more and more important role in many industrial installations. It is of importance to enhance its thermal performance as much as possible while the pumping power requirement is maintained at an acceptable level. Due to the limited space in engineering applications, a heat exchanger with a compact configuration becomes a preferred choice.

Relevant studies have been conducted with the aim to better utilize the thermal and hydraulic performances of a compact heat exchanger. Fully developed flows through single- and double- trapezoidal or hexagonal ducts were studied by Safasivam et al. [1999]. It was found that both Nusselt number and friction factor were depended on the duct geometry significantly, which directly influenced the capability and performance of the heat exchanger. In addition, as mentioned in Chapter 1, application of artificially roughened surfaces, which can be obtained by machining processes (e.g. milling, shaping, casting and sand blasting) or produced by fixing ribs or cutting grooves along the axial length of the flow passage, has been proven to be an effective method to improve the thermal performance of a heat exchanger.

Therefore, a study on the effects of flow passage geometry of the heat exchanger and artificial roughness on the flow passage surface becomes prosperous. However, due to the introduction of the roughened surfaces, the resultant geometry of the heat exchanger becomes more complicated. The investigation of a compact heat exchanger system with internal roughened surfaces is thus challenging.

2.1 Ducts with Smooth Internal Surfaces

Till now, many investigations have been performed to study the heat-transfer characteristics of flows in pipes or ducts with arbitrary cross-sections under laminar/turbulent flow conditions. A comprehensive review of the relevant literature was conducted by Incropera [1988] and Peterson et al. [1990].

2.1.1 Under Laminar Flow Conditions

When a fluid flows smoothly without interruptions and thus no vortices or other turbulence generated, the flow is called laminar. Laminar flow conditions attract interests of many researchers not only for low velocity, laminar flows, but also for some relative-high velocity, turbulent flows, in which a laminar layer often exists and plays an important role in heat transfer behavior of the turbulent flow. Therefore, laminar flows in various ducts under different thermal boundary conditions are substantially studied in many literatures.

Zhang et al. [1990] and Yilmaz et al. [1993] investigated the forced convection of a fully developed laminar flow in irregular ducts under constant wall temperature condition. General equations for heat transfer calculations were presented and the results obtained from these equations were compared well with the theoretically calculated values available in the literatures. As another commonly used thermal condition, uniform heat flux thermal condition was also applied additional to the constant wall temperature condition in the investigation of a hydro-dynamically laminar flow in ducts with arbitrary cross-sections [Uzun et al. 1997]. Generally higher local and averaged Nusselt numbers were obtained under the uniform heat flux boundary conditions than those under the uniform wall temperature conditions.

Xin et al. [1994] reported several cases of forced convection inside ducts including circular pipe, parallel plates, rectangular duct, isosceles triangular duct, and hexagonal duct. Heat transfer of ambient fluid to the duct was considered in addition to that inside the duct, which was approximated by the third thermal boundary condition (i.e. convective heat transfer between the ambient fluid and the duct surface). The Biot number was found to have significant effects on both the temperature distribution and Nusselt number. Effects of combined convective-radiative heat transfer of thermally developing gas flows in rectangular and equilateral triangular ducts were reported by Yang et al. [1991]. It was concluded that the influence of the radiation-conduction parameter on the thermal characteristic of the medium was substantial.

The work of Baliga et al. [1986] was related to the prediction of forced convective heat transfer in triangular cross-sectional plate-fin ducts under constant axial heat-transfer rate with arbitrary peripheral thermal boundary conditions. Heat conduction in the fin and convection in the fluid were analyzed simultaneously as a conjugate problem. They concluded that the average Nusselt number of the duct, which used hydraulic diameter as the characteristic physical dimension, was a constant and equal to 3.11 for the equilateral-triangular sectioned duct in laminar flow conditions. It was in good agreement with the findings of Shah [1975]. Compared to those obtained by Uzun et al. for the triangular duct: 3.018 under uniform heat flux condition, and 2.353 under constant wall temperature condition, a higher Nusselt number and thus a better heat transfer performance was obtained in this case.

Therefore, it can be concluded that the thermal condition applied has a great influence on the flow thermal performance.

2.1.2 Under Turbulent Flow Conditions

Compared to a smooth and undisturbed laminar flow, a turbulent flow refers to a fluctuant and jumbled flow, coming with eddies and chaotic motion that increases the resistance significantly and thus leads to a higher pressure required for a higher volume flow rate. The turbulent flow starts to occur at a certain Reynolds number, for example, a hydraulic-diameter-based Reynolds number of about 2,000 for the internal flow.

Investigations on turbulent flows have been conducted in many literatures. Wilson et al. [1968] employed the heat and momentum transfer analogy to analyze the heat transfer phenomena for turbulent flow in concentric annuli. A modification of the velocity distribution, which was suggested by Van Driest [1956], had been assumed. Thermal resistance was indicated to exist primarily in the sublayers. Once the sublayers were penetrated, diffusion of the heat over the entire annular gap became rapid and effective. Non-dimensional equations were also developed to predict maximum velocity, friction factor as well as temperature distribution.

Emery et al. [1980] predicted the velocity and temperature fields for both developing and fully developed turbulent flow in a square duct under constant wall temperature, constant wall heat flux or asymmetric heating conditions. Predicted values of Nusselt numbers in the entrance region of the heated duct were some lower than their fully developed counterparts. In addition, local wall shear stress and heat flux distributions exhibited peaking behaviors between the duct mid-plane and corner region.

Fully developed turbulent flows in rectangular, trapezoidal and triangular ducts were studied by Rokni et al. [2001]. These ducts were in either straight or wavy shape, with a common cross-section aspect ratio of 5 to 3. Velocity and temperature contours in ducts with different configurations were investigated in detail, and it was found that the cross-flows in wavy ducts were much stronger than the corresponding ones in the straight ducts, and that different cross-sectional shapes brought in insignificant thermal behavior differences between each other; however, taking the heat-transfer enhancement by the duct waviness into consideration, the triangular wavy duct provided a best performance. In addition, a triangular duct with an equilateral triangle cross-section was proven to be the optimum choice among various kinds of triangular configurations for the convective heat transfer performance [Leung et al. 1997].

The study of Ince et al. [1988] was related to a turbulent natural convection of air in rectangular enclosures. The convection was driven by buoyant forces, which came from the temperature difference between a vertical hot wall with uniform heat flux and an opposite vertical cold wall with constant temperature. Higher velocity levels were observed near the top than near the bottom. The thin upward-moving shear layer adjacent to the hot wall near the bottom of the cavity and the downward-moving flow near the top of the cold wall were found to be laminar. Mean Nusselt number was verified to increase with Rayleigh number (i.e. $Nu \propto Ra^{1/3}$), and the effects of aspect ratio were small.

2.2 Application of Surface Roughness

2.2.1 Ribbed Internal Surface

As the rib-attaching method is efficient to increase roughness of a surface, an enhancement potential in heat transfer rate between the fluid flow and a ribbed solid wall is prospective. Ohara et al. [1991] conducted an experimental investigation on a narrow vertical channel with ribbed internal surfaces. Effect of incorporating repeated transverse rectangular ribs on forced convective heat transfer was reported. A similar study was performed by Zhang et al. [1994]. The steady-state heat transfer was measured from the rectangular channels with ribbed internal surfaces. They all came to the conclusion that ribbed surfaces could enhance the heat transfer rate significantly.

Relevant studies have also been conducted to investigate the influence of adding uniformly spaced ribs on the thermal performance of a flat surface. Leung et al. [2001] carried out a study and discovered that in this situation, ribs acted not only as heat-transfer-area enlargers, but also as important turbulent-secondary-flow promoters. A study conducted by Kiml et al. [2001] on heat transfer and flow behaviors in a rectangular passage revealed that the rib-induced secondary flow attributed most to the heat transfer enhancement.

From the above investigations, it is undoubted that addition of ribbed surfaces is an effective way for heat transfer enhancement. However, the magnitude of this enhancement depends on many parameters related to the ribs including their shape, size, pitch, alignment, arrangement and material. All of them have influence on the flow performance. To understand the effects of these geometrical and physical

parameters on the forced convective flow, many investigators have made good efforts to study the flows in channels with rib-roughened surfaces [Lehmann et al. 1984 & 1985, Kwon et al. 2000].

Han [1984] measured the turbulent flow in a square duct with two or four opposite walls roughened with square cross-sectioned ribs. Effects of the rib size and pitch on heat transfer coefficient and friction factor were studied. It was discovered that a larger rib-size could produce not only higher heat transfer rates, but also higher friction factors; while a reversed situation was found for the rib pitch: a smaller rib pitch was recommended if higher heat transfer rates and friction factors were expected. Hereon, the effects of rib size and rib pitch on the thermal performance of a ribbed duct seem to be clear defined. However, a nearly opposite conclusion was obtained in some recent literatures. The work of Young et al. [1998, 1998] on the forced convection cooling of a heated obstacle mounted upon a channel wall with finite element formulation recovered that, smaller, widely spaced obstacles (compared to the findings of Han) were here found more effectively to dissipate heat instead.

More recently, a study on the effects of duct height-to-rib height and rib's width-to-height ratios on convective heat transfer characteristics in a laminar-flow region of a horizontally/vertically orientated simulated printed circuit board (PCB) assembly were conducted by Leung et al. [1997, 1998] from both experimental and numerical approaches. Electronically heated square ribs were mounted at a uniform spacing on one of the principal walls. It was found that for a larger duct height-to-rib height ratio, the heat was dissipated more efficiently, and natural convection became significant when this ratio was greater than 8; while a higher rib's width-to-height

ratio produced higher heat transfer coefficients, which implied a flat rib with a large top surface should be adopted to enhance heat dissipation.

Furthermore, both rib pitch-to-height ratio and Reynolds number also have great influence on the distribution of local heat transfer coefficient over ribbed surfaces [Hishida 1996]. However, the information available for the relationship between rib size and rib pitch with heat transfer coefficient and friction factor seems confusing, especially on the exact quantitative effects of the rib size and rib pitch on the thermal system involved. Continuous efforts are being made to solve this problem.

For the effects of rib shape, configuration and arrangement, relevant literatures focused on the studying of these parameters can be found. Han et al. [1978] investigated the effects of rib-angle-of-attack on friction factor and heat transfer coefficient for developing flow in rectangular ducts. The rib-angle-of-attack was varied from 90° to 30° . It was concluded that adding ribs at a 60° rib-angle-of-attack had a superior heat transfer performance at a given friction power over the other rib configurations. Later, Han et al. [1992] varied the orientations and arrangements of the ribs and measured local heat transfer characteristics of the roughened surface. They suggested that broken ribs had a higher heat transfer augmentation than the continuous ones. Moreover, the 60° V-shaped broken ribs gave the best thermal performance. A similar arrangement problem was studied by Leung et al. [1995], while the square-sectional ribs attached on the bottom surface of a rectangular duct were either cross- or parallel- arranged. Greater improvement was obtained by the cross-arranged ribbed surface than the traditional parallel-ribbed surface. However, a drawback of a higher friction factor and hence a larger pressure drop along the duct occurred. Moreover, ribs in either staggered or in-line alignments were applied by

Hong et al. [1993] to the internal surfaces of a rectangular or square channel. As a general conclusion, ducts with in-line ribs were operated with a better efficiency than those with staggered ribs.

Beside effects coming from rib size, spacing, and shape, and rib orientation and arrangement, other parameters related to the rib or the flow also have influences on the thermal performance of the ribbed duct, for example, the way of heating the ribbed surface [Uzun et al. 1997], the material of the ribbed tube [Hishida, 1996], and the orientation of the ribbed duct [Leung et al. 1997, 1998]. Specifically, a rib made of material of high thermal conductivity can achieve an effective isothermal distribution, and thus enhances the heat transfer rate of the thermal system [Young et al. 1998].

2.2.2 Grooved Internal Surface

The grooved internal surface is one of the most typical structures applied in engineering cooling systems. The segmentation of the grooved surface breaks the thermal boundary and increases the heat transfer area, thus enhances the thermal performance of the system. Extensive studies have been performed previously concerning heat transfer and fluid-friction characteristics for a channel with grooved inner surfaces.

Ghaddar et al. [1986] investigated the fully developed grooved channel flow based on a numerical method. The interaction between the groove shear layer and Tollmien-Schlichting waves in the bulk flow was found to have great influence on determining the flow characteristic. A resonant heat transfer enhancement was obtained when Reynolds number was greater than a critical value of $Re = 2,000$.

Greiner et al. [1991, 1991] experimentally studied the thermal performance of a channel with groove-roughened internal surfaces. It was stated that the rate of forced convection could be increased significantly by having the inner surfaces grooved, with the grooves arranged orthogonally to the mean flow. Later, Greiner et al. [2000, 2002] used spectral element technique to simulate a three-dimensional flow and augmented convection in a fully developed, symmetrically grooved passage as well as the flat passage downstream. Constant temperature boundary conditions were applied and a method was developed to calculate the fully developed heat transfer coefficient. The velocity and temperature fields were observed to evolve from steady-state two-dimensional flow to coherent traveling wave structures, and finally to three-dimensional mixing stage with increasing Reynolds number. Further downstream, unsteady flow that developed in the grooved region persisted several groove-lengths into the flat passage, which enhanced local heat transfer, even relative to the fully developed grooved passage.

As seen from the studies of Greiner et al., the groove-plus-flat passage affects the turbulent flow in a different way to either grooved-only or flat-only passage. However, thermal behavior by introducing grooves to ducts of other cross-section is yet uncertain. Zhang et al. [1994] conducted an investigation by applying compound tabulators formed by ribs plus grooves and considered the combined-effect of these two rougheners on the thermodynamic characteristics in rectangular ducts with opposite ribbed-grooved walls. A flatter velocity profile and higher turbulence intensity were obtained for rib-groove-roughened duct than either the rib- or groove-roughened duct; hence a higher heat transfer was produced. Stanton number and

friction factor values for the ribbed-grooved duct decreased with increasing rib-groove-pitch-to-rib-height ratio.

The effects of V-groove angle on heat transfer and pressure drop characteristics of an equilateral triangular-sectional duct were started to investigate experimentally by Leung et al. [2000]. An optimum apex angle of the V-groove corresponding to a maximum Nusselt number was suggested to occur within the range from 15° to 18° . However, the study was conducted with a fixed Reynolds number of $Re = 6,150$.

2.2.3 Other Types of Roughness

Experimental studies were essentially carried out on heat transfer in single channels with surface mounted rectangular obstacles [Sparrow et al. 1982, Han et al. 1988, and Sridhar et al. 1990].

Huang et al. [1994] assessed the enhancement of forced convection in a channel using various arrangements of multiple emplaced porous obstacles. A significant improvement in heat transfer performance was observed and vortex control was able to obtain by alterations of some governing physical parameters. Similar porous fins were also adopted by Kiwan et al. [2001] to enhance the heat transfer over a given surface. It was found that porous fins achieved a higher enhancement than solid fins, especially at large Darcy numbers. Moreover, it was suggested that an optimum limit for the thermal conductivity ratio existed, at which a best fin performance could be obtained. While in the simulation study of Ould-Amer et al. [1998], a porous material was inserted between the uniformly spaced blocks in a laminar forced convection cooling system. The results showed an enhancement of heat transfer by

the application of a porous medium, the effective thermal conductivity of which was much higher than the fluid conductivity.

A surface-roughness-increase method by fixing transverse thin circular-sectioned wires in a regular pattern was applied by Saini et al. [1997]. The local heat transfer coefficient and friction factor in a rectangular duct were investigated experimentally. The maximum values of Nusselt number and friction factor were detected at the angle of attack values of 61.9° and 72° , respectively. In addition, correlations were developed for Nusselt number and friction factor, in which both flow and roughness characteristics (i.e. Reynolds number, relative longway length, shortway length and height of the mesh) were taken into consideration. Likewise, Kang et al. [1998] and Leung et al. [1998] investigated the effect of surface roughness on the forced convection inside horizontal isosceles triangular ducts. The surface roughness was produced by various machining processes. It was observed that a duct with a higher surface roughness would have a better heat transfer performance. Non-dimensional expressions for the heat transfer coefficient determination in the triangular duct with different surface roughness were also developed.

In the work of Hosni et al. [1991], some hemispheres with a diameter of 1.27mm were used as the roughness elements. The heat transfer for the turbulent boundary layer airflows was measured. It was indicated that effect of the magnitude of the roughness on the heat transfer increased with decreased roughness element spacing, but diminished when the spacing was too small.

2.3 Secondary Flow

Basically, the secondary flow can be defined as a small disturbance on a primary flow, where the primary flow is the main two-dimensional flow. There are many sources for the secondary flow formation. From the viewpoint of outer factors, a sudden block on the flow way, a particular geometry of the flow passage, or a variation on the flow conditions, these all can attribute to it; while from the viewpoint of the flow itself, the secondary flow is indeed a characteristic phenomenon of the anisotropic turbulent flow.

The secondary flow was first referred as a nonzero mean flow existing in the transverse planes of some straight noncircular pipes by Niluradse [1926]. This secondary flow exists independent of end effects, while has a profound effect on the overall flow characteristics, though its magnitude is very small compared to that of the axial mean velocity. After an initial discovery of the secondary flow, the origin of the secondary flow in pipes of noncircular cross-section was examined theoretically by Speziale et al. [1982]. It was proven mathematically that the secondary flow was resulted from a nonzero difference in the normal Reynolds stresses on the planes perpendicular to the axial flow direction. A similar conclusion was drawn later by Haque et al. [1983] through a critical examination of the analytical expressions for the secondary flow production terms.

Hitherto, the basic image of the secondary flow is formed. However, since the existence and strength of the secondary flow often have significant effects on both flow and heat/mass-transfer characteristics, in addition, because of the wide forming-conditions mentioned above, secondary flows exist in many situations, either for

laminar or turbulent flows, great eagerness is being paid by many investigators on related topics. The main aims are to better understand the secondary flow as well as its effects on engineering applications.

2.4 Triangular Sectional Ducts

Though ducts with various geometries have been studied either experimentally with different thermal conditions or numerically with various models and techniques under laminar or turbulent flow conditions, investigations on triangular ducts are yet rare even though they are frequently encountered in engineering applications. Sahin [1998, 1998] compared ducts of various cross-sections with respect to entropy generation and pumping power requirement in order to determine the possible optimum duct geometry with minimum energy loss under laminar flow and constant wall temperature or heat flux conditions. It was shown that the optimum duct geometry for constant thermophysical properties depended on the Reynolds number; however, the circular duct geometry was found to be the most favorable one especially when the frictional contribution of entropy generation becomes dominant. Triangular and rectangular duct geometries were in general the less preferred choices for both entropy generation and pumping power requirement. A similar conclusion was drawn by Sparrow et al. [1965], who carried out a study on laminar flows in isosceles-triangular, right-triangular and circular-section ducts with uniform heat flux provided per unit length and a circumferentially uniform wall temperature in each cross section.

However, considering the compactness and lower construction cost, a compact plate-fin heat exchanger with tightly-packed triangular-sectional flow passages becomes a more preferred choice in practical applications. A comprehensive review of the theoretical and experimental studies on forced convection in triangular ducts up to the 1970s was conducted by Shah et al. [1978].

Because of the complex geometry formed by the sharp corners in the triangular duct, the flow characteristics is far more complicated than usually met circular, rectangular or square duct. The turbulent heat transfer characteristics of a two-pass triangular duct with smooth wall, where one pass was for the radial outward flow and the other for the radial inward flow, were studied by Dutta et al. [1994]. It was concluded that the triangular ducts provided more restriction than the square ducts to the formation of the secondary flow, and the right-angle triangular duct avoided the formation of symmetric vortex structures in the cross flow plane. Shah [1975] investigated the influence of passage geometry on the heat exchanger design and it was found that the rounding of corners of an equilateral triangular duct had only a small effect on the heat exchanger performance.

However, the secondary flow formed in a triangular duct had evident effects in the cross-sectional distributions of mean axial velocity, wall shear stresses and Reynolds stresses, as well as in the turbulent kinetic energy distributions [Aly et al. 1978]. To predict the generation of the secondary flow, Sugiyama et al. [1991] suggested a modified Reynolds stress equation model. Governing equations were transformed from the physical plane to the calculation plane by boundary-fitted coordinate systems. For the flow prediction, the vorticity production terms were expressed by modeling the Reynolds stresses in the plane of the cross-section in terms of gradients

in the mean axial velocity and a geometrically calculated turbulence length scale. Later, Sugiyama et al. [1997] reported numerical data for turbulent flow developing in a right-angle triangular duct, with the other two internal angles of 60° and 30° , which had no plane of symmetry. In the calculation, an algebraic Reynolds Stress model (RSM) was adopted in order to predict the anisotropic turbulence precisely, and a boundary fitted coordinate system was introduced as the method of coordinate transformation.

On the other hand, due to the very complicated geometry, prediction of the distributions of the heat-transfer coefficient in a triangular duct is difficult. As recommended by Dittus et al. [1930], the average heat-transfer coefficient for a forced turbulent flow inside a smooth circular duct can be predicted by the well-known empirically obtained non-dimensional equation, namely, $Nu = 0.023Re^{0.8}Pr^{0.4}$. However, it is not directly applicable to a triangular-sectioned duct because the forced convection will be suppressed rather significantly by the corners of the triangular duct. Leung et al. [1995] carried out an investigation of forced convection in an equilateral triangular duct from laminar to turbulent flow conditions, and suggested that $Nu = 3.25$ could be used for laminar flow conditions whereas $Nu = 0.012Re^{0.83}$ for turbulent flow conditions.

The geometry of the triangular duct also affects the flow and heat transfer performance. The work of Chen et al. [2000] was related to the forced convection in smooth triangular ducts with different apex angles of 15° , 30° , 60° and 90° under fully developed laminar flow conditions, which were predicted numerically using a finite volume method. Both the friction factor and Nusselt number showed a strong

dependence on apex angle of the triangular duct. When the apex angle was 60° , the duct provided the highest steady-state forced convection from its inner surface to the airflow under laminar flow conditions. An optimum apex angle also occurred at 60° when the flow in an isosceles triangular duct was under turbulent flow conditions [Leung et al. 1997].

2.5 Numerical Predictions of Internal Flow

2.5.1 Laminar Flow

Thermal and hydrodynamic performances of laminar flows in pipes or ducts are investigated frequently by numerical approaches in many literatures.

Shah [1975] provided the heat transfer characteristics for irregular ducts through a numerical study. A least-squares-matching technique to analyze the fully developed laminar flow and its heat transfer in ducts of arbitrary cross-sections was proposed. In this method, equidistant points were not required. It employed real and imaginary parts of a complex variable in a cylindrical coordinate system, and thus further minimized the roundoff errors. Later, Yang et al. [1991] developed an explicit finite-difference procedure for laminar gas flow, which took advantage of the method of lines, and solved the resulting set of simultaneous integro-partial differential equations numerically using the method of moments.

Local Nusselt number of a laminar flow in irregular ducts was predicted by Uzun et al. [1997]. The partial differential equations of an arbitrary irregular plane were transformed from the physical domain into a square shaped computational domain by using the elliptic grid generation technique. Over-relaxation numerical method

was used in computing velocity and temperature distributions. It was found that using a smaller step size in the axial direction of the simulated duct, the calculated Nusselt number would be more accurate. Likewise, in the prediction of the laminar forced convection in smooth triangular ducts, instead of the rectangular grid, Chen et al. [2000] employed an unstructured triangular grid method, where the grid was generated by a Delaunay method. The SIMPLE-like algorithm was applied to solve the pressure-velocity coupling discretization. Distributions of the friction factor and Nusselt number were presented for triangular ducts with different apex angles.

2.5.2 Turbulent Flow

On the other hand, because of frequent applications and unneglected importance, turbulent flows attract many practical interests. While as a characteristic phenomenon of turbulent flow, the secondary flow thus receives particular attentions. Emery et al. [1980] studied both developing and developed turbulent flows in a square duct. The computations utilized an explicit numerical difference scheme and an algebraic closure model based on a three-dimensional mixing length. It was found that the secondary flow was sensitive to grid spacing effects, while for local primary flow behavior, the effect was insignificant. Transport effects of the secondary flow on the velocity and temperature distributions were displayed.

However, due to the complexity in prediction of the secondary flow, not all turbulence models are suitable. Speziale et al. [1982] discovered that the standard $\kappa - \varepsilon$ turbulence model had no natural mechanism for the development of secondary flows, but some second-order closure models were found to have such ability.

In respect that the standard $\kappa - \varepsilon$ model has no ability to predict the secondary flow, Rokni et al. [1996, 1998, 1999, 2000] added non-linear terms to the constitutive relation for the Reynolds stresses to study the forced convection in different ducts. The nonlinear $\kappa - \varepsilon$ model of Speziale was combined with the Lam-Bremhorst damping functions for low Reynolds numbers and it was shown that this non-linear $\kappa - \varepsilon$ model was able to predict the fully developed flow and temperature fields reasonably well. However, a disadvantage of this model was identified as *return to isotropy at the duct's corners*. Demuren [1991] used an algebraic stress model, which was derived by simplifying the transport equations for the individual Reynolds stresses, to calculate the turbulent stresses and suggested that the irregular physical geometry could be transformed into a regular one in the computational space, and the flow equations be then solved with a finite volume numerical procedure. The developed procedures enabled the predictions of both the turbulence-driven secondary flow and the anisotropy of the Reynolds stresses. However, it failed in the predictions of complex flows. A modification to the traditional algebraic stress models was attempted and the explicit algebraic stress models were thus reported by Gatski [1993] for two- and three-dimensional turbulent flows in non-inertial frames, which were obtained for a hierarchy of second-order closure models that were tensorially linear in the Reynolds stress anisotropy. These models were obtained using the standard local equilibrium hypothesis and, therefore, constituted the explicit solution to the traditional algebraic stress models to include non-inertial effects and a range of pressure-strain models.

Efforts are still carried on for the prediction of the secondary flow. Particularly, the rib-disturbed turbulent flows are focused on. Hitoshi et al. [1998] conducted a

numerical analysis for the fully developed turbulent flow in rectangular ducts with smooth and rough walls with an algebraic RSM. The wall functions and the universal law of the wall, which were used as the boundary conditions of turbulent energy and dissipation, were applied in the analysis without taking the shape of roughness element into account. A computational analysis of a turbulent flow passing a horizontal surface attached with two-dimensional transverse ribs was performed by Lee et al. [2001] through a computational fluid dynamic (CFD) model: FLOTRAN. The velocity and temperature profiles, local heat transfer coefficients, as well as turbulence characteristics were successfully predicted. Vortices, flow separation and attachment were detected at both upstream and downstream of the ribs. In addition, Acharya et al. [1993, 1994, 1996, 1998] conducted a series of numerical studies as well as experimental measurements of the fully developed turbulent flow in ribbed ducts using a non-linear $k - \varepsilon$ model of Speziale. Bredberg et al. [2000] applied a new wall boundary condition for the standard $k - \omega$ model to predict the heat transfer of a turbulent flow in a rib-roughened channel. They all provided reasonably good predictions of the turbulent flows.

Since many turbulence models can be applied to predict the rib-interrupted flow, the prediction ability of different models is aimed to be compared. Saidi et al. [2000] predicted the thermal characteristics of a certain type of ducts with ribs fabricated on internal surfaces using two turbulence models, namely, a simple eddy viscosity model (EVM) and an explicit algebraic stress model (EASM). The prediction capabilities of these two models for determining the turbulent Reynolds stresses were also analyzed and compared. It was found that EASM had some superiority

over EVM in the prediction of the velocity field structure, but a higher CPU times was required as penalty.

However, due to its simplicity and good overall properties, a linear $k - \varepsilon$ model is however often used in the prediction of turbulence flow though it has not possessed the ability to predict the secondary flow. In the investigation of Iacovides et al. [1996] on a periodic flow in the stationary and rotating square ducts with rib-roughened walls, a low- Re version of the basic Dynamic Smagorinsky Model (DSM) as well as a $k - \varepsilon$ model with only 1-equation of k transport across the near-wall regions was applied for the simulations. The former model, which was able to reproduce most of the features of the turbulence field under both cases, was found to be superior over the $k - \varepsilon$ model on thermal computations. However, the wall heat transfer coefficient was not well predicted. Bonhoff et al. [1999] then used the RSM and $k - \varepsilon$ model to simulate developed flows in coolant channels with the opposing 45-degree square ribs staggered to the duct's centerline. In their study, to evaluate the CFD simulations, a large solid database was also obtained by applying a Particle Image Velocimetry (PIV) system for the velocity measurements. It was found that the results obtained by the RSM were more consistent with the experimental results than those obtained by the $k - \varepsilon$ model.

Recently, Ooi et al. [2002] studied turbulent flows in two-dimensional cavities and three-dimensional ribbed ducts by using three types of eddy-viscosity turbulence models: $v^2 - f$, $S-A$ and two-layer $k - \varepsilon$. Heat transfer predictions by the $v^2 - f$ model were found to be closest to the experimental values, though the predicted results did not concur with the experimental data. It might due to the inability of

eddy-viscosity models (i.e. the $S-A$ and $k-\varepsilon$ model) to properly simulate the secondary flow.

2.6 Visualization of Internal Flow

Since roughness disturbs the channel flow and promotes turbulence, secondary flows thus form and enhance the flow heat transfer rate. To investigate the flow pattern of the turbulent flow or the mechanism of heat transfer augmentation, flow visualization methods are often used, such as Laser Doppler Velocimetry (LDV), Particle Image Velocimetry (PIV), and liquid crystal technique. Most useful flow visualization techniques can be found in Smits et al. [2000]. Visualizations of the macro/micro flows are useful for better understanding of the flow mechanisms as well as the evaluation of numerical simulations. For example, the flow structures in the near-wall regions, especially the secondary flows, usually determine the heat transfer performance between the fluid and solid medium.

Lots of studies have been conducted related to flow visualization, especially for flows in roughened ducts, in which the secondary flow usually further developed and strengthened, and more important as well. As a typical roughened surface, various kinds of ducts attached with ribs on internal surfaces are given particular interests. Effects of the rib on the flow are also investigated by visualization.

Rau et al. [1998] carried out two-dimensional LDV investigations on forced convection of turbulent flow in rib-roughened square ducts and provided a description of the aerodynamic flow field, as well as the effects of rib on the channel thermal performance at the lateral walls. A three-dimensional flow structure around

a rib was detected, and a second impingement on the smooth sidewall was observed in front of the rib. Liou et al. [1993] studied the periodic fully developed turbulent flow in a channel with ribs attached on the internal surface based on LDV measurements. The turbulence-generated secondary flow was successfully reported. Later, Liou et al. [1999] used LDV again to study the fluid flow field and measure the local heat transfer coefficient distributions in a smooth channel with an 180° sharp corner turning on a near laminar flow condition. Thermocouple probes were also applied for the measurements. Similarly, local heat transfer coefficients and static pressure drops in a leading-edge triangular duct, which was cooled by impinging jets, were investigated by Hwang et al. [2001]. The transient liquid crystal technique was instead used for the measurements.

Gao et al. [2001, 2004] analyzed the heat transfer and flow characteristics of the flow field using both liquid crystal thermography and PIV techniques in rectangular ducts roughened by different rib configurations. Strong effects of the inclined ribs on the flow behavior by the development of the secondary flows were observed. In addition, periodic heat transfer distributions were obtained between adjacent ribs. Likewise, Schabacker et al. [1998, 1999] conducted PIV studies of the flow passage of a U-channel with or without the installation of ribs. The passages were either with two ducts connected by a sharp 180° bend or 45° rib arrangement. The flow characteristics of these two kinds of rib arrangements were analyzed, respectively. For the localized effects of high Reynolds number flow on heat transfer enhancement, a detailed investigation in a two-pass square channel with a smooth wall and a 90° rib-roughened wall were performed by Son et al. [2002] from PIV experiments. It was reported that the flow impingement was the primary factor for

the two-pass channel heat transfer enhancement rather than the flow turbulence level itself.

2.7 Summary of Literature Review

Most above literatures are concerned with studies of rectangular or square channel flows, but there is no sufficient information about the flow characteristics in a channel with a triangular cross-sectional passage. Since the triangular duct possesses the advantages of compactness and low construction cost characteristics, it is usually used in engineering applications. Therefore, it is necessary to better understand the flow and thermal characteristics of the triangular duct.

In addition, from the investigations conducted on various kinds of surface roughness such as ribs and grooves, it can be concluded that artificially roughened surfaces are rather effective to enhance the forced convective heat transfer of the channel flow. However, there is still a dearth of quantitative knowledge concerning forced convection and fluid friction of the fluid flow through the triangular cross-sectioned duct with internal roughened surfaces: no further information is available about the effects of roughness size and spacing as well as flow conditions on the thermal and hydrodynamic performances of the triangular duct. Forced convection and fluid friction for a laminar or turbulent flow through a channel is dependent directly on several parameters including geometry, hydraulic diameter and axial length of the flow passage, Prandtl number and Reynolds number of the inside flow. Moreover, due to the presence of the roughened surfaces, these dependence relationships will be more complicated, which need be dealt with and thus reasonably applied in practice.

With current insufficient available information, it is unable to better utilize the thermal performance of the triangular flow-passage compact heat exchanger, even though the ribbed or grooved internal surface has been identified to be the most possible method [Wong et al. 2002].

On the other hand, the very complicated flow pattern involved due to the complex geometry formed by the three sharp corners of the triangular duct together with the ribbed or grooved internal surfaces need be investigated to explain the mechanism of its influence on forced convection and fluid friction of the flow. However, due to the difficulty and complexity in the experimental study, it is hoped that a two-dimensional or even a more complicated three-dimensional numerical model can be developed to predict the turbulent flow in the triangular duct with uniformly ribbed or grooved surface.

Present investigation consists of both experimental and numerical simulation studies of an air-cooled horizontal equilateral triangular duct with uniformly ribbed or grooved internal surfaces. The investigation will be intended to conduct under fully developed turbulent flow conditions, since they are encountered frequently in practical heat exchangers. It is aimed to identify quantitatively the effects of geometry of the triangular duct, attached ribs or grooves, as well as Reynolds number of the flow on its forced convection and fluid friction characteristics, and thus obtain valuable information to fully utilize this practical heat enhancement method. The experimental results will be used as a solid foundation to develop non-dimensional equations for the predictions of heat transfer coefficient and fanning friction factor of these duct assemblies, and also for evaluations of their associated numerical simulations.

Focus will also be placed on the development of secondary flow at the near-wall regions of the duct, as well as the mechanism of detachment and reattachment of the periodic flow and formation of vortex around the ribbed or grooved surface.

Such information is very essential to achieve a knowledge about the thermal and hydrodynamic performances of the triangular-sectional flow-passage compact heat exchanger. In addition, the results obtained in the present study would also be applicable as a reference to ducts with complex cross-sectional geometries.

3 EXPERIMENTAL ARRANGEMENT

Nowadays the investigation of forced convective heat transfer in pipes or ducts attracts interest of many engineers because of its wide application in many types of industrial equipments, such as heat exchangers, electronic systems and nuclear reactors. It is important to transfer heat from the devices and dissipate the heat to the surrounding environments rapidly and effectively to maintain proper functions of the equipments. To enhance forced convective heat transfer between the fluid flow and the solid wall, artificially roughened surface is often applied and proposed to be a good and efficient method.

As one of the main objectives in the present study, the effects of internal roughened surfaces as well as flow conditions on thermal performance of the turbulent flow in a horizontal equilateral triangular duct are now paid particular interests. Because of ripeness, convenience and practicality, square ribs and V-grooves are considered and applied as the rough-elements. Experimental method is adopted to basically recover the influence of duct geometry, artificial roughness as well as flow conditions on forced convection and fluid friction of the turbulent flow in such a thermal system.

In this chapter, experimental set-up, procedures, measurements, instrument calibrations as well as data postprocessing and generalization are described, respectively. Since no measurements are perfect, an experimental reliability analysis is also conducted and provided.

3.1 Design of the Test Rig

A typical experimental test rig of the present investigation is shown schematically in Fig. 3-1.

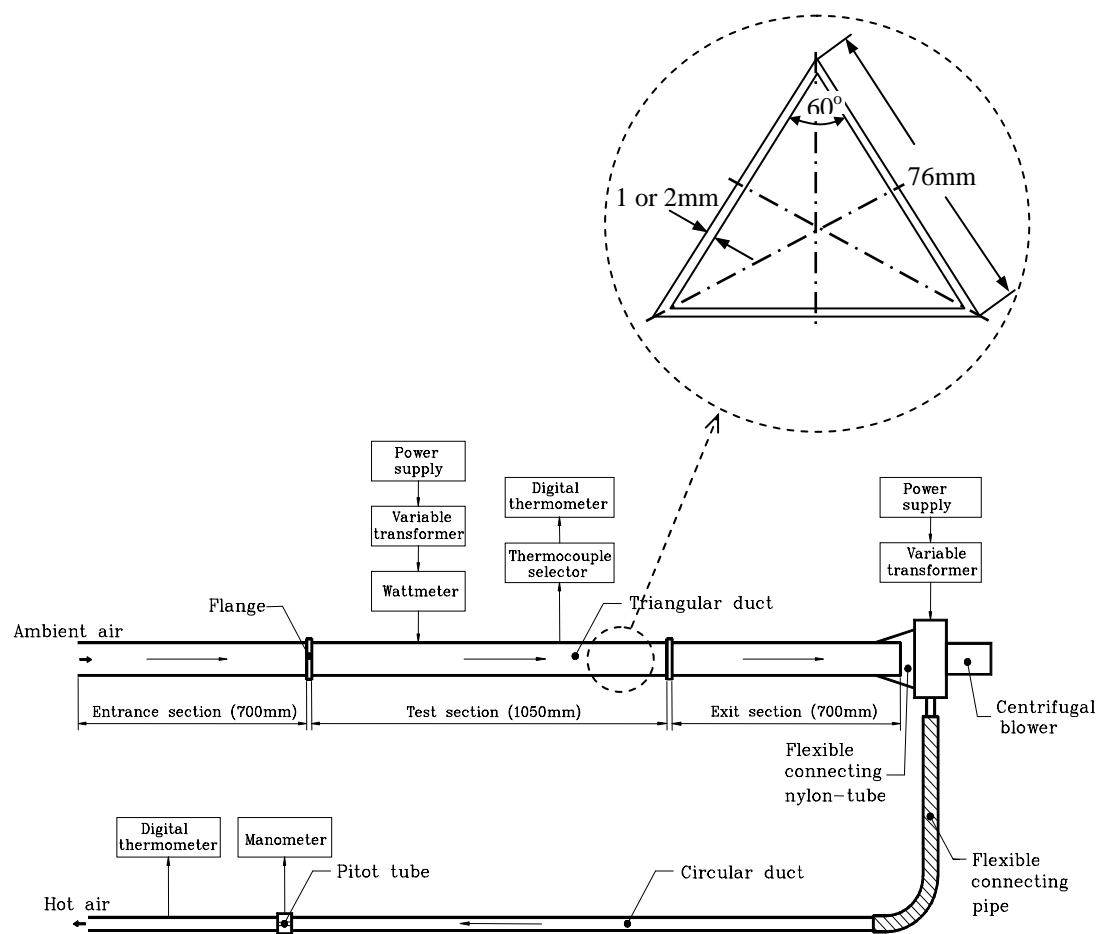


Fig. 3-1 The schematic experimental set-up

Several geometrically identical equilateral triangular duct assemblies were fabricated from a 1 mm (for ribbed surface) or 2 mm (for V-grooved surface) thick duralumin

plate (i.e. thermal conductivity $k_w = 180 \text{ W/(m}\cdot\text{K)}$). Each of these duct assemblies consisted of three consecutive triangular sections: a 700 mm long entrance duct for the flow better developing, a 1050 mm long test duct for the forced convection and fluid friction measurement performing, and a 700 mm long exit duct for the end effects on the test flow minimizing [Aly et al. 1978]. In addition, total length of the entrance duct and the test duct was over 40 times of the hydraulic diameter (i.e. $D = 44\text{mm}$), which ensured a fully developed turbulent flow in a significant portion of the test section [White 1994]. These three sections were all fabricated with sharp corners, and of identical cross-sectional shapes and dimensions, namely, each edge was $a = 76 \text{ mm}$ in length as shown in Fig. 3-1. However, they were thermally insulated from each other by the applications of formica sheets, gaskets as well as seals.

Uniform heating was provided from an electrically heated nichrome wire, which was wound uniformly around the external surfaces of the triangular duct. The electric power (E) supplied to heat the nichrome wire was monitored by a wattmeter (see Appendix III) and was maintained at 200W via a variable-voltage transformer (see Appendix III) throughout every experiment. Since the nichrome wire was able to achieve an excellent efficiency of 99%, nearly all the supplied electric power was therefore converted to heating power. A very thin wall thickness (i.e. $\leq 2\text{mm}$, as above-mentioned) was used to achieve an efficient heat transfer from the outer attached nichrome wire to the inner surfaces of the triangular duct by minimizing the thermal resistance through the duct wall due to conduction. To provide a uniform heat flux through the duct wall and to ensure the same heating power was supplied to each of these triangular ducts under investigation, the separation between two

3 EXPERIMENTAL ARRANGEMENT

adjacent nichrome wires was maintained at 10 mm throughout the entire axial length of the triangular duct.

The whole triangular duct assembly was thermally insulated from its ambient environment by the sandwich of a 1 mm thick formica sheet, a 8.5 mm thick plywood sheet and a 35 mm thick fiberglass blanket. A cross-sectional view of the triangular test duct is presented in Fig. 3-2. The assembly was supported at two points only so that the entire external surfaces were exposed to the same ambient condition. A level gauge was used to ensure that the assembly had been placed horizontally.

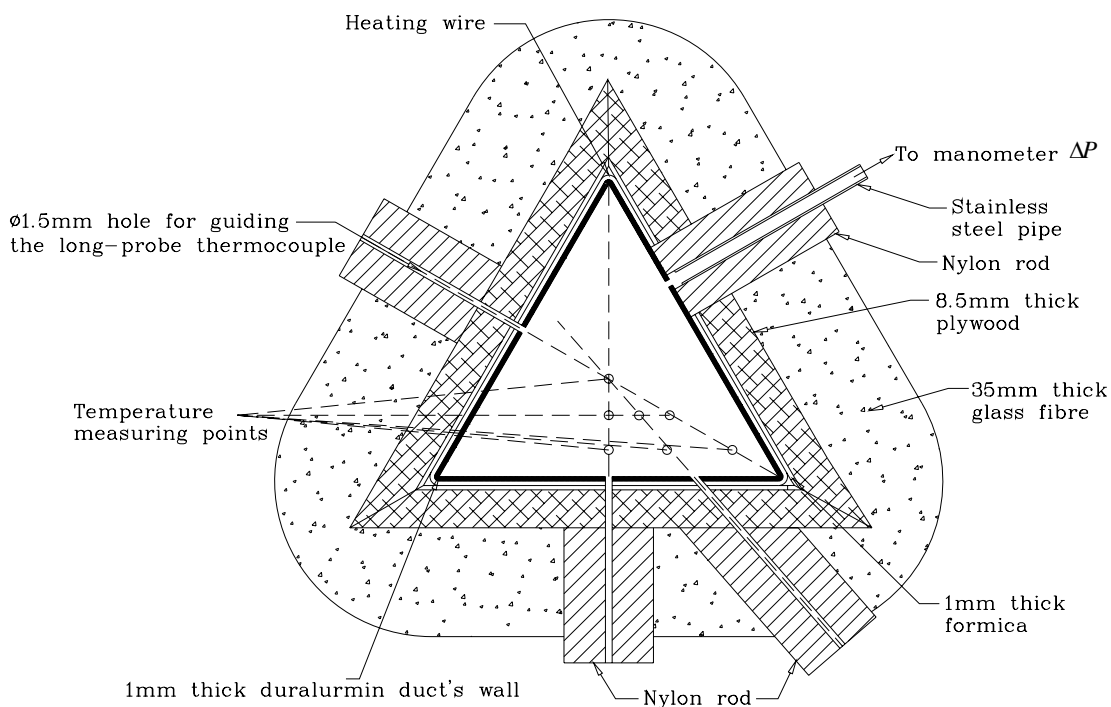


Fig. 3-2 Cross view of the triangular duct

The ambient air around 16°C was driven through the triangular duct assembly by a 550 W centrifugal blower (see Appendix III), which was installed at the end of the exit duct, as shown in Fig. 3-1. The blower was physically isolated from the triangular duct to avoid transmission of its vibration to the assembly. In addition, to reduce the extraneous heat loss from the end of the triangular duct to the blower, a thin nylon tube of very low thermal conductivity was thus employed as their connection. Since the experiments were performed at different flow conditions, electric power supplied to drive the blower was adjusted through another variable-voltage transformer, which enabled the present study to be operated at a wide range of Reynolds numbers from 4,000 to 23,000. The blower exit was connected to a long circular pipe by a flexible pipe to facilitate a more stable and steady flow rate measurement afterwards. All connecting parts were joined with gaskets and seals to prevent air leakage, and soap bubble was used to detect any air leakage at each joint.

Length of the circular pipe was 2230 mm and its diameter was 54mm. As the ratio of its length to diameter exceeded 40, velocity profile could be determined at a cross-sectional plane near to its exit where the flow was already fully developed [White 1994].

All the instruments used in the present study, including the K-type thermocouples, had been well pre-calibrated. The detailed methods and procedures were described in Section 3.3. The temperatures and pressures obtained from the experimental investigation were used to calculate the forced convection and fluid friction accordingly as presented in Section 3.5. Together with the velocities and the other experimental parameters, these results were rearranged to give non-dimensional

equations in terms of Nusselt number (Nu), Reynolds number (Re), Prandtl number (Pr) and fanning friction factor (f).

3.2 Measurement of Experimental Parameters

3.2.1 Temperatures

3.2.1.1 Wall Temperatures

A digital thermometer connected with K-type thermocouples (see Appendix III) which were installed at six junctions along the axial length of the test duct, was used to record the duct's internal surface temperatures (i.e. T_{wi} , $i = 1, 2, \dots$) as shown in Fig. 3-3. These data were then averaged to give the mean wall temperatures of the test duct (T_w), which were ranged from 345 K to 380 K. Because of the excellent thermal conductivity of duralumin, variation in surface temperatures of the entire test duct was less than 10°C in every measurement. Each thermal junction consisted of three K-type thermocouples installed on the three internal surfaces of the triangular duct at the same cross-sectional plane, which was perpendicular to the mean airflow direction. Every thermocouple was spot welded and embedded inside a narrow hole of the duct wall. Heat transfer compound was applied to fill the residual cavity between the junction and the wall to ensure a good thermal contact. This method enabled the point of measurement to be placed closer to the internal surface of the wall, where the temperature readings were more desirable, and more accurate temperature measurement was thus achieved [Altemani et al. 1980].

As for the plywood, which was attached to the outer surface of the heated plate of the triangular duct to reduce heat loss to the surroundings, another two

thermocouples were used to measure its inside and outside temperatures. Then the difference of these two temperatures was regarded as the temperature drop when heat was conducting through the plywood.

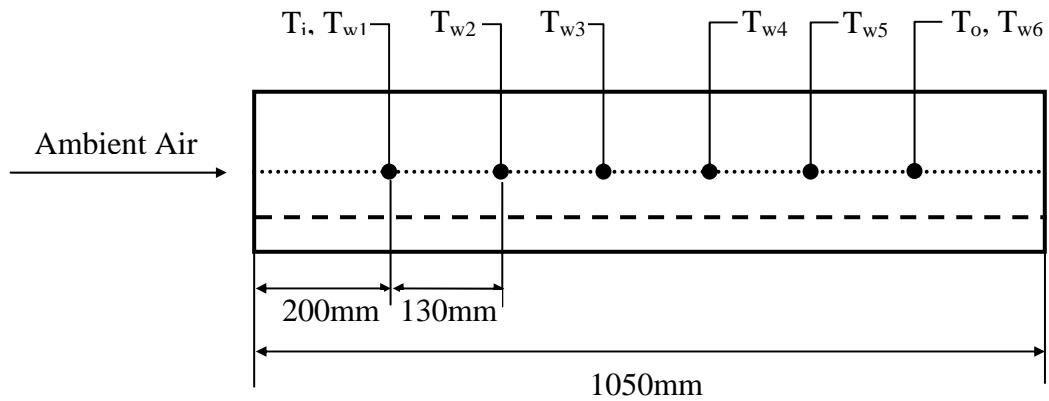


Fig. 3-3 Locations of temperature measurement along the triangular duct

3.2.1.2 Airflow Temperatures

Steady-state temperatures of the airflow at entrance and exit of the test duct were measured by a K-type long-probe thermocouple connected to the digital thermometer. The diameter of this long probe thermocouple was only 1.5 mm, which led to a negligible effect on the flow pattern during each measurement [Benedict 1977]. Air temperatures were measured at seven different locations on the same cross-sectional plane as shown in Fig. 3-4, which was normal to the airflow direction. Two planes for these measurements were chosen: each of them was 200 mm away from entrance and exit of the test duct, respectively. The temperatures

3 EXPERIMENTAL ARRANGEMENT

attained on the same plane were then averaged to gain the mean inlet or outlet air temperatures.

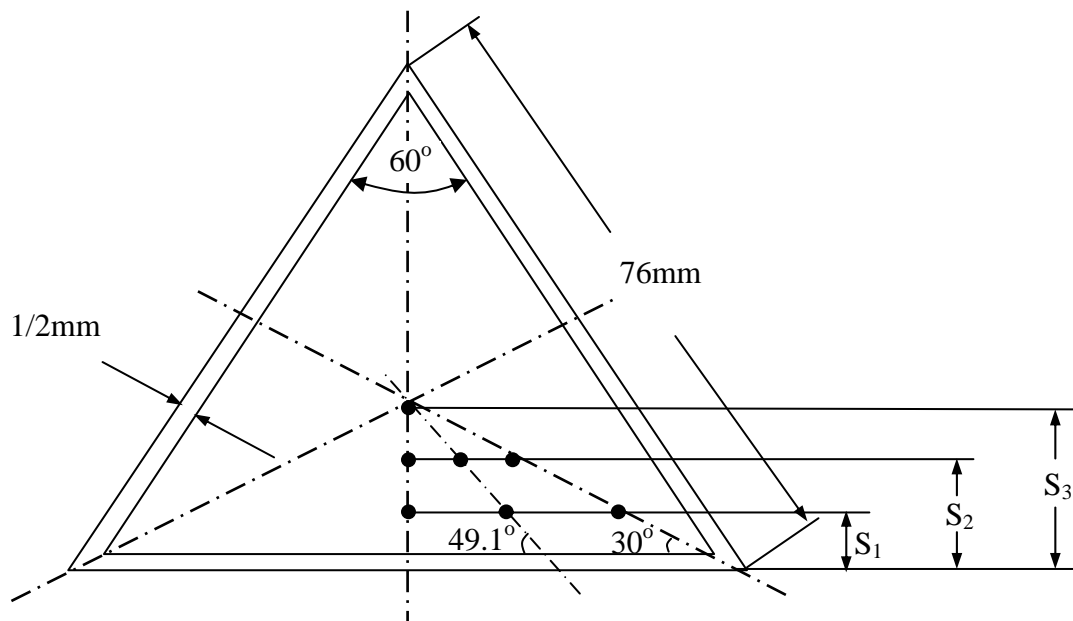


Fig. 3-4 Locations of temperature measurement in a cross-sectional plane of the triangular duct ($S_1 = 7.31\text{mm}$, $S_2 = 14.63\text{mm}$, $S_3 = 21.94\text{mm}$)

3.2.2 Pressure Drop

To determine the axial pressure drop (ΔP) along the test section of the horizontal triangular duct, two static pressure taps fabricated from nylon rods and stainless steel tubes were installed at the same cross-sectional positions where the long-probe thermocouple was applied. Five different locations in each of these two planes were chosen for the measurement, as shown in Fig. 3-5. The determination of the locations was based on an area-averaged method.

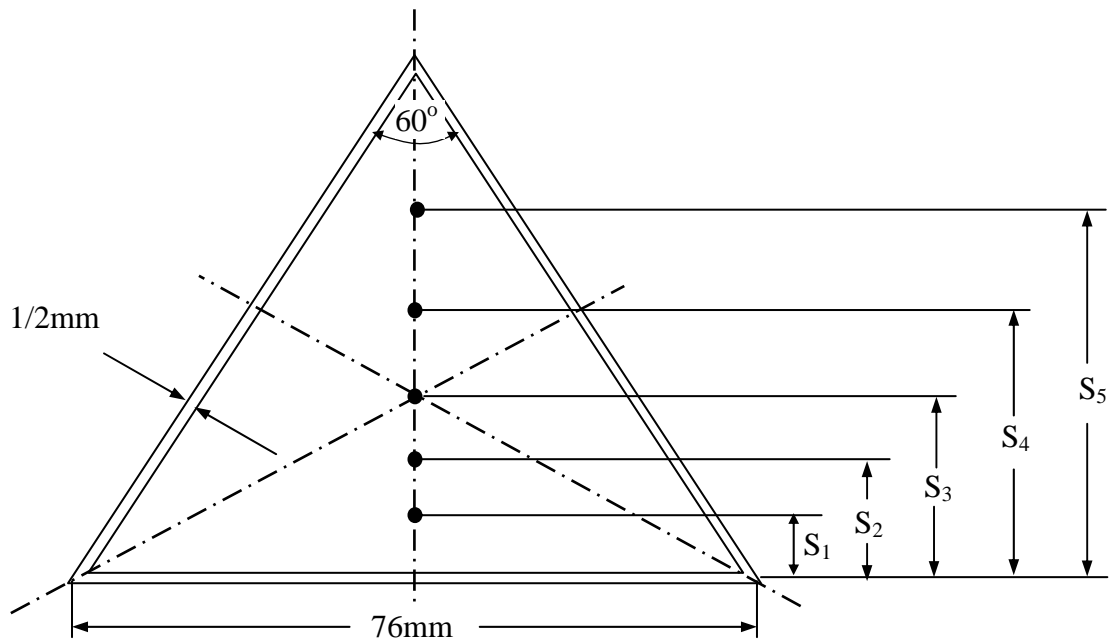


Fig. 3-5 Locations of pressure measurement in a cross-sectional plane of the triangular duct ($S_1 = 3.4\text{mm}$, $S_2 = 10.8\text{mm}$, $S_3 = 19.4\text{mm}$, $S_4 = 29.9\text{mm}$, $S_5 = 46.2\text{mm}$)

There were two steel tubes inserted vertically into the test flow for the pressure measurement. The tubes were of a diameter of 2mm as recommended by Benedict [1977], such that their effect on the flow was negligible. Accurate positioning of the tubes in the triangular duct was achieved through a vertical traversing mechanism mounted on a vernier caliper. The tubes were connected to a manometer during each measurement, but taken away from the pressure taps and then blocked off by plugs at all other times to prevent any air leakages.

In addition, it was assumed that the axial pressure drop along the triangular test duct was entirely due to the fluid friction. The data obtained at the five locations were then averaged to give the final mean pressure drop.

3.2.3 Airflow Rate

According to the equation: $P_v = \rho V^2 / 2$, the air velocity distributions in the circular pipe were determined from the knowledge of corresponding mean pressures of the airflow. To measure the mean pressure of the airflow in the circular pipe, a pitot tube was used, which was equipped with a manometer, at 200mm from the exit of the circular pipe where the flow was assumed fully developed. The measurement was taken at fourteen different locations on the same cross-sectional plane, at 2mm intervals along the pipe radius from its centerline. Similarly, accurate positioning of the pitot tube was achieved by using the vertical traversing mechanism mounted on another vernier caliper. A K-type thermocouple and a barometer (see Appendix III) were used to obtain the mean airflow temperature and the atmospheric pressure at the exit of the circular pipe, which were then used to determine the air density (ρ) at this location. With the above information, the velocity profile in the circular pipe was determined and thus the mass flow rate (\dot{m}) through the circular pipe could be obtained (see Appendix II). According to the principle of mass conservation, mass flow rate of air through the triangular duct was then attained, which was equal to that passing through the circular pipe. Altogether, mass flow rate of air through the triangular duct could be determined under a less fluctuating condition.

The mean air velocity (U) through the triangular duct with a cross-sectional area of A_c was then determined by applying *the Continuity Equation* with the aid of the determined \dot{m} :

$$U = \frac{\dot{m}}{\rho \cdot A_c} \quad (3-1)$$

3.3 Calibration of Instruments

The static characteristics of a sensor can be found by determining the indication or output of the sensor with respect to that of a standard at a sufficient number of known values. With acceptable means of interpolation, the indication or output of the sensor can be calibrated over the entire range of use.

For a calibration process to be reliable, the following items must be available:

- Means for measuring output of the sensor;
- A satisfactory measurement standard;
- Controlled environments for measurement;
- A scheme for interpolating between calibration points.

As a result of proper attention to application details, the means for measuring indications or outputs of all common sensors within acceptable uncertainties are available for certain fixed points, certain standard instruments and certain interpolating equations [Benedict 1977].

3.3.1 Calibration of Thermocouple

Calibration environments can be divided into two classes depending on the method of determining the temperature of the test sensor [Benedict 1977]:

- (1) The sensor is exposed to a fixed-point environment that, under certain prescribed conditions, naturally exhibiting a state of quasi-thermal equilibrium whose temperature is established numerically by the international partial temperature scale (IPTS) without recourse to a temperature standard.

3 EXPERIMENTAL ARRANGEMENT

(2) The test sensor and a temperature standard are exposed simultaneously to a controlled temperature environment whose temperature is established by the standard instruments.

In the present study, the method by comparing a test thermocouple to a standard instrument, which was referred as thermocouple calibrator as shown in Fig. 3-6, was introduced. The thermocouple calibrator had high reliability and high accuracy, and remained almost stable during the entire measurement. A thermocouple was placed into the measurement box, which was already installed in the thermocouple calibrator. Hence the measurement data were obtained by comparing with the calibrator values.



Fig. 3-6 Thermocouple calibrator

3.3.2 Calibration of Manometer

The Dywer U-manometer combined with microtector for water gauge measurement was used for the present manometer calibration. The U-manometer consists of a transparent glass tube bent constructing in the form of an elongated 'U', which is partially filled with suitable liquids: mercury and water, because of available detailed information of their specific weights. To measure the pressure of a fluid that is less dense than and immiscible with the manometer fluid, it is applied to the top one of the tubes of the manometer while a reference fluid pressure is applied to the other tube in the steady state. The difference between the unknown pressure and the reference pressure is balanced by the weight per unit area of the equivalent displaced manometer liquid column, i.e.

$$\Delta P = w_M \Delta h_E \quad (3-2)$$

Where, w_M , the corrected specific weight of the manometer fluid, depends on factors such as temperature and local gravity. While the equivalent manometer fluid height, Δh_E , depends on the factors such as temperature, relative specific weights, heights of the fluids involved and capillary effects [Roger 2000].

3.3.3 Calibration of Wattmeter

A digital multi-meter as shown in Fig. 3-7 was applied to calibrate the wattmeter. The calibration was taken at a 220V-AC-supply as the reference point of the measurement.



Fig. 3-7 A digital multi-meter for wattmeter calibration

3.4 Experimental Procedures

The following preparations were performed during every experiment before the data measurements:

1. Installed the square ribs or cut the V-grooves uniformly with a certain spacing on the duralumin plates.
 2. Combined three identical rectangular plates together to form an equilateral triangular duct. Then conglutinated them by tin tapes and gasket wall seals.
 3. Fixed four nylon cylinders at the same cross-sectional plate at a distance of 200mm away from one end of the test duct. The same procedure was repeated at the other end of the test duct.
 4. Installed the eight K-type thermocouples with their ends spot-welded by electrode machine at the test duct. Heating wire was wound uniformly with a certain separation around the outer surfaces of the test duct. The separation between two adjacent heating wires was kept constant at 10mm.
-

-
-
5. To provide a good thermal insulation on the test duct, formica sheet and plywood were applied to cover the outer side of the test duct. Another two K-type thermocouples were used to measure the inside and outside temperatures of the plywood. Moreover, glass fiber was added onto the surface of the plywood to reduce heat loss to the surroundings.
 6. A blower connector and a flexible connecting pipe were used to connect the triangular duct and the circular duct, respectively.
 7. Rubber pads and glass adhesive were added to avoid heat conduction loss between two connections.
 8. Twelve thermocouples were connected to the digital thermocouple thermometer. The digital thermocouple thermometer was linked to a computer by a RS232 cable to facilitate data acquisition.
 9. A pitot tube was inserted vertically into the circular pipe at a distance of 200mm away from the pipe's end. A vertical caliper was used to hold the pitot tube to ensure the occurrence of accurate data from the connected manometer.
 10. Another manometer was installed at the inlet and outlet of the test duct to measure the pressure drop along the axial length.
 11. Two transformers were connected to the system: one was connected to the blower and the other to the heating wire. The bottoms of both transformers were supported by rubber pads to avoid vibration.
 12. Additionally, two digital wattmeters were connected to the transformers to control the heating power and flow rate, respectively.

After the above preparation procedures had been completed, the following procedures for data measurements were then conducted:

3 EXPERIMENTAL ARRANGEMENT

- I. Adjusted the transformer, which was connected to the blower, to ensure a Reynolds number could be obtained within the range from 4000 to 23000. Based on these two extreme values, these were ten Reynolds numbers chosen, which were distributed evenly over this range.
- II. Turned on the electric power ($E = 200W$) to heat up the test duct. Waited for about two hours until the steady state of the system was obtained.
- III. Recorded the data of temperatures, pressures, and ambient conditions as mentioned previously. Each set of data was repeatedly measured for ten times under the same operation conditions, which were then averaged to minimize the error gained during data acquisition.
- IV. Adjusted the transformer for the blower to alter the Reynolds number and then repeated the above procedures.

3.5 Handling of Experimental Data

Firstly, it was assumed that all the physical properties of the solid were kept constant in the present study.

Steady-state convection heat transfer from the internal surfaces of the triangular duct to the airflow (Q_c) can be deduced from the input power (E) as shown below:

$$Q_c = E - Q_r - Q_l \quad (3-3)$$

In Equation (3-3), rate of conduction heat loss through the external surfaces of the whole triangular duct assembly to the ambient air (Q_l) is estimated by using the Fourier's Law, with the aid of thermal conductivity (k_p), heat transfer area (A),

temperature drop (ΔT_p) and thickness (l) of the outer-attached plywood as shown below:

$$Q_l = k_p A \frac{\Delta T_p}{l} \quad (3-4)$$

While radiation heat loss through both ends of the triangular duct to its surroundings (Q_r) is estimated by the following equation:

$$Q_r = \sigma A_c F \varepsilon_r (T_w^4 - T_\infty^4) \quad (3-5)$$

Where σ is the Stefan-Boltzmann constant, A_c is the cross-sectional area, F is the view factor between the duct and its surrounding and is taken to be unity, and ε_r is the surface emissivity of duralumin and is measured to be 0.1 by using a Minolta infrared spot thermometer.

To ensure its accuracy, Q_c obtained from Equation (3-3) is also counter-checked with the internal energy increased by the airflow, which can be calculated by:

$$Q_c = \dot{m} C_p (T_{ao} - T_{ai}) \quad (3-6)$$

In addition, convection heat transfer between a solid surface and a fluid passing over it can be expressed by the Newton's Law of Cooling:

$$Q_c = hA\Delta T \quad (3-7)$$

3 EXPERIMENTAL ARRANGEMENT

The term ‘ ΔT ’ is the difference between the mean steady-state temperatures of the surface and the airflow, i.e. $(T_s - T_a)$. Thus, convective heat transfer coefficient from the heated triangular duct to the airflow (h) can be obtained from Equation (3-7):

$$h = \frac{Q_c}{A(T_w - T_a)} \quad (3-8)$$

The steady-state air temperature (T_a) was obtained by averaging the inlet and outlet air temperatures. It was used as the reference temperature to determine the fluid properties.

Currently, many compact heat exchangers adopt flow-passage of other geometries rather than circular cross-section, and it has been found that the same turbulence intensity and friction factor may prevail if the ratio of the flow passage area to the wetted perimeter is kept constant. Therefore, in the present investigation, the hydraulic diameter of the triangular duct (i.e. $D = \frac{4 \times \text{FlowArea}}{\text{Perimeter}}$) was adopted as the characteristic dimension to define the Reynolds number (Re), Nusselt number (Nu), as well as fanning friction factor (f), which can be determined from the pressure drop (ΔP) along the test duct and mean velocity of the airflow (U):

$$Re = \frac{\rho U D}{\mu} = \frac{U \cdot D}{\nu} \quad (3-9)$$

$$Nu = \frac{h \cdot D}{k} \quad (3-10)$$

$$f = \frac{\Delta P \cdot g_c \cdot (D/L)}{2\rho U^2} \quad (3-11)$$

To describe the relationship of the forced convection heat transfer from the horizontal heated triangular duct to the internal flowing air fluid with the flow conditions under different internal attached square rib or V-groove arrangements, the dimensionless parameters (i.e. Nusselt number, Reynolds number and Prandtl number) are related as follow:

$$Nu = C_1 Re^{n_1} Pr^{n_2} \quad (3-12)$$

In Equation (3-12), the Prandtl number (Pr), which should be an important parameter affecting the heat and mass transfer of the triangular duct, is defined as:

$$Pr = \frac{C_p \mu}{k} \quad (3-13)$$

However, Pr had not been separately considered in the present study since air was the only fluid used and its Prandtl numbers in the considered temperature range (T_a : ranging from 300K to 320K) remained almost constant (i.e. $Pr = 0.707$). Hence, Equation (3-12) can be simplified as:

$$Nu = C_2 Re^{n_1} \quad (3-14)$$

Similarly, for the fanning friction factor of a turbulent flow through a channel, Blasius (1911) proposed an empirical relation in the following form:

$$f = C_3 Re^{n_3} \quad (3-15)$$

3.6 Generalizations for Nusselt Number and Friction Factor

Since these parameters affect the turbulent flow in a triangular duct simultaneously, it is better to draw a generalization, which can generally describe the influence of both roughness and flow condition on forced convection in a single expression. It will also be useful for predictions of Nu and f in a triangular duct fabricated with either uniformly spaced square ribs or V-grooves on its internal surfaces.

To describe quantitatively the influences of flow conditions (i.e. Re was only used since the effect of Pr was not considered in the present investigation as explained previously) and roughness characteristics (i.e. relative rib size (H/D), relative rib-to-rib spacing (S_r/W), V-groove apex angle (\mathcal{G}) and relative groove-to-groove spacing (S_v/D)) on forced convection heat transfer between the triangular duct and the airflow, Nu is expressed as:

$$\text{For ribbed surface:} \quad Nu = f_1(Re, H/D, S_r/W) \quad (3-16)$$

$$\text{For V-grooved surface:} \quad Nu = f_2(Re, \mathcal{G}, S_v/D) \quad (3-17)$$

Similarly, a relationship for f of the turbulent flow through a horizontal equilateral triangular duct is proposed as:

$$\text{For ribbed surface:} \quad f = f_3(Re, H/D, S_r/W) \quad (3-18)$$

$$\text{For V-grooved surface:} \quad f = f_4(Re, \mathcal{G}, S_v/D) \quad (3-19)$$

3.7 Experimental Reliability

Since the present experimental study was performed with different values of Reynolds number, rib size, rib-to-rib spacing, as well as V-groove apex angle and groove-to-groove spacing, same experimental environments and operation conditions should be maintained to ensure repeatability of the experiments.

The instruments used to measure the temperature, pressure drop and airflow rate were all well pre-calibrated. The precision of every instrument is described in Appendix III. Error analysis method used to estimate the experimental uncertainties was based on the method proposed by Montgomery [2001]. For the entire experimental study, a confidential level of 95% was assumed.

Uncertainty analyses for Reynolds number, Nusselt number and friction factor in the present experimental study were carried out. There were several sources of uncertainty caused by different aspects including experimental set-up, precision of instrumentations, and measurements of relevant parameters: air temperature (T_a), wall surface temperature (T_w), pressure drop (ΔP) along the test duct, as well as the mass flow rate of air. Since the experimental set-up was well designed and instrumentations involved (i.e., thermocouples, manometers, pitot tube and wattmeters) had been well pre-calibrated, the major uncertainty came essentially from measurements of the above parameters. Typically, a maximum uncertainty associated with the average Reynolds number was determined to be less than $\pm 8\%$, and the most influential parameter involved was the mass flow rate. For the average Nusselt number, the uncertainty analysis indicated that a maximum uncertainty was $\pm 4.1\%$, while discrepancy between the calculated and experimental values was only

3 EXPERIMENTAL ARRANGEMENT

$\pm 2\%$. Similarly, a maximum uncertainty of $\pm 12\%$ and a discrepancy of $\pm 11\%$ between the calculated and experimental values were observed for the fanning friction factor.

Detailed procedures used to estimate the experimental uncertainties are summarized in Appendix I.

4 THERMAL AND HYDRODYNAMIC

PERFORMANCES OF THE RIBBED TRIANGULAR

DUCT

Rib-roughened internal surface, as a commonly met application in industrial equipments for internal cooling, is proposed to be a most efficient method to improve heat transfer rate when compared to other kinds of roughened surfaces [Leung et al. 2001]. In this chapter, focus is put on the study of the equilateral triangular duct with uniformly spaced square ribs attached on its internal surfaces as roughness elements. A similar study was carried out by Braga et al. [1996]. The triangular duct was attached with short pin fins on two uniformly heated walls while the third wall was kept smooth and insulated. Average heat transfer coefficients and friction factors for the system operated under turbulent flow conditions were investigated; however, the effects of rib size, rib-to-rib spacing, as well as Reynolds number on the flow and heat transfer characteristics of the triangular duct were not yet defined. Leung et al. [2001] conducted an experimental study on the influence of rib size on forced convection and flow friction in the triangular duct. Three rib-size-to-hydraulic-diameter ratios of 0.144, 0.217 and 0.289 were adopted, and a best thermal performance was obtained at the ratio of 0.144. Effect of relative rib-to-rib spacing on forced convection and flow friction in the ribbed triangular duct was investigated by Soo et al. [2002] with three pitch ratios, namely, S_r/W of 4, 8, and 16. It was concluded that the ribbed duct with the ratio of $S_r/W = 8$ could produce a superior heat transfer enhancement.

Though rough studies on rib size and rib-to-rib spacing have been conducted previously, to better utilize the thermal performance of the triangular duct with ribbed internal surfaces, information is still insufficient. Present investigation is aimed to fill up this gap.

4.1 Arrangement of Ribs

Repeated square-sectional ribs (i.e. $H = W = e$) of the same size were fixed on all three internal surfaces of the triangular duct at a uniform spacing of S_r , as shown in Fig. 4-1. To investigate the effect of rib size (e) on forced convection and fluid friction of a fully developed turbulent flow in a triangular duct, square ribs of five different sizes were applied, as shown in Table 4-1. In addition, as proposed in a previous study [Wong et al. 2002], the best thermal performance of a ribbed triangular duct would likely be obtained at a relative rib size (H/D) between 0.1 and 0.2, therefore H/D ratio used in the present study was varied from 0.1136 to 0.2045.

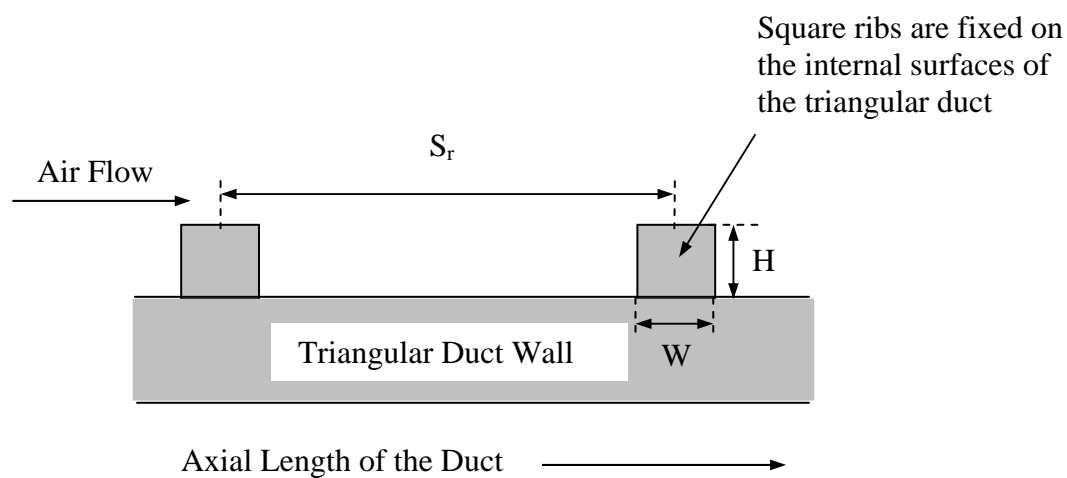


Fig. 4-1 Schematic representation of the ribbed surface

Table 4-1 Ranges of rib size and rib-to-rib spacing ($D = 44\text{mm}$)

Configuration	Square Rib Sizes ($H = W = e$) [mm]	Rib-to-Rib Spacing (S_r) [mm]
(1)	$5 (H/D = 0.1136)$	$57 (S_r/W = 11.4)$
(2)	$6 (H/D = 0.1364)$	$57 (S_r/W = 9.5)$
(3)	$7 (H/D = 0.1591)$	$57 (S_r/W = 8.14)$
(4)	$7.9 (H/D = 0.1795)$	$27 (S_r/W = 3.41)$
(5)	$7.9 (H/D = 0.1795)$	$47 (S_r/W = 5.95)$
(6)	$7.9 (H/D = 0.1795)$	$57 (S_r/W = 7.22)$
(7)	$7.9 (H/D = 0.1795)$	$67 (S_r/W = 8.48)$
(8)	$7.9 (H/D = 0.1795)$	$75 (S_r/W = 9.49)$
(9)	$7.9 (H/D = 0.1795)$	$110 (S_r/W = 13.93)$
(10)	$9 (H/D = 0.2045)$	$57 (S_r/W = 6.33)$

For the investigation of the rib-to-rib spacing (S_r)’s effect, ratio of rib spacing to rib width (S_r/W) was varied from 3.41 to 13.93 (see Table 4-1).

4.2 Average Nusselt Number

4.2.1 Effects of Rib Size

Since the hydraulic diameter of the triangular duct (D) used in the present study was equal to 44mm, rib sizes (e) of 5mm, 6mm, 7mm, 7.9mm and 9mm were adopted, respectively. The ribs were fixed on the duct’s internal surfaces with a constant separation of $S_r = 57\text{mm}$ between their centerlines at a direction along the main

4 THERMAL AND HYDRODYNAMIC PERFORMANCES OF THE RIBBED TRIANGULAR DUCT

airflow. The experimental results were obtained over a wide range of Reynolds numbers (Re) varying from 4,000 to 23,000 under steady-state conditions.

The experimental data were rearranged in a relationship between average Nusselt number (Nu) and Reynolds number (Re), as presented graphically in Fig. 4-2. To facilitate comparison, experimental results obtained from a similar triangular duct with smooth internal surfaces in a previous study [Leung et al. 2001] were also provided on the same diagram. The following expressions, in the form suggested by Equation (3-14), were obtained from the experimental data with the least-square method (see Appendix I), and were valid when $4,000 \leq Re \leq 23,000$:

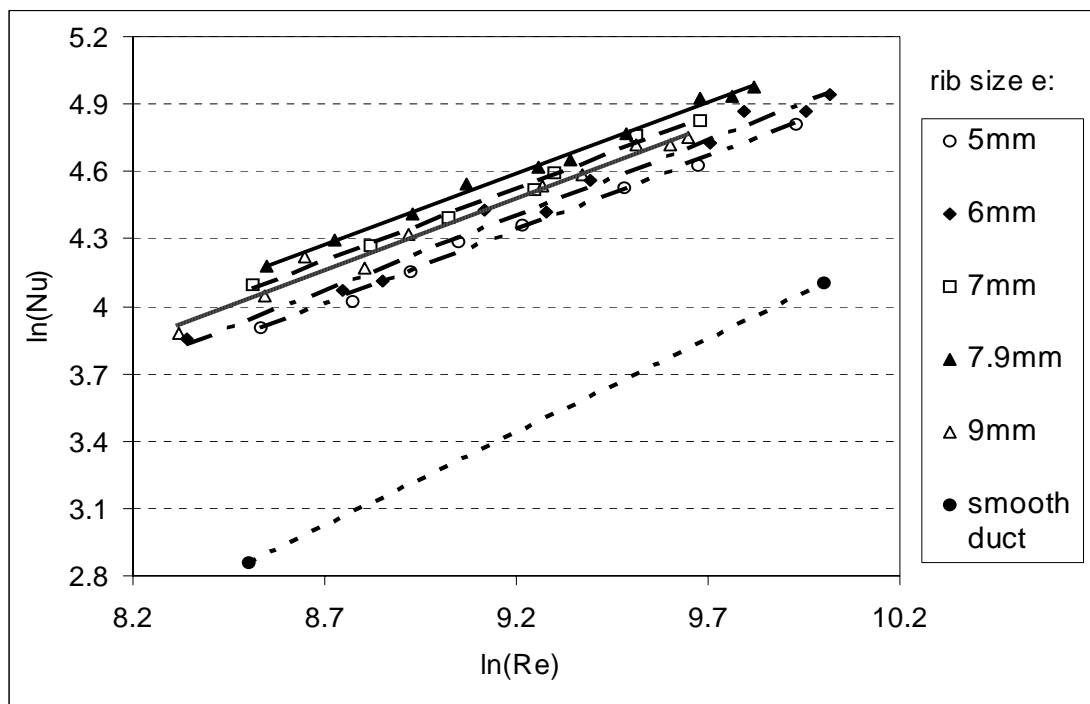


Fig. 4-2 Variation of Nu with Re for square ribs of different e 's

$$\text{Smooth surface [i.e. } \left(\frac{H}{D}\right) = 0] \text{ [Leung et al. 2001]: } Nu = 0.015Re^{0.82} \quad (4-1)$$

$$\text{Ribbed surface with 5mm ribs [i.e. } \left(\frac{H}{D}\right) = 0.1136]: Nu = 0.188Re^{0.6534} \quad (4-2)$$

$$\text{Ribbed surface with 6mm ribs [i.e. } \left(\frac{H}{D}\right) = 0.1364]: Nu = 0.175Re^{0.6682} \quad (4-3)$$

$$\text{Ribbed surface with 7mm ribs [i.e. } \left(\frac{H}{D}\right) = 0.1591]: Nu = 0.255Re^{0.6443} \quad (4-4)$$

$$\text{Ribbed surface with 7.9mm ribs [i.e. } \left(\frac{H}{D}\right) = 0.1795]: Nu = 0.307Re^{0.6273} \quad (4-5)$$

$$\text{Ribbed surface with 9mm ribs [i.e. } \left(\frac{H}{D}\right) = 0.2045]: Nu = 0.240Re^{0.642} \quad (4-6)$$

It can be seen from the above results that by adding ribs to the internal surfaces, it is able to enhance the forced convective heat transfer in the triangular duct significantly. The square ribs act effectively as turbulence promoters to facilitate the development of a thinner boundary layer along the flow direction, which leads to a higher average heat transfer coefficient and hence an enhanced forced convection in the triangular duct. In addition, it can be observed from Fig. 4-2 that the enhancement in forced convection varies with the relative rib height. For the ribbed surface with 7.9mm rib ($H/D = 0.1795$) at a rib-to-rib spacing of 57mm ($S_r/W = 7.22$), enhancements of 313.9% at $Re = 4,000$ and 195.5% at $Re = 23,000$ are obtained, respectively. The enhancement decreases with increasing Reynolds number. Therefore, it can be deduced that the thermal enhancement induced by the

4 THERMAL AND HYDRODYNAMIC PERFORMANCES OF THE RIBBED TRIANGULAR DUCT

ribbed surface is negligible when the Reynolds number is high enough. In order to examine clearly the effect of relative rib height, variations of Nu against H/D are shown graphically in Fig. 4-3, at a constant $Re = 10,400$ and a fixed $S_r = 57\text{mm}$ (i.e. $S_r/W = 7.22$). A maximum average Nusselt number Nu_{\max} is achieved at $e = 7.9\text{mm}$ (i.e. $H/D = 0.1795$).

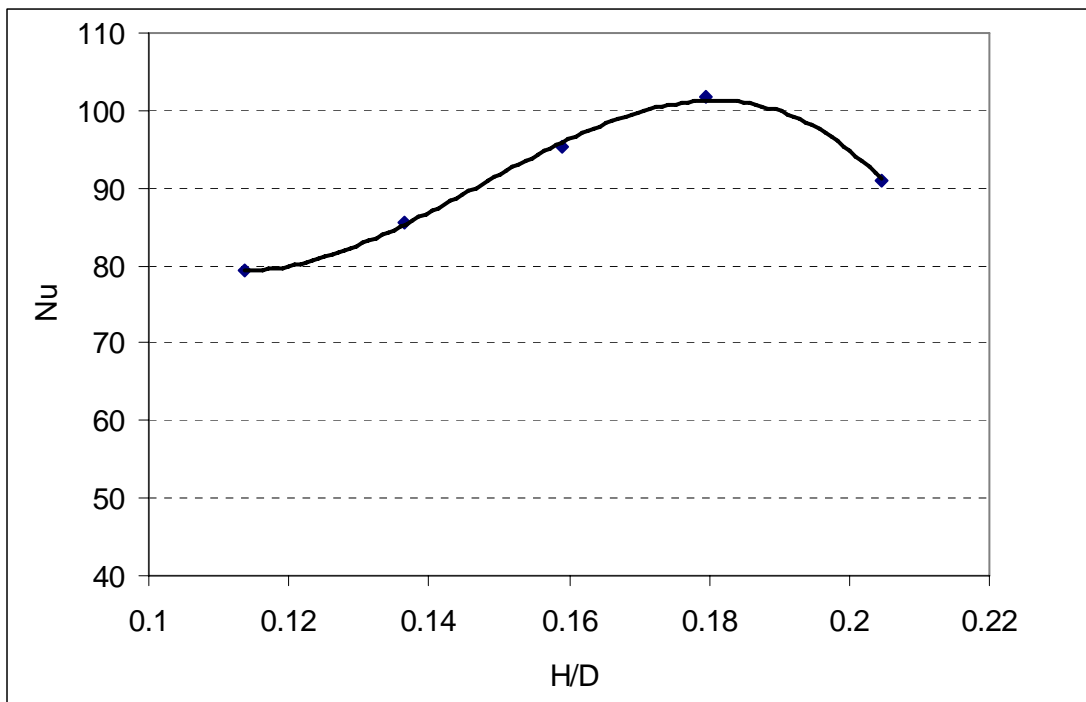


Fig. 4-3 Variation of Nu with H/D ($Re = 10,400$, $S_r/W = 7.22$)

In fact, the airflow is disturbed when flowing over the ribs and vortices are formed around each rib. The vortices' size and strength, which affect forced convection directly, depend on many parameters such as flow conditions, hydraulic diameter of

the triangular duct, size of the rib, as well as spacing between two consecutive ribs. The last parameter had been maintained constant throughout, therefore its effect on forced convection was not directly observed. At a constant flow condition, rib size and hydraulic diameter (i.e. directly proportional to flow area) of the triangular duct become two contradicting factors to affect the overall thermal performance of the duct.

On the one hand, size and strength of the vortices firstly increase with the increasing rib size (when the relative rib size is smaller than 0.1795), which lead to a more active secondary flow. As the rib gets larger, the cross-sectional flow area decreases and a higher effective flow velocity is caused. A more rapid fluid movement reduces the thickness of the thermal boundary layer and leads to a higher Nusselt number. In addition, a larger heat transfer area is induced as a result of increasing rib size, which also contributes to a higher heat transfer rate.

However, on the other hand, use of a larger rib implies a greater sudden-contraction in the flow area, which provides a higher pressure-drop along the airflow direction. Loss of pressure leads to a decay in kinetic energy of the fluid flow (see Chapter 7), which reduces the strength of the secondary flow as well as vortices (details are presented in Section 4.3.1). As the flow fields between the ribs are dominated by the secondary flow, a higher pressure-loss brings a negative effect to the duct's thermal performance. When the rib gets larger than a critical value (i.e. a relative rib size of 0.1795), the above-mentioned positive effects of larger ribs can not pay the penalty of higher pressure loss and finally, the heat transfer rate begins to decrease with increasing rib size. Therefore, from Fig. 4-3, it can be easily seen that because of such conflicting factors, Nu is firstly increased from $e = 5\text{mm}$ ($H/D = 0.1136$) until

a maximum value, Nu_{\max} , is obtained at $e = 7.9\text{mm}$ ($H/D = 0.1795$) and then decreases with a larger rib size of $e > 7.9\text{mm}$ ($H/D > 0.1795$).

4.2.2 Effects of Rib-to-Rib Spacing

Variations of average Nusselt number (Nu) with Reynolds number (Re) at different rib-to-rib spacings (S_r), which were ranged from 27mm to 110mm, were presented in Fig. 4-4. Experimental data were obtained with a constant rib size of $e = 7.9\text{mm}$, and $4,000 \leq Re \leq 23,000$. Similarly, to clearly observe the effect of relative rib-to-rib spacing on forced convection in the triangular duct, the experimental data were rearranged in the plot of Nu against S_r/W , as shown in Fig. 4-5, at a constant Reynolds number of $Re = 10,400$ and a fixed relative rib height of $H/D = 0.1795$.

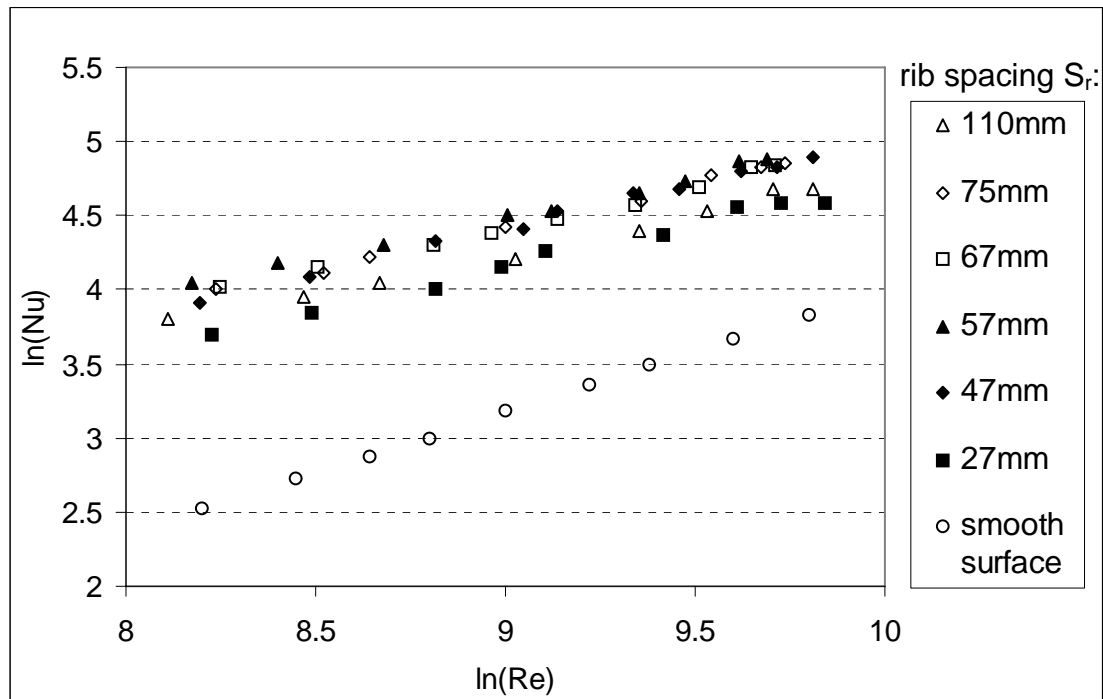


Fig. 4-4 Variation of Nu with Re for square ribs of different S_r 's

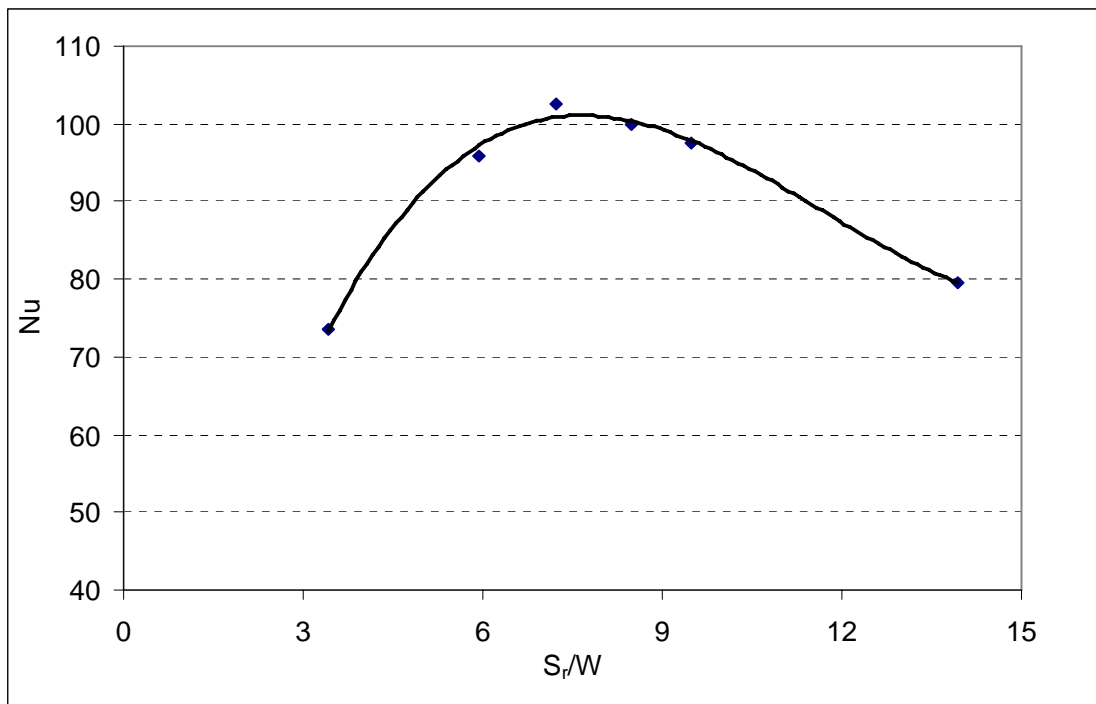


Fig. 4-5 Variation of Nu with S_r/W ($Re = 10,400$, $H/D = 0.1795$)

A similar trend line is observed to that for relative rib size: Nusselt number firstly increases with increasing rib-to-rib spacing until gets a maximum value of Nu_{\max} at $S_r/W = 7.22$, and then decreases with larger rib-to-rib spacing. It can be explained as: at the beginning, a larger rib-to-rib spacing is beneficial to the development of the secondary flow between two consecutive ribs, which as previously mentioned dominates this gap region and influences the forced convection consequently. An enhanced heat transfer rate is hence generated. However, as the rib-to-rib spacing gets larger, for a certain duct assembly, less ribs can be applied, which leads to smaller area for heat transfer, and the overall thermal performance of the duct is thus

negatively influenced. When latter ‘negative effect’ of rib-to-rib spacing overthrows its former ‘positive effect’, Nusselt number stops increasing with increasing rib-to-rib spacing and begins to decrease instead (namely, when $S_r/W \geq 7.22$).

In addition, from Fig. 4-5, it is noticeable that the maximum average Nusselt number is able to maintain for quite a wide range of relative rib-to-rib spacings, which gives a large flexibility in choosing a suitable rib-to-rib spacing in engineering applications.

4.2.3 Effects of Reynolds Number

From Figs. 4-2 and 4-4, it is seen that the average Nusselt number always increases with increasing Reynolds number. On the one hand, with a higher Reynolds number, which means a higher flow velocity and a greater mass flow rate, a more efficient heat transfer between the flow and the triangular duct is achieved, which results in a higher Nusselt number and hence a better thermal performance of the triangular duct. On the other hand, the flow is more turbulent at a higher Reynolds number, which also contributes to the improvement of heat transfer efficiency.

The effects of Reynolds number and relative rib size on the average Nusselt number can be considered simultaneously by rearranging all of the experimental data as presented in Fig. 4-2. A non-dimensional expression for the determination of the average Nusselt number, in terms of both Reynolds number and relative rib size, is formed in a similar form as suggested by Equation (3-14):

$$Nu = \phi\left(Re, \frac{H}{D}\right) \quad (4-7)$$

Firstly, rearrange all the experimental data in the relationship of $\ln(Nu)$ with $\ln(Re)$ at different e 's (as shown graphically in Fig. 4-6). With the aid of least-square method, a best-fit line with an equation in the following form is obtained:

$$\ln(Nu) = 0.6416\ln(Re) - 1.3856 \quad (4-8a)$$

Then, effect of H/D ratio is taken into consideration by plotting the values of $\ln(Nu / Re^{0.6416})$ against $\ln(H/D)$ as shown in Fig. 4-7. Similarly, the data points are matched with a polynomial line to give an equation in the following form:

$$\ln(Nu / Re^{0.6416}) = -0.7954[\ln(H/D)]^2 - 2.6235\ln(H/D) - 3.4789 \quad (4-8b)$$

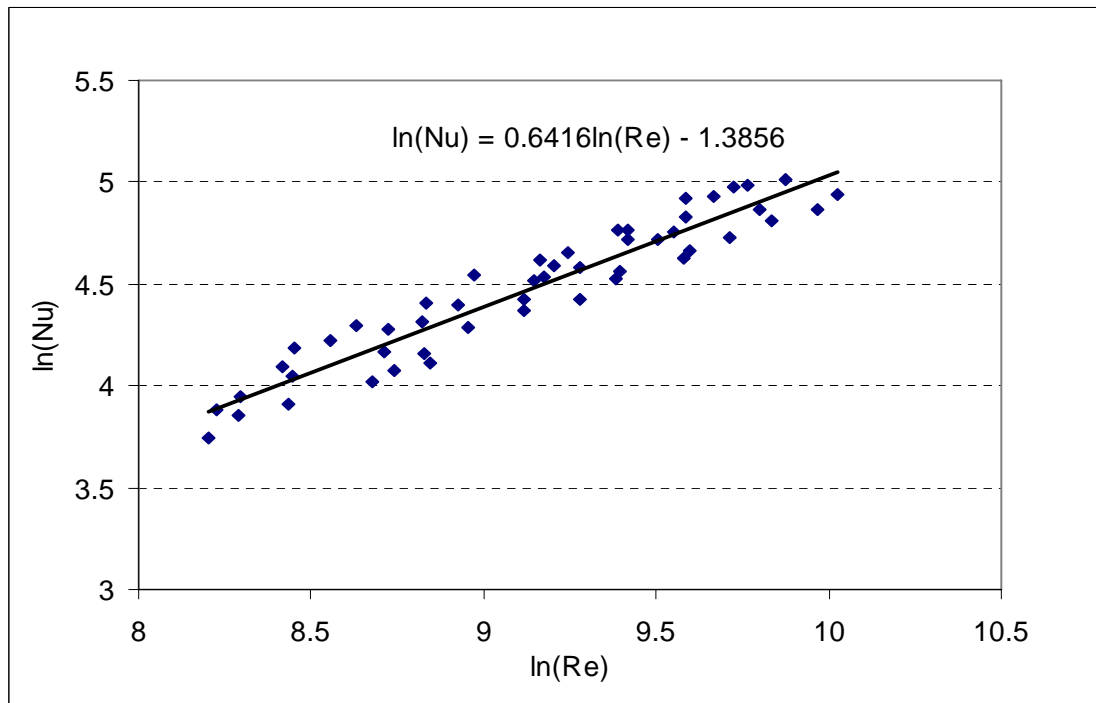


Fig. 4-6 Plot of effect of Re on Nu

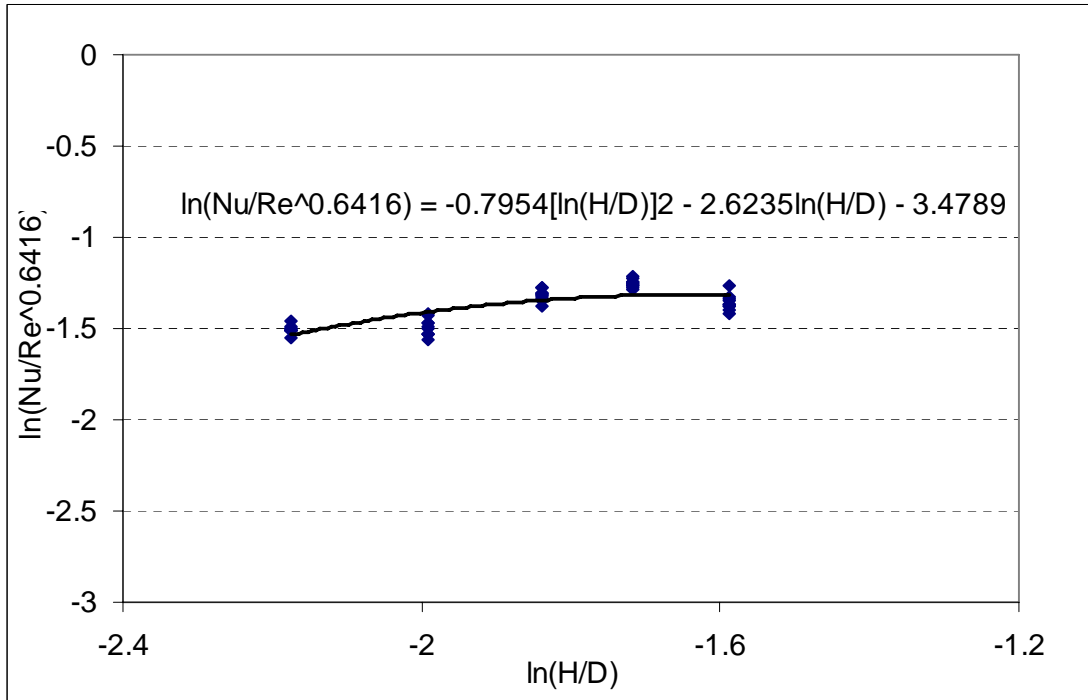


Fig. 4-7 Plot of effect of H/D on Nu

By rewriting Equation (4-8b), a final relationship between Nu , Re and H/D is achieved:

$$Nu = 0.03 Re^{0.6416} \left(\frac{H}{D}\right)^{-2.6235} \exp\left(-0.7954 \left(\ln \frac{H}{D}\right)^2\right) \quad (4-8)$$

Equation (4-8) is valid when $4,000 \leq Re \leq 23,000$ and $0.11 \leq \frac{H}{D} \leq 0.21$.

Similarly, to consider the integrated effects of Reynolds number and relative rib-to-rib spacing on the average Nusselt number, all the experimental data presented in Fig. 4-4 need be rearranged. Non-dimensional expression for the determination of

average Nusselt number, in terms of both Reynolds number and relative rib-to-rib spacing, can be written in the following form:

$$Nu = \phi_1 \left(Re, \frac{S_r}{W} \right) \quad (4-9)$$

The rearrangements of the experimental data are shown graphically in Figs. 4-8 and 4-9. With the aid of the least-square method, the following equations are obtained

with $4,000 \leq Re \leq 23,000$ and $3.41 \leq \frac{S_r}{W} \leq 13.93$:

$$Nu = 0.058 Re^{0.5872} \left(\frac{S_r}{W} \right)^{2.0151} \exp \left(-0.5066 \left(\ln \frac{S_r}{W} \right)^2 \right) \quad (4-10)$$

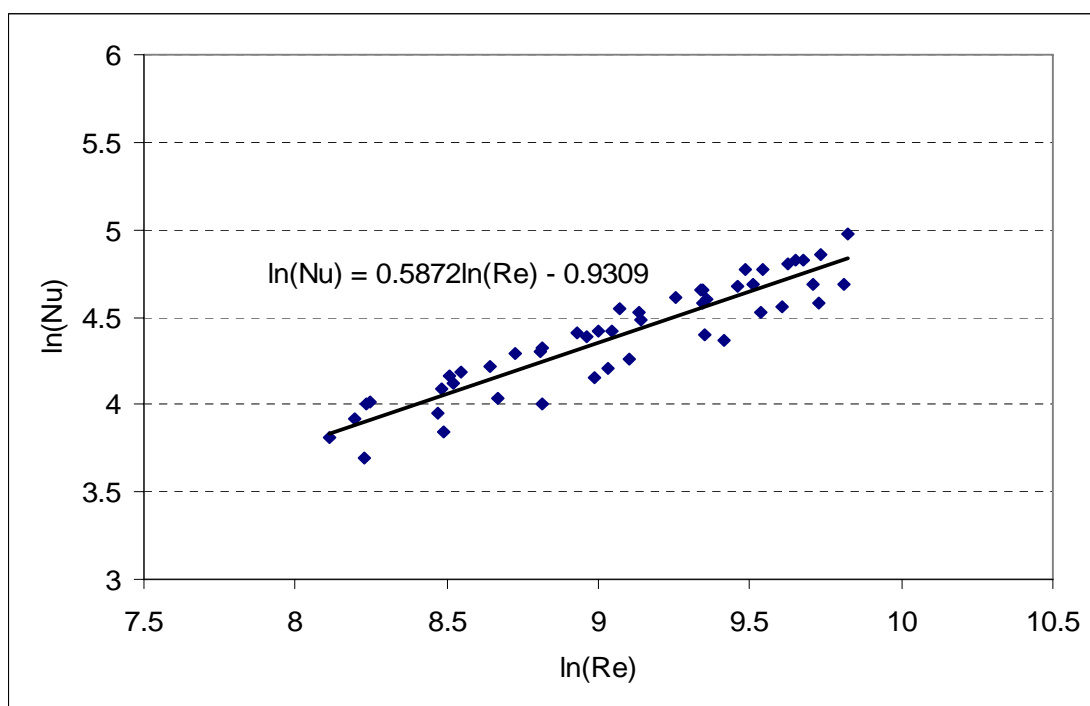


Fig. 4-8 Plot of effect of Re on Nu

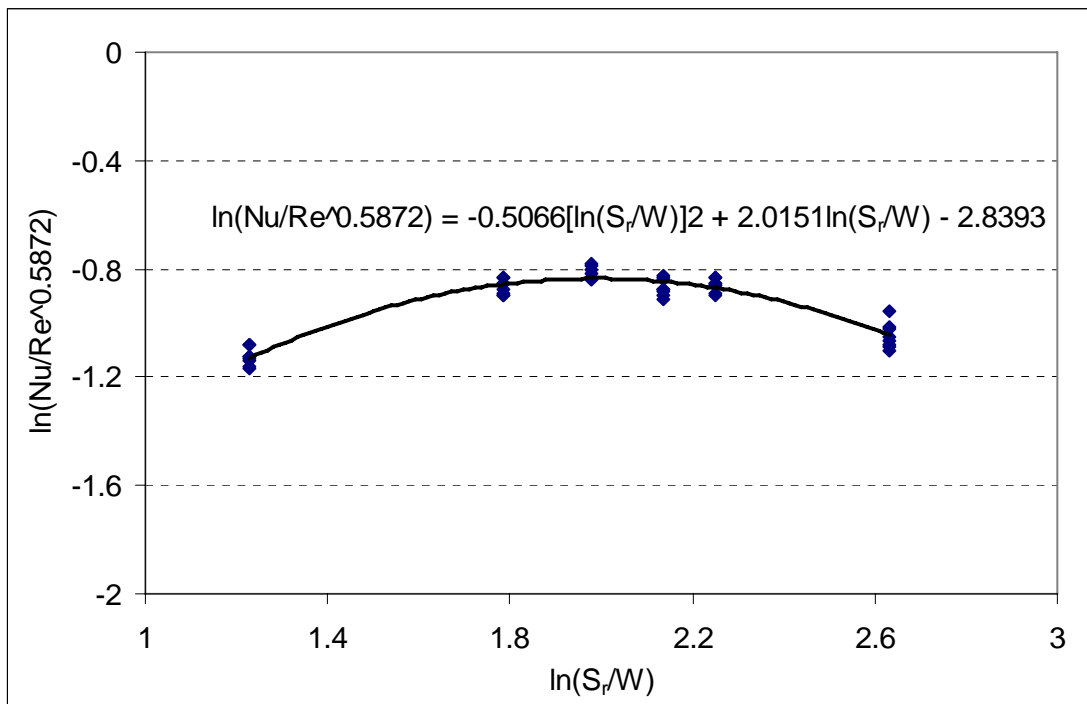


Fig. 4-9 Plot of effect of S_r/W on Nu

4.2.4 Generalization of Average Nusselt Number

From the above discussions and result analyses, it is found that the introduction of artificial roughness can enhance the Nusselt number efficiently. However, the magnitude of enhancement shows a strong dependence on several parameters including geometrical structure and dimension of the roughness, separation between two adjacent roughness elements, as well as flow conditions.

As suggested in Section 3.5, generalizations for the forced convection and fluid friction in such a ribbed triangular duct at different flow conditions and rib arrangements will be very useful and convenient. Thus, it is necessary to develop some expressions to define the relationships of the parameters (i.e. Nu and f) with

their impact factors (i.e. Re , H/D , and S_r/W). These expressions will also be useful for the predictions of Nu and f .

The following steps are carried out to fulfill the task. A similar data deduction approach as described in a previous study [Saini et al. 1997] is applied.

All experimentally obtained average Nusselt numbers are plotted against their corresponding Reynolds numbers and presented in Fig. 4-10. The following relationship is achieved by the least-square method:

$$Nu = A_0 Re^{A_1} \quad (4-11)$$

The power index A_1 is found to be 0.5924 and the numerical constant A_0 is a function of the other two involved parameters: H/D and S_r/W .

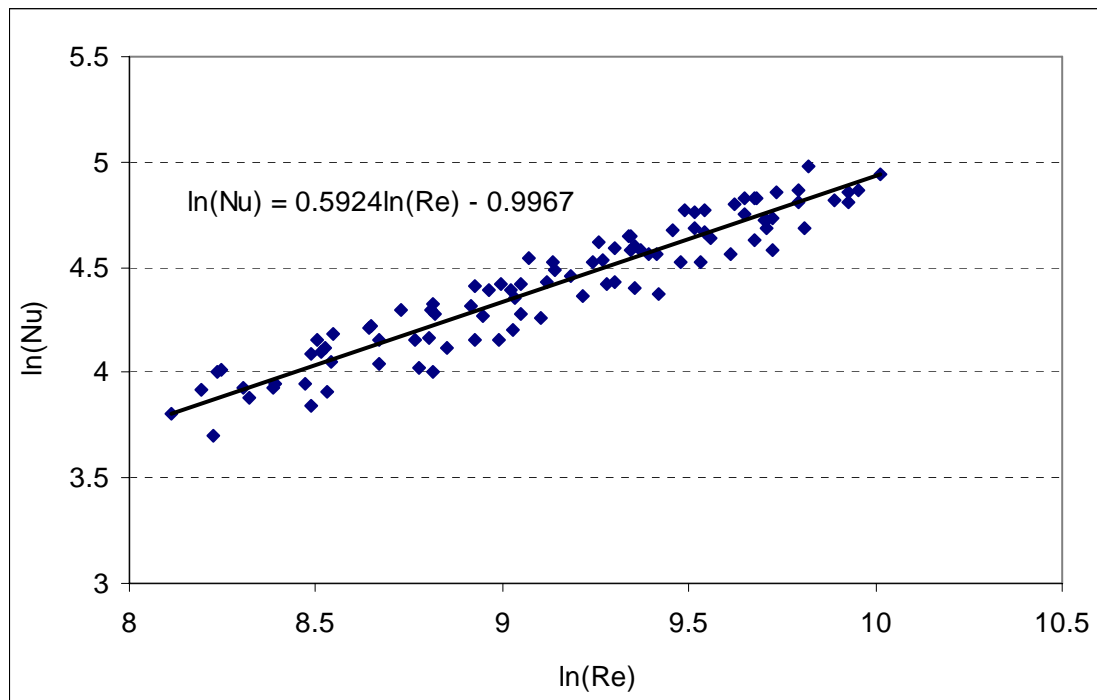


Fig. 4-10 Plot of effect of Re on Nu

4 THERMAL AND HYDRODYNAMIC PERFORMANCES OF THE RIBBED TRIANGULAR DUCT

To investigate the relationship of relative rib-to-rib spacing (S_r/W) with Nusselt number (Nu), (Nu/Re^A) is plotted against (S_r/W) as shown in Fig. 4-11. A polynomial line is achieved with a second-order quadratic equation in the following form:

$$\ln(Nu/Re^A) = B_0 + B_1 \ln(S_r/W) + B_2 [\ln(S_r/W)]^2 \quad (4-12)$$

The constants B_1 and B_2 are determined to be 1.8414 and -0.4684, respectively, whereas the constant B_0 is a function of the last involved parameter: H/D .

Finally, to reveal the relationship between relative rib height (H/D) and Nusselt

number (Nu), ($\frac{Nu}{Re^A (\frac{S_r}{W})^{B_1} [\exp\{B_2 (\ln(\frac{S_r}{W}))^2\}]}$) is plotted against (H/D) as

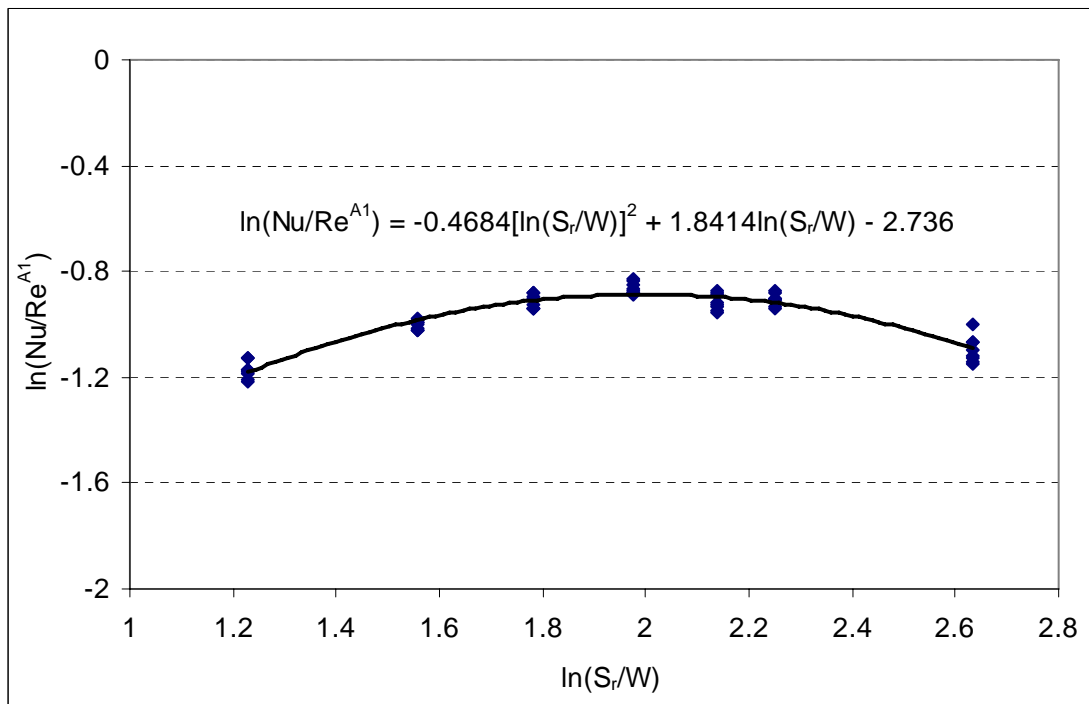


Fig. 4-11 Plot of effect of S_r/W on Nu

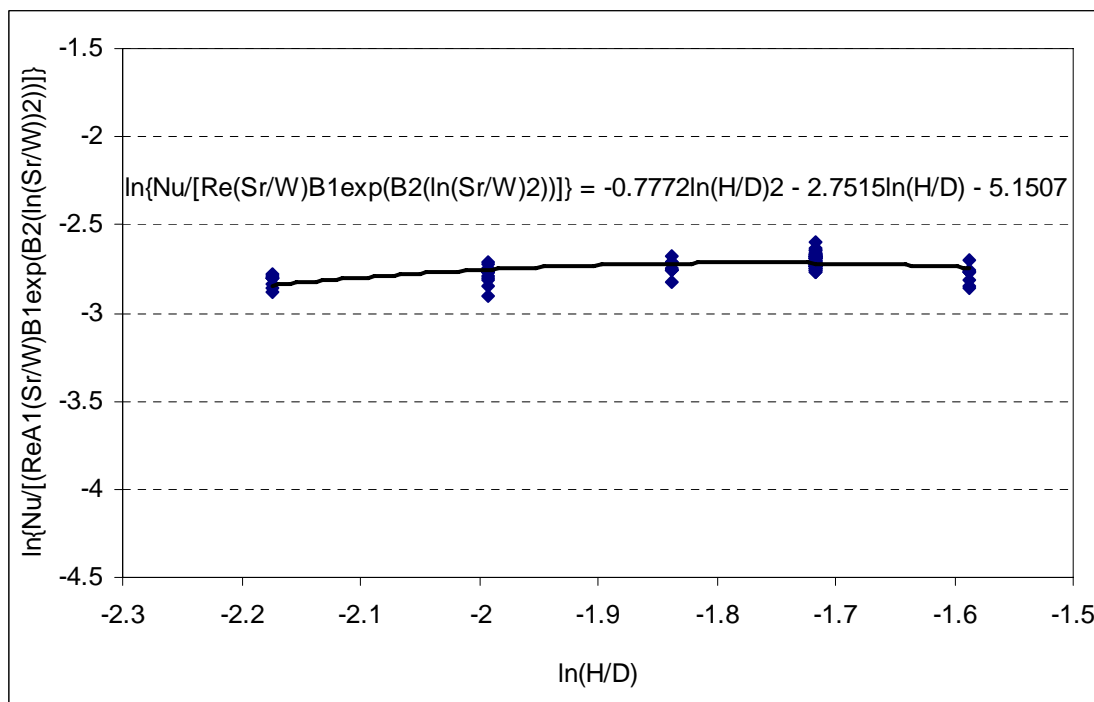


Fig. 4-12 Plot of effect of H / D on Nu

shown in Fig. 4-12. The following equation is obtained to fit these points well:

$$\ln \left(\frac{Nu}{Re^{A_1} \left(\frac{S_r}{W} \right)^{B_1} \left[\exp \left\{ B_2 \left(\ln \left(\frac{S_r}{W} \right) \right)^2 \right\} \right]} \right) = C_0 + C_1 \ln(H/D) + C_2 [\ln(H/D)]^2 \quad (4-13)$$

The constants C_0 , C_1 and C_2 are determined to be -5.1507, -2.7515 and -0.7772, respectively.

Then, a non-dimensional relationship between Nu , Re , H/D and S_r/W in the form suggested by Equation 3-14 is obtained below:

$$Nu = 0.0058Re^{0.5924} \left(\frac{H}{D}\right)^{-2.7515} \left(\frac{S_r}{W}\right)^{1.8414} \exp\left\{-0.7772\left(\ln\left(\frac{H}{D}\right)\right)^2\right\} \exp\left\{-0.4684\left(\ln\left(\frac{S_r}{W}\right)\right)^2\right\}$$

(4-14)

for the ranges: $4,000 \leq Re \leq 23,000$, $0.11 \leq \frac{H}{D} \leq 0.21$ and $3.41 \leq \frac{S_r}{W} \leq 13.93$.

4.3 Average Friction Factor

4.3.1 Effects of Rib Size

For different rib sizes of 5mm, 6mm, 7mm, 7.9mm and 9mm, variations of friction factor with increasing Reynolds number are shown in Fig. 4-13. The rib-to-rib spacing was kept constant at 57mm for each experiment, with Reynolds number ranged from 4,000 to 23,000. Available results in a previous study [Leung et al. 2001] of a smooth triangular duct with the same dimension were also presented. It is obvious to see that a great enhancement in friction factor is recorded by the application of ribbed surface, which leads to a higher pressure-drop along the flow direction. For the ribbed surface with 7.9mm rib ($H/D = 0.1795$) at a rib-to-rib spacing of 57mm ($S_r/W = 7.22$), enhancements of 973.8% at $Re = 4,000$ and 1505.1% at $Re = 23,000$ are obtained, respectively. The enhancement increases with increasing Reynolds number. Compared to the enhancement of Nu as discussed in Section 4.2.1, it can be concluded that when the Reynolds number is high enough, the negative effects induced by the additional ribs (i.e. enlarged pressure drop) are far more significant than the positive effects of the ribs (i.e. improved thermal performance).

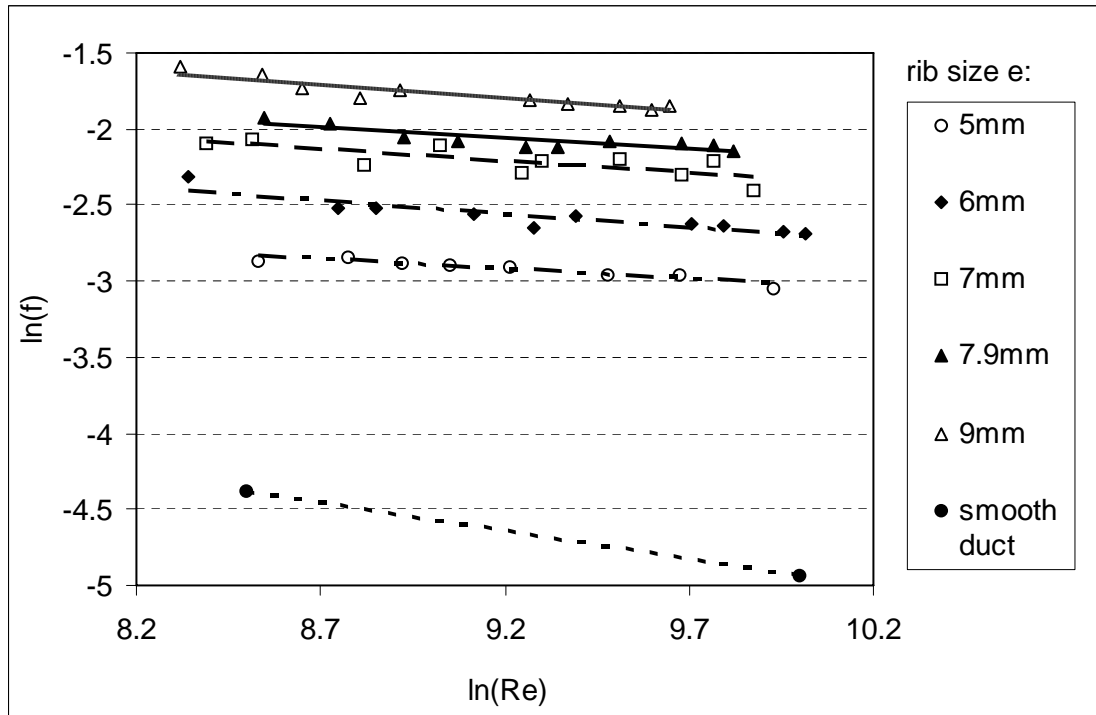


Fig. 4-13 Variation of f with Re for square ribs of different e 's

Similarly, the following expressions for the average friction factor, in the form suggested by Equation (3-13), were obtained from the experimental data with the least-square method, and were valid when $4,000 \leq Re \leq 23,000$:

$$\text{Smooth surface [i.e. } \left(\frac{H}{D}\right) = 0 \text{] [Leung et al. 2001]: } f = 0.29 Re^{-0.37} \quad (4-15)$$

$$\text{Ribbed surface with 5mm ribs [i.e. } \left(\frac{H}{D}\right) = 0.1136 \text{]: } f = 0.176 Re^{-0.1286} \quad (4-16)$$

$$\text{Ribbed surface with 6mm ribs [i.e. } \left(\frac{H}{D}\right) = 0.1364 \text{]: } f = 0.391 Re^{-0.1757} \quad (4-17)$$

4 THERMAL AND HYDRODYNAMIC PERFORMANCES OF THE RIBBED TRIANGULAR DUCT

$$\text{Ribbed surface with 7mm ribs [i.e. } \left(\frac{H}{D}\right) = 0.1591]: f = 0.354 Re^{-0.1189} \quad (4-18)$$

$$\text{Ribbed surface with 7.9mm ribs [i.e. } \left(\frac{H}{D}\right) = 0.1795]: f = 0.463 Re^{-0.1402} \quad (4-19)$$

$$\text{Ribbed surface with 9mm ribs [i.e. } \left(\frac{H}{D}\right) = 0.2045]: f = 0.865 Re^{-0.1796} \quad (4-20)$$

Application of ribs on the internal surfaces leads to the occurrence of larger friction factors. The magnitude of the enhancement varies with the rib size. To clearly discover the effect of the rib size on friction factor, variations of f against H/D are shown graphically in Fig. 4-14, at a constant Reynolds number of $Re = 10,400$ and a

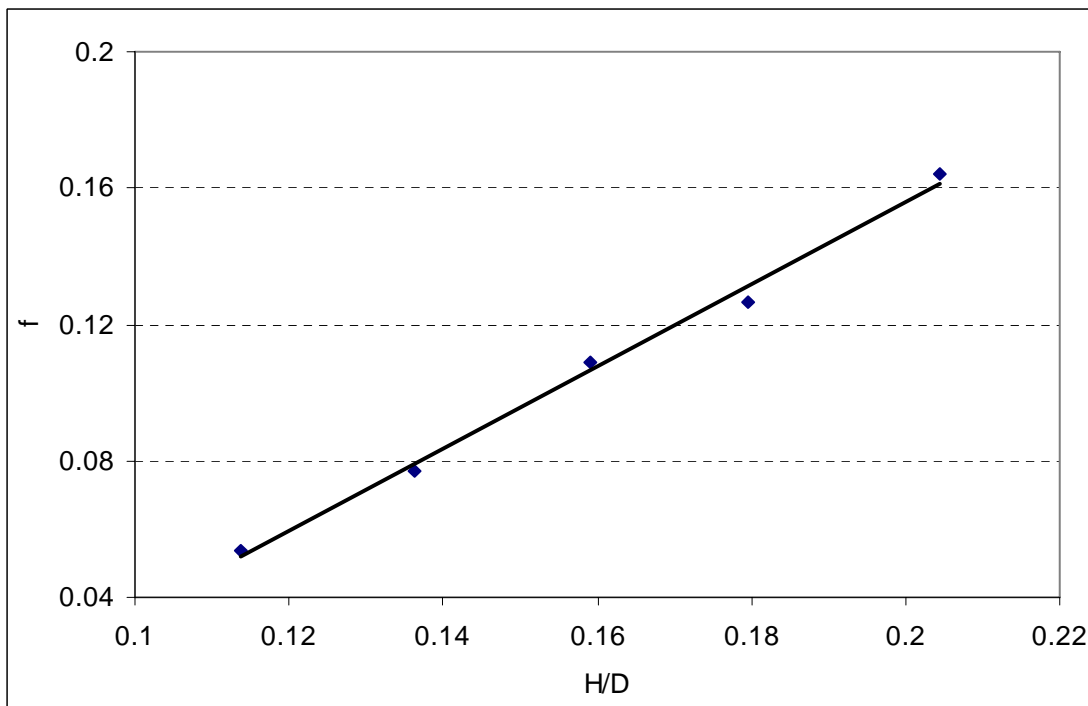


Fig. 4-14 Variation of f with H/D ($Re = 10,400$, $S_r/W = 7.22$)

constant rib-to-rib spacing of $S_r = 57\text{mm}$ (i.e. $S_r/W = 7.22$). A linear increasing trend line is obtained for friction factor with increasing relative rib size. It implies that the pressure drop encountered by the fluid stream flowing through a triangular duct is enhanced significantly by attaching uniformly spaced square ribs on its internal surfaces. Such pressure drop increases nearly linearly with the rib size. Use of a larger rib provides a greater sudden-contraction in the flow area, which generates a higher pressure-loss along the streamwise direction of airflow.

4.3.2 Effects of Rib-to-Rib Spacing

Variations of f for different applications of rib-to-rib spacing are not significant, as shown in Fig. 4.15. The Reynolds number is fixed at $Re = 10,400$ for a relative rib

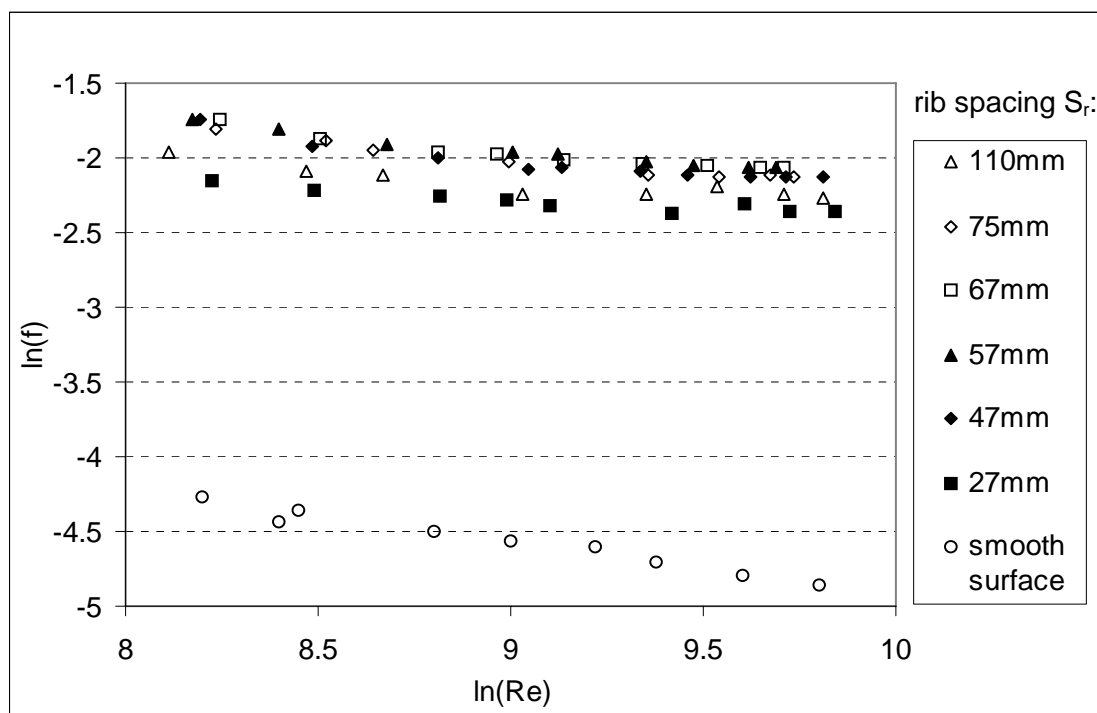


Fig. 4-15 Variation of f with Re for square ribs of different S_r 's

4 THERMAL AND HYDRODYNAMIC PERFORMANCES OF THE RIBBED TRIANGULAR DUCT

height of $H/D = 0.1795$. Similarly, a direct relationship between friction factor and rib size is explored in the form of f against S_r/W and plotted in Fig. 4-16. A similar variation of flow friction to that of Nusselt number with the relative rib-to-rib spacing is observed. Both Nu and f obtaining their maximum values at $S_r/W = 7.22$. However, the fluctuation in flow friction against different rib-to-rib spacings is much smaller. As explained previously, a larger rib-to-rib spacing means less ribs applied to the ribbed surface. When the rib-to-rib spacing is large enough (such as $S_r/W \geq 7.22$), the ribbed surface is gradually dominated by the gap space between two consecutive ribs, which makes the surface flatter and thus a less pressure drop along the duct ensues. On the other hand, when the rib-to-rib spacing gets smaller (such as $S_r/W \leq 7.22$), more ribs are applied, which makes the ribbed surface

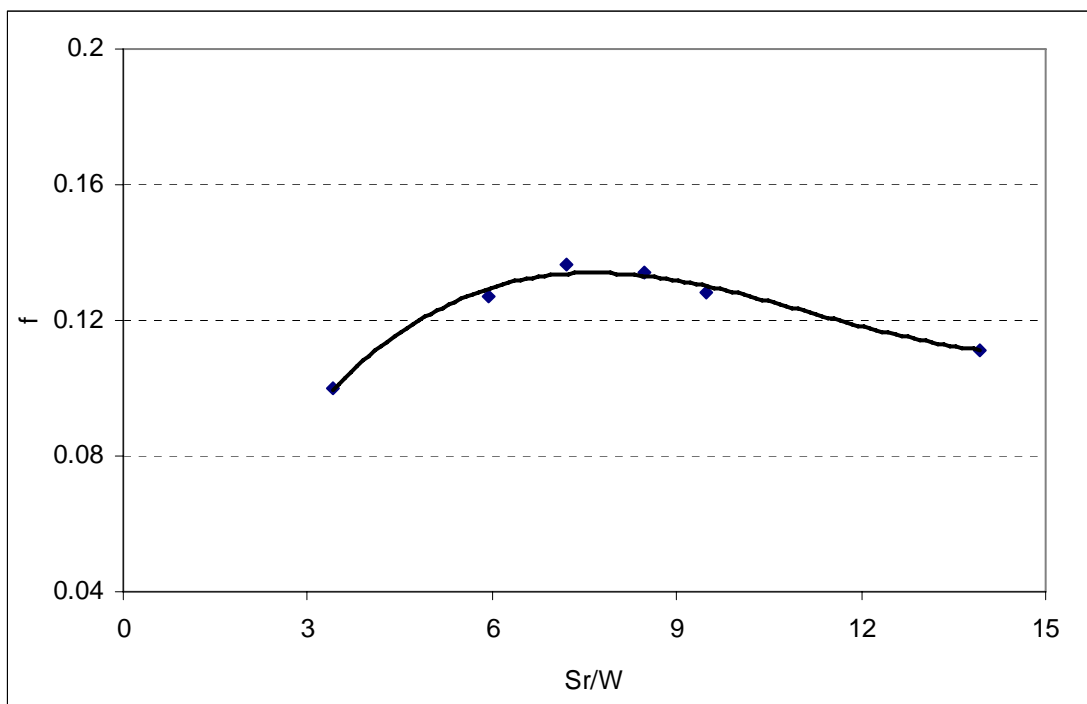


Fig. 4-16 Variation of f with S_r/W ($Re = 10,400$, $H/D = 0.1795$)

gradually dominated by the ribs' top surface instead and to some extent, the surface becomes flatter again and thus generates a less pressure loss. Therefore, friction factor firstly increases with increasing rib-to-rib spacing until gets a maximum value of f_{\max} at $S_r/W = 7.22$ and then inversely decreases with the rib-to-rib spacing.

4.3.3 Effects of Reynolds Number

As shown in Figs. 4-13 and 4-15, unlike Nusselt number, smaller friction factors are obtained for higher Reynolds numbers. It can be explained from its definition (i.e., Equation 3-11). For a certain pipe or duct, a higher Reynolds number usually means a higher flow velocity, square of which is in inverse ratio with friction factor, even though a higher pressure drop and a higher requirement of power input for driving the fluid flow is generated.

Similarly, rearranging the experimental data presented in Figs. 4-13 and 4-15 with the method described in Section 4.2.3, non-dimensional expressions were obtained for the average friction factor in terms of Reynolds number and relative rib size, Reynolds number and relative rib-to-rib spacing, respectively, as shown in Figs. 4-17 to 4-20:

$$f = 50 Re^{-0.2584} \left(\frac{H}{D} \right)^{1.9916} \quad (4-21)$$

$$f = 0.123 Re^{-0.1876} \left(\frac{S_r}{W} \right)^{1.7614} \exp \left(-0.4322 \left(\ln \frac{S_r}{W} \right)^2 \right) \quad (4-22)$$

Equations (4-21) and (4-22) were valid when $4,000 \leq Re \leq 23,000$, $0.11 \leq \frac{H}{D} \leq 0.21$

and $3.41 \leq \frac{S_r}{W} \leq 13.93$.

4 THERMAL AND HYDRODYNAMIC PERFORMANCES OF THE RIBBED TRIANGULAR DUCT

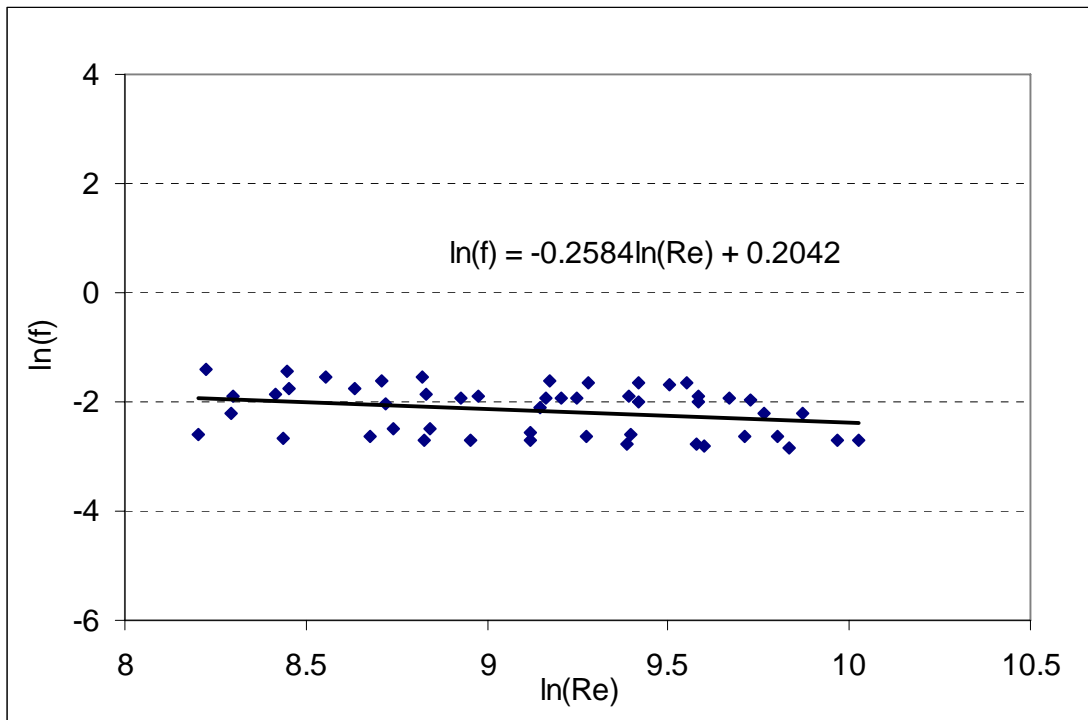


Fig. 4-17 Plot of effect of Re on f

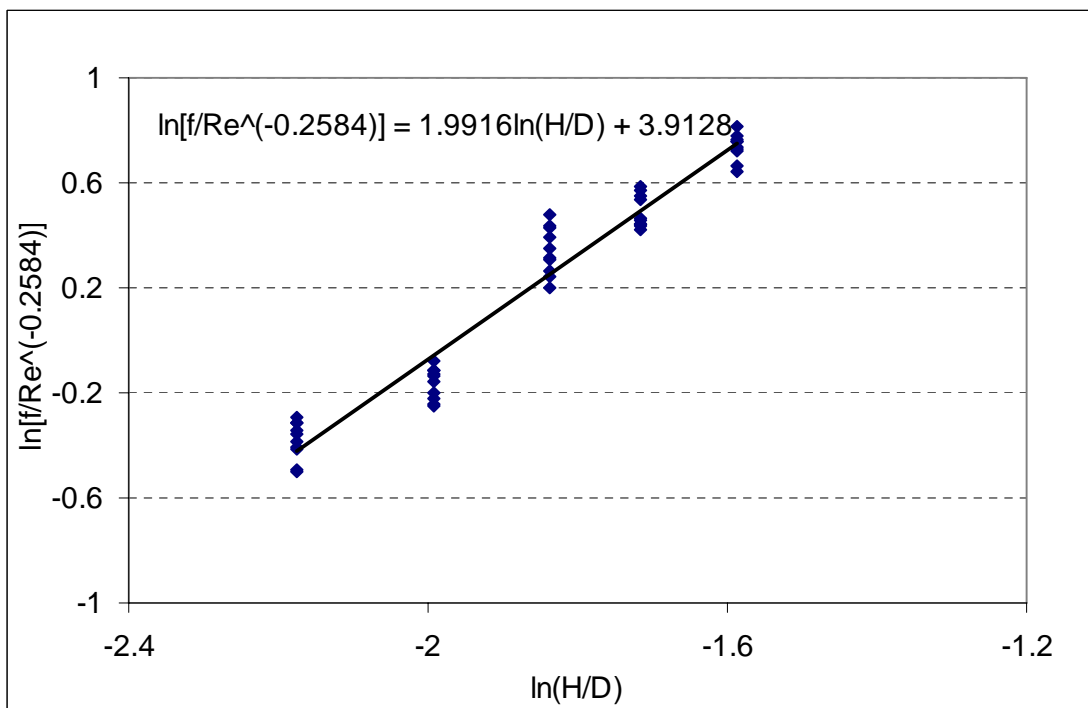


Fig. 4-18 Plot of effect of H/D on f

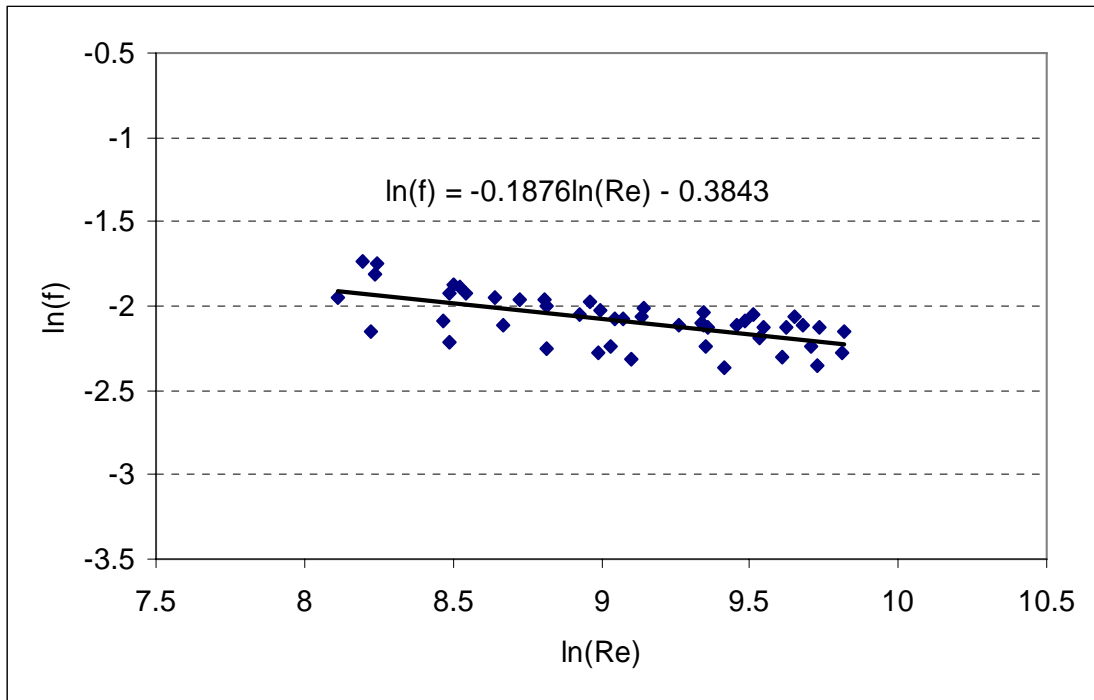


Fig. 4-19 Plot of effect of Re on f

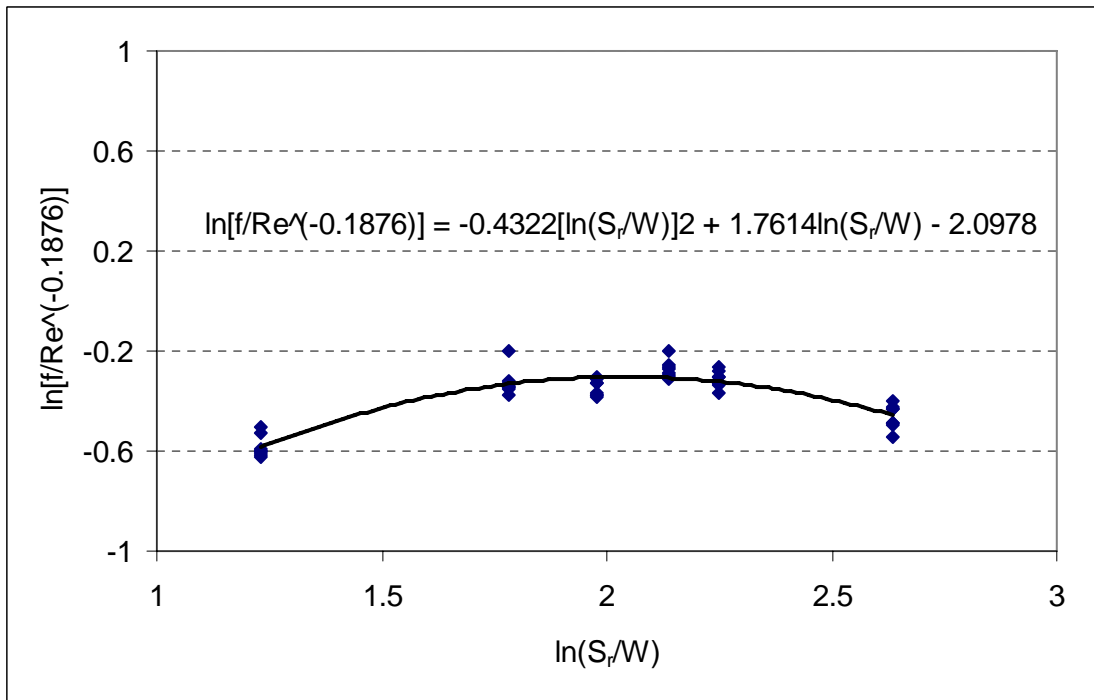


Fig. 4-20 Plot of effect of S_r/W on f

4.3.4 Generalization of Average Friction Factor

A non-dimensional equation for predicting the average friction factor (f) in terms of Re , H/D , S_r/W (in form of Equation 3-16) was developed by employing the similar procedures as described in Section 4.2.4. Figures 4-21 to 4-23 depict the stages of obtaining such a relationship in the following form:

$$f = 5.04 Re^{-0.2897} \left(\frac{H}{D}\right)^{1.6224} \left(\frac{S_r}{W}\right)^{1.7842} \exp\left\{-0.4407 \left(\ln\left(\frac{S_r}{W}\right)\right)^2\right\} \quad (4-23)$$

for the ranges: $4,000 \leq Re \leq 23,000$, $0.11 \leq \frac{H}{D} \leq 0.21$, and $3.41 \leq \frac{S_r}{W} \leq 13.93$.

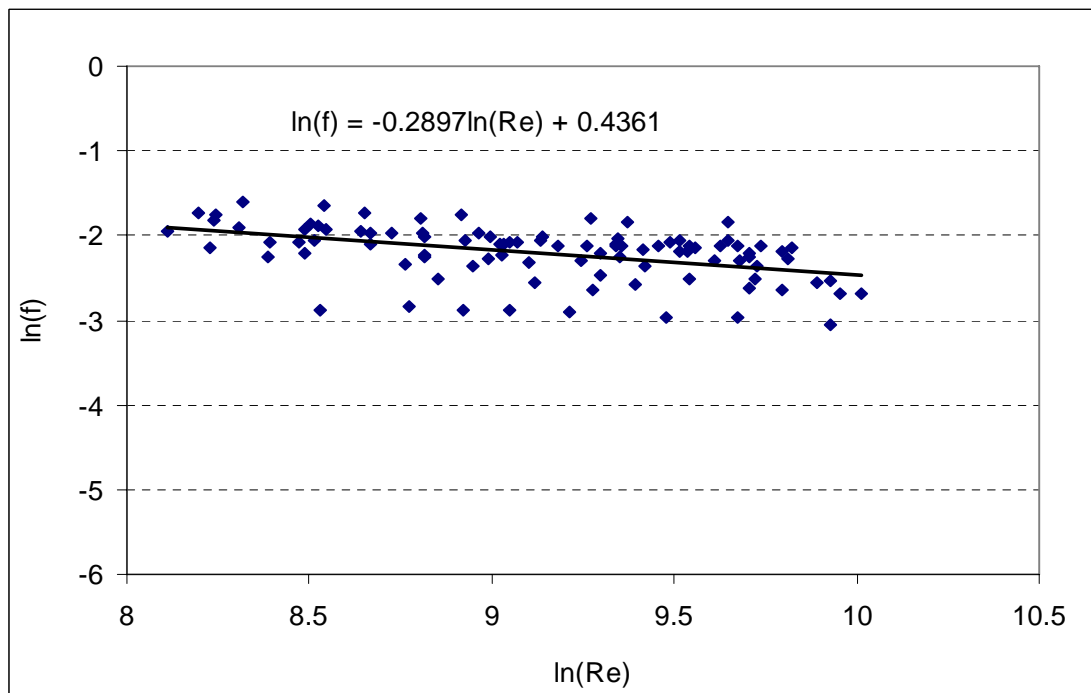


Fig. 4-21 Plot of effect of Re on f

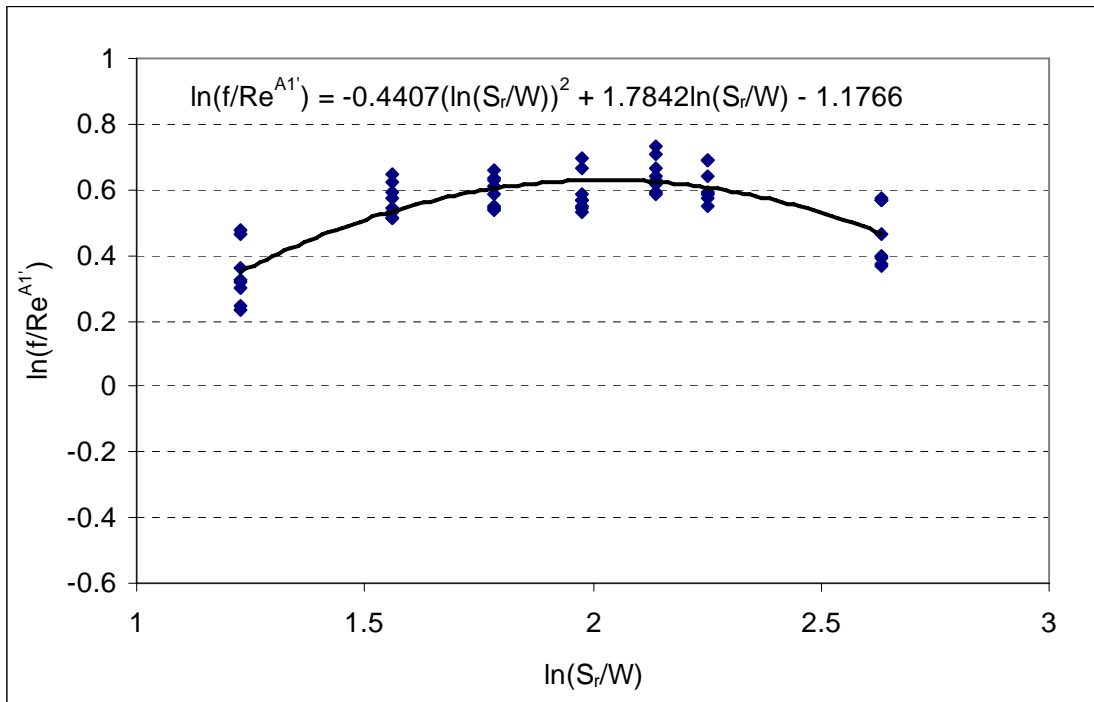


Fig. 4-22 Plot of effect of S_r/W on f

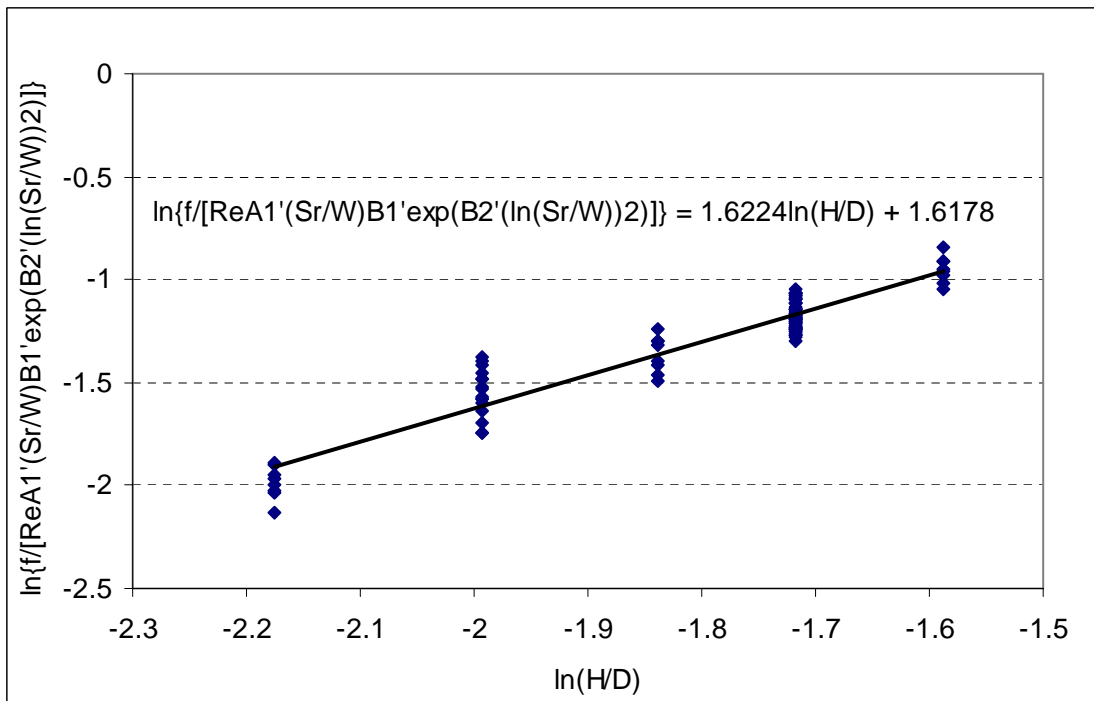


Fig. 4-23 Plot of effect of H/D on f

4 THERMAL AND HYDRODYNAMIC PERFORMANCES OF THE RIBBED TRIANGULAR DUCT

From the expressions for S_r/W in Equations (4-14) and (4-23), namely,

$$Nu \propto \left(\frac{S_r}{W}\right)^{1.8414} \exp\left(-0.4684\left(\ln\left(\frac{S_r}{W}\right)\right)^2\right) \text{ and } f \propto \left(\frac{S_r}{W}\right)^{1.7842} \exp\left(-0.4407\left(\ln\left(\frac{S_r}{W}\right)\right)^2\right),$$

it can be found that both average Nusselt number (Nu) and average friction factor (f) have very similar variation trends with relative rib-to-rib spacing (S_r/W): increase firstly with the increasing S_r/W and then decrease after a certain S_r/W is exceeded. However, for the relative rib height (H/D), the situation is quite different: Nu obtains a maximum value at an optimum H/D ratio of 0.1795, but f increases rather linearly with H/D , which is a big drawback to the enhancement of thermal performance of the ribbed triangular duct. Moreover, because of the complicated construction of the triangular duct under consideration, the effect of Reynolds number on forced convection in this thermal system ($Nu \propto Re^{0.5924}$ and $f \propto Re^{-0.2897}$) is not so significant as it does in a similar smooth triangular duct ($Nu \propto Re^{0.83}$ and $f \propto Re^{-0.37}$) [Leung et al. 2001]. Taking these three factors' effects on this thermal system into consideration, it is found that when the flow becomes highly turbulent, effect of Reynolds number (Re) is more obvious than that of the duct geometry (H/D and S_r/W). It can be deduced that attaching ribs to the internal surfaces of the triangular duct to enhance its thermal performance will be more effective when Reynolds number of the turbulent flow is relative low.

In addition, comparing the experimentally obtained Nusselt numbers and friction factors with those predicted by Equations (4-14) and (4-23), as represented in Figs. 4-24 and 4-25, it can be seen that the empirically predicted Nu and f agree reasonably well with the experimentally obtained Nu and f . Error estimations are

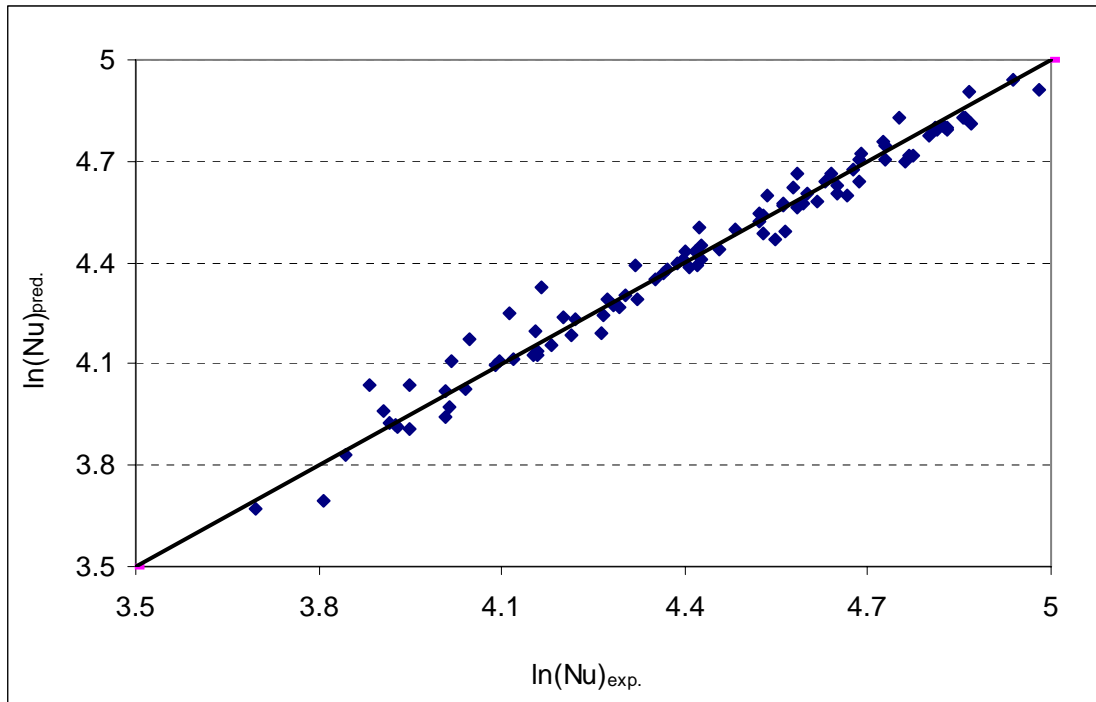


Fig. 4-24 Plot of experimental and predicted values of Nu

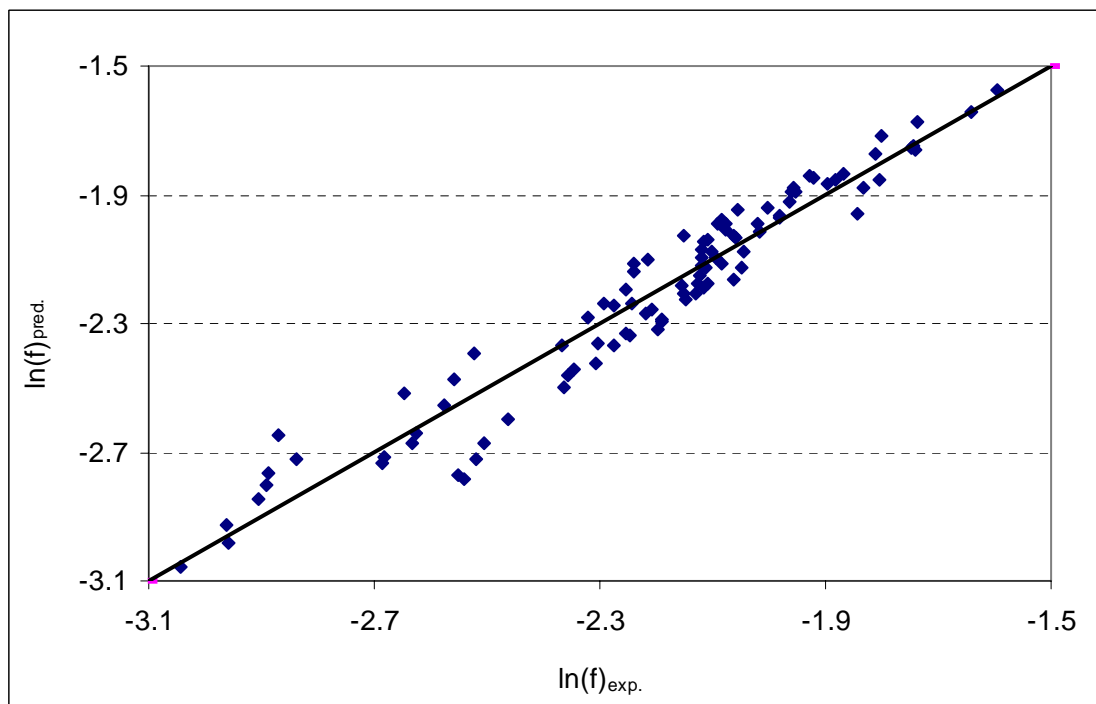


Fig. 4-25 Plot of experimental and predicted values of f

carried out and maximum percentage deviations between the experimental and predicted values are found to be $\pm 3.5\%$ and $\pm 8.7\%$ for Nu and f , respectively.

4.4 Volume Goodness Factor

As found from above sections, a highest Nusselt number is obtained at the rib size of 7.9mm, however a highest friction factor is also induced. Because of these two conflicting effects, it is hard to tell and identify an optimum rib size corresponding to the best cost-effectiveness. Similar situation is also applied to the rib-to-rib spacing. To evaluate the overall performance of the triangular duct with ribbed internal surfaces including its cost-effectiveness, it is necessary to consider the forced convection and fluid friction characteristics simultaneously. Figures 4-26 and 4-27 show the performance evaluation of the triangular duct with attached ribs of different sizes and separations using the ‘volume goodness factor’ proposed by Kays et al. [1984]. The evaluation includes the comparison of the standard pumping power per unit heat transfer area (Es) and the heat transfer coefficient (h). The standard condition is defined as a condition at 20°C under atmospheric pressure, and Es is expressed as:

$$Es = \frac{\dot{m}\Delta p}{\rho A} \quad (4-24)$$

From Figs. 4-26 and 4-27, it can be seen that for a same value of Es , benefit in applying a rib size of $e = 7.9\text{mm}$ (i.e. relative rib height $H/D = 0.1795$) and a rib-to-rib spacing of $S_r = 57\text{mm}$ (i.e. relative rib-to-rib spacing $S_r/W = 7.22$) is obvious.

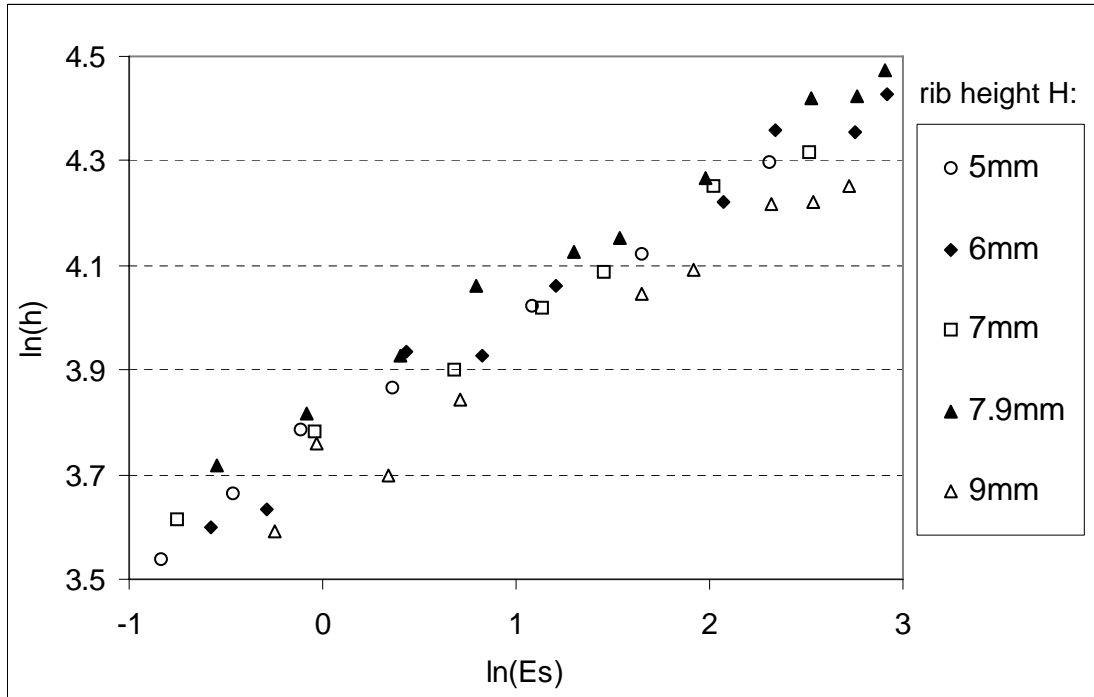


Fig. 4-26 Variation of h with Es for different e 's

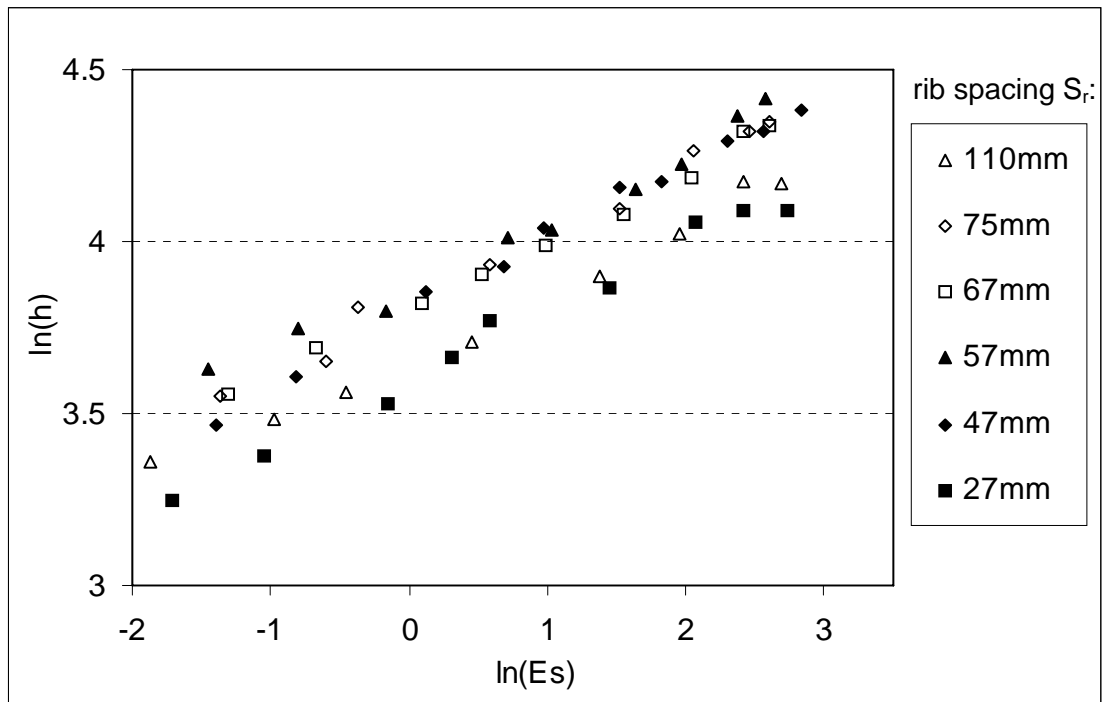


Fig. 4-27 Variation of h with Es for different S_r 's

4.5 Summary

The present study focused on the investigation of forced convection and flow friction characteristics of a steady-state turbulent flow in a horizontal air-cooled equilateral triangular duct with ribbed internal surfaces. The hydraulic diameter of the triangular duct was maintained constant at $D = 44\text{mm}$. There were five rib sizes used ranging from 5mm to 9mm (corresponding to a range of relative rib size (H/D) from 0.1136 to 0.2045) and six rib-to-rib spacings from 27mm to 110mm (corresponding to relative rib-to-rib spacing (S_r/W) ranging from 3.41 to 13.93).

Based on the experimental results obtained, effects of relative rib size and relative rib-to-rib spacing on thermal and hydrodynamic performances of such a thermal system can be concluded as following:

- Application of roughened internal surfaces by fixing uniformly spaced ribs could efficiently enhance the forced convection heat transfer between the turbulent flow and the triangular duct, but it also caused a big drawback in inducing a higher axial pressure drop along the triangular duct. When the Reynolds number was high enough, the negative effects induced by the additional ribs (i.e. enlarged axial pressure drop) were far more significant than the positive effects of the ribs (i.e. enhanced heat transfer).
- A maximum average Nusselt number was obtained at the relative rib size of $H/D = 0.1795$, which implied a maximum forced convection from the heated duct to the airflow. The pressure drop due to fluid friction increased almost linearly with the rib size and did not show the existence of an optimum value.

- The optimum relative rib-to-rib spacing to enhance the forced convection was obtained at $S_r/W = 7.22$, which led to a maximum convection heat transfer from the heated duct to the airflow. Pressure drop along the triangular duct did not vary linearly with the relative rib-to-rib spacing. A maximum pressure loss was also obtained at the relative rib-to-rib spacing of $S_r/W = 7.22$.
- Non-dimensional expressions were developed for the determinations of average Nusselt number and average friction factor in the equilateral triangular duct with uniformly spaced square ribs of different sizes attaching on its internal surfaces. They were applicable in a range of hydraulic-diameter-based Reynolds numbers from 4,000 to 23,000.
- In order to take into consideration the effects of both flow condition and ribs on heat transfer and flow friction characteristics of the triangular duct with internal ribbed surfaces, non-dimensional relationships in terms of Reynolds number (Re), relative rib height (H/D) and relative rib-to-rib spacing (S_r/W) for the predictions of average Nusselt number (Nu) and average friction factor (f) had been developed, respectively. The maximum percentage deviations for these two empirical equations were $\pm 3.5\%$ and $\pm 8.7\%$, respectively.

5 THERMAL AND HYDRODYNAMIC

PERFORMANCES OF THE V-GROOVED

TRIANGULAR DUCT

Corrugated or V-groove roughened surface is another means which is often used to enhance heat transfer rate. To develop the heat exchanger for the removal of danger-potential waste heat from the equipment, repeated V-grooves are fabricated on the internal surfaces of the flow passages in a transverse direction to the mean flow.

The objective of this chapter is to study possible mechanisms for increasing heat transfer between the V-grooved surface and the fluid at a minimal pumping cost. Concentrations will be put on the investigation of the relationships between heat transfer coefficient and fluid friction with the geometry of V-grooves and flow conditions in the V-groove roughened triangular duct, in particular, effects of apex angle of the V-groove (θ), relative groove-to-groove spacing (S_v / D) and Reynolds number (Re) on the turbulent forced convection (Nu) and fluid friction (f) characteristics.

5.1 Arrangement of V-Grooves

To study the effects of V-groove apex angle, groove-to-groove spacing as well as Reynolds number on forced convection and pressure-drop characteristics of fully developed turbulent flows in air-cooled, horizontal triangular ducts, several equilateral-triangle-sectional ducts, which could provide a maximum forced

convection heat transfer comparing to other triangle-sectional ducts as recommended by Leung et al. [1997], were fabricated from a 2 mm thick duralumin plate (i.e. thermal conductivity $k_w = 180 \text{ W/(m}\cdot\text{K)}$). All the ducts under consideration were of the same geometry and machined with uniformly spaced parallel V-grooves, which were orthogonal to the mean airflow, on their three internal surfaces, as shown in Fig. 5-1.

The V-groove had a uniform depth of $d = 1\text{mm}$. However, the applied V-groove apex angle (θ) was ranged from 45° to 150° and groove-to-groove spacing (S_v) from 24mm to 54mm, corresponding to the relative groove-to-groove spacing (S_v/D) varied from 0.54 to 1.23, as listed in Table 5-1.

Table 5-1 Ranges of V-groove's apex angle and spacing
($D = 44\text{mm}$, $d = 1\text{mm}$)

Configuration	Apex Angle (θ)	Groove-to-Groove Spacing (S_v) [mm]
(1)	$45^\circ (0.79 \text{ rad})$	$34 (S_v/D = 0.77)$
(2)	$60^\circ (1.05 \text{ rad})$	$34 (S_v/D = 0.77)$
(3)	$75^\circ (1.31 \text{ rad})$	$34 (S_v/D = 0.77)$
(4)	$120^\circ (2.09 \text{ rad})$	$34 (S_v/D = 0.77)$
(5)	$150^\circ (2.62 \text{ rad})$	$34 (S_v/D = 0.77)$
(6)	$45^\circ (0.79 \text{ rad})$	$24 (S_v/D = 0.54)$
(7)	$45^\circ (0.79 \text{ rad})$	$44 (S_v/D = 1)$
(8)	$45^\circ (0.79 \text{ rad})$	$54 (S_v/D = 1.23)$

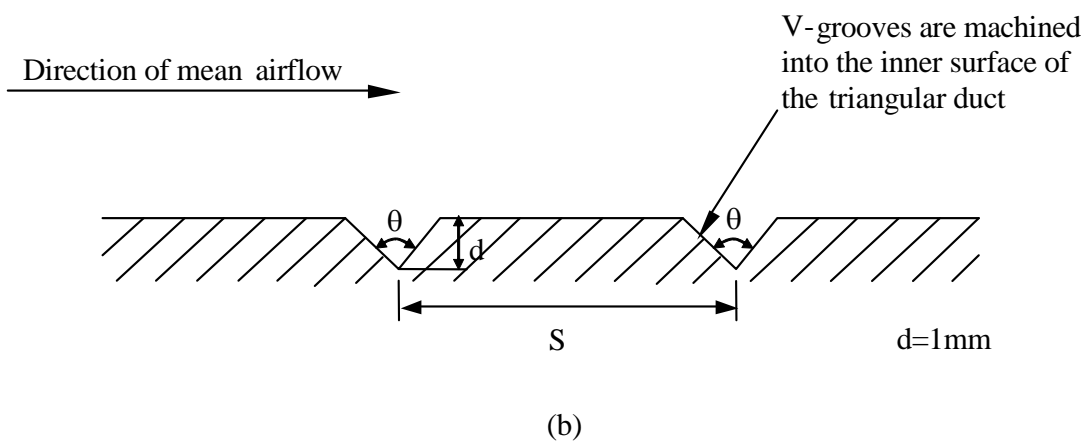
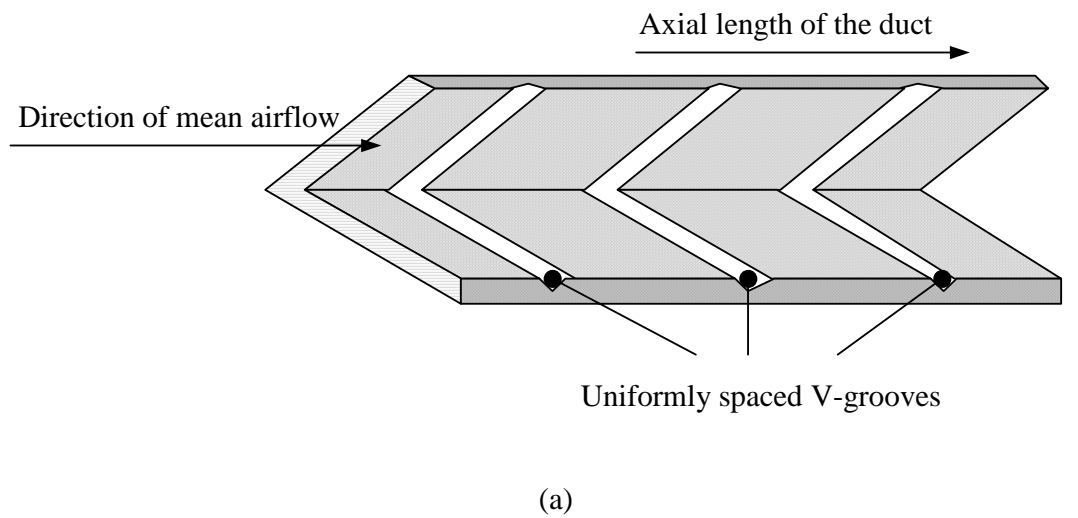


Fig. 5-1 Schematic representation of the uniformly-spaced V-grooved surface

5.2 Average Nusselt Number

5.2.1 Effects of V-Groove Apex Angle

Figure 5-2 shows the variations of average Nusselt number (Nu) with Reynolds number (Re) for different V-groove apex angles (θ) at a constant groove-to-groove spacing of $S_v = 34\text{mm}$ (i.e. $S_v/D = 0.77$). Results obtained from a similar

triangular duct with smooth internal surfaces in a previous study [Leung et al. 2001] are also provided to facilitate comparison. Enhanced average Nusselt number is achieved by fabricating uniformly spaced V-grooves on the internal surfaces of the triangular duct. For the V-grooved surface with $\theta = 45^\circ$ and $S_v / D = 0.77$, enhancements of 77.5% at $Re = 5,200$ and 19.7% at $Re = 35,500$ are obtained, respectively. The enhancement decreases with increasing Reynolds number. However, difference in the magnitude of that enhancement is not so significant between different V-groove apex angles. It might be due to the limited enlarged flow area by the additional roughness of V-grooves, which has a depth of $d = 1\text{mm}$ in the present study. In addition, it is found that a higher Nusselt number is obtained at a smaller apex angle when $45^\circ \leq \theta \leq 150^\circ$.

5.2.2 Effects of Groove-to-Groove Spacing

By keeping the V-groove apex angle (θ) constant at 45° and changing the groove-to-groove spacing (S_v) from 24mm to 54mm (namely, S_v / D from 0.54 to 1.23), it is found that the highest average Nusslet number is obtained at $S_v = 24\text{mm}$ (i.e. $S_v / D = 0.54$) and for different groove-to-groove spacings, the average Nusselt number has not been changed significantly, as shown in Fig. 5-3. It can be concluded that the effect of the relative groove-to-groove spacing on forced convection heat transfer is not so significant. In fact, a larger groove-to-groove spacing reduces the secondary flow area induced by the grooves, while when this spacing is too small, it limits the development of the secondary flow, and weakens the thermal performance of the triangular duct.

5 THERMAL AND HYDRODYNAMIC PERFORMANCES OF THE V-GROOVED TRIANGULAR DUCT

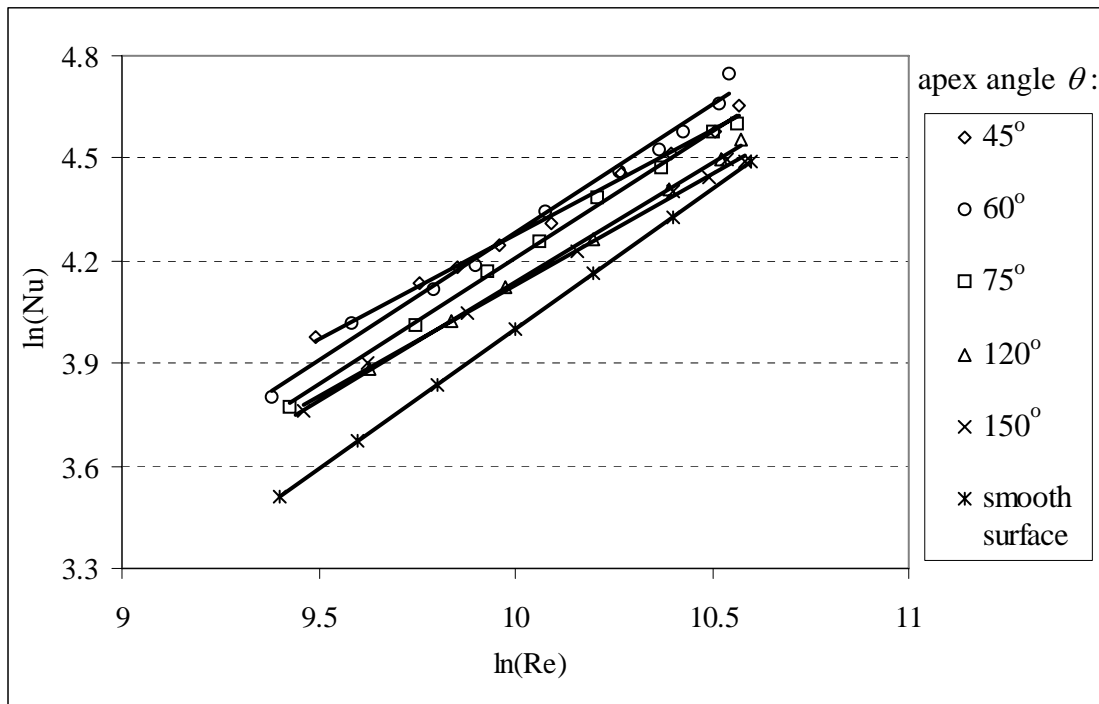


Fig. 5-2 Variation of Nu with Re for different θ 's

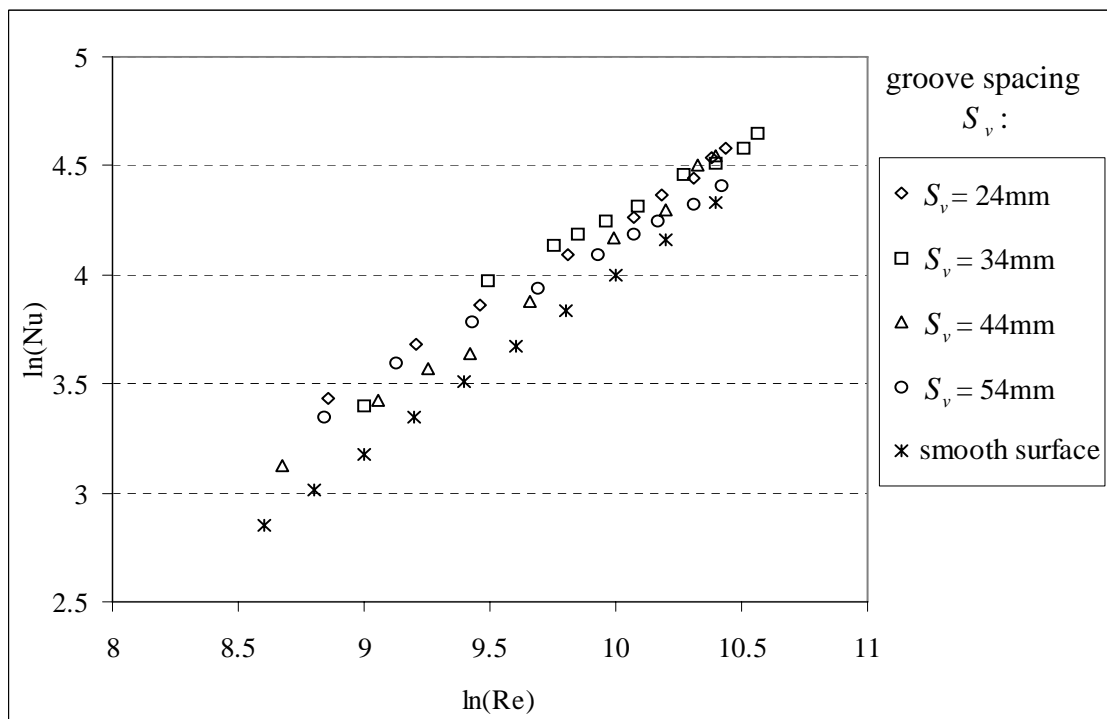


Fig. 5-3 Variation of Nu with Re for different S_v 's

Generally, for a fully developed turbulent flow, its near-wall region is occupied by a laminar sublayer, where the molecular thermal conduction and viscous action affect the heat transfer and fluid friction dominantly. The fabrication of uniformly spaced V-grooves on the internal surfaces of the triangular duct breaks up the laminar viscous sublayer in the near-wall region and thus leads to the formation of a thinner boundary layer, which enhances the heat transfer coefficient. In addition, the mixing length and eddy diffusivity also become finite near the wall. As a result, heat can be transferred by eddy thermal conductivity from the V-grooved surface more effectively than that in a similar triangular duct with smooth internal surfaces.

On the other hand, as the airflow is disturbed when it is flowing over the V-grooves, vortices are formed inside the V-grooves. Their length and strength are dominant factors to affect the recirculation of the turbulent flow and hence the magnitude of the forced convection. The geometric configuration of the V-groove, namely, apex angle's depth and groove-to-groove spacing, as well as the flow condition have contributed to the vortices' length and strength. The depth of the V-groove, which is usually limited by the thickness of the triangular duct wall, had been kept constantly at $d = 1\text{mm}$ in the present study and therefore its effect on the forced convection and flow friction is yet uncertain.

5.2.3 Effects of Reynolds Number

From Figs. 5-2 and 5-3, it can be concluded that the average Nusselt number increases with increasing Reynolds number. For a V-grooved triangular duct with a groove apex angle of $\theta = 45^\circ$ and a groove-to-groove spacing of $S_v = 34\text{mm}$ (i.e. $S_v / D = 0.77$), when Reynolds number increases from 5,200 to 35,500, the average

Nusselt number increases by 225.9%. It is due to that, to obtain a higher Reynolds number, a higher flow velocity and thus a higher mass flow rate are applied, which lead to a higher heat transfer rate between the flow and the triangular duct and hence a higher Nusselt number. In addition, a more turbulent flow at a higher Reynolds number also contributes to it. Similar conclusion was drawn from the study of ribbed surfaces.

5.2.4 Generalization of Average Nusselt Number

Rearranging all the experimental data as shown in Figs. 5-4 to 5-6 by using the method suggested in Section 4.2.4, a resulting best-fit line in the form of Equation 3-15 for the average Nusselt number was obtained:

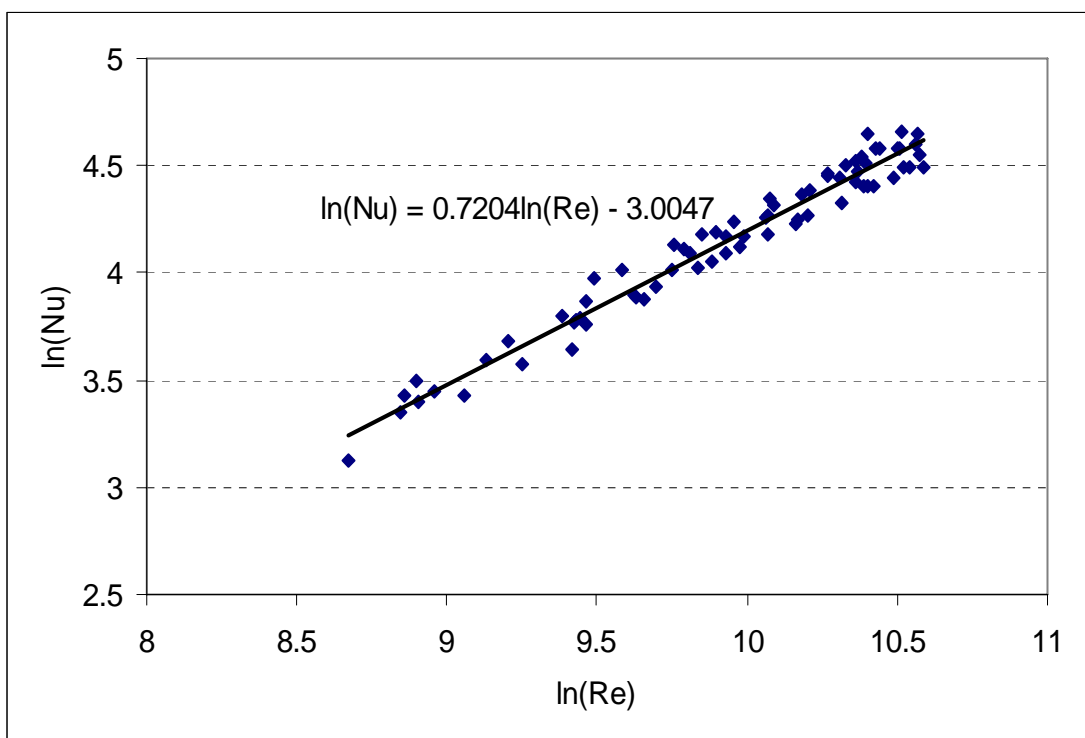


Fig. 5-4 Plot of effect of Re on Nu

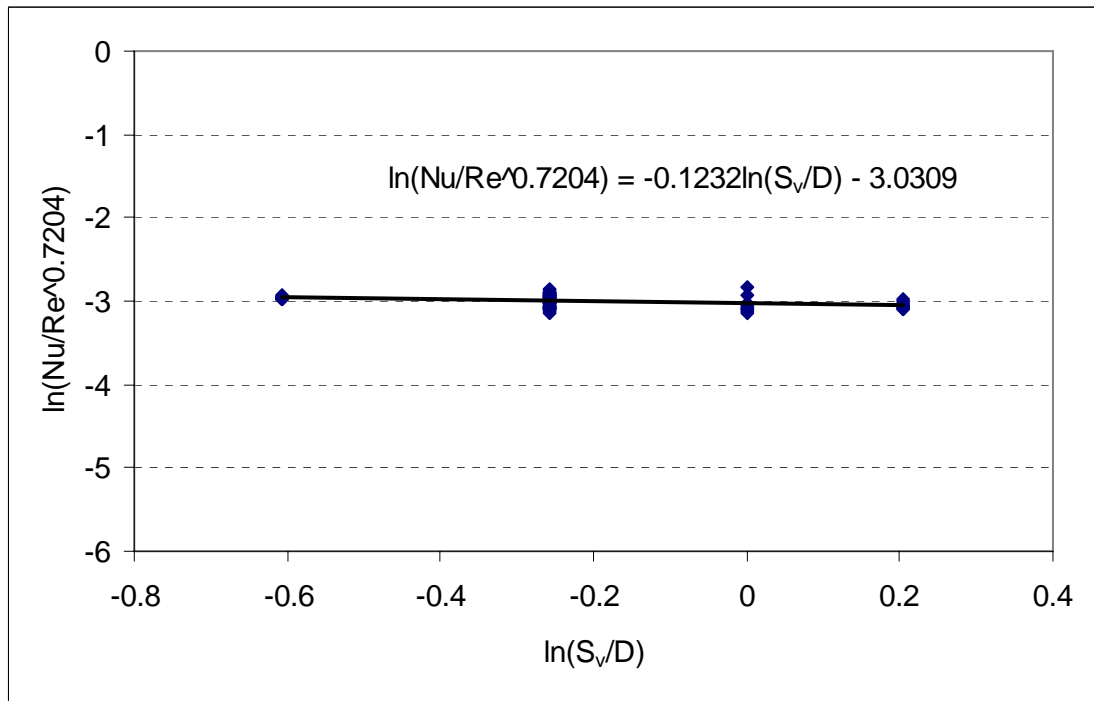


Fig. 5-5 Plot of effect of S_v / D on Nu

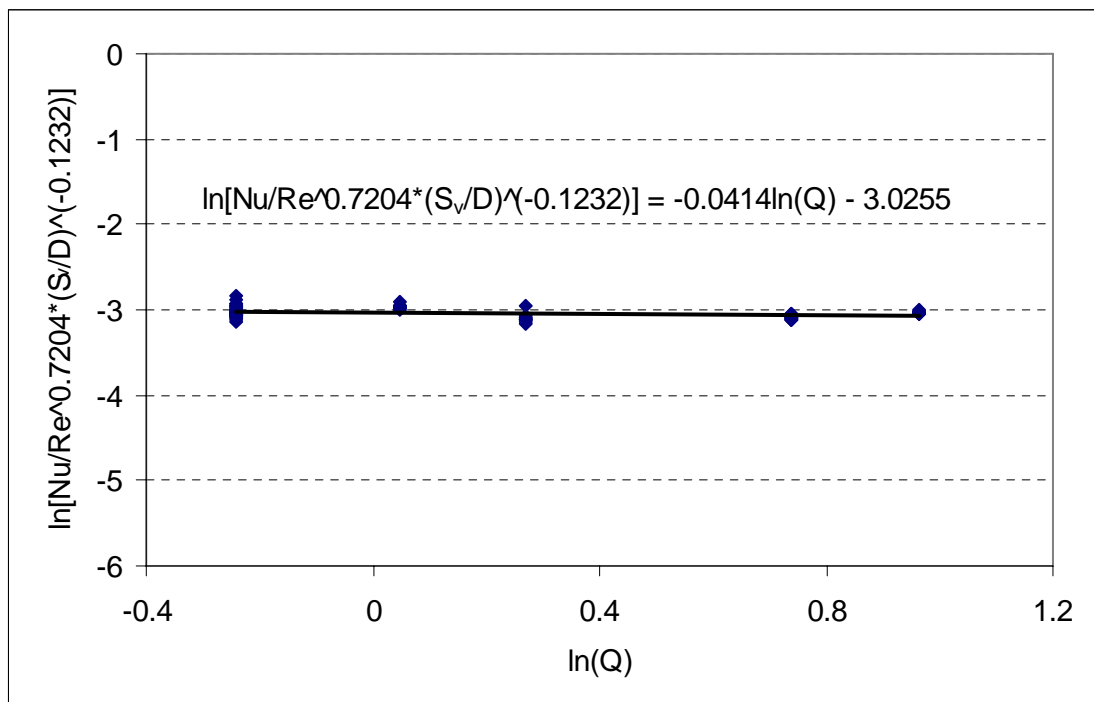


Fig. 5-6 Plot of effect of Q on Nu

$$Nu = 0.0485 Re^{0.7204} \left(\frac{S_v}{D} \right)^{-0.1232} \mathcal{G}^{-0.0414} \quad (5-1)$$

Where $\mathcal{G} = \frac{\theta}{180} \pi$, $45^\circ \leq \theta \leq 150^\circ$, $5,200 \leq Re \leq 35,500$ and $0.54 \leq \frac{S_v}{D} \leq 1.23$.

From Equation (5-1), it can be seen that compared to the effect of Re on Nu (i.e.

$Nu \propto Re^{0.7204}$), S_v / D has a not significant effect on Nu (i.e. $Nu \propto \left(\frac{S_v}{D} \right)^{-0.1232}$), and

moreover, dependence of Nu on \mathcal{G} is rather negligible (i.e. $Nu \propto \mathcal{G}^{-0.0414}$).

5.3 Average Friction Factor

5.3.1 Effects of V-Groove Apex Angle

The friction factors for the V-grooved triangular ducts obtained at different V-groove apex angles are presented in Fig. 5-7, with $5,200 \leq Re \leq 35,500$. A higher pressure-drop compared to that of a smooth triangular duct is observed. However, the enhancement is not significant. It might be due to the limited enlarged secondary flow area induced by the additional roughness of V-grooves with a depth of $d = 1\text{mm}$. For the V-grooved surface with $\theta = 45^\circ$ and $S_v / D = 0.77$, enhancements of 17.8% at $Re = 5,200$ and 55.4% at $Re = 35,500$ are obtained, respectively. The enhancement increases with increasing Reynolds number. Compared to the enhancement of Nusselt number as discussed in Section 5.2.1, a conclusion can be drawn that at high Reynolds numbers, the positive effects of the V-grooves on the forced convection heat transfer are not comparable to their negative effects. In addition, friction factor achieves a highest value at apex angle of $\theta = 45^\circ$.

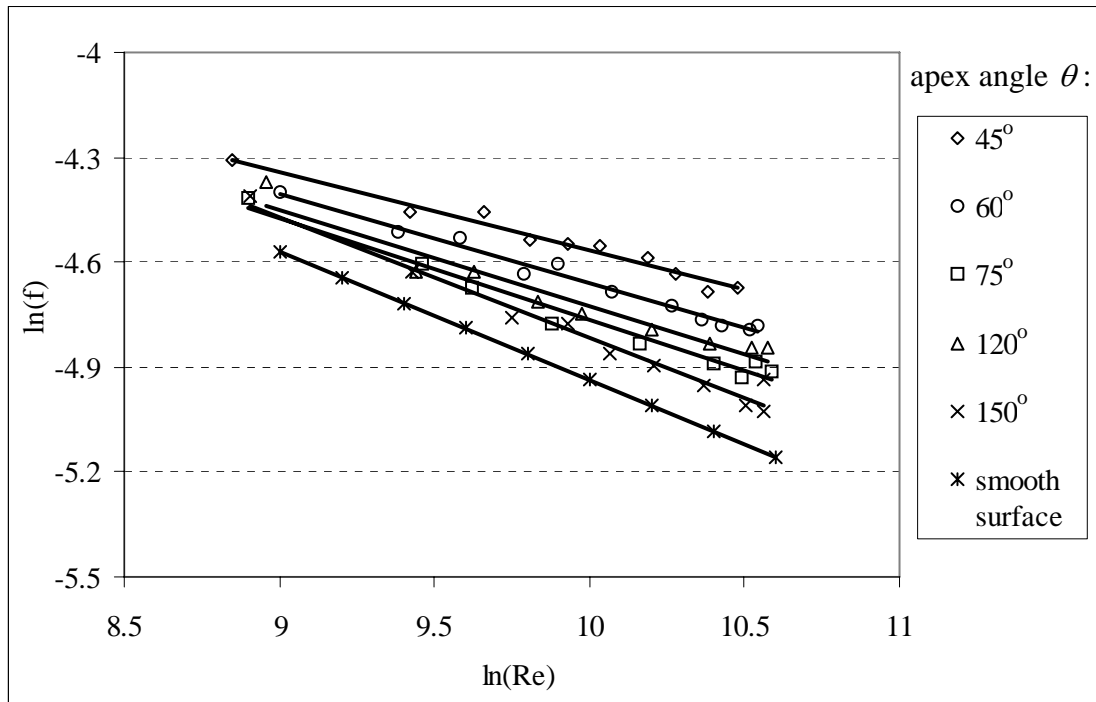


Fig. 5-7 Variation of f with Re for different θ 's

5.3.2 Effects of Groove-to-Groove Spacing

The effect of groove-to-groove spacing on the average friction factor for the V-grooved triangular duct is presented in Fig. 5-8. An increment in flow friction compared to the smooth surface is detected with the V-grooved surface. Again, by changing the groove-to-groove spacing from 24mm to 54mm (namely, S_v/D from 0.54 to 1.23), it is noticeable that average friction factor decreases with increasing groove-to-groove spacing, though the reduction in average friction factor becomes slighter when the groove-to-groove spacing gets larger. It is because the roughened surface becomes flatter when the V-grooves get sparser, which leads to a less pressure drop along the airflow direction. In addition, due to the mild enlargement

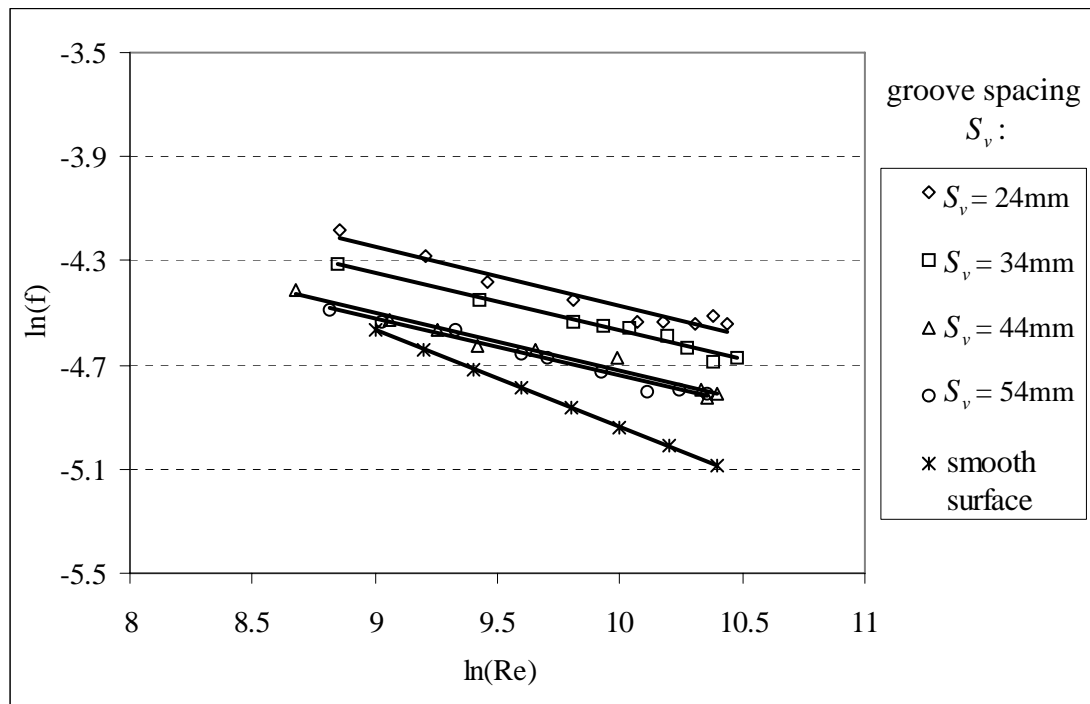


Fig. 5-8 Variation of f with Re for different S_v 's

of the secondary flow area from the V-grooved surface, and that flow area enlargement decreases with the increasing separation between two consecutive parallel grooves, the effect of the V-grooves on the hydrodynamic performance of the triangular duct becomes fainter when the groove-to-groove spacing gets larger and gradually close to a smooth surface.

5.3.3 Effects of Reynolds Number

Though a higher Reynolds number leads to a larger Nusselt number as concluded in the previous sections, for friction factor, the situation is reversed: smaller friction factors are obtained at higher Reynolds numbers. For a V-grooved triangular duct with a groove apex angle of 45° and a groove-to-groove spacing of 34mm (i.e.

$S_v/D = 0.77$), when the Reynolds number increases from 5,200 to 35,500, the average friction reduces by 35.2%.

5.3.4 Generalization of Average Friction Factor

Similarly, a generalization for friction factor was carried out, based on the method described in Section 3.5. The procedure is presented in Figs. 5-9 to 5-11, and the following equation was obtained:

$$f = 0.144 Re^{-0.2809} \left(\frac{S_v}{D} \right)^{-0.3763} \mathcal{G}^{-0.1736} \quad (5-2)$$

Equation (5-2) was valid when $45^\circ \leq \theta \leq 150^\circ$, $5,200 \leq Re \leq 35,500$ and

$0.54 \leq \frac{S_v}{D} \leq 1.23$, where $\mathcal{G} = \frac{\theta}{180} \pi$.

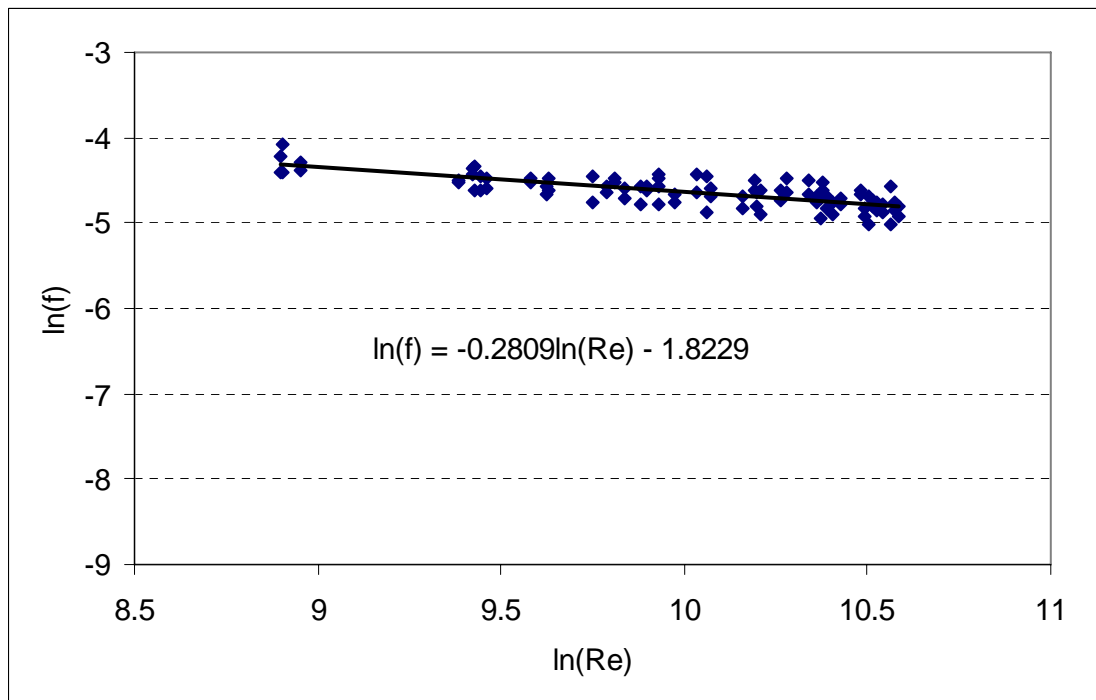


Fig. 5-9 Plot of effect of Re on f

5 THERMAL AND HYDRODYNAMIC PERFORMANCES OF THE V-GROOVED TRIANGULAR DUCT

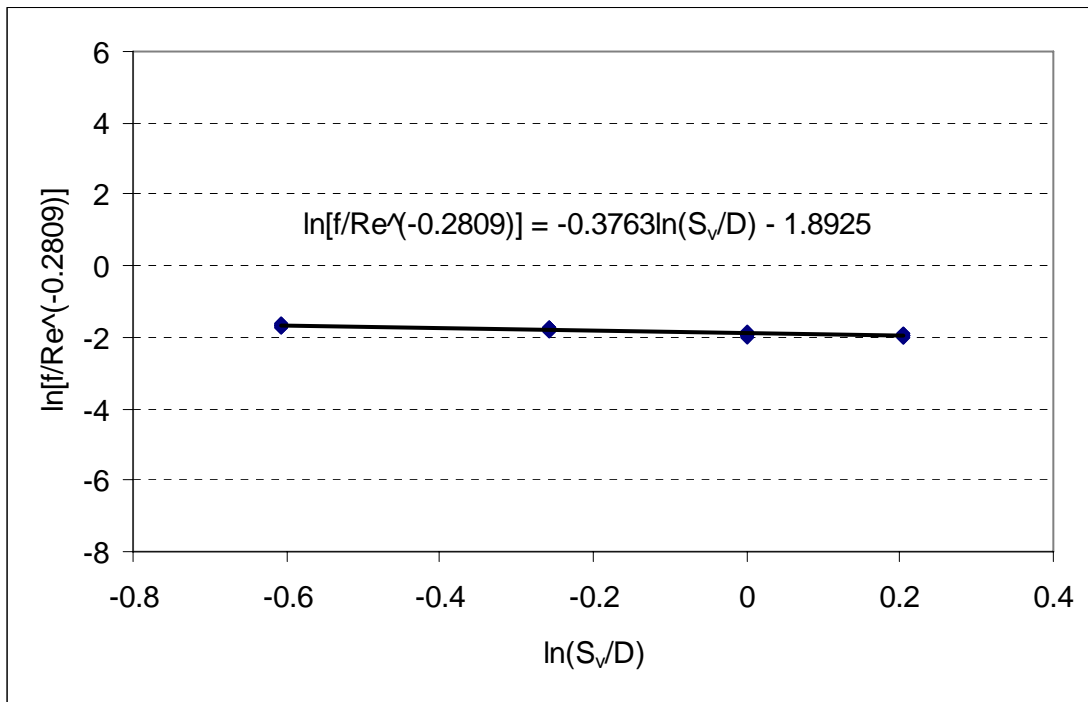


Fig. 5-10 Plot of effect of S_v/D on f

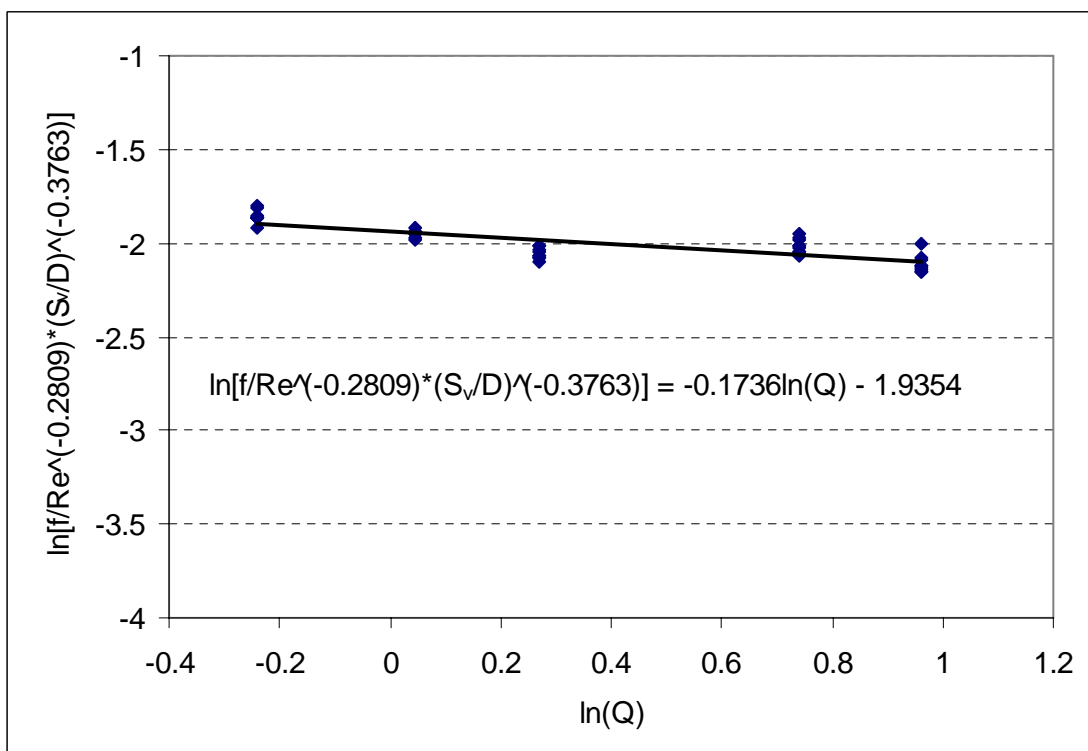


Fig. 5-11 Plot of effect of Q on f

A comparison of the average Nusselt number and the average friction factor as predicted by applying Equations (5-1) and (5-2) with those obtained experimentally was conducted, as shown in Figs. 5-12 and 5-13. For the average Nusselt number, a maximum discrepancy of $\pm 3.6\%$ between the predicted and experimental values was obtained.

Similarly, a maximum discrepancy of $\pm 7.6\%$ between the predicted and experimental values was determined for the average friction factor.

5.4 Comparison between Ribbed and Grooved Surfaces

As discussed in the former chapter and sections, it can be concluded that both ribbed and V-grooved surfaces can effectively enhance the average Nusselt number and the average friction factor of the turbulent flow in a triangular duct. However, the enhancement ability of these two kinds of roughened surfaces is not yet compared. In addition, thermal and hydrodynamic performances, being two important parameters to determine the capability of a heat exchanger, need to be considered simultaneously, in the forms of forced convection and fluid friction characteristics.

Based on a triangular duct with a hydraulic diameter of $D = 44\text{mm}$, the optimum rib size and rib-to-rib spacing to obtain a best thermal performance of the system were proposed to be 7.9mm and 57mm, respectively; while for the present studied range of V-groove arrangements, a apex angle of 45° with a groove-to-groove spacing of 24mm is proposed to be a best arrangement to get a highest heat transfer of the triangular duct, though with a smaller apex angle and a smaller groove-to-groove spacing, the duct may obtain an optimum thermal performance. However, from the

5 THERMAL AND HYDRODYNAMIC PERFORMANCES OF THE V-GROOVED TRIANGULAR DUCT

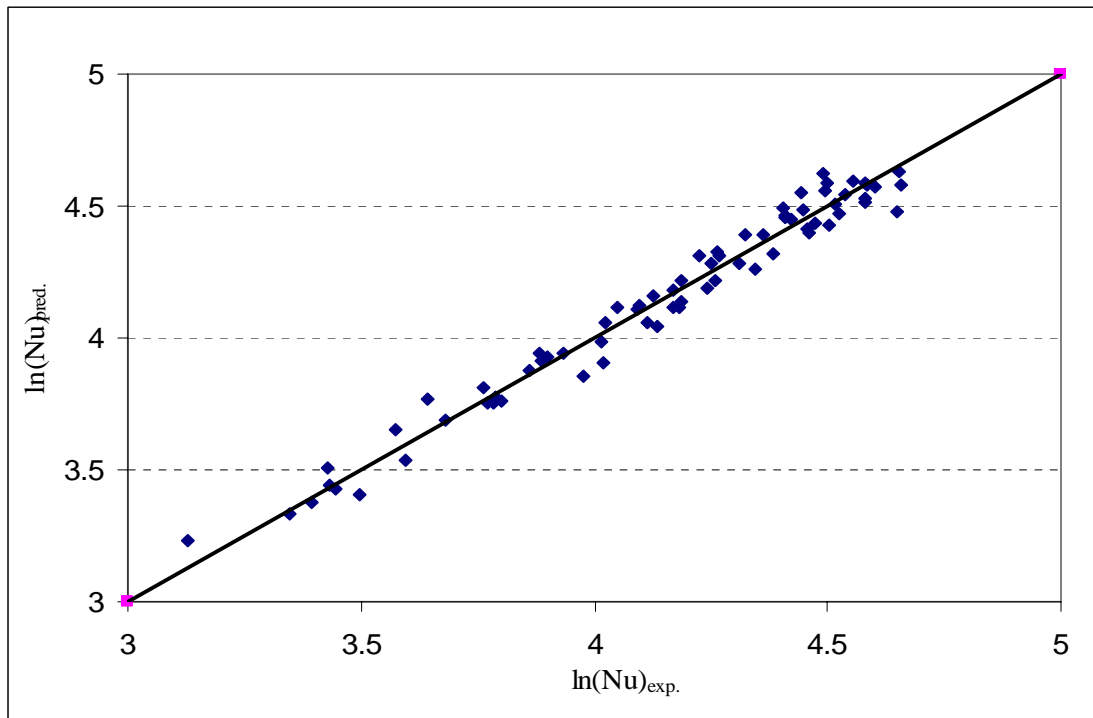


Fig. 5-12 Comparison of predicted and measured values of Nu

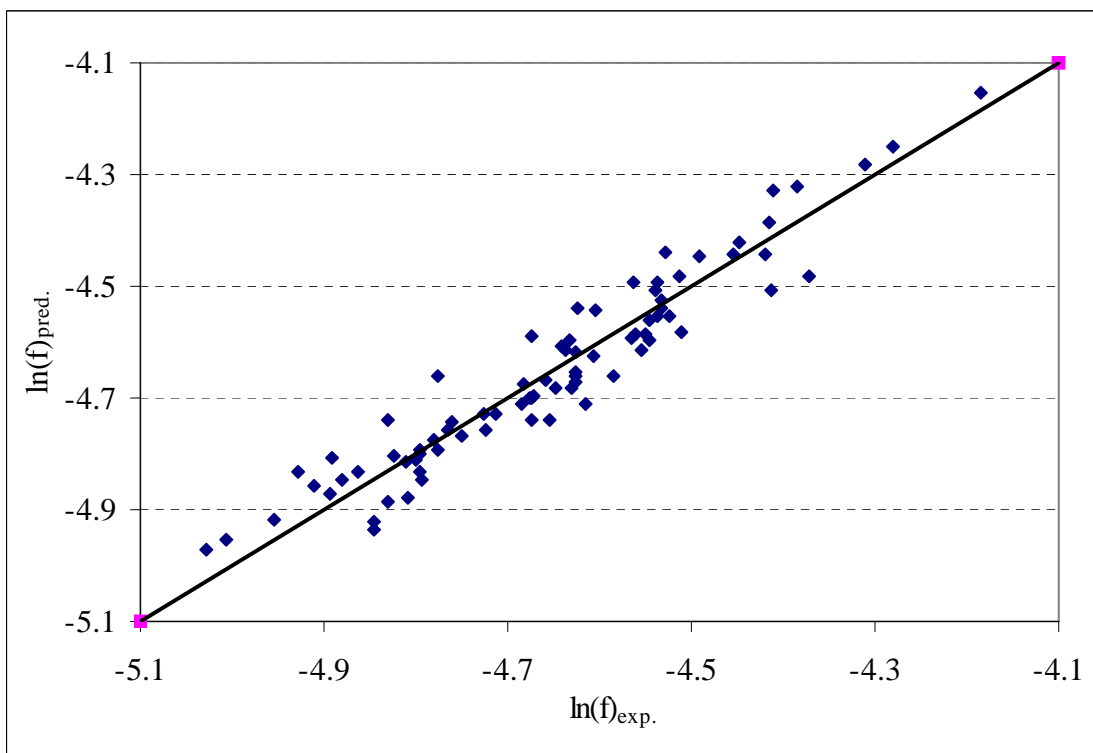


Fig. 5-13 Comparison of predicted and measured values of f

results presented in Figs. (5-2,3) and (5-7,8), and also as suggested by Leung et al. [2000], the effects of different V-groove apex angles and groove-to-groove spacings on the forced convection and fluid friction are not varied significantly, thus it can be deduced that even with an optimum arrangement of V-grooves, its results will not differ from those obtained with a apex angle of 45° and a groove-to-groove spacing of 24mm very much. Therefore, to facilitate the comparison of these two kinds of roughened surfaces, these two roughness configurations, namely, a ribbed surface with rib size of 7.9mm and rib-to-rib spacing of 57mm, and a V-grooved surface with apex angle of 45° and groove-to-groove spacing of 24mm, were selected as two typical cases for following comparison.

5.4.1 Forced Convection Characteristics

Since Nusselt number is the dimensionless heat transfer coefficient and represents the ratio of actual heat transferred between the plates by a moving fluid to the heat transfer that would occur by conduction, heat transfer enhancements of the ribbed and V-grooved internal surfaces to the triangular duct, which reflect the forced convection characteristics of the turbulent flow, are expressed in a relationship between average Nusselt number and Reynolds number, as shown in Fig. 5-14. The results of a smooth triangular duct [Leung et al. 2001] are also presented to facilitate comparison.

It can be clearly seen that, though both roughened surfaces can improve the Nusselt number effectively, the ribbed surface obtains enhancements of 293.5% at $Re = 5,200$ and 195.5% at $Re = 23,000$, while the V-grooved surface only achieves 77.5%

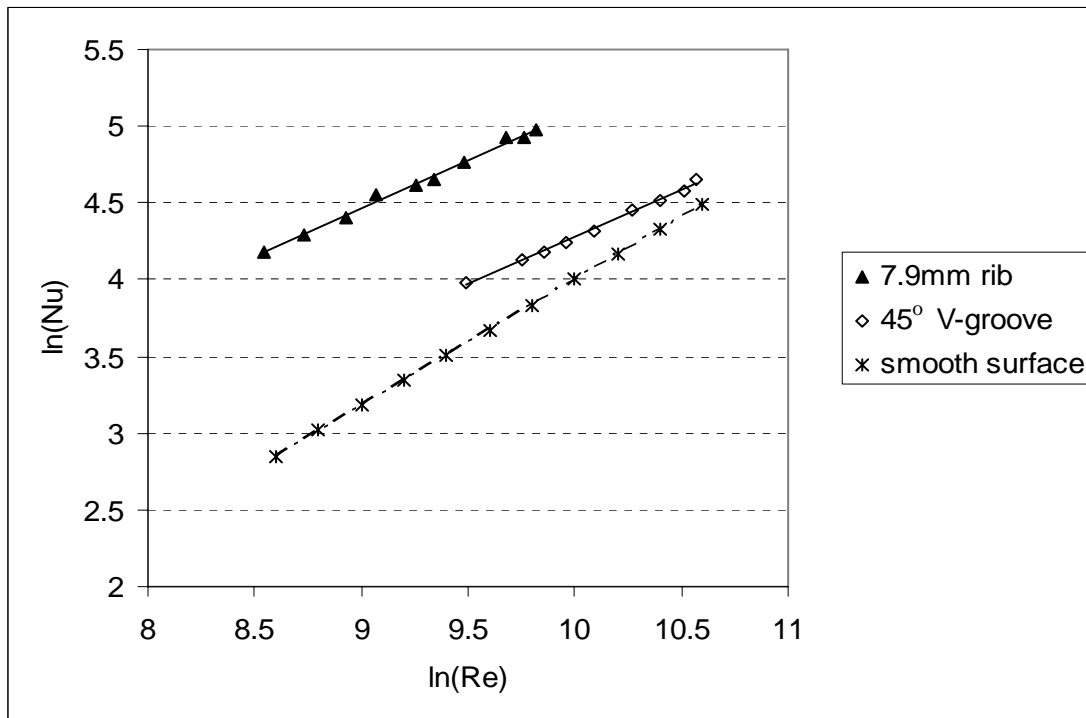


Fig. 5-14 Comparison of Nu for ribbed and grooved surfaces

at $Re = 5,200$ and 30.9% at $Re = 23,000$: the difference is rather significant. The ribbed surface has a definite thermal advantage over its counterpart.

5.4.2 Fluid Friction Characteristics

The fluid friction characteristics, which is proportional to the pressure drop along the axial direction of the triangular duct and thus reflects the pumping power required to drive the fluid through the duct, is represented as the relationship between average friction factor and Reynolds number and shown in Fig. 5-15.

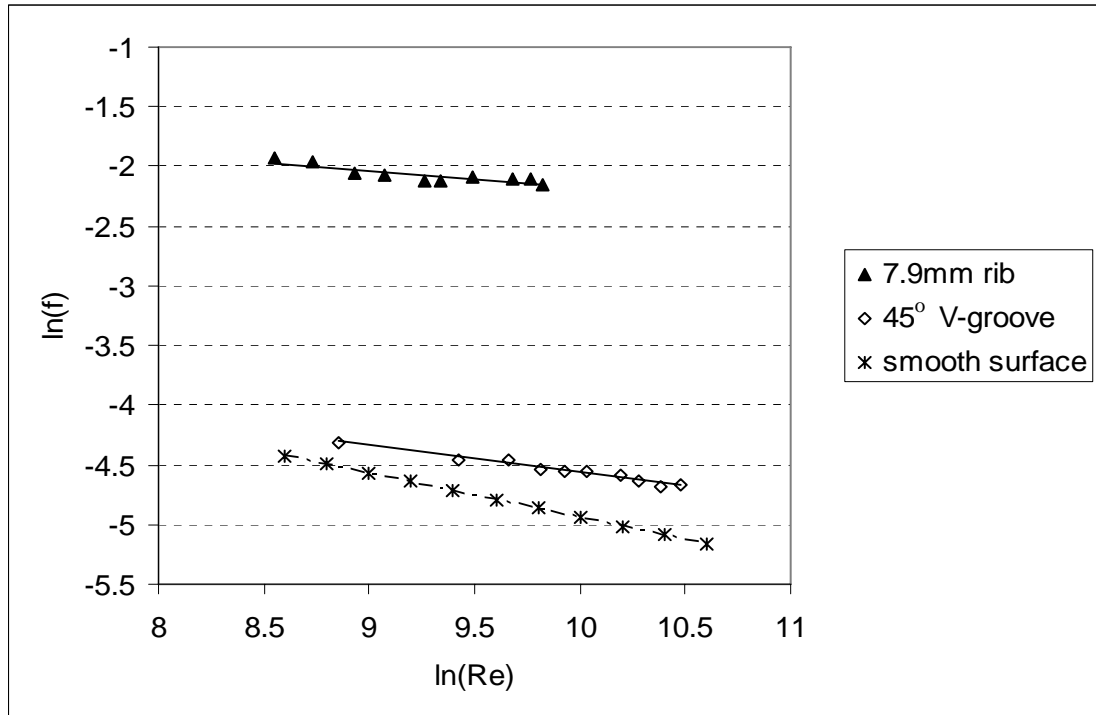


Fig. 5-15 Comparison of f for ribbed and grooved surfaces

Enhancements in friction factors compared to those for the smooth triangular duct are obtained for both kinds of roughened surfaces: 1040.6% at $Re = 5,200$ and 1505.1% at $Re = 23,000$ for the ribbed surface and only 17.8% at $Re = 5,200$ and 46.0% at $Re = 23,000$ for the V-grooved surface. Much higher pressure-drops along the triangular duct are generated for the ribbed surface, which lead to greater pumping powers required to drive the fluid through the ribbed triangular duct.

5.4.3 Volume Goodness Factor

As discussed from the former two sections, a better thermal performance was achieved by the rib-roughened surface; however, a bigger drawback of higher pressure-drop was also obtained. It was difficult to tell which kind of roughened

surfaces, ribbed or grooved, was more cost effective for the propose of applying to triangular duct. Once again, the Volume Goodness Factor, Es , as introduced in Section 4.4, was adopted for the comparison.

Variations of the heat transfer coefficient with Volume Goodness Factor for both roughened surfaces are shown in Fig. 5-16. It is rather obvious to see that a better overall performance is obtained from the ribbed surface instead of the V-grooved surface. Conclusively, ribbed surface is a more preferred choice in achieving a good balance between heat transfer enhancement and flow friction loss. In addition, from the viewpoint of practical application, the V-grooved surface has a restriction that its depth is limited by the thickness of the plate that need be roughened, which is absent for the rib-roughened surface.

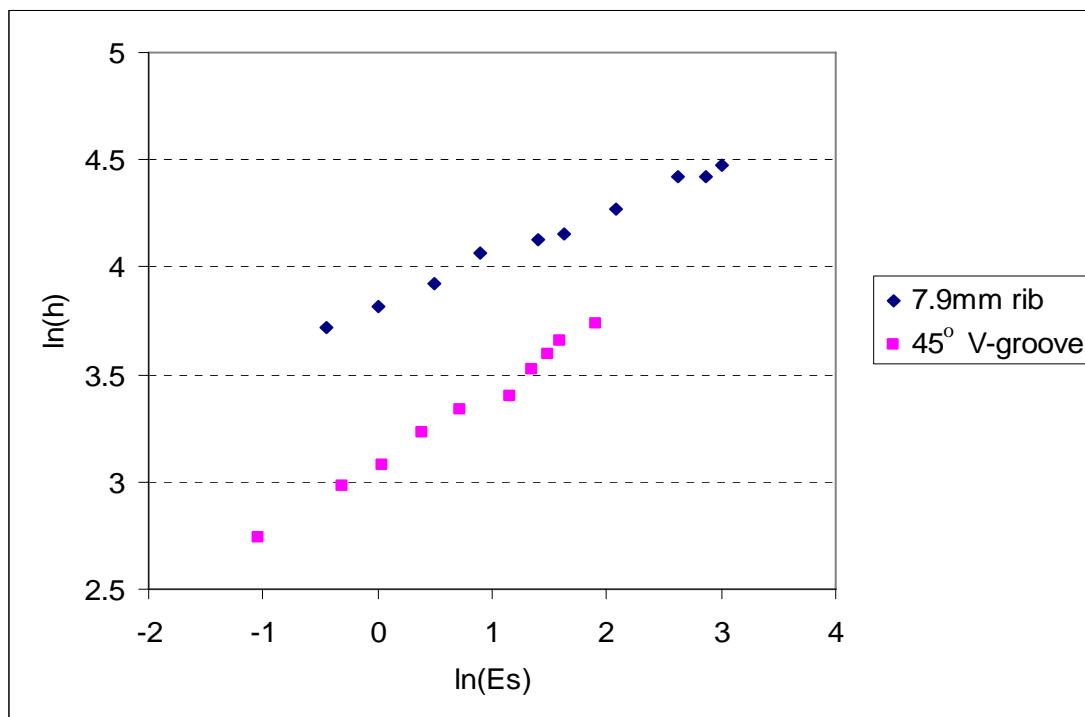


Fig. 5-16 Comparison of h for ribbed and grooved surfaces

5.5 Summary

V-groove-roughened surface was applied to enhance the forced convection and undesirably the flow friction of the turbulent flow in a horizontal equilateral triangular duct. The validity of the present structure in a triangular duct was confirmed by experiments in which the fluid flow passing over the grooves was disturbed. In addition, effects of V-groove apex angle, relative groove-to-groove spacing and Reynolds number on forced convection and fluid friction characteristics in the triangular duct were investigated, respectively. Since the depth of the V-groove was kept constant in the present study, its effect on forced convection and flow friction in the triangular duct was not yet determined.

After an experimental study of the triangular duct with V-grooved internal surfaces being conducted, following conclusions are obtained:

- An enhanced thermal performance of the triangular duct with V-grooved internal surfaces was obtained, comparing to that of a smooth triangular duct.
- The V-grooved surface could yield a relatively significant increment in heat transfer without a distinct increase in pumping power requirement.
- Both forced convection and fluid friction increased with decreasing apex angle and groove-to-groove spacing.
- The size and arrangement of the V-grooves, namely, apex angle and groove-to-groove spacing, had rather small effects on the average Nusselt number when

$$5,200 \leq Re \leq 35,500, \quad 45^\circ \leq \theta \leq 150^\circ \quad \text{and} \quad 0.54 \leq \frac{S_v}{D} \leq 1.23.$$

- A comparison of the thermal improvement ability between ribbed surface and V-grooved surface showed that the ribbed surface had superiority over the V-grooved surface.
-
-

6 VISUALIZATION OF THE TURBULENT FLOW IN THE TRIANGULAR DUCT

The experimental work in Chapters 4 & 5 is conducted from a macroscopic viewpoint to investigate the effects of roughness (i.e. ribs and V-grooves) on the forced convection and fluid friction in the triangular duct, but how the roughness affects the turbulent flow and hence influences the thermal and hydrodynamic performances of the triangular duct is still not clear. Since the inner flow pattern is disturbed and becomes more complicated after the introduction of the artificial roughness to the internal surfaces of the triangular duct, it is important and challenging to explain the mechanisms of the forced convective turbulent flow, the turbulence-generated secondary flow, and thus the heat transfer argumentation by the application of additional roughness.

Investigations with the methods of flow visualization and numerical simulation are often conducted, which are able to discover the inside influenced flow characteristics in the triangular duct after the application of roughness from a microscopic viewpoint and thus to explain the mechanisms of the roughness element's effects on the thermal and hydrodynamic performances of the triangular duct.

As concluded from Chapter 5, the rib-roughened internal surface has more significant effects on the forced convection and fluid friction in the triangular duct than the V-groove-roughened internal surface, which however has not shown obvious influences on the inside turbulent flow. In addition, because of its particular geometry, the turbulence-generated secondary flow should be easier to visualize for

the ribbed surface. Hence it is more worthwhile and meaningful to better understand the flow patterns generated after the introduction of additional ribs. From this chapter on, focus is put on the study of ribbed surface, which will be conducted based on methods of flow visualization (present Chapter 6) and numerical simulation (Chapters 7-9) from a microscopic viewpoint.

In the present study, Particle Image Velocimetry (PIV), which recovers the instantaneous two- and three- dimensional velocity vector fields from multiple photographic images fields within a plane or volumetric slab of an illuminated seeded flow [Smits et al. 2000], is applied for visualization of the turbulent flow in an equilateral triangular duct attached with uniformly spaced square ribs on its internal surfaces. The experimental results will also be used to develop qualified data for comparison with the associated numerical prediction.

6.1 Experimental Set-Up

An air-cooled horizontal equilateral triangular test duct with internal ribbed surfaces was applied for the present flow visualization study, as shown in Fig. 6-1.

Similarly, the ribbed triangular duct consisted of three identical consecutive sections: an entrance section for the flow to better develop, a test section for flow measurement to perform, and an exit section to minimize the end effect. The duct had a cross-sectional dimensions of the edge $a = 76\text{mm}$ and the height $b = 65.8\text{mm}$, and a length $L = 700\text{mm}$. Thus the hydraulic diameter (D) of the triangular duct could be calculated as:

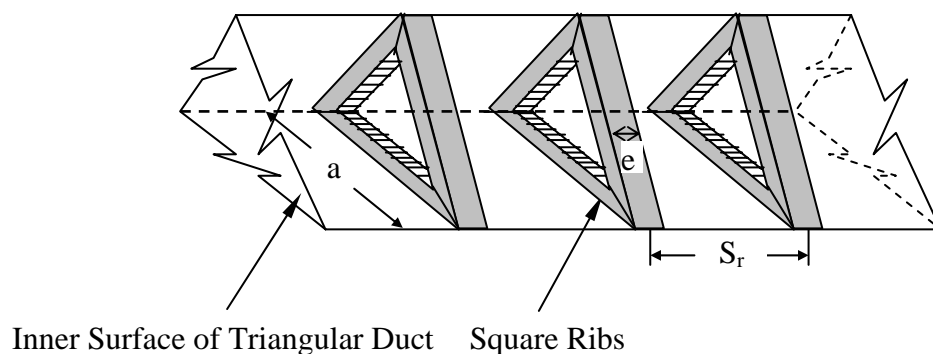


Fig. 6-1 Equilateral triangular duct with internal ribbed surfaces

$$D = \frac{4(\text{Cross-sectional Area})}{\text{perimeter}} = 44\text{mm}$$

Uniformly square ribs with a cross-section of 9mm by 9mm (i.e., $e = 9\text{mm}$) were fixed on the internal surfaces of the test triangular duct at a constant rib-to-rib spacing of 57mm (i.e., $S_r = 57\text{mm}$). Thus, the ratio of rib size (e) to the duct's hydraulic diameter (D), as well as the ratio of rib-to-rib spacing (S_r) to rib size (e) were fixed at $e/D = 0.2$ and $S_r/e = 6.33$, respectively. For a fully developed turbulent flow, a Reynolds number of $Re = 10,800$ was obtained and kept constant throughout the whole experiment.

Due to the symmetry of the equilateral triangular duct, three planes in the gap region right behind the ribs were given particular interest, as shown by the shadowed parts in Fig. 6-2: (a) a cross-sectional Plane *I* which was perpendicular to the flow-wise direction at a distance of e beyond the ribs (i.e., $z/e = 1$); (b) a horizontal Plane *II*

which was parallel to the bottom plate at a distance of $0.5e$ above the floor (i.e., $y/e = 0.5$), with a width of $c = 3e$; (c) a vertical Plane *III* which was consistent with the symmetry plane of the duct (i.e., $x/a = 0.5$), with a width of $c = 3e$.

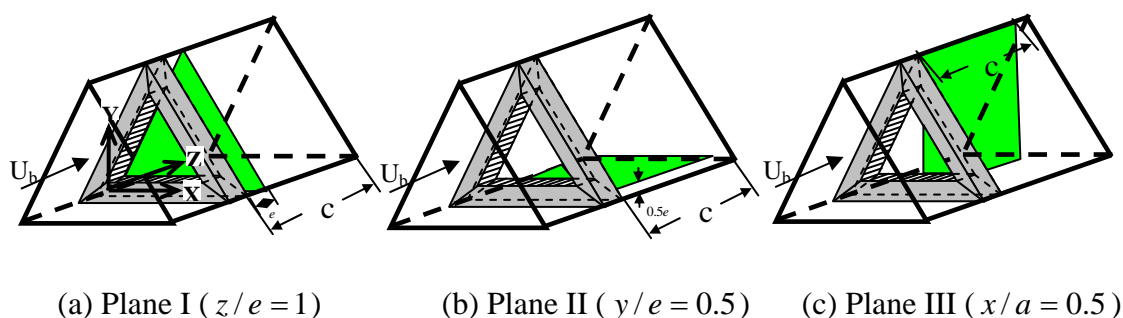


Fig. 6-2 Measurement planes for the triangular duct with internal ribbed surfaces

It was aimed to look into the flow patterns in the duct corners, lateral development of the secondary flow, as well as vortex formation beyond the ribs. For the triangular duct with smooth internal surfaces, three corresponding planes *I'*, *II'*, *III'* were chosen at the same locations to those as above-mentioned to facilitate comparison. It was expected that effects of the ribs on the flow characteristics of the turbulent flow could be observed.

6.2 Experimental Methodology

Because of the point measurement property of the LDV, it cannot provide information of the simultaneous spatial structure of a flow field. Therefore its

application is quite limited when flow phenomena are dominated by spatial structures, for example, a turbulent flow [Smits et al. 2000]. The PIV technique overcomes this disadvantage. It is possible to obtain the instantaneous velocity field in a flow plane by imaging large concentration of seeding particles. A map of mean velocities is then obtained by correlating statistically the sampled numbers throughout the image field, which avoids identification of individual particles. Hence in the present study of the turbulent flow through a triangular duct with internal ribbed surfaces, the PIV technique was used to facilitate the flow visualization.

6.2.1 Particle Image Velocimetry (PIV)

In fact, according to the different image recording method, there are two kinds of PIV approaches: photographic/conventional PIV and digital PIV. In the conventional PIV approach, the images are recorded on photographic film. Then the films are developed and analyzed by computing the spatial correlation in small interrogation images one by one, which yields accurate measurements of the particle-image displacement. The typical resolution for the computed spatial correlation in the interrogation images is 256×256 pixels. However, this analysis process is so slow and time-consuming that measurements with conventional PIV technique are limited to a certain extent. To increase the recording and processing speeds, digital PIV is thus recommended, which provides a rapid interrogation analysis by recording the images directly with a CCD camera and using only 32×32 pixels for the computation of spatial correlation. Since digital PIV avoids any overhead for the processing of photographic film and for translating the interrogation optics, the time needed for the interrogation-image-analysis is thus reduced efficiently. A drawback of digital PIV compared to conventional PIV is that a reduction in the pix resolution

of the interrogation image may affect the accuracy. To overcome this problem, Gaussian peak-fit estimator is proposed, by which estimation error at low pixel resolution can be reduced considerably [Willert et al. 1991]. In addition, a comparison between the conventional and digital implementations of the PIV method for a fully developed turbulent pipe flow was conducted and it was validated that digital PIV was satisfactory to measure the unsteady turbulent flows with a small enough sampling error [Westerweel et al. 1996]. In the present study, the digital PIV technique was adopted and it was named as ‘PIV’ for the purpose of simplicity.

As mentioned in the above sections, PIV was applied by obtaining the instantaneous velocity field in a flow plane with the aid of imaging large concentration of seeding particles, which were illuminated with a pulsed laser sheet. A high-resolution CCD camera (i.e. HiSense type 13, gains \times 4, double frames, 1280 \times 1024 pixels), at a 30 frame per second video rate, was applied to record the images of the reflected particles. Whereas a wide-angle lens, with the optical axis perpendicular to the plane of the laser light sheet, was used to ensure each image was able to cover an interested flow field. Each image was single exposed. Two instantaneous digital images of a particular particle-laden flow field at two consecutive times (i.e. τ and $\tau + \Delta\tau$) were obtained by the CCD camera. Since $\Delta\tau$ was very small (\sim 33ms), linear motion of the particle field in the composite image was sensed. From the knowledge of space distance and time difference, the instantaneous velocity could thus be obtained.

Varying the positions of the laser source and the CCD camera, different cross-sections of the ribbed triangular duct were investigated and thus flow pattern of the

whole area could be obtained. A detail description of the digital PIV technique was presented by Willert et al. [1993].

6.2.2 Setting up of the Test Rig

The experimental set-up as well as the PIV exploration used in the present study is shown in Fig. 6-3. Upon a proper position selection, the flow field was illuminated with a pulsed laser sheet by two New-Wave standard laser sources, each having a maximum energy output of 120mJ. The laser sheet had a thickness of 1mm, with a wavelength of 532nm by using an optical green filter in front of the laser lens.

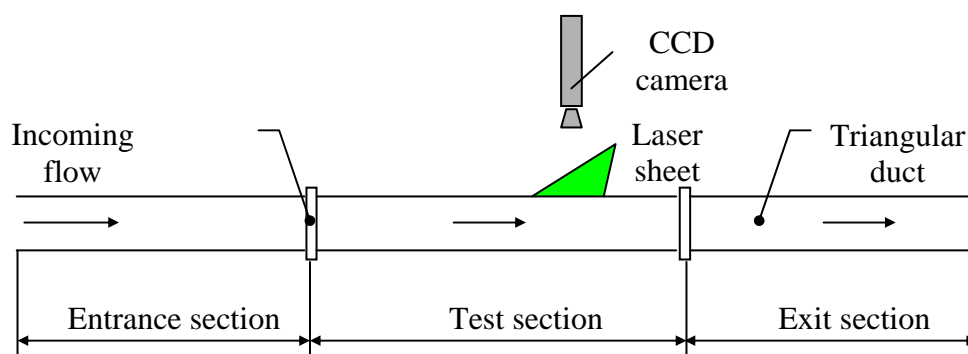


Fig. 6-3 PIV experimental set-up

For the transparency consideration, the test section was fabricated with glass having a thickness of 2mm, while the other two sections were fabricated with plexiglas. To reduce the effect of the laser light reflection, the duct's inner wall surfaces as well as the ribs were posted with non-gloss black paper with a thickness of 0.16mm, except for the optical access area for the laser lighting and camera imaging.

Since ambient air was transparent, a SPT smoke generator (i.e. Model 10D90) was applied to generate a white smoke consisting of paraffin oil droplets, which was introduced at the entrance of the triangular duct to the flow to facilitate visualization. The oil droplets had an average diameter of $1 \mu\text{m}$.

The whole test rig was placed inside a 2.4m-long square cross-sectional wind tunnel, which was of closed-circuit type and provided a uniform incoming flow through the triangular duct as shown in Fig. 6-4.

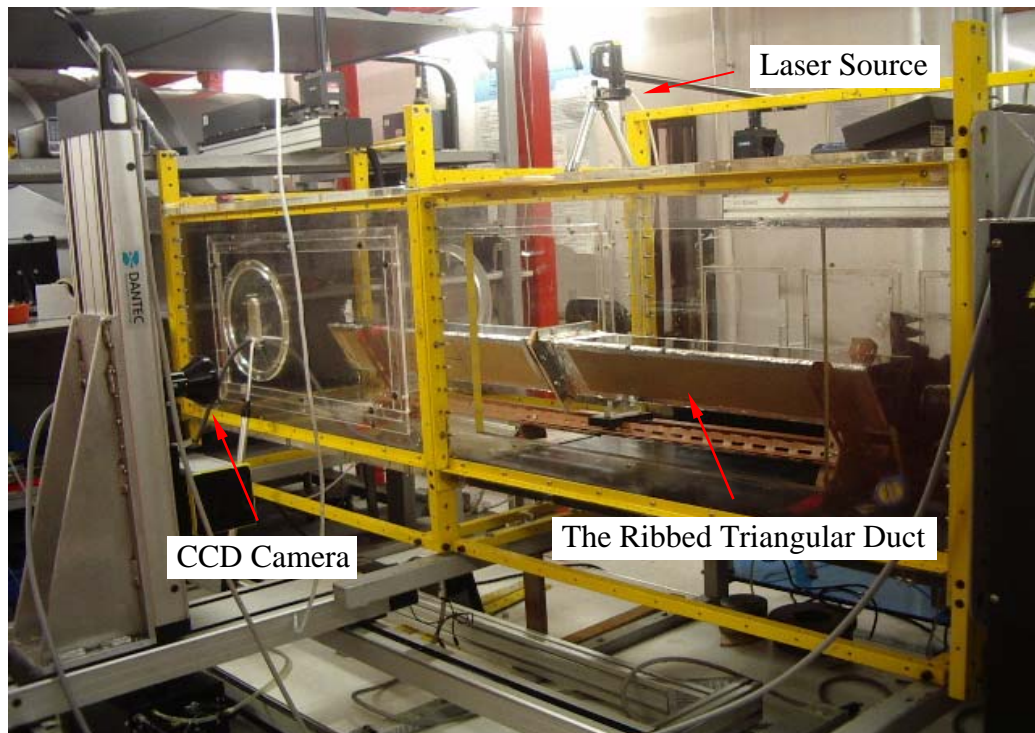


Fig. 6-4 A photo of the PIV experiment: the ribbed triangular duct placed in the wind tunnel

6.2.3 Analysis of Experimental Data

The time interval between two laser pulses was $\Delta T = 50 \mu s$ and the duration time of each laser pulse was $\Delta t = 0.01 \mu s$. For a bulk flow velocity $U_b = 3.6 m/s$ (i.e., corresponding to a hydraulic-diameter based Reynolds number of $Re = 10,800$), the friction velocity $u_* = 0.23 m/s$ could be estimated from the Blasius' semi-empirical law for the skin-friction coefficient (c_f) as [Schlichting et al. 1979]:

$$c_f \equiv 2\left(\frac{u_*}{U_b}\right)^2 = 0.07910 Re^{-\frac{1}{4}} \quad (6-1)$$

The root-mean-square (RMS) displacement of the seeding particles perpendicular to the laser sheet was estimated to be " $u_* \cdot \Delta T \sim 11.5 \mu m$ ", which was much smaller than the thickness of the laser sheet. Hence, the loss-of-correlation due to the particle out-of-plane motion could be ignored [Eggels et al. 1994]. In addition, the flow was treated as frozen during a laser pulse, and a travel distance of 0.18mm (i.e. 2.8 pixels) was obtained for a particle during the time interval between two consecutive laser pulses. Images of the reflected particles with an active area of 1280×1024 pixels, corresponding to an interested flow field of $82.5mm \times 66mm$ with a magnification factor of $M = 15.5 \text{ pixel/mm}$ in both the longitudinal and lateral control, were recorded by a high-resolution CCD camera at a 30 frame per second video rate.

The interrogation area had a size of 32×32 pixels and was 50% overlapped with the next area both horizontally and vertically, to obtain 4977 vectors (i.e. 79×63 vectors) for each image pair and minimize the occurrence of erroneous vectors. During the

PIV data analysis, the raw velocity-vectors generated by the cross-correlation were validated by setting the peak-height ratio and velocity range. Moving average validation based on comparison between neighboring vectors were applied to remove false vectors. Sequentially, estimated-vectors calculated from surrounding vectors were used to substitute the rejected-vectors. Furthermore, a 3×3 convolution low pass filtering operation was applied to remove the high frequency jitter caused by localizing the low particle density.

The PIV data processing was conducted through the software FlowManager, which was provided by Dantec. Two hundreds of instantaneous velocity measurements were obtained for statistical averaging to get the mean velocity distribution. The resulting velocity fields had a spatial resolution, which was defined by the size of the first interrogation window, of $0.5\text{mm} \times 0.5\text{mm}$. A measurement error of $\Delta x = 0.06$ pixel, or 0.2% of the diameter of the interrogation region was obtained (a measurement accuracy typically for PIV technique, as suggested by Willert et al. [1991] and Westerweel [1993]), which resulted in an uncertainty of $\pm 2.3\%$ in the velocity measurement.

6.3 Results and Discussions

Figure 6-5 presents a sample of the CCD camera recordings. A desirable number density of seeding particles (e.g. ~ 12 particles per interrogation volume) was provided to scatter sufficient laser light to facilitate the camera detection.



Fig.6-5 A sample of the camera image recordings

6.3.1 Velocity Fields and Distributions of Plane I

6.3.1.1 Smooth Triangular Duct

The velocity field and corresponding vorticity map in Plane I for the triangular duct with smooth internal surfaces are shown in Fig. 6-6. Secondary flows driven by the non-zero gradients of the normal Reynolds stresses in Plane I, which is perpendicular to the mean flow direction, are developed. Due to the suppression on the flow, provided by the sharp corners of the triangular duct, two counter-rotating vortices as shown in Fig. 6-6(b) are formed in each of the three corners of the triangular duct, which are consistent with the findings of Masoud et al. [2001].

The six vortices carry high momentum fluid towards the duct corners along the bisectors and then outwards to the middle plane along the walls. However, the secondary flows are not observed quantitatively in the velocity field shown in Fig. 6-6(a). It may be due to a perspective error of the present two-dimensional PIV technique, which has contaminated the measurements in this plane. Insufficient

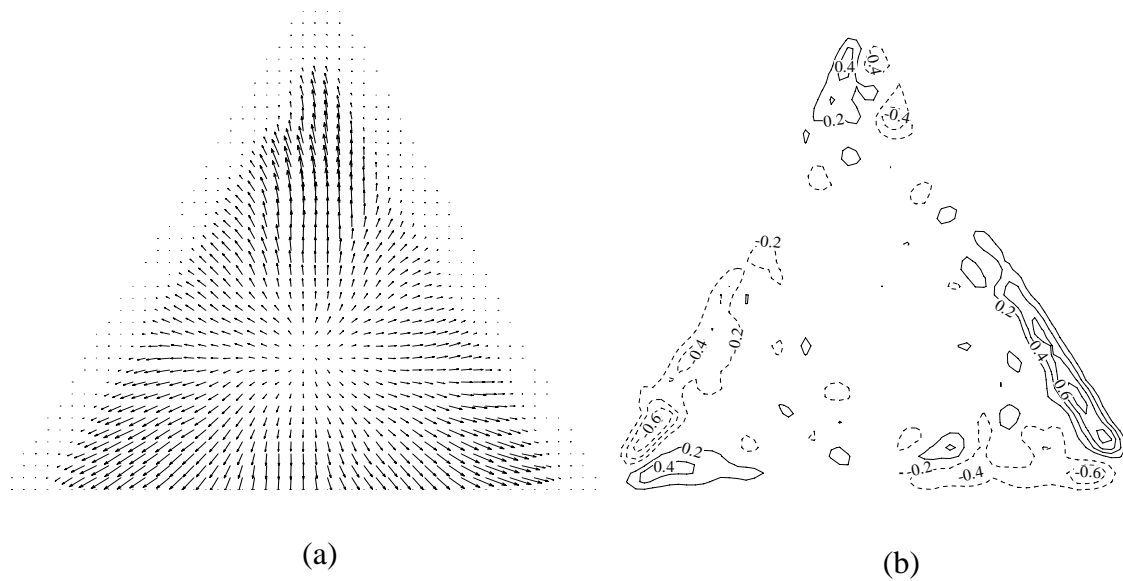


Fig. 6-6 (a) Velocity field and (b) corresponding vorticity map in Plane I for the smooth triangular duct

quality of the view of the velocity field may also contribute to it. The appearance of this error occurs when the out-of-plane components of the velocity are large compared to the in-plane components. Possibly, a three-dimensional Stereo PIV system need be applied to solve this problem.

6.3.1.2 Ribbed Triangular Duct

The velocity field in the same plane but for the triangular duct attached uniformly with square ribs on its internal surfaces is shown in Fig. 6-7. A disturbed flow field can be detected in the downstream area of the ribs. Counter-rotating vortices, as shown in the smooth triangular duct, move from the corners to the locations right above the ribs. It is due to the strong three-dimensional motions of the secondary flow formed beyond the ribs. In addition, the sudden expansion of the cross-

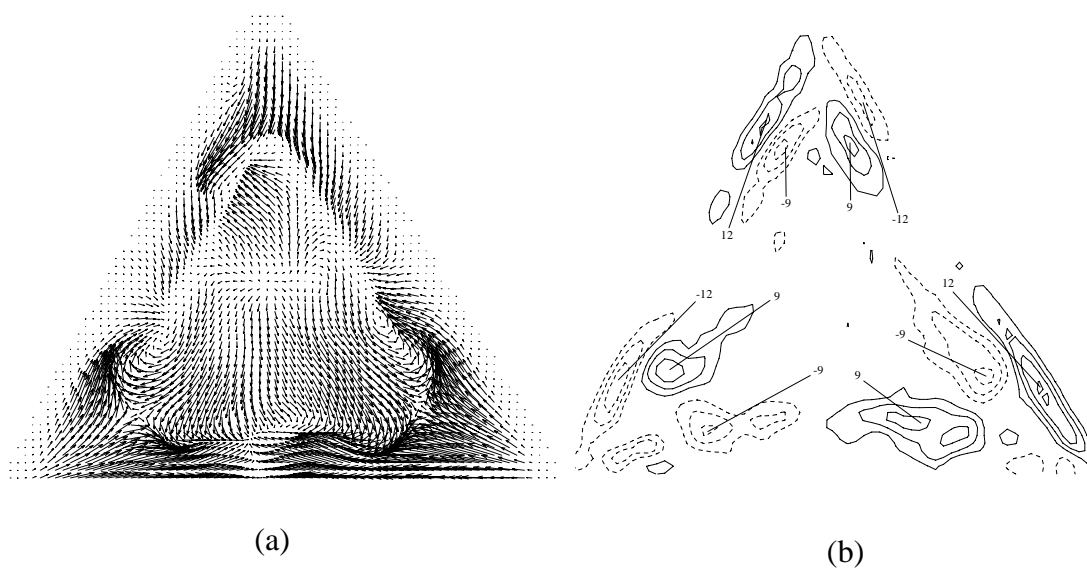


Fig. 6-7 (a) Velocity field and (b) corresponding vorticity map in Plane I for the ribbed triangular duct

sectional flow area, which leads to an acceleration of the secondary flow, also provides significant contributes to such a phenomenon. However, the symmetrical characteristic of the vortex is not clearly observed. It might be due to the failure to obtain a very close view of the secondary flow in the corners.

6.3.2 Velocity Fields and Distributions of Plane II

6.3.2.1 Smooth Triangular Duct

The flow pattern of a fully turbulent flow in Plane II for the smooth duct is presented in Fig. 6-8. Since no disturbance existed downstream of the coming main flow, a straight flow profile over the flat surface is observed. In Fig. 6-8, 'c' stands for a distance of $3e$ behind the ribs.

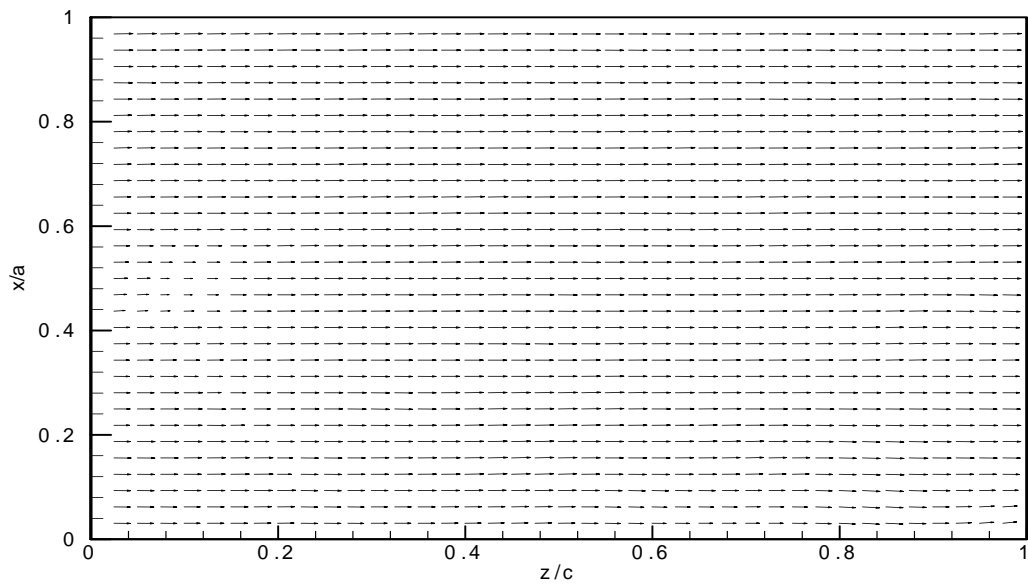


Fig. 6-8 Velocity profile in Plane II for the smooth triangular duct
($c = 3e$)

6.3.2.2 Ribbed Triangular Duct

The flow field in Plane II for the ribbed triangular duct is shown in Fig. 6-9. It is interesting to note that one large vortex cell exists in each half part of this plane. Considering the secondary flow patterns in the cross-sectional Plane I behind the ribs as shown in Fig. 6-7, it can be seen that these secondary flow carry high momentum fluid from the sharp corners of the triangular duct towards the middle plane along the duct walls, and move in a three-dimensional way following the streamwise direction. These two symmetrical vortices present in Fig. 6-9 are thus formed, and again carry high momentum fluid from the side wall of the triangular duct along the lateral side surface of the rib towards the middle plane. For a heat exchanging system of a triangular duct assembly with internal ribbed surfaces, heat is thus transferred from

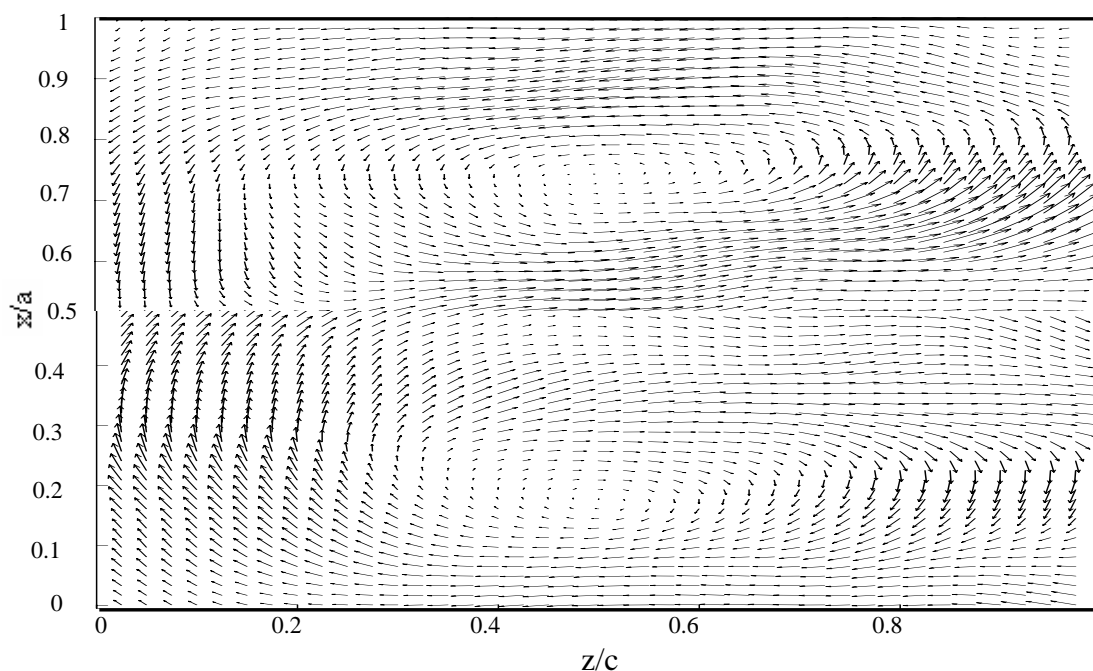


Fig. 6-9 Velocity profile in Plane II for the ribbed triangular duct

the duct to the fluid flow. In addition, because of the presence of these secondary flows induced by the additional ribs, heat is transferred in a more efficient way than that with smooth internal surfaces.

On the other hand, presence of the vortices, which is symmetrical about the centre line of $x/a = 0.5$, can be explained as the result of the difference in non-zero normal Reynolds stress $\overline{v'v'}$. Compared to the flow pattern in the smooth triangular duct as shown in Fig. 6-8, it is suggested that the three-dimensional flow structures are generated after the introduction of the attached ribs.

6.3.3 Velocity Fields and Distributions of Plane III

6.3.3.1 Smooth Triangular Duct

In Fig. 6-10, the velocity field in Plane III of the smooth triangular duct is presented. In addition to the straight and uniform velocity profiles obtaining along the streamwise direction, there are much smaller velocity magnitudes to the middle main flow observed in the near the wall regions. It is owing to the laminar boundary layers developed in the near-wall regions.

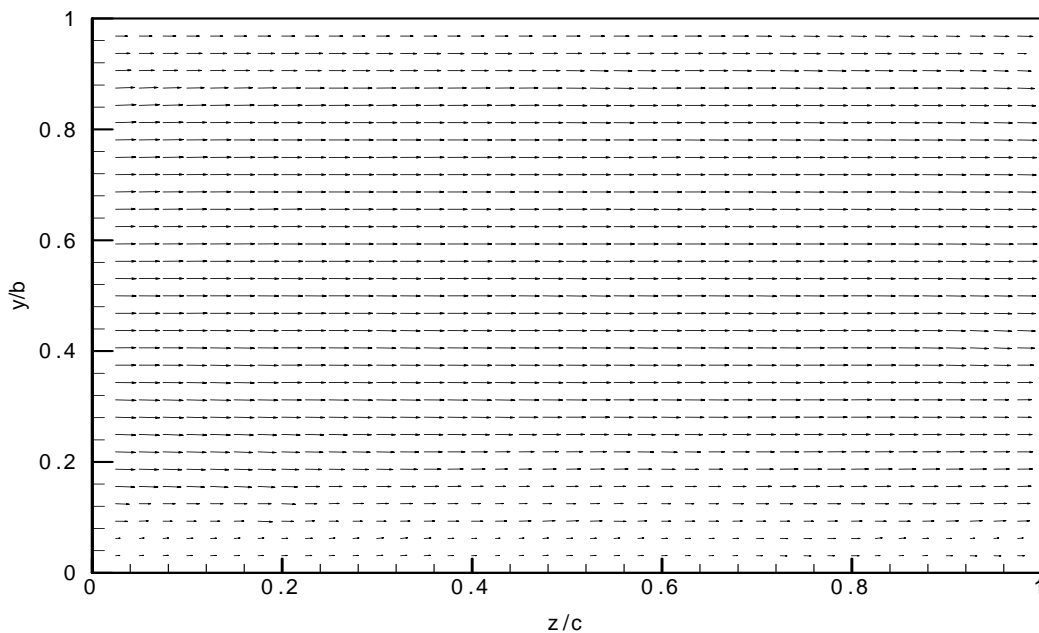
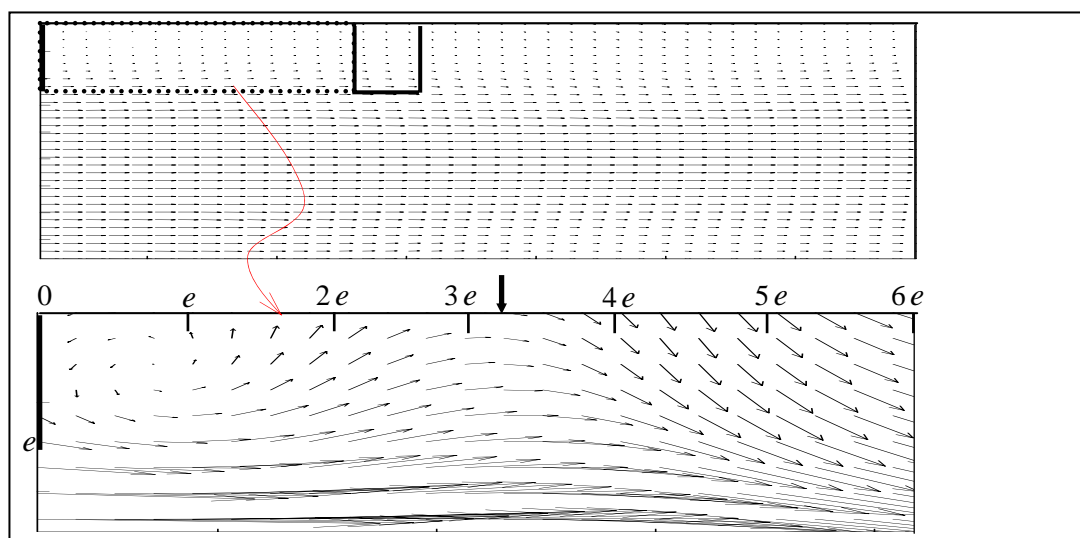


Fig. 6-10 Velocity profile in Plane III for the smooth triangular duct

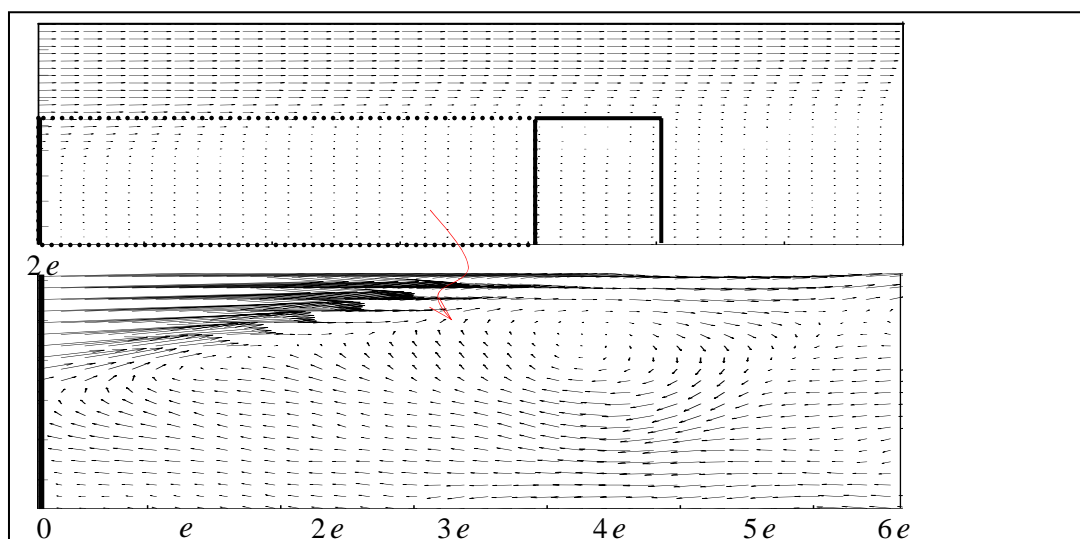
6.3.3.2 Ribbed Triangular Duct

In order to obtain a clear observation of the flow patterns in Plane III, an enlarged region between two consecutive ribs with a width of $2c$ (i.e. $\sim 6e$) was investigated.

The PIV visualization of the vertical plane III downstream of the ribs was conducted by dividing the plane into two parts: upper part ($1e$ in height) and lower part ($2e$ in height), respectively, as shown in Fig. 6-11.



(a)



(b)

Fig. 6-11 Velocity profiles in Plane III for the ribbed triangular duct
(a) the upper part; (b) the lower part.

Due to the sudden expansion of the flow field and hence the formation of low pressure regions behind the ribs, secondary flows are found to separate from the main turbulent flow at the up-right-corner of the ribs. Vortices are also observed after the ribs. It is due to the effect of the attached ribs. Because of existence of the ribs, which promote the turbulence in the flow, high turbulence intensities and velocity gradients are generated downstream of the ribs, which contribute to the formation of vortices in the separation zones.

Flow reattachment to the floor plane is detected in the upper part of Plane III, which is happened about $3\sim 4e$ away from the back surface of the upstream rib as shown by the solid arrow. However, such phenomenon is not observed in the lower part of this plane, where a recirculating flow is formed in the cavity between two adjacent ribs. In fact, in the upper part, the ‘block’ height is same as the ‘rib’ size, namely, e , so the ‘block’ spacing to ‘block’ height ratio is $S_r/e = 6.33$. Whereas in the lower part, because of the different alignment, the ‘block’ height is double of the rib size, which results in a ‘block’ spacing to ‘block’ height ratio of $S_r/2e = 3.17$. As discussed in Hishida [1996], when the rib spacing to rib height ratio was less than 5, a recirculating flow was formed in the cavity between two consecutive ribs, however, there was no flow reattachment achieved, which agreed well with the findings at the lower part in the present study.

Compared to the flow patterns in the smooth triangular duct as shown in Fig. 6-10, it can be concluded that the rib-generated secondary flows contribute to the enhancement of the forced convection in the triangular duct.

6.4 Summary

Turbulent flows in a triangular duct with or without ribbed surfaces were investigated through visualization method with the aid of PIV technique. After a comparison of velocity fields between these two kinds of triangular ducts, following conclusions can be drawn accordingly:

1. Development of the turbulence-generated secondary flows was studied in detail, which were further disturbed by the attached ribs on the internal surfaces. It was observed that the secondary flow detached from the main turbulent flow at the up right corner of the rib; however, flow attachment was not observed for a rib-to-rib spacing over rib-size ratio of 3.17, while for a ratio of 6.33, the flow attached to the bottom wall at a distance of $3\sim 4e$ away from the rib.
2. Because of the suppression on the flow provided by the installed ribs and the sharp corners of the triangular duct, vortices were developed in the regions near the ribs as well as the duct corners.
3. The rib-induced secondary flow at the near-wall regions of the duct as well as vortex around the rib were concluded to contribute most to the enhancement of turbulence (and thus heat transfer) of the present system.
4. Since the structures of the vortices were not clearly visualized in the cross-sectional plane behind the rib, which may be due to the application limitation of present two-dimensional PIV technique, further investigation by using three-dimensional Stereo PIV system needs to be conducted to better understand the flow characteristics in the micro-regions close to the wall.

7 FLOW PREDICTIONS BY TWO TURBULENCE

MODELS

Turbulent flow in the artificially roughened triangular duct had been investigated experimentally from both macroscopic and microscopic views as presented in former chapters. Due to the difficulties existing in the experimental method, numerical analyses of the flow and forced convection characteristics in the artificially roughened duct need to be performed to better understand its thermal performance.

Rib-roughened triangular duct was still given particular interest because of its advantages in investigation of the secondary flow. A numerical study had been conducted previously by Leung et al. [2000] to analyse the forced convection of the laminar flow in parallel plates with square ribs attached on its bottom plate. Development of vortex around the rib and local Nusselt number were successfully predicted with the use of a very fine mesh density. Tam et al. [1993] performed an investigation of turbulent flow in a horizontal ribbed duct, which was used to simulate a PCB assembly. Effects of the geometry of the system were studied and a non-dimensional correlation for predicting the heat transfer rate was proposed.

However, information for the simulation of a turbulent flow in the ribbed triangular duct is yet very insufficient. A very complicated three-dimensional heat and mass transfer problem is resulted from the integration of a ribbed surface and a triangular duct. To fully solve this problem involves very significant computation resources and difficulty. In this chapter, forced convection of the turbulent flow between two parallel plates with the bottom plate attached with uniformly spaced square ribs was

studied using a finite volume numerical technique. It was aimed to simulate the flow over one of the three walls of a ribbed triangular duct, the results of which would be useful for a more complicated numerical simulation of the entire three-dimensional duct in a later further study. Considering the applicability and basic features, two turbulence models, the Standard $k - \varepsilon$ Model and Reynolds Stress Model (RSM), were applied. It was expected that prediction abilities of these two turbulence models on channel turbulent flow were to be compared, since choosing a suitable and effective turbulent model for later simulation of the ribbed triangular duct was of importance. In addition, the turbulence-generated secondary motions of flow recirculation, detachment and reattachment were expected to be viewed in the vicinity of the ribs.

Special emphasis was also given on the local distribution of Nusselt number along the ribbed surface, which had been studied experimentally in previous studies [Aliaga et al. 1994 and Lorenz et al. 1995]. Therefore, to facilitate comparison, experimental results from Lorenz et al. [1995] were applied to validate against the present numerical predictions. Thus, suitability in applying these two models to predict the flow and forced convection characteristics of turbulent flow in the ribbed triangular duct could be examined.

7.1 Problem Description and Analysis

Corresponding to the assembly used in Lorenz et al. [1995], a horizontally oriented simulated printed circuit board (PCB) assembly, which was formed by two parallel

plates: a thermally insulated top smooth plate and a uniformly heated bottom rib-roughened plate, was applied in the present study.

Eight uniformly spaced square ribs of identical size were fixed on the internal surface of the bottom wall, as depicted in Fig. 7-1. A steady, incompressible, fully-turbulent, Newtonian fluid was taken into consideration, which was flowing through the two-parallel-plate channel with a uniform coming velocity of U_∞ . The hydraulic diameter D of this plate channel was equal to $2L$, while the rib's width-to-height ratio was fixed at $W/H = 2$, spacing-to-width ratio at $S_r/W = 2$ and height-to-hydraulic-diameter ratio at $H/D = 0.25$.

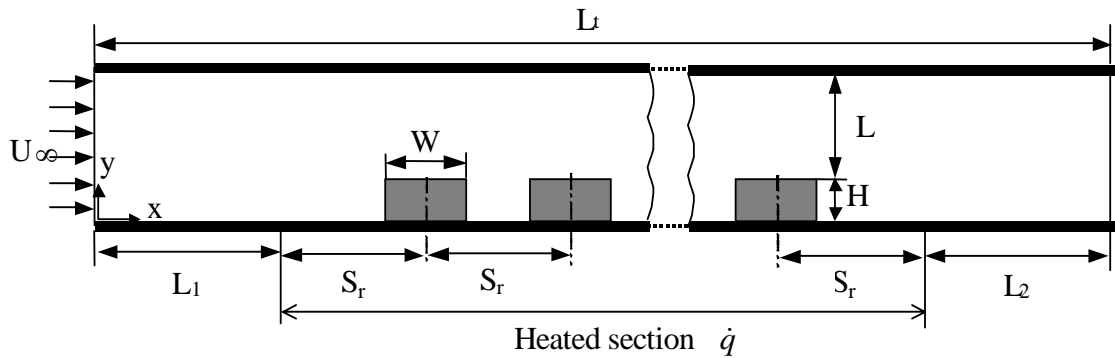


Fig. 7-1 Geometry of the two-parallel-plate channel with eight identical ribs

7.2 Governing Equations

Dynamic simulation of the channel flow under consideration was based on the following governing equations, namely, *steady-state continuity* (i.e. *conservation of mass*), *momentum balance* and *energy balance* equations:

$$\frac{\partial}{\partial x_j}(\rho U_j) = 0 \quad (7-1)$$

$$\frac{\partial}{\partial x_j}(\rho U_j U_i) = -\frac{\partial P}{\partial x_i} + \frac{\partial}{\partial x_j} \left[\mu \left(\frac{\partial U_i}{\partial x_j} + \frac{\partial U_j}{\partial x_i} \right) \right] + \frac{\partial}{\partial x_j}(-\rho \overline{u_i u_j}) \quad (7-2)$$

$$\frac{\partial}{\partial x_j}(\rho U_j T) = \frac{\partial}{\partial x_j} \left[\frac{\mu}{\text{Pr}} \frac{\partial T}{\partial x_j} - \rho \overline{u_j t} \right] \quad (7-3)$$

In the above equations, the two unknown variables: the turbulent shear stress $(-\rho \overline{u_i u_j})$ and the turbulent heat flux $(-\rho \overline{u_j t})$, would be required to be modelled.

As the walls are the main source of mean vorticity and turbulence, and the solution variables would have large gradients at the near-wall regions where the momentum and other scalar transports occur most vigorously, the near-wall modelling could affect significantly the accuracy of numerical solutions. Accurate representation of the flow in the near-wall regions has significant influence on the successful predictions of the wall-bounded turbulent flow.

7.3 Turbulence Models

In the present study, two semi-empirical turbulence models, namely, the Standard $\kappa - \varepsilon$ Model and the Reynolds Stress Model (RSM), were used in conjunction with the wall functions in dealing with the wall boundary layer for the predictions.

7.3.1 Standard $k - \varepsilon$ Model

The Standard $\kappa - \varepsilon$ Model [Launder et al. 1974] is a semi-empirical linear eddy viscosity model based on the model transport equations for the turbulence kinetic energy k and its dissipation rate ε . The model transport equation for k is derived from the exact equation, whereas that for ε is obtained from physical reasoning and has little resemblance to its mathematically exact counterpart, namely,

$$\frac{\partial(\rho u_i k)}{\partial x_i} = \frac{\partial}{\partial x_j} \left(\frac{\mu_t}{\sigma_k} \frac{\partial k}{\partial x_j} \right) + G_k - \rho \varepsilon \quad (7-4)$$

$$\frac{\partial(\rho u_i \varepsilon)}{\partial x_i} = \frac{\partial}{\partial x_j} \left(\frac{\mu_t}{\sigma_\varepsilon} \frac{\partial \varepsilon}{\partial x_j} \right) + C_1 \frac{\varepsilon}{k} G_k - C_2 \rho \frac{\varepsilon^2}{k} \quad (7-5)$$

where $\mu_t = \rho C_\mu k^2 / \varepsilon$, and $G_k = -\rho u_i u_j \frac{\partial u_j}{\partial x_i}$.

The empirical constants are assigned their usual values, i.e.,

$$\{ C_1, C_2, C_\mu, \sigma_k, \sigma_\varepsilon \} = (1.44, 1.92, 0.09, 1.0, 1.3).$$

The Reynolds-stress tensor is calculated according to the Boussinesq hypothesis, and the dynamic viscosity is replaced with an effective viscosity (i.e. $\mu_{\text{eff}} = \mu + \mu_t$, the sum of molecular and turbulent viscosities). In the derivation of the $\kappa - \varepsilon$ model, the flow is assumed to be fully turbulent, and the effects of molecular viscosity are negligible. Because of its robustness, economy, simplicity and overall good performance properties, the Standard $\kappa - \varepsilon$ Model is often a preferred choice in practical engineering flow calculations.

7.3.2 Reynolds Stress Model (RSM)

Without the isotropic eddy-viscosity hypothesis, the Reynolds Stress Model (RSM) [Launder et al. 1975] closes the Reynolds-averaged Navier-Stokes equations by solving transport equations for the Reynolds stress, $\overline{\rho u_i u_j}$, as shown in Equation (7-6), together with an equation for the dissipation rate.

$$\begin{aligned} \frac{\partial}{\partial x_k} (\overline{\rho u_k u_i' u_j'}) = & -\frac{\partial}{\partial x_k} \left[\overline{\rho u_i' u_j' u_k'} + \overline{p(\delta_{kj} u_i' + \delta_{ik} u_j')} \right] + \frac{\partial}{\partial x_k} \left[\mu \frac{\partial}{\partial x_k} (\overline{u_i' u_j'}) \right] \\ & - \rho \left(\overline{u_i' u_j'} \frac{\partial u_j}{\partial x_k} + \overline{u_j' u_k'} \frac{\partial u_i}{\partial x_k} \right) + \overline{p \left(\frac{\partial u_i'}{\partial x_j} + \frac{\partial u_j'}{\partial x_i} \right)} - 2\mu \overline{\frac{\partial u_i'}{\partial x_k} \frac{\partial u_j'}{\partial x_k}} \end{aligned} \quad (7-6)$$

In the above equation, the Buoyancy-induced effects are not included. The individual Reynolds stress is then used to obtain closure of Reynolds-averaged momentum equation (i.e. Equation (7-4)). In the steady-state transport equations for the Reynolds stress $\overline{\rho u_i u_j}$, modelling is not required for the convection, molecular diffusion and stress production terms. However, the turbulent diffusion, pressure strain and dissipation terms need to be modelled for the closure of transport equations. The turbulent heat flux term $-\overline{u_j t}$ is modelled using the commonly applied simple eddy-diffusivity model.

On the other hand, since the RSM creates a high degree of coupling between the momentum equations and the turbulent stresses in the flow, the calculation with RSM can be more prone to stability and convergence difficulties than with the $k - \varepsilon$ model.

7.3.3 Standard Wall Functions

The wall functions [Launder et al. 1974] are a collection of semi-empirical formulas and functions that are used to bridge the viscosity-affected region between the wall and the fully turbulent region. A similar logarithmic law for mean temperature is used from Reynolds' analogy between momentum and energy transport. In the $\kappa - \varepsilon$ model and the RSM (if wall boundary conditions are obtained from the κ equation), the κ equation is solved in the whole domain including the near-wall regions. However, the values of κ thus calculated are only needed near the wall in the RSM. The boundary condition for κ imposed at the wall is

$$\frac{\partial k}{\partial n} = 0 \quad (7-7)$$

Where n is the local coordinate normal to the wall.

In the κ equation, the generation of turbulence kinetic energy, G_k , and its dissipation rate, ε , at the wall-adjacent cells, are computed on the basis of the local equilibrium hypothesis, namely, G_k and ε are assumed to be equal in the wall-adjacent control volume.

7.4 Assumptions

The following assumptions were applied in the present numerical study:

- The turbulent flow was under steady-state condition.
 - Heat capacity of the plates was negligible.
-

- Thermal physical properties of both fluid and solid were taken as constant because the range of temperatures under consideration was small.
- Buoyancy-induced effects were assumed negligible due to the weakly coupling of the momentum and energy equations through the convective terms.
- Heat conduction in the flow direction was negligible when compared to the forced convection.
- The top plate was adiabatic, while the bottom plate was provided with a uniform heat flux \dot{q} , which did not vary with time.
- Since the ribs were ‘small’ comparing to the unribbed surface, the heat flux \dot{q} through a rib was evenly distributed, namely, the heat flux transferred from the top and side surfaces of a rib to the convective fluid were identical.
- Radiation heat transfer from and to the ribs was neglected, since the temperatures of the system under consideration were rather low (i.e., less than 310K).
- The thermal resistance between the rib and the bottom wall was negligible.
- Heat loss and heat gain from the surroundings was negligible (i.e. the outer wall of the triangular duct was adiabatic).
- The fluid was even distributed among channels and a plug flow was assumed due to the high turbulence in the channels.

7.5 Boundary Conditions

Fluid entered the channel at the ambient temperature ($T_0 = 293\text{K}$) with a uniform velocity U_∞ . In order to isolate the physical domain solution from the effect of computational outflow boundary conditions [Vakai et al. 1990], extended

computational domains of an inlet length of $L_1 = 10L$ and an outlet length of $L_2 = 10L$ were adopted. The upper and lower plates were assumed to be insulated thermally, except the interested section on the bottom plate fabricated with uniformly-spaced square ribs ($L_1 < x < (L_t - L_2)$), which was provided with a uniform heat flux of \dot{q} . No-slip boundary conditions were enforced at all the plate walls and the rib surfaces. Zero streamwise gradients of velocity components and temperature in the axial direction were applied at the exit plane of the channel, where the flow was assumed fully developed. To facilitate the comparison with the experimental study of Lorenz et al. [1995], Reynolds numbers of the airflow under consideration were ranged from 22,000 to 94,000.

According to above, the boundary conditions were given as:

1. Along the upper surface ($0 < x < L_t$, $y = e + L$):

$$u = 0, \quad v = 0, \quad \frac{\partial T}{\partial y} = 0 \quad (7-8)$$

2. Along the lower surface ($y = 0$):

$$u = 0, \quad v = 0, \quad \frac{\partial T}{\partial y} = 0 \quad \text{at } 0 < x < L_1 \text{ or } (L_t - L_2) < x < L_t \quad (7-9)$$

$$u = 0, \quad v = 0, \quad -k_f \left. \frac{\partial T}{\partial y} \right|_{y=0} = \dot{q} \quad \text{at } L_1 < x < (L_t - L_2) \quad (7-10)$$

3. At the inlet plane ($x = 0$, $0 < y < e + L$):
-

$$u = U, \quad v = 0, \quad T = T_0 \quad (7-11)$$

4. At the outlet plane ($x = L_t$, $0 < y < e + L$):

$$\frac{\partial u}{\partial x} = 0, \quad \frac{\partial v}{\partial x} = 0, \quad \frac{\partial T}{\partial x} = 0 \quad (7-12)$$

7.6 Numerical Scheme

Residual is a useful method to judge convergence not only by examining the residual levels, but also by monitoring the relevant integrated quantities such as drag coefficient or heat transfer coefficient. The convergence criterion applied in the present study required the residuals as defined by Equations (7-13) to decrease to 10^{-3} for all equations except the energy equation, for which the criterion was 10^{-6} . The residuals were calculated as below:

$$R^\phi = \frac{\sum_{cells,p} \left| \sum_{nb} a_{nb} \phi_{nb} + b - a_p \phi_p \right|}{\sum_{cells,p} \left| a_p \phi_p \right|} \quad (7-13)$$

Where a_p was the centre coefficient, a_{nb} was the influence coefficient for the neighbouring cell, b was the contribution of the constant part of the source term of the boundary conditions, ϕ_p was a general variable at the *cell p* and N was an iteration number [Fluent Inc. Documentation 6.0].

A highly variable non-uniform mesh was employed in the present study as shown in Fig. 7-2. This mesh was designed to capture the sharp gradients and boundary layers

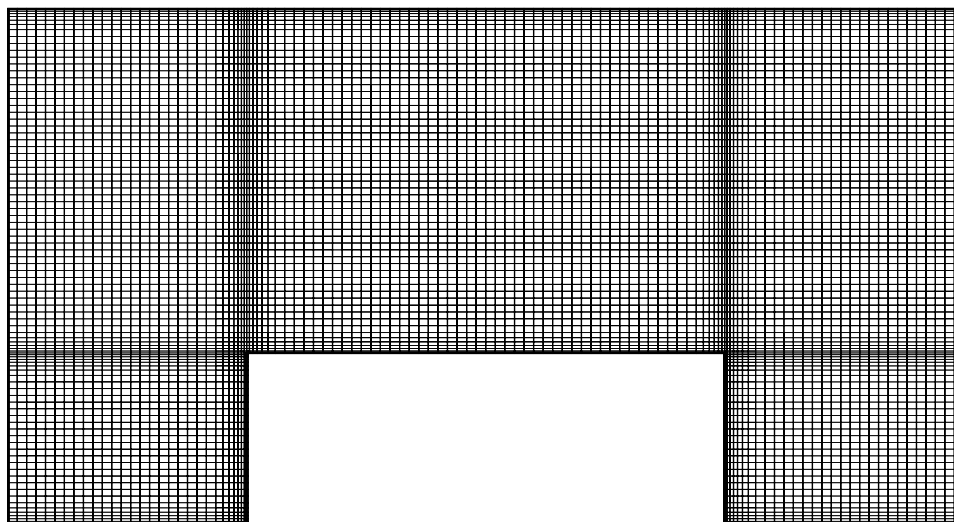


Fig. 7-2 The mesh distribution of the typical computational domain

near the fluid-solid interfaces and to provide sufficient mesh density at the rib and the smooth surface with minimal element distortion. Confirmation of the grid independence of the model was conducted, which required extensive tests to be carried out with increasing mesh densities and various mesh gradings until further refinement showed a difference in the results of less than 1%. The meshes employed in the present calculation were 1544×72 in the x and y directions, respectively.

7.7 Solution Techniques

In this study, a control-volume-based technique was used to convert the governing equations to algebraic equations that could be solved numerically. The FLUENT program was applied to integrate the governing equations for each control volume and to yield discrete equations conserving each quantity on a control-volume basis. For the pressure-velocity coupling discretization, the SIMPLE algorithm was

adopted, which used a relationship between velocity and pressure corrections to enforce mass conservation and to obtain the pressure field.

In the segregated solution method approach, the governing equations were solved sequentially. Because of the nonlinearities in the governing equations, pressure, momentum, turbulence kinetic energy, turbulence dissipation rate and Reynolds stresses were all under-relaxed. Moreover, since the governing equations were non-linear and coupled, several iterations of the solution loop were performed before a convergent solution could be obtained. During the iteration process, the large linear system of equations was solved with an iterative Line-Gauss-Seidel algorithm.

In addition, to enhance the calculation accuracy, a second-order upwind scheme was adopted and a sufficient mesh density was arranged near the wall regions. The y^+ value of the first grid point adjacent to the wall was about 40.

7.8 Results and Discussions

The present work was conducted to better understand the local distribution of Nusselt number over the ribbed-surface, and to compare the ability of two turbulence models in predicting the flow and forced convection characteristics of a fully developed turbulent flow through two parallel plates with heated ribs attached uniformly on the bottom surface.

Here, the local Nusselt number is defined as:

$$Nu_x = \frac{h_c L}{k_f} = -\frac{1}{\theta_{wall}} \frac{\partial \theta_f}{\partial y} \quad (7-14)$$

Corresponding experimental results from Lorenz et al. [1995] were available and included to facilitate comparison.

7.8.1 Flow Patterns around the Ribs

Figures 7-3 and 7-4 show the streamline characteristics of the ribbed channel predicted by the Standard $k - \varepsilon$ Model and the RSM at different Reynolds numbers, respectively. It is clearly observed that an anticlockwise vortex is predicted at downstream surface of the rib by both models. However, the length and relative strength of the vortex predicted by the RSM is larger and stronger, as shown in Fig. 7-4, than those predicted by the Standard $k - \varepsilon$ Model, as shown in Fig. 7-3. As Reynolds number increases, the vortex predicted by the Standard $k - \varepsilon$ Model decreases in both length and relative strength but remains almost unchanged for that predicted by the RSM. In addition, due to the sudden expansion of the cross-sectional flow-area, a low-pressure zone behind the rib occurs and a clockwise recirculating flow separating from the main flow is formed in the inter-rib region. As Reynolds number increases, the increasing axial momentum of the fluid, caused by the constriction of the bypass region, inhibits its expansion into the full channel downstream of the rib. There are no reattachments of the mainstream flow to the bottom floor observed in the present study with $S_r / h = 4$.

To facilitate clear illustration, only the isotherm distributions at the Reynolds number of 94,000 are presented in Fig. 7-5. It is clearly observed that the secondary flow in the downstream region of the rib affects the temperature field significantly. It is concluded that the thermal characteristics have been fully developed at the interested section.

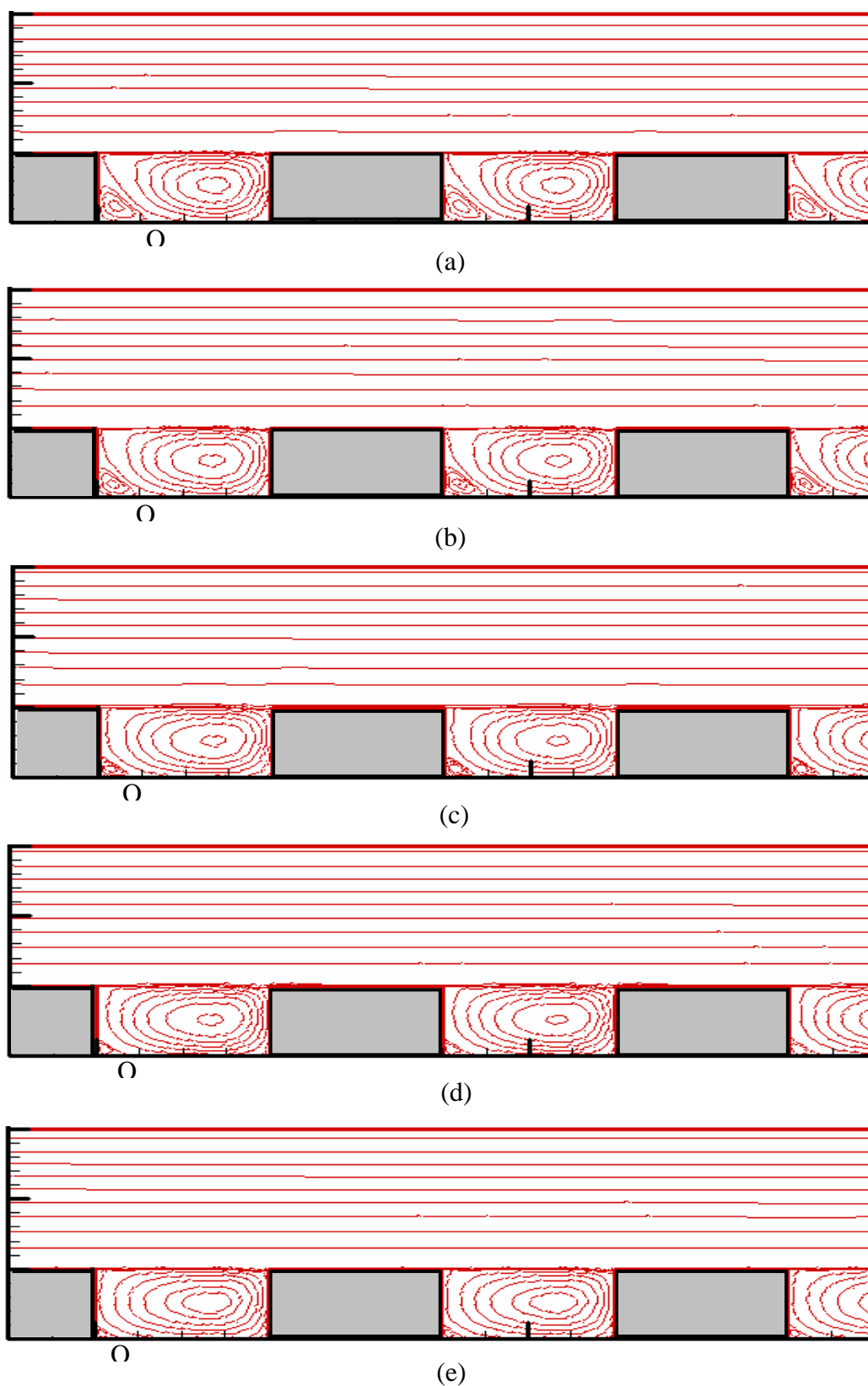


Fig. 7-3 Predicted streamlines of the turbulent flow in the channel at different Reynolds numbers by the Standard $k-\varepsilon$ Model (a) $Re = 22,000$; (b) $Re = 44,000$; (c) $Re = 63,000$; (d) $Re = 80,000$; (e) $Re = 94,000$.

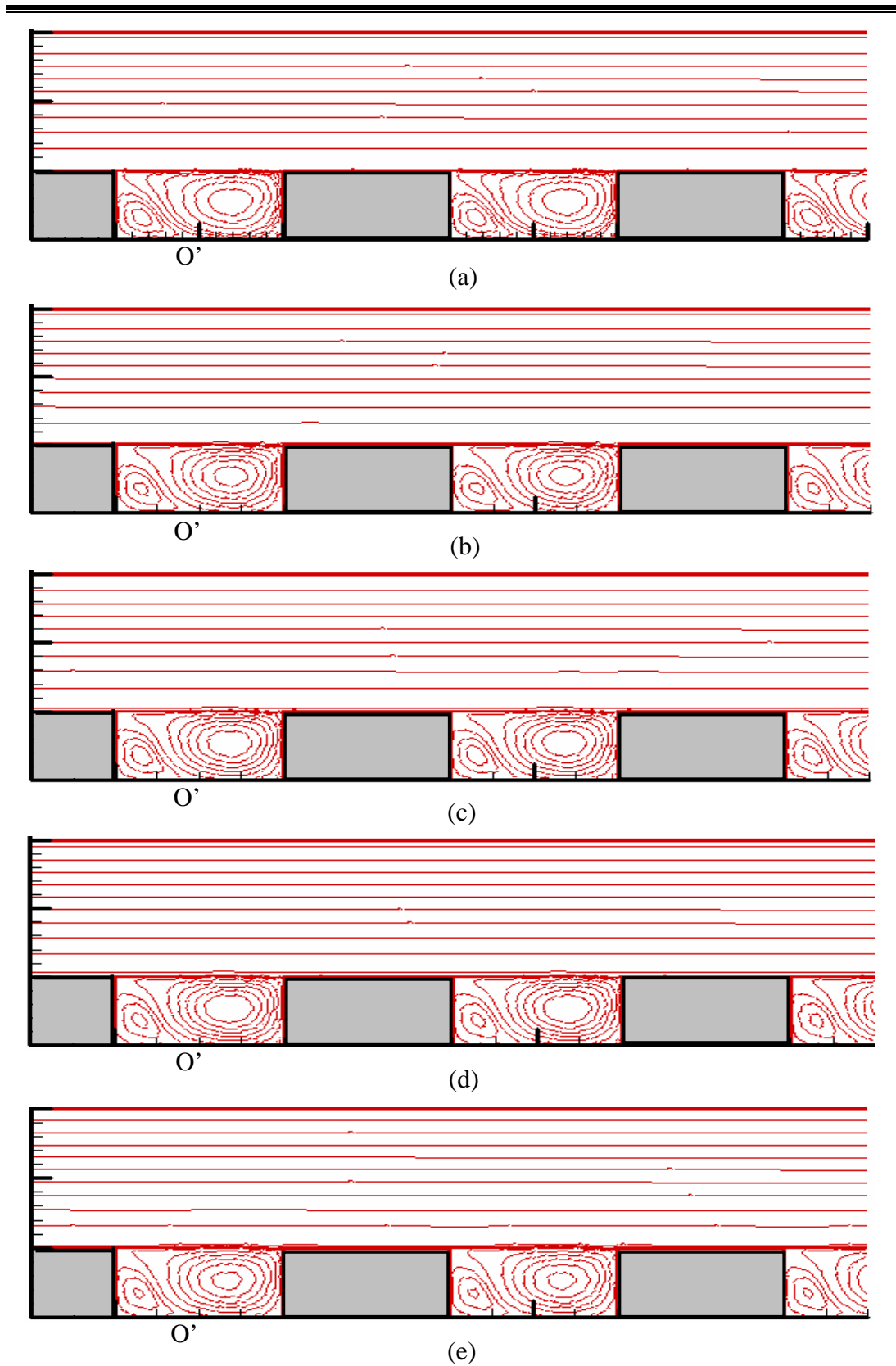


Fig. 7-4 Predicted streamlines of the turbulent flow in the channel at different Reynolds numbers by the RSM (a) $Re = 22,000$; (b) $Re = 44,000$; (c) $Re = 63,000$; (d) $Re = 80,000$; (e) $Re = 94,000$.

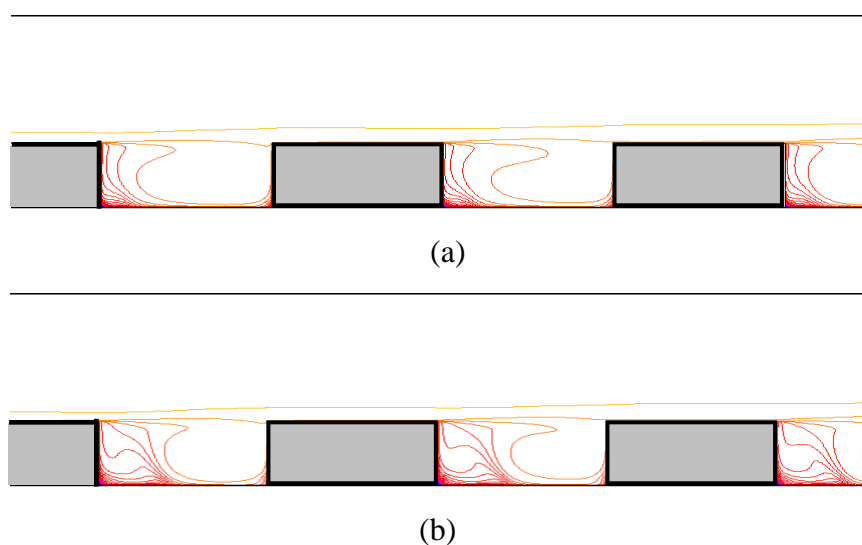


Fig. 7-5 Isotherms of the turbulent flow around the ribs as predicted by (a) the Standard $k-\varepsilon$ Model; (b) the RSM

7.8.2 Distributions of Local Nusselt Number along the Ribbed-Surface

The local Nusselt number distribution on the ribbed-surface including eight uniformly-spaced ribs at $Re = 94,000$ is shown in Fig. 7-6, where the peripheral distance axis measuring the running distance moves clockwise from the lower left corner of the rib. A similar local Nusselt number distribution is predicted by using either the Standard $k-\varepsilon$ Model or the RSM. It can be seen that the periodic thermal condition is established after the second rib, and there are two maximum values occurred around each rib: one is immediately in front of the rib, and the other is around the rib's upper left corner. They contribute to the flow recirculation and the impact at the vicinity of the rib, which will be discussed in the following section. In addition, a decay in the heat transfer enhancement is detected with the flow traversing in the streamwise direction, which was also observed by Lee et al. [2001]. When the fluid is flowing downstream, the turbulent kinetic energy drops due to the

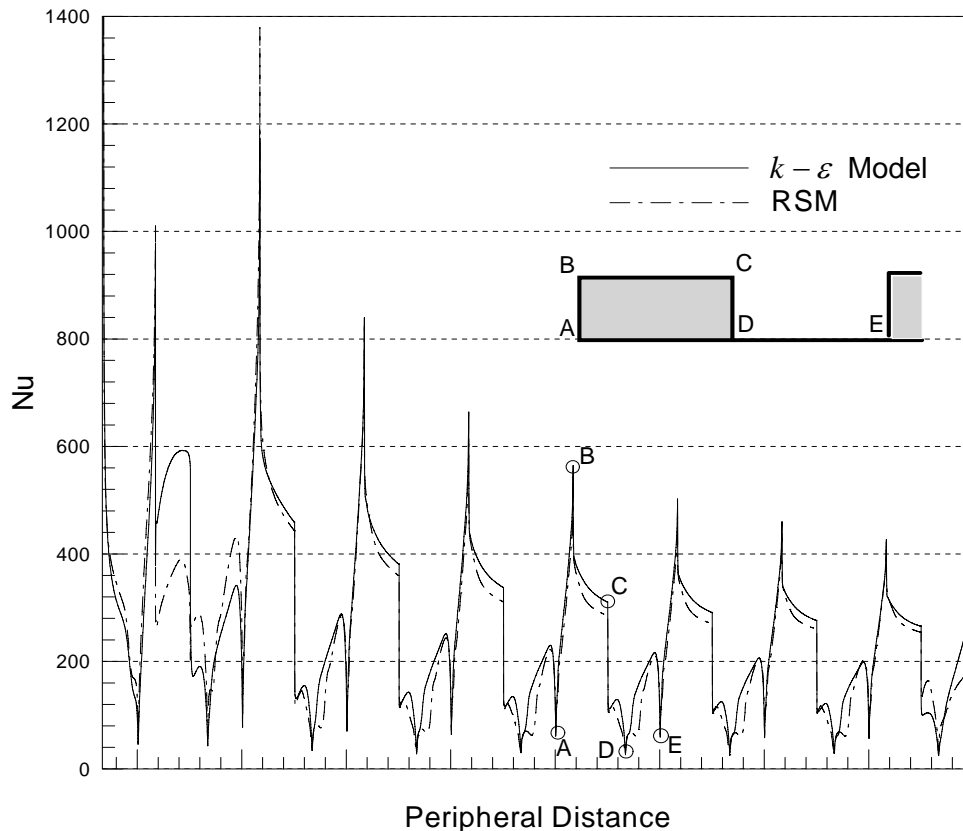


Fig. 7-6 Predicted distribution of local Nusselt number along the ribbed surface at $Re = 94,000$

pressure loss. The eddy viscosity and diffusivity of the flow in the subsequent ribbed-region decrease consequently, and a thicker thermal boundary layer is then formed. In addition, the fact that a larger portion of the surface is remote from the leading edge and therefore leads to a lower local Nu also contributes to it.

A comparison between the predicted Nusselt number distributions over the seventh rib obtained by the above two models with the experimental results of Lorenz et al. [1995] was carried out for $Re = 94,000$, as shown in Fig. 7-7. Very close predictions of Nusselt number distribution along the rib's left surface (i.e. $A \rightarrow B$) were obtained

with these two models. In fact, the existence of the rib reduces the cross-sectional flow area of the channel, which leads to a higher-pressure region before the rib and an acceleration of the core flow towards the rib. The upstream flow impinges on the rib's left surface and forms a clockwise recirculating flow there. As the flow moves down along the rib side, the thermal boundary layer becomes thicker and therefore, the Nusselt number increases almost linearly at the surface of $A \rightarrow B$. In addition, a sharp increase of the Nusselt number around point B is clearly predicted by both models. It is induced by the interaction between the recirculating flow in front of the rib and the upstream core flow. The interaction affects the temperature field: near the lower left corner the isotherms spread upstream due to the recirculation effect of the corner vortex, while near the top left corner the isotherms are crowded by the core flow. These two effects account for increase in the magnitude of the local temperature gradients, which directly affect the local Nusselt numbers. However, the predicted values are much greater than those suggested by Lorenz et al. [1995], and the variation is sharper as well. It may be due to the use of a relatively coarse mesh near this corner.

Further downstream, a thermal boundary layer is developed on the top surface of the rib (i.e. $B \rightarrow C$), and the Nusselt number decreases almost linearly along the top surface. From Fig. 7-7, it is clear that both models have predicted a more gently decrease in Nusselt number than the experimental result obtained by Lorenz et al. [1995]. However, it is interesting to note that very good agreements are obtained for the mean Nusselt number on the top surface between the numerical predictions and the experimental results.

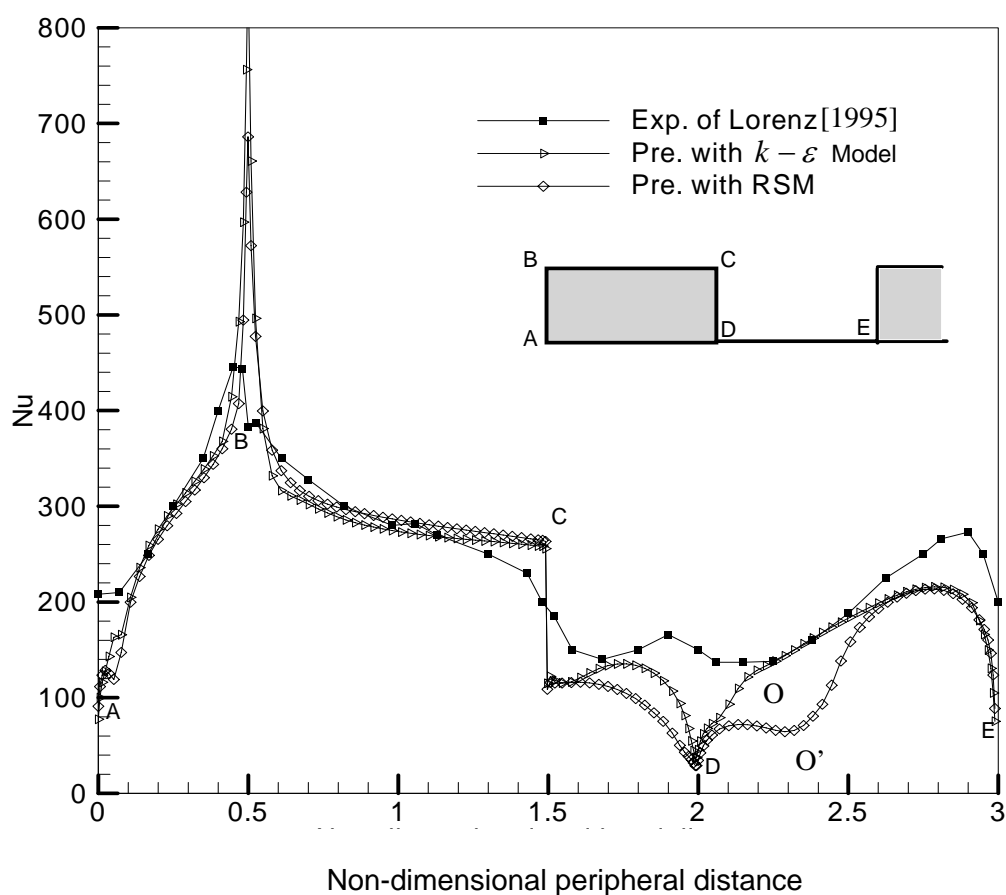


Fig. 7-7 The distribution of Nusselt number above the seventh rib at $Re = 94,000$

On the right side of the rib, due to the sudden expansion of the cross-sectional flow area, a low-pressure region is formed behind the rib. The mainstream flow separates at the rib's right upper corner C as shown in Fig. 7-7. As there is less fluid heated by the rib, a rapid decrease of Nusslet number is observed at the separating point C . Again, the incline is much rapider than the experimentally measured values. An S-shaped distribution of local Nusselt number at the rib's right surface (i.e. $C \rightarrow D$), is predicted by the Standard $k - \varepsilon$ Model, which is rather similar to the experimental finding of Lorenz et al. [1995]. However, such phenomenon is not predicted by

using the RSM. In addition, it is noted that both models underpredict the local Nusselt number along the rib's right surface. In the region near the rib's right lower corner (i.e. D), a significant drop of Nusselt number to a very low value is detected by both two models, but it is not observed from the experimental result. It may be due to the existence of a blind spot there during the experimental measurement. On the smooth surface between two adjacent ribs (i.e. $D \rightarrow E$), because of the effects of vortex and recirculating flow in this region, the distribution of local Nusselt number becomes rather interesting, which will be discussed in the following section. Around the rib surface, it can be concluded that a closer prediction to the experimental results [Lorenz et al. 1995] is obtained by using the Standard $k - \varepsilon$ Model instead of by the RSM.

7.8.3 Distributions of Local Nusselt Number at Different Reynolds Numbers

Figures 7-8 and 7-9 present the distributions of local Nusselt number over the seventh rib at different Reynolds numbers. As Reynolds number increases, magnitude of the temperature gradient increases near the upstream upper corner. The more rapid fluid movement associated with a higher Reynolds number reduces the thickness of the thermal boundary layer, and magnitude of the temperature gradient is therefore increased. Based on this reason, the local Nu has a higher value at a higher Re . The S-shape distribution of local Nusselt number becomes flatter with decreasing Reynolds number, which agrees well with the experimental results obtained by Lorenz et al. [1995]. At the inter-spacing between adjacent ribs (i.e. $D \rightarrow E$), due to the influence of the interaction of the vortex behind the rib with the recirculating flow, a transition process (i.e. $D \rightarrow O$) occurs before Nusselt

number increases nearly linearly along the bottom surface. Referring to Fig. 7-3, it is found that the transition points (O 's) coincides very well with the detachment points of the vortex and the recirculating flow. As mentioned above, the length and relative strength of the vortex predicted by using the Standard $k - \varepsilon$ Model decrease with increasing Reynolds number, and thus contribute to a decreasing transition process, which was also presented in the experimental results of Lorenz et al. [1995]. In fact, with the use of a higher Reynolds number, the fluid impinges and expands into the inter-rib region with a greater flow rate and a larger axial momentum, which leads to a decrease in the length and relative strength of the vortex. However, the

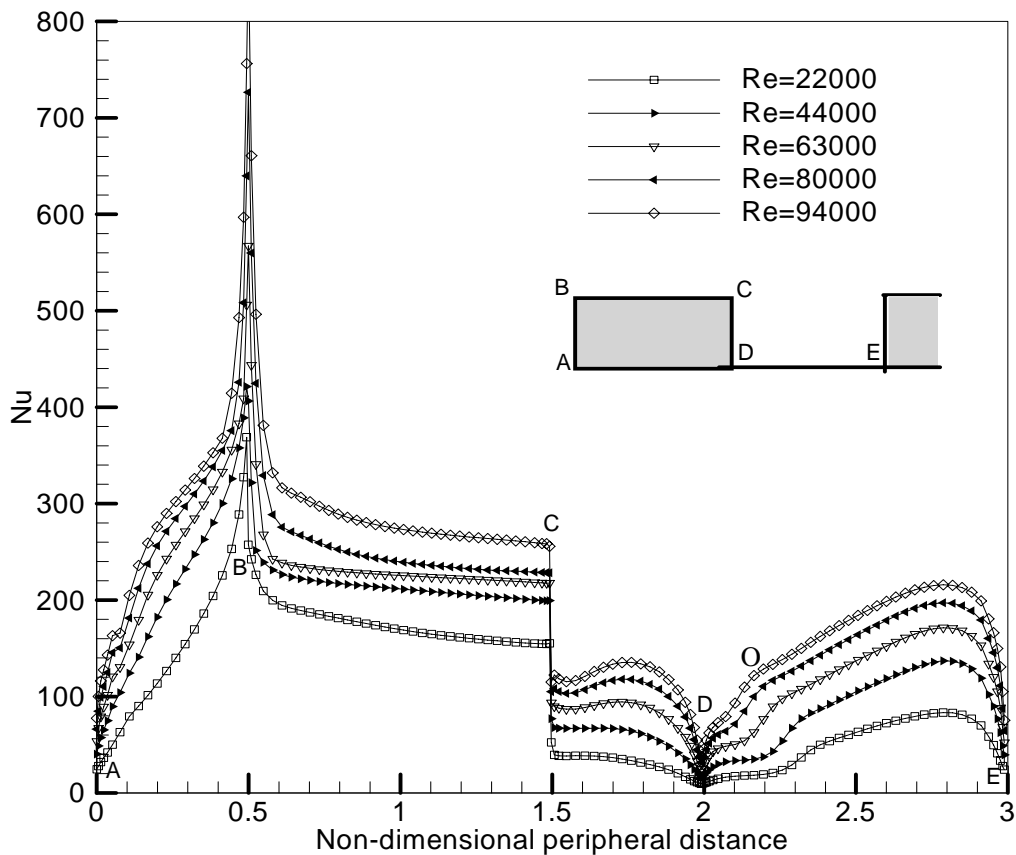


Fig. 7-8 The distribution of Nusselt number at different Reynolds numbers predicted with the Standard $k - \varepsilon$ Model

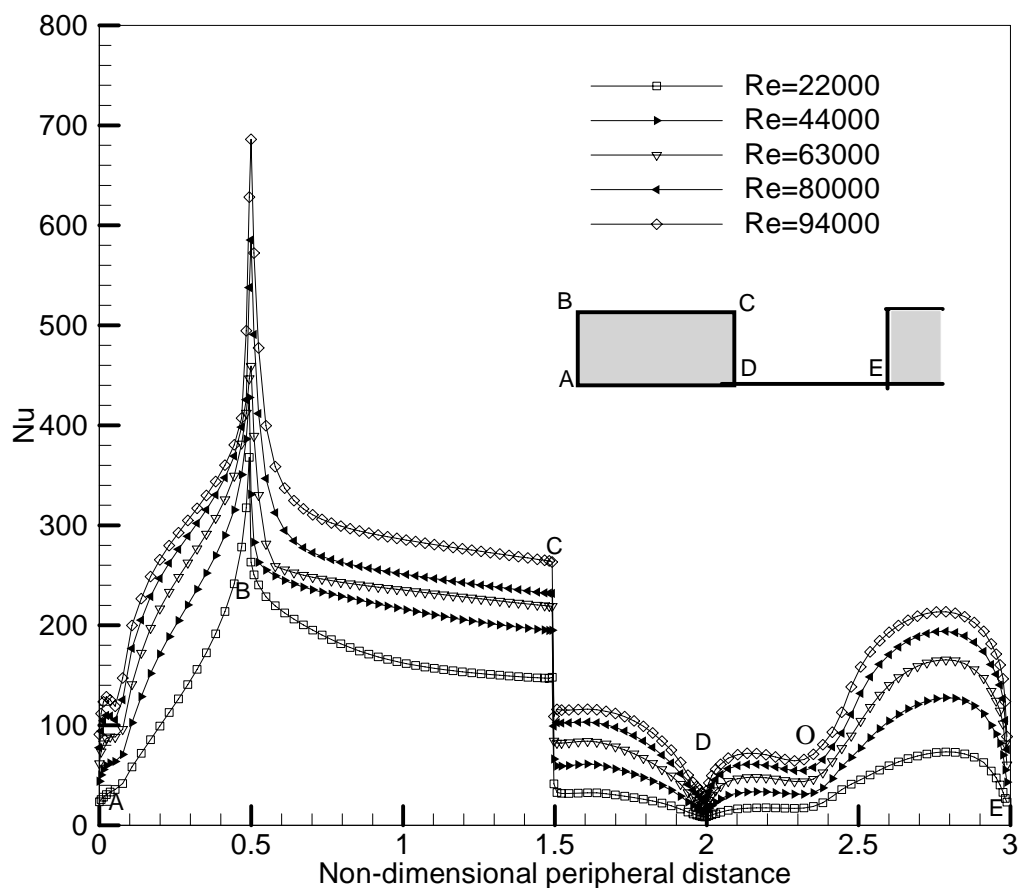


Fig. 7-9 The distribution of Nusselt number at different Reynolds numbers predicted with the RSM

predicted transition length maintains nearly constant by using the RSM, as shown in Fig. 7-9. Again, it is a significant discrepancy. Further downstream to the vicinity of the next rib, a second local maximum Nusselt number is obtained just in front of the rib's left lower corner, which is caused by the compaction and vortex formed in front of the rib. The impinging effect of the secondary structure on the rib's upstream surface is responsible for the high local heat transfer rate. According to the above comparison results, it can be concluded again that the Standard $k - \varepsilon$ Model is able to provide a closer prediction to the experimental results instead of the RSM.

7.8.4 Comparison between Two Models

As mentioned above, in the prediction of the flow and forced convection characteristics of the fully turbulent flow through two-dimensional parallel plates with ribbed bottom surface, it was concluded that the Standard $k - \varepsilon$ Model gave a better prediction than the RSM in general, even though the RSM was stated to be able to account for the effects of streamline curvature, swirl and rapid change in strain rate in a more rigorous manner than the Standard $k - \varepsilon$ Model [Launder et al. 1975]. It might be due to the application of the assumption of equilibrium, which had overlooked the effects of convection and diffusion in the transport equations for the stresses in the RSM when it was applied in the present two-dimensional ribbed-channel with turbulent forced convection. It could be deduced that the RSM turbulence model was not so suitable for the present two-dimensional problem. In addition, since the RSM closed the Reynolds-averaged Navier-Stokes equations by solving the transport equations for the Reynolds stresses, it took larger computational power and memory than the Standard $k - \varepsilon$ Model.

7.9 Summary

The present study was focused on the predictions of the turbulent flow and forced convection characteristics between two parallel plates with a uniformly spaced ribbed bottom surface. The bottom-ribbed surface was subjected to a uniform heating. There were two turbulence models: the Standard $k - \varepsilon$ Model and the Reynolds Stress Model (RSM), applied to perform the simulations. The SIMPLE algorithm was used in the calculations to handle the pressure-velocity coupling. The

numerical predictions were validated against the experimental results obtained by Lorenz et al. [1995]. The following findings are obtained:

- A decay of the heat transfer rate was detected along the streamwise direction over the ribbed surface, which agreed well with the previous study of Lee et al. [2001].
- Local Nusselt number distribution over the ribbed surface had been analysed in detail. It was observed that the Standard $k - \varepsilon$ Model could predict a more reasonable result than the RSM for the present kind of ribbed channel, especially at the downstream region of the rib.
- Both models underpredicted the Nusselt number, to different extents, on the downstream surface of the rib.
- An S-shape distribution of Nusselt number, as reported in the previous experimental work of Lorenz et al. [1995], was predicted successfully by using the Standard $k - \varepsilon$ Model, but not by the RSM.
- No reattachment pattern of the mainstream flow was observed in the present study with a rib's pitch-to-height ratio of $p/e = 4$, which was less than 5, and such suggestion agreed well with the previous studies of Shiina [1975] and Hishida [1996].
- A finer mesh density should be applied in the regions around the rib's corners in order to achieve more accurate predictions of the Nusselt number over the ribs.
- Based on this numerical simulation task, the Standard $k - \varepsilon$ Model should be chosen instead of the RSM for the future simulation study of the channel turbulent flow.

8 SIMULATION OF GEOMETRY EFFECTS ON THE RIB-DISTURBED TURBULENT FLOW

Rib- and corner-caused secondary flows are developed simultaneously in the triangular duct, which is attached with uniformly spaced square ribs, as suggested from the previous experimental work described in the former chapters. As sufficient experimental results have been obtained, it may already be mature to tackle the problem via the numerical simulation approach. In order to better understand the flow and thermal characteristics of such a complicated three-dimensional ribbed triangular duct, it may be necessary to view numerically the mechanism of detachment and reattachment of the periodic flow at the duct's near-wall regions, the formation of vortex around the rib, and the development of secondary flow in the sharp-corners.

In order to fulfill these objectives, the numerical solution can be approached via two individual relatively simple numerical models: a two-dimensional model to simulate the longitudinal section of the ribbed triangular duct (namely, along the flowwise direction), and a three-dimensional model to simulate the transverse section of the ribbed triangular duct (namely, a cross-sectional plane orthogonal to the flowwise direction).

On the one hand, development of the secondary flow along the flowwise direction was investigated with a horizontally oriented parallel plate assembly: the upper smooth plate was thermally insulated whereas the bottom plate was attached with square ribs and was heated uniformly. The bottom plate attached with equally

spaced square ribs perpendicular to the mean airflow was used to simulate one of the three walls of the ribbed triangular duct. As concluded from Chapter 7, the Standard $k - \varepsilon$ Model is more suitable than the RSM to predict the turbulent flow in such a two-dimensional channel with ribs attached uniformly on one plate.

On the other hand, since the linear $k - \varepsilon$ model has not the ability to predict secondary flows, a non-linear $k - \varepsilon$ model, the RSM, was applied for the prediction of the corner-caused secondary flow. The numerical study was conducted based on a three-dimensional horizontal equilateral triangular duct with smooth internal surfaces, and the RSM was used in conjunction with the wall functions to deal with the wall boundary layer for the predictions.

8.1 Problem Description and Analysis

A steady-state, incompressible and fully-developed turbulent Newtonian fluid was chosen to represent the flow through: (i) a channel formed by two parallel plates with three identical square ribs mounted on the bottom surface at a uniform spacing of $S_r = 1.3$ (corresponding to a rib-to-rib spacing of $S_r = 57\text{mm}$ with a hydraulic diameter of $D = 44\text{mm}$ in Chapter 4): the rib size used in the present study was $H = 0.2$ (corresponding to a rib size of $H = 9\text{mm}$ with a hydraulic diameter of $D = 44\text{mm}$ in Chapter 4), as shown in Fig. 8-1(a); (ii) a horizontal oriented equilateral triangular duct with smooth internal surfaces, the hydraulic diameter D of which was equal to 44mm , as shown in Fig. 8-1(b).

The mean values of Nusselt number for the rib's side surfaces (i.e. Nu_L , Nu_T , Nu_R) and overall rib mean value (i.e. Nu) are calculated from:

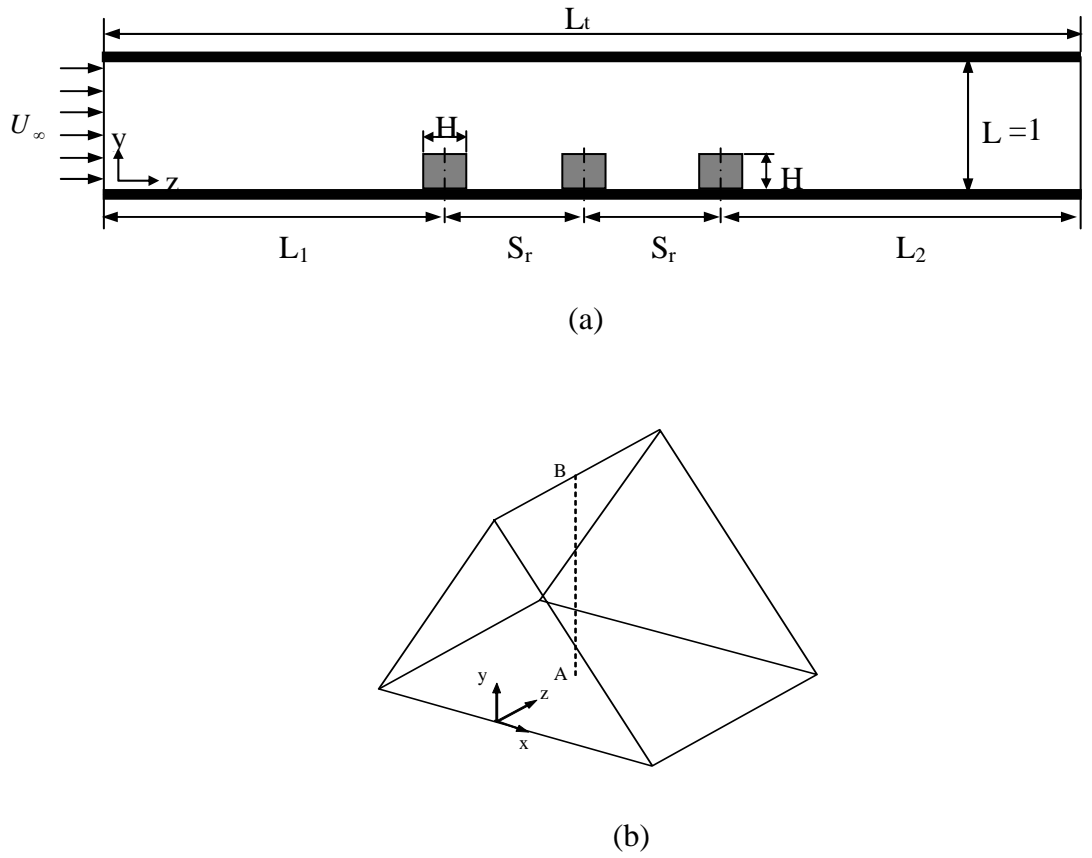


Fig. 8-1 The geometry of (a) a parallel plate channel with three identical ribs; (b) an equilateral triangular duct with smooth internal surface.

$$Nu_i = \frac{\int_{A_i} Nu_x dx}{A_i} \quad (8-1)$$

$$Nu = \frac{\sum_{i=L,T,R} Nu_i A_i}{A_L + A_T + A_R} \quad (8-2)$$

Where, Nu_x is the local Nusselt number for the rib's side surfaces, A_i is the area of exposed side surface i of the rib. Thus the overall rib mean value is an area-weighted average of the exposed surface mean values.

The Governing equations applied in the present study were same as Equations (7-1) to (7-3) in Chapter 7, namely, *steady-state continuity*, *time-averaged momentum*, and *energy equations* for turbulent flow:

$$\frac{\partial}{\partial x_j}(\rho U_j) = 0 \quad (7-1)$$

$$\frac{\partial}{\partial x_j}(\rho U_j U_i) = -\frac{\partial P}{\partial x_i} + \frac{\partial}{\partial x_j} \left[\mu \left(\frac{\partial U_i}{\partial x_j} + \frac{\partial U_j}{\partial x_i} \right) \right] + \frac{\partial}{\partial x_j}(-\rho \overline{u_i u_j}) \quad (7-2)$$

$$\frac{\partial}{\partial x_j}(\rho U_j T) = \frac{\partial}{\partial x_j} \left[\frac{\mu}{Pr} \frac{\partial T}{\partial x_j} - \rho \overline{u_j t} \right] \quad (7-3)$$

8.2 Assumptions

The following assumptions were applied during simulations:

- The turbulent flow was under steady-state condition.
 - Thermal-physical properties of both fluid and solid were constant.
 - Buoyancy effects were negligible.
 - Heat conduction along the flow direction was negligible.
 - Heat flux (\dot{q}) did not vary with time.
 - Heat loss to and heat gain from the surroundings were negligible since outer surfaces were adiabatic;
 - The fluid was evenly distributed among the channels and a plug flow occurred due to the high turbulence in the channel.
 - Heat capacity of plates or walls was negligible.
-

There were particular assumptions made for the ribbed parallel plate assembly:

- The upper plate was adiabatic while the bottom plate was provided with a uniform heat flux \dot{q} .
- The heat flux (\dot{q}) through the rib was evenly distributed, namely, the heat flux from the top and sides of the ribs to the fluid were identical.
- Thermal resistance between the rib and the bottom wall was negligible.
- Radiation heat transfer from and to the ribs was neglected.

Similarly, for the smooth equilateral triangular duct assembly, the following particularly assumption was made:

- The turbulent flow was under regular periodic-flow conditions: a constant mass flow rate and a constant inlet temperature were achieved.

8.3 Boundary Conditions

8.3.1 Uniformly Ribbed Parallel Plates

For the simplification and convenience, the dimensionless rib-height h^* (i.e. ratio of rib height to channel hydraulic diameter, $h^* = H/L$, where $L=1$) was used in this study.

The fluid entered the channel at the ambient temperature T_0 (20°C or 293K) with a uniform velocity $U = 3.6\text{m/s}$, which was expressed as follow:

$$w^* = 1, \quad v^* = 0, \quad \theta = 0 \quad \text{at} \quad z^* = 0, \quad 0 < y^* < 1 \quad (8-3)$$

Where, w^* , v^* and θ were the dimensionless velocities and temperature, which were defined as: $w^* = w/U$, $v^* = v/U$, and $\theta = \frac{T - T_0}{Q/k_f}$, respectively.

The rate of mass flow was specified to create a flow field. Reynolds number, which was corresponding to the mass flow rate, was coupled to the non-periodic pressure gradient. To ensure the occurrence of a fully developed turbulent flow in the interested region and isolate the physical domain solution from the effect of computational outflow boundary conditions [Vakai et al. 1990], extended computational domains of an inlet length of $L_1 = 10$ and an outlet length of $L_2 = 10$ were adopted.

The upper plate was thermally insulated while the bottom plate was fabricated with uniformly spaced square ribs and was provided with a uniform heat flux of $\dot{q} = 63.5\text{W/m}^2$ to keep consistent with that applied in the previous experimental work of Chapter 4 (i.e. which was corresponding to the experiment heat input of $E = 200\text{w}$ and an axial length of $L = 1.05\text{m}$). In addition, no-slip boundary conditions were enforced at the interfaces of the fluid and solid surface. Continuities of temperature and heat flux were accounted as:

$$w^* = 0, v^* = 0, \frac{\partial \theta}{\partial y^*} = \dot{q} \quad \text{at } 0 < z^* < L_t, y^* = 0 \quad (8-4)$$

$$w^* = 0, v^* = 0, \frac{\partial \theta}{\partial y^*} = 0 \quad \text{at } 0 < z^* < L_t, y^* = 1 \quad (8-5)$$

At the exit plane, it was assumed that the fluid was fully developed and zero streamwise gradients were prescribed:

$$\frac{\partial w^*}{\partial z^*} = 0, \frac{\partial v^*}{\partial z^*} = 0, \frac{\partial \theta}{\partial z^*} = 0 \quad \text{at } z^* = L_t, 0 < y^* < 1 \quad (8-6)$$

8.3.2 Smooth Equilateral Triangular Duct

In the fully developed turbulent flow, because of the occurrence of the cyclic velocity and dimensionless temperature profiles, there is no need to deal with the developing region when only the fully-developed region is of interest. By imposing the periodic conditions to the main flow direction, it is sufficient to solve the flow and thermal characteristics of the fully developed region. Thus, the computation time decreases considerably because the number of grid points in the main flow direction is reduced significantly. In the present investigation of a fully turbulent flow with a repeated wall heat flux, following periodic conditions, i.e. constant pressure drop along a ribbed duct with a periodic length of \tilde{L} and identical temperature profiles with a constant increment at the inlet and outlet of the duct, were imposed to achieve the fully developed state:

$$P = -\beta \frac{z}{\tilde{L}} + P_0 \quad (8-7)$$

$$T = \frac{\dot{q}}{\dot{m}C_p} \frac{z}{\tilde{L}} + T_0 \quad (8-8)$$

Where, β was the non-periodic pressure gradient, P_0 and T_0 were the periodic parts of pressure and temperature in the main flow direction, respectively.

A mass flow rate ($= 0.11 \text{ kg/m}^3$) corresponding to a typical turbulent-flow state with a Reynolds number of $Re = 10,400$ was specified to create a flow field and the mass-flow-rate-based Reynolds number was coupled to the non-periodic pressure gradient. Every surface of the equilateral triangular duct was provided with the same uniform heat flux of $\dot{q} = 63.5 \text{ W/m}^2$.

8.4 Numerical Scheme

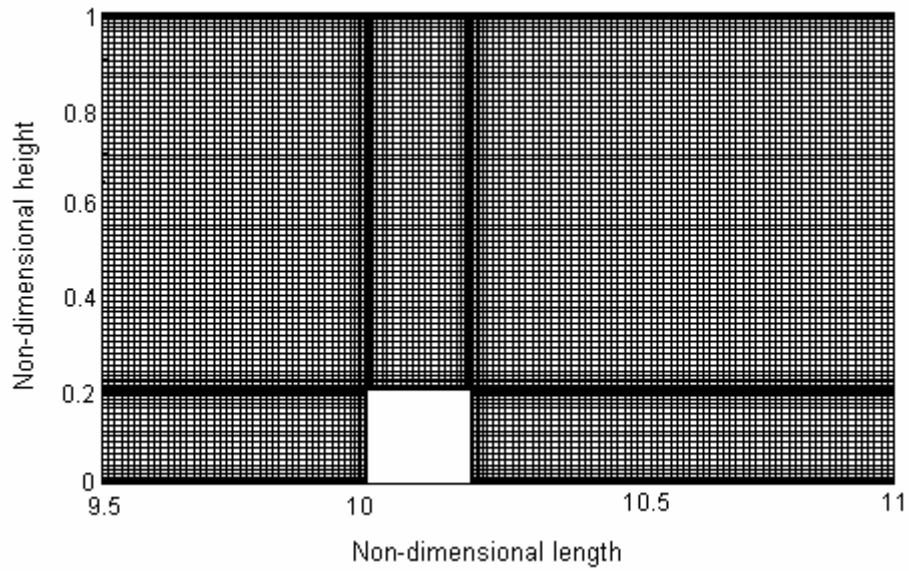
8.4.1 Uniformly Ribbed Parallel Plates

A highly variable non-uniform mesh was employed in present study, as shown in Fig. 8-2(a). This mesh was designed to capture the sharp gradients and boundary layers near the fluid-solid interfaces and to provide sufficient mesh density at the rib surfaces and the smooth surfaces with minimal element distortion. The y^+ value of the first grid point adjacent to the wall was about 40.

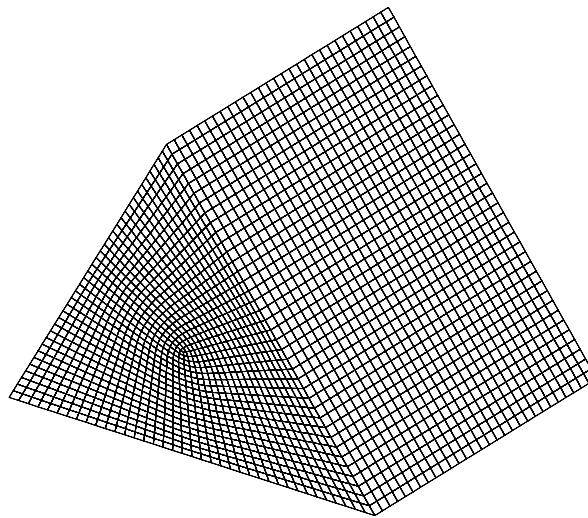
8.4.2 Smooth equilateral triangular duct

The computational domain consisted of hexahedral grids was shown in Fig. 8-2(b). The non-uniform hexahedral grids were used because they were able to fit better into the cross-section of the triangular duct.

Extensive tests for the confirmation of grid independence of the model were carried out by increasing the mesh density and adopting various mesh gradings until further refinement showed a difference of less than 1% in two consecutive sets of results was obtained. The y^+ value of the first grid point adjacent to the wall was less than 5.



(a)



(b)

Fig. 8-2 Mesh distribution of a typical computational domain of
(a) the ribbed parallel plates; (b) the equilateral triangular duct

8.5 Solution Techniques

In the present study, the FLUENT, a finite volume code using a cell-centered non-staggered grid, was used to perform the calculations. Fluent uses a control-volume-based technique to convert the governing equations to algebraic equations that can be solved numerically. This control volume technique consists of integrating the governing equations about each control volume, yielding discrete equations that conserve each quantity on a control-volume basis. In the segregated solution method approach, the governing equations are solved sequentially. Because of the nonlinearities in the governing equations, pressure, momentum, turbulence kinetic energy, turbulence dissipation rate and Reynolds stresses were all under-relaxed. The pressure correction algorithm SIMPLE was used to solve the Reynolds-averaged Navier-Stokes and the transport equations of the turbulent quantities. During the iteration process, the large linear system of equations would be solved with an iterative Line-Gauss-Seidel algorithm.

8.6 Results and Discussions

8.6.1 Uniformly ribbed parallel plates

To investigate the effect of ribbed surface on the flow and forced convection characteristics, three uniformly spaced identical square ribs were fabricated on the bottom wall of the parallel plates, as shown in Fig. 8-1(a). The bottom surface was uniformly heated with a heat flux of $\dot{q} = 63.5\text{W/m}^2$, whereas the top wall was thermally insulated.

The basic characteristics of the streamlines at $Re = 10,400$ are shown in Fig. 8-3. It is observed that a clockwise vortex is developed at the front corner of the rib. In addition, sudden expansion of the cross-sectional flow area leads to the formation of a low-pressure zone behind the rib and a clockwise recirculating flow besides the main flow is therefore formed downstream of the rib. As very fine meshes are arranged around the rib, a very weak anticlockwise vortex can be observed at the back of its lower right corner.

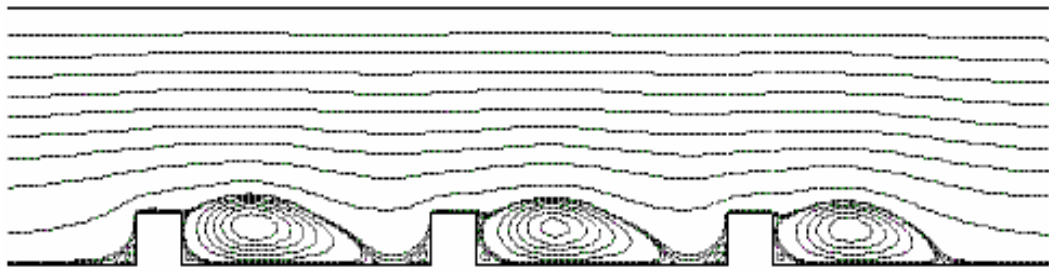


Fig. 8-3 Streamlines around the ribs at $Re = 10,400$

Figure 8-4 presents the local Nusselt number distribution around the ribs at $Re = 10,400$, where the peripheral distance is started to measure from the left lower corner of a rib. Two maximum values are obtained around the rib: one is around the rib's left top corner (point B) and another is immediately in front of the next rib (point O). They are formed by the impact of the main flow at the vicinity of the rib, the reaction of the reattachment of the main flow to the bottom floor and the separation of the recirculating flow behind the rib.

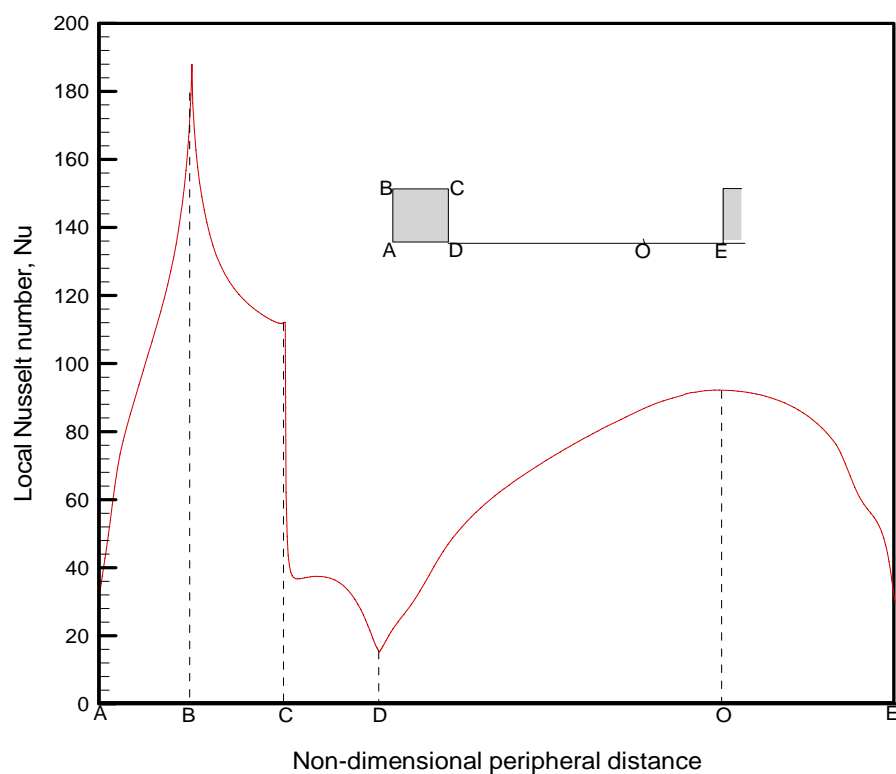


Fig. 8-4 The local Nusselt number distribution around the rib at $Re = 10,400$

The corresponding isothermal lines around the ribs are presented in Fig. 8-5. As indicated from Figs. 8-4 and 8-5, it is obviously seen that the secondary flow in the downstream region of the rib affects the temperature field significantly. Very rapid temperature gradients are observed around the corners of the rib, where the turbulent flow has been significantly enhanced by the existence of the ribs.

8.6.2 Smooth equilateral triangular duct

The secondary flow velocity vectors predicted by applying the RSM in a smooth equilateral triangular duct in the fully developed region are shown in Fig. 8-6, which are in good agreement with those suggested by Aly et al [1978]. In a turbulent flow,

the secondary flow motions are generated essentially by the gradients of the normal turbulent stresses. The turbulent shear stresses also play an important role in generating the secondary flow motions. The driving forces are concentrated towards the regions close to each corner, however, these secondary flows are not observed under laminar flow conditions.

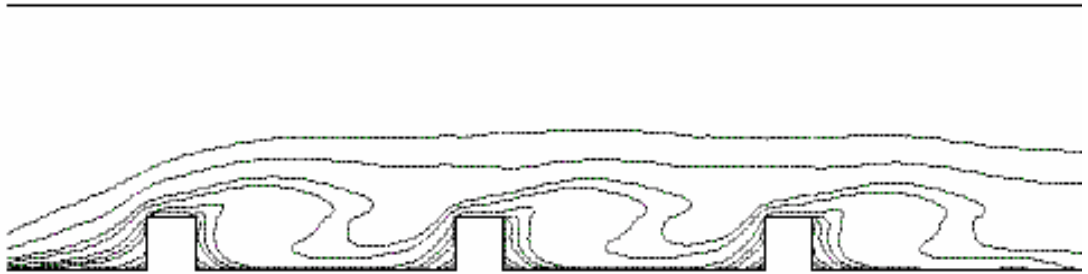


Fig. 8-5 The isotherms around the ribs at $Re = 10,400$

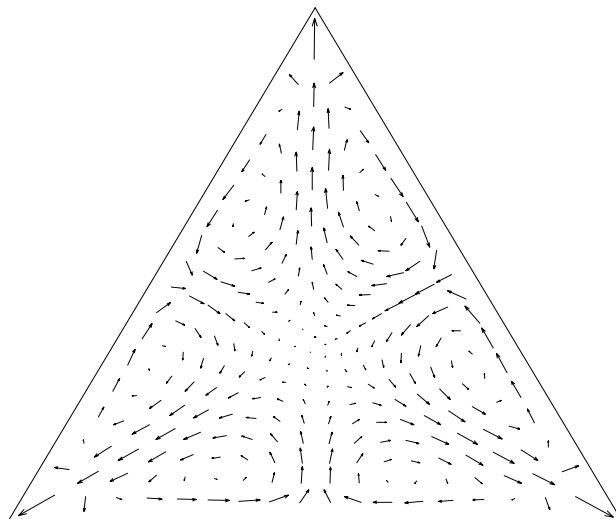


Fig. 8-6 Velocity vectors in the cross section of an equilateral triangular duct at $Re = 10,400$

The normal stresses along the bisector lines (such as **AB** as shown in Fig. 8-1(b)) are presented in Fig. 8-7, where the transport equations of the Reynolds stresses are solved. Expressions for the normal stresses are different from each other, since the diffusion terms are component dependent and therefore lead to different results for each of the Reynolds stresses. It can be used to explain the formation of secondary flows in the triangular duct.

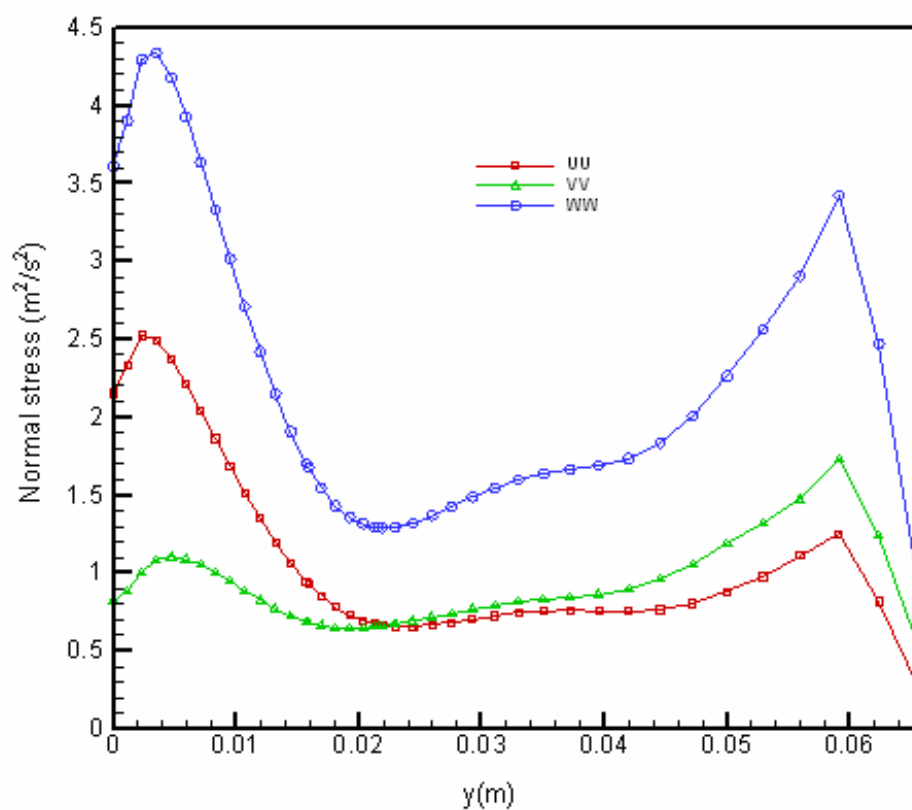


Fig. 8-7 Normal stresses along the bisector lines of an equilateral triangular duct at $Re = 10,400$

8.6.3 Comparison

Figure 8-8 shows the predicted average Nusselt numbers of the parallel plates with ribbed bottom surface and of the equilateral triangular duct with smooth internal surfaces, respectively, with $2,980 \leq Re \leq 12,000$. To facilitate comparison, experimental results obtained from equilateral triangular ducts with ribbed (Chapter 4) and smooth [Leung et al. 2001] internal surfaces are also presented on the same diagram. Good agreements are found between the predicted and experimental results in the following two cases: (i) the ribbed parallel plates comparing with the ribbed triangular duct; and (ii) the triangular ducts with smooth surfaces comparing with each other.

Besides the finding of a great enhancement of average Nusselt number being obtained by building uniformly spaced ribs on the internal surfaces of the duct, it is also interesting to note that the configuration of the ribbed parallel plates, even though without the existence of the corner geometry, is able to simulate closely the forced convection characteristics in the triangular duct with internal ribbed surfaces. However, the triangular duct with internal smooth surfaces gives significantly lower predicted heat transfer results than the experimental results obtained from the ribbed triangular duct. A conclusion can thus be drawn that the effect of the additional ribs on the forced convection in the triangular duct is far more significant than that of the duct sharp corners.

In addition, though the sharp corners of the triangular duct create significant secondary flows, which lower its heat transfer performance to a certain extent, however, such negative effect diminishes as the Reynolds number increases. When

the Reynolds number of a fully turbulent flow becomes high enough to counteract this negative effect caused by the corner geometry, such as $Re \geq 10,400$, it becomes slightly important. It can therefore be proposed that the parallel plate model with ribbed bottom surface is more capable to simulate the fully turbulent flow and thermal characteristics of the ribbed equilateral triangular duct, rather than the smooth equilateral triangular duct model. In other words, the simplified parallel plate model is rather sufficient to simulate the ribbed triangular duct at high Reynolds numbers; hence a much more complicated and time-consuming three-dimensional ribbed triangular duct model can be avoided to apply.

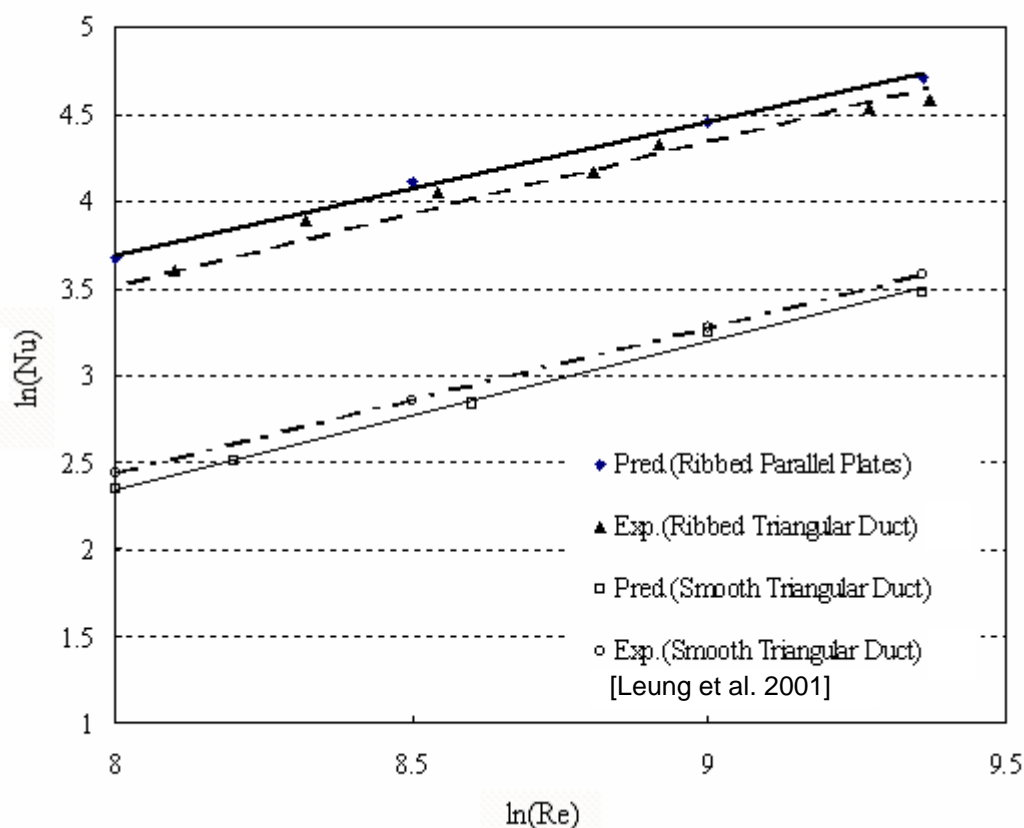


Fig. 8-8 Comparison of experimental and predicted Nu 's

8.7 Summary

The three-dimensional forced convection characteristics of a turbulent flow following through an equilateral triangular duct with ribbed internal surfaces were simulated via two individual approaches: (1) the axial streamwise section was simulated with a two-dimensional model formed by two horizontal parallel plates with the bottom plate attached with uniformly spaced square ribs; and (2) the transverse cross-sectional plane was simulated with a three-dimensional model formed by an equilateral triangular duct with smooth internal surfaces. Uniform heat flux was applied to the inner walls of both channels. From the present study, following conclusions are obtained:

- Secondary flows in the triangular duct with ribbed internal surface were predicted successfully by using two simplified turbulence models.
 - From the comparison between predicted and experimental results, it was observed that the parallel plate model with ribbed bottom surface was more capable than the smooth triangular duct model to simulate the turbulent flow and forced convection characteristics in the triangular duct with ribbed internal surfaces, even though the effect of the duct's sharp corners on the secondary flows was not included.
 - Uniformly spaced ribs attached on the internal surfaces were able to produce a great enhancement on the turbulent forced convection in a triangular duct, whereas the negative effect provided by the duct's corner geometry on the forced convection diminished at high Reynolds numbers. Therefore, the smooth triangular duct model gave much lower predictions of average Nusselt number than the ribbed triangular duct, especially when the Reynolds number was low.
-
-

- It was concluded that a suitable two-dimensional numerical model was able to simulate well the turbulent flow and forced convection characteristics in a triangular duct with ribbed internal surfaces, for example, the parallel plate model with ribbed bottom surface, such that the application of a much more complicated and expensive three-dimensional model could be avoided.

9 SIMULATION OF TURBULENT FLOW IN THE RIBBED TRIANGULAR DUCT WITH 3-D MODELS

In the former chapter, numerical simulation of the three-dimensional (3-D) triangular duct with ribbed internal surfaces was approached by dividing the system into two parts: each of them was simulated with a relatively simple turbulence model. The first model was consisted of two parallel plates with the bottom surface attached with uniformly spaced square ribs, which was used to simulate the longitudinal plane of the ribbed triangular duct. The second model was consisted of a triangular duct with smooth internal surface, which was applied to simulate the transverse cross-sectional plane of the ribbed triangular duct. Effects of the ribs and sharp-corners of the triangular duct on thermal and hydrodynamic performances of the triangular duct were reasonably well predicted. However, effects of the secondary flow generated in the complicated triangular duct system with additional attached ribs were yet uncertain. This problem was attempted to tackle by flow visualization method as described in Chapter 6. Though basic contours of the velocity fields in the triangular duct had been obtained, however, because of the difficulties existing in the experimental approach, numerical simulation method is expected to develop. In addition, based on the results obtained from the experimental study, perhaps, it may be mature to develop a more accurate 3-D numerical model to simulate the flow patterns and hence the forced convection characteristics in the triangular duct with uniformly spaced ribs fixed on its internal surfaces.

In this chapter, attention was paid to solving the problems encountered during the development of the secondary flow, as well as attaining qualitative information on the flow field. It was aimed to provide a better understanding of the forced convective turbulent flow in the triangular duct with internal ribbed surfaces. It was also expected to visualize the turbulence-generated secondary motions of flow recirculation, flow detachment and reattachment, as well as formation of the vortex in the vicinity of the ribs.

9.1 Three-Dimensional (3-D) Turbulence Model

9.1.1 Development of 3-D Model

Three-dimensional Reynolds Stress Model (RSM) was applied for present simulation of an incompressible, fully developed, turbulent flow through a triangular duct with smooth or ribbed internal surfaces. The governing equations could be written as:

$$\frac{\partial u}{\partial x} + \frac{\partial v}{\partial y} + \frac{\partial w}{\partial z} = 0 \quad (9-1)$$

$$u \frac{\partial u}{\partial x} + v \frac{\partial u}{\partial y} + u_k \frac{\partial u}{\partial z} = -\frac{1}{\rho} \frac{\partial P}{\partial x} + \nu \left(\frac{\partial^2 u}{\partial y^2} + \frac{\partial^2 u}{\partial z^2} \right) - \frac{\partial \overline{uv}}{\partial y} - \frac{\partial \overline{uw}}{\partial z} \quad (9-2)$$

$$u \frac{\partial v}{\partial x} + v \frac{\partial v}{\partial y} + u_k \frac{\partial v}{\partial z} = -\frac{1}{\rho} \frac{\partial P}{\partial y} + \nu \left(\frac{\partial^2 v}{\partial y^2} + \frac{\partial^2 v}{\partial z^2} \right) - \frac{\partial \overline{v^2}}{\partial y} - \frac{\partial \overline{vw}}{\partial z} \quad (9-3)$$

$$u \frac{\partial w}{\partial x} + v \frac{\partial w}{\partial y} + u_k \frac{\partial w}{\partial z} = -\frac{1}{\rho} \frac{\partial P}{\partial z} + \nu \left(\frac{\partial^2 w}{\partial y^2} + \frac{\partial^2 w}{\partial z^2} \right) - \frac{\partial \overline{vw}}{\partial y} - \frac{\partial \overline{w^2}}{\partial z} \quad (9-4)$$

$$u \frac{\partial T}{\partial x} + v \frac{\partial T}{\partial y} + w \frac{\partial T}{\partial z} = \alpha \left(\frac{\partial^2 T}{\partial y^2} + \frac{\partial^2 T}{\partial z^2} \right) - \frac{\partial \bar{v}t}{\partial y} - \frac{\partial \bar{w}t}{\partial z} \quad (9-5)$$

In the above equations, the Buoyancy-induced effects were neglected. Code FLUENT was used to perform the calculations.

A typical mesh distribution of the triangular duct is shown in Fig. 9-1, where three ribs are fixed in the middle of the grid mesh (shaded parts). The rib size to duct's hydraulic diameter ratio was set to $H/D = 0.2$ (corresponding to the rib size applied in the former study in Chapter 8). Nonuniform hexahedral grids were adopted, since they were able to fit better into the cross-sectional plane of the triangular duct. The mesh was of sufficient mesh density to capture the sharp gradients and boundary layers near the fluid-solid interfaces. Confirmation of grid independence of the model was conducted by increasing the mesh density and applying various mesh gradings. The process continued until further refinement showed a difference of less than 1% in two consecutive sets of results. In addition, to enhance the calculation

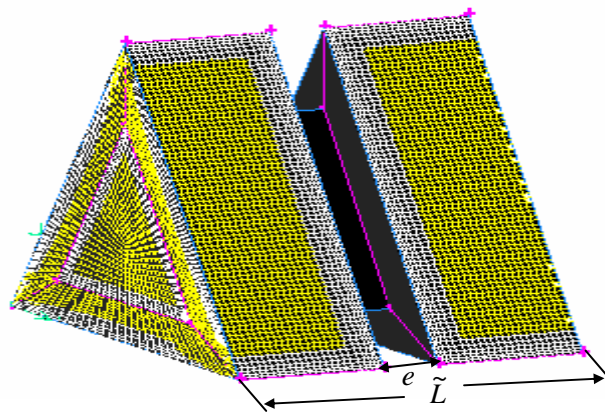


Fig. 9-1 The mesh distribution of the ribbed triangular duct

accuracy, a second-order upwind scheme was adopted and a very fine mesh density was applied around the ribs and in the near-wall regions. The y^+ value of the first grid point adjacent to the wall was less than 5.

9.1.2 Assumptions

The following assumptions were applied in the present study:

- The flow was incompressible.
- The turbulent flow was under steady-state condition.
- The turbulent flow was under regular periodic-flow conditions.
- Buoyancy-induced effects were negligible.
- Heat conduction in the flow direction was neglected.
- Thermal-physical properties of both fluid and solid were constant.
- The fluid was evenly distributed among channels and a plug flow was due to the high turbulence in the channels.

9.1.3 Periodic Conditions

Again, periodic flow conditions for the present fully developed turbulent flow were imposed at the inlet and outlet of the duct. Constant pressure drop along the duct and identical temperature profiles with a constant increment as shown in Equations (8-8) and (8-9), were applied. The mass flow rate ($\dot{m} = 0.11 \text{ kg/m}^3$) was specified to create a flow field and achieve the fully developed state. The Reynolds number, which was based on the mass flow rate and constant at $Re = 10,400$, was coupled to the non-periodic pressure gradient. The reasons to assume periodic flow had been presented in the previous chapter.

$$P = -\beta \frac{x}{\tilde{L}} + P_0 \quad (8-8)$$

$$T = \frac{\dot{q}}{mC_p} \frac{x}{\tilde{L}} + T_0 \quad (8-9)$$

9.2 Solution Procedures

The local values of variable ϕ (i.e., u , v , w and T) were calculated by using the grid pattern shown in Fig. 9-2, where $\phi_{i,j,k}$ was located at the center of the computational-cell.

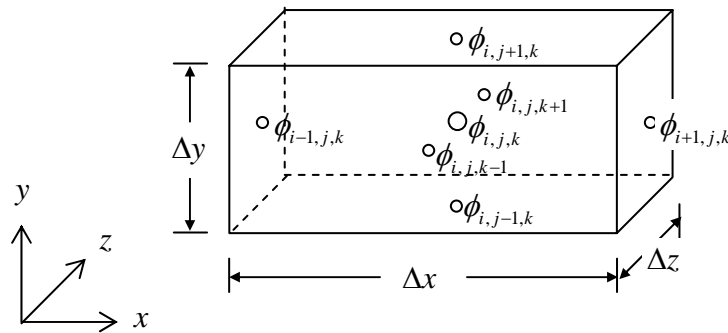


Fig. 9-2 Schematic computational-cell with the nodal grid pattern

A control-volume-based technique was used to discretize the governing equations mentioned in Section 9.1.1 into algebraic forms that would be solved numerically. For Equation (9-2), it could be rewritten as:

$$\begin{aligned}
 & \overline{u}_{i,j,k} \left(\frac{u_{i+1,j,k} - u_{i-1,j,k}}{2\Delta x} \right) + \frac{v_{i,j+1,k} + v_{i,j,k}}{2} \left(\frac{u_{i,j+1,k} - u_{i,j,k}}{\Delta y} \right) + \frac{w_{i,j,k+1} + w_{i,j,k}}{2} \left(\frac{u_{i,j,k+1} - u_{i,j,k}}{\Delta z} \right) \\
 = & \\
 & - \frac{1}{\rho} \left(\frac{\overline{P}_{i+1} - \overline{P}_{i-1}}{2\Delta x} \right) + \frac{(\mu_{eff})_{i,j+1/2,k}}{\rho} \left(\frac{u_{i,j+1,k} - u_{i,j,k}}{\Delta y^2} \right) - \frac{(\mu_{eff})_{i,j-1/2,k}}{\rho} \left(\frac{u_{i,j,k} - u_{i,j-1,k}}{\Delta y^2} \right) + \\
 & \frac{(\mu_{eff})_{i,j,k+1/2}}{\rho} \left(\frac{u_{i,j,k+1} - u_{i,j,k}}{\Delta z^2} \right) - \frac{(\mu_{eff})_{i,j,k-1/2}}{\rho} \left(\frac{u_{i,j,k} - u_{i,j,k-1}}{\Delta z^2} \right) \quad (9-2)'
 \end{aligned}$$

For the pressure-velocity coupling discretization, a suitable algorithm SIMPLE using a relationship between velocity and pressure corrections to enforce mass conservation and to obtain the pressure field, was applied. Assuming known pressures and temperatures, it was possible to get a velocity field from the momentum equations of (9-2), (9-3) and (9-4). The predicted velocity field was then used to solve the pressure correction equation to obtain the corrected values of pressure such that the velocities and pressures could be corrected. The iterative solution process could be repeated for numerous times until the absolute residuals of all the variables were less than 10^{-6} .

9.3 Results and Discussions

Velocity fields were investigated in detail in three typical planes around the ribs in the triangular duct, which were located at the same positions as those visualized in the experimental study in Chapter 6 (i.e. Plane **I**, **II** and **III**, as shown in Fig. 6-2): (a) a Plane **I** (XY plane) which was cross-sectional and perpendicular to the flow-

wise direction at a distance of e beyond the ribs (i.e., $z/e = 1$); (b) a Plane **II** (XZ plane) which was parallel to the bottom plate at a distance of $0.5e$ above the bottom floor (i.e., $y/e = 0.5$), with a width of $c = 3e$; (c) a Plane **III** (YZ plane) which was in the flowwise vertical symmetry of the duct right after the ribs (i.e., $x/a = 0.5$), with a width of $c = 3e$. In addition, velocity distributions along the centerlines of these three planes (Line **A**: $x/a = 0.5$ on Plane **I**, Line **B**: $z/c = 0.5$ on Plane **II**, and Line **C**: $z/c = 0.5$ on Plane **III**, as shown in Fig. 9-3) were also studied.

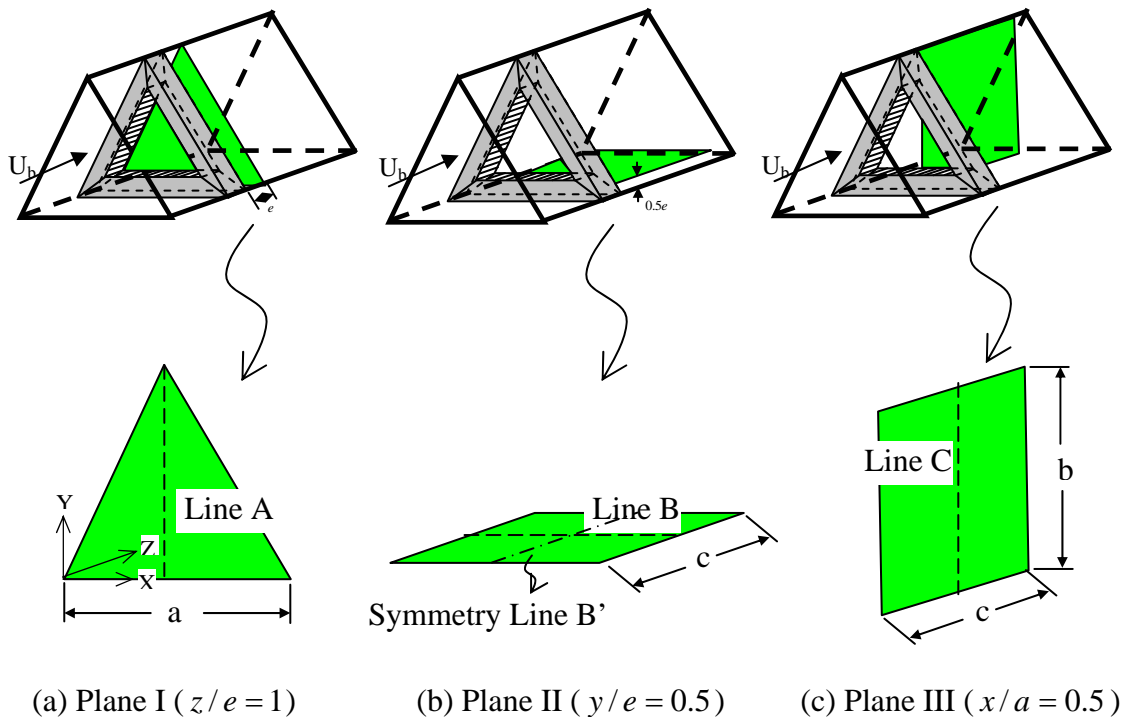


Fig. 9-3 Locations of planes (**I**, **II**, **III**) and lines (**A**, **B**, **C**) in the triangular duct with internal ribbed-surfaces

9.3.1 Velocity Fields and Distributions in Plane I

9.3.1.1 Smooth Triangular Duct

Turbulent flow in a triangular duct with smooth internal surfaces had been analyzed both by experimental and numerical methods as described in Chapters 6 and 8, respectively. To facilitate comparison, the velocity-field results in Plane *I* (XY Plane) obtained from both methods are presented together here in Fig. 9-4.

Secondary flows driven by the non-zero gradients of the normal Reynolds stresses in Plane *I*, which is perpendicular to the mean flow direction, are developed. Two counter-rotating vortices are formed in each corners of the triangular duct, which is consistent with the findings suggested in a previous investigation of Masoud et al. [2001]. However, the vortices around these corners are not measured by PIV technique. Perhaps, it is due to the perspective error of the PIV, which has contaminated the measurements in this plane. Insufficient quality of the view of the velocity field may also contribute to it. The appearance of this error occurs when the out-of-plane components of the velocity are large compared to the in-plane components, which can be seen from the predicted velocity field in Fig. 9-4(b). In order to express the vortices in the corners, the corresponding vorticity maps are presented in Fig. 9-4. Results obtained from both PIV visualization and RSM simulation studies present a good agreement. The six vortices carry high momentum fluid towards the three corners along the bisectors of the duct, and then outwards to the middle plane along the walls.

Figure 9-5 shows the velocity distribution ($U_1 = \sqrt{u^2 + v^2}$) along the vertical centerline in Plane *I* (i.e. XY Plane, Line **A**: $x/a = 0.5$). There are two maximum

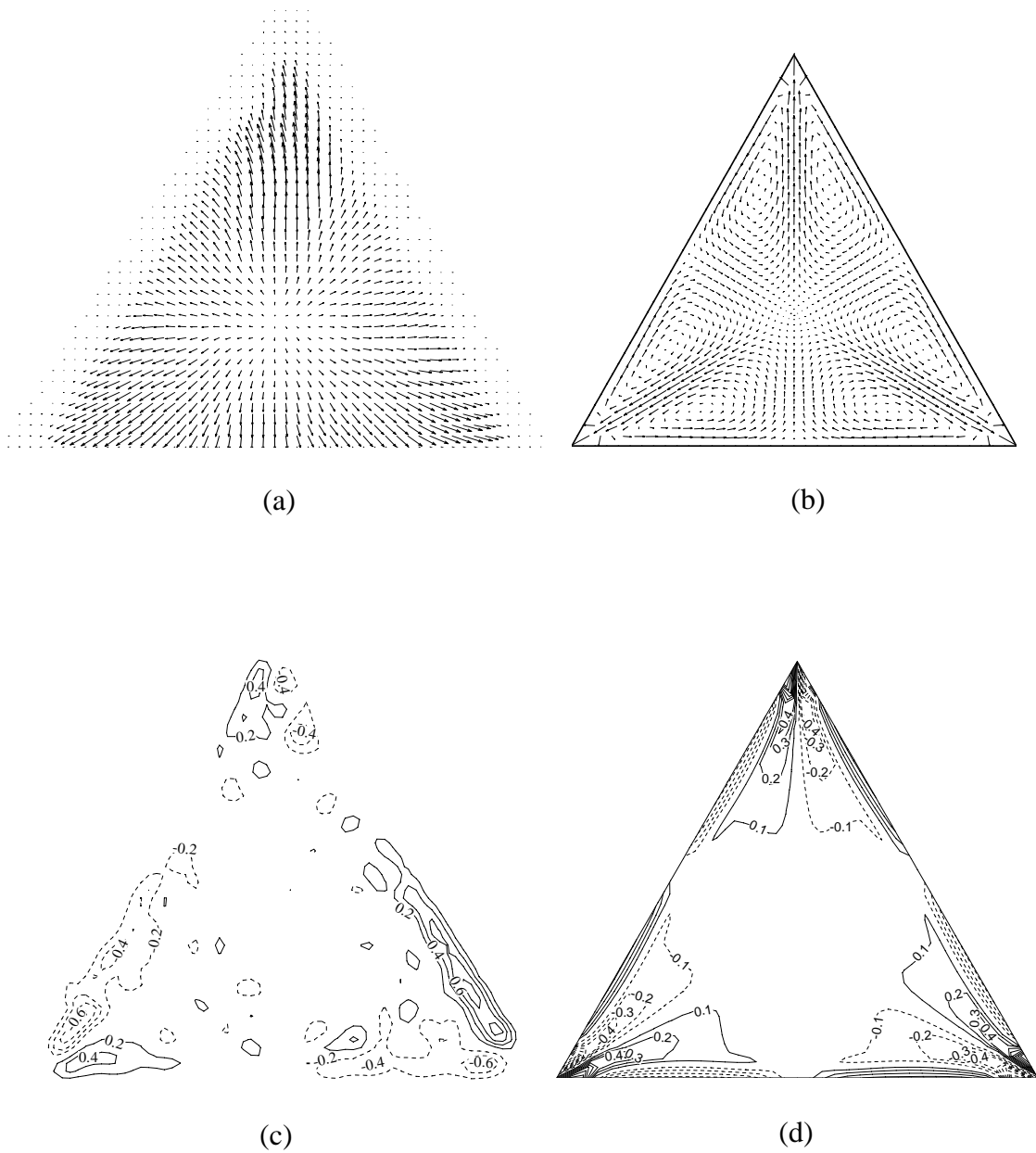
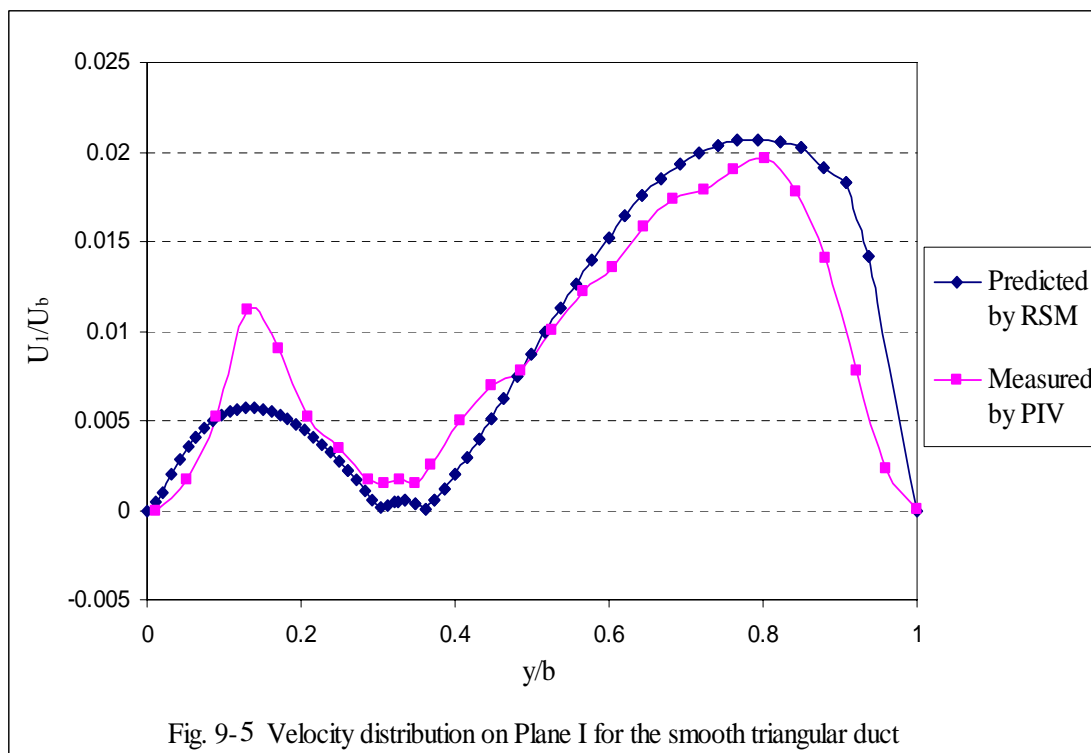


Fig. 9-4 Velocity profiles in Plane I of the smooth triangular duct as, (a) measured by PIV in Chapter 6; (b) predicted by RSM in Chapter 8, and corresponding vorticity maps as, (c) measured by PIV in Chapter 6; (d) predicted by RSM in Chapter 8.

values detected: the first one is close to the triangle corner ($y/b = 1$) and the second one is close to the bottom ($y/b = 0$). A trough is found to appear at about $y/b =$

0.33, which is corresponding to the maximum normal Reynolds stress \overline{ww} . On the one hand, the non-zero Reynolds stress difference drives the secondary flows to accelerate from the trough along the corner-bisector: the first one is driven towards the corner and the second one moves towards the bottom. On the other hand, the secondary flows decelerate until they turn outwards along the walls close to the corner and the bottom, and move towards the middle plane of the duct. Such secondary flows counteract the incoming flow. Thus two maximum values are occurred with the one near the corner much larger than that one near the bottom, as explained previously. However, the experimentally measured values are slightly higher than those predicted numerically for the maxima close to the triangular duct's corner, with an average deviation of 0.02% of the bulk velocity observed.



9.3.1.2 Ribbed Triangular Duct

The velocity profiles and corresponding vorticity maps at the same Plane *I* (XY Plane) but for the triangular duct with internal ribbed-surfaces are shown in Fig. 9-6. The experimentally measured results presented in Fig. 6-6 are also provided to facilitate comparison. A disturbed flow field is found in the downstream area of the ribs. The counter-rotating vortices are also observed, which move from the corners towards the locations right above the ribs. Its occurrence is due to the strong three-dimensional motions of the secondary flows at the locations beyond the ribs. In addition, sudden expansion of the cross-sectional flow area leads to the acceleration of the secondary flows, which also contributes to the occurrence of this phenomenon.

The corresponding velocity distribution along the vertical centerline in this plane (i.e. XY Plane, Line **A**: $x/a = 0.5$) is shown in Fig. 9-7. A much larger variation in velocity distribution is observed when the flow characteristic of a ribbed triangular duct is compared to that of the smooth triangular duct as shown in Fig. 9-5. As explained previously, it is due to the acceleration of the secondary flows, which are resulted from the sudden expansion of the cross-sectional flow area and the resultant low-pressure region right after the ribs.

However, because of the disturbance caused by the attached ribs, it is interesting to see that a sharp decrease occurs at each of the two reversing secondary flows before they reach their maximum values, respectively, as compared to results obtained from the smooth triangular duct as shown in Fig. 9-5. In addition, a small extremum value is predicted numerically by using the RSM at each corner along the bisector, but it is not measured by applying the PIV technique. Closer views near to the walls need to

9 SIMULATION OF TURBULENT FLOW IN THE RIBBED TRIANGULAR DUCT WITH 3-D MODELS

be taken in the visualization study or perhaps, a three-dimensional Stereo PIV system should be applied instead of the present two-dimensional PIV system.

Besides, the numerical predictions are slightly higher than the experimental

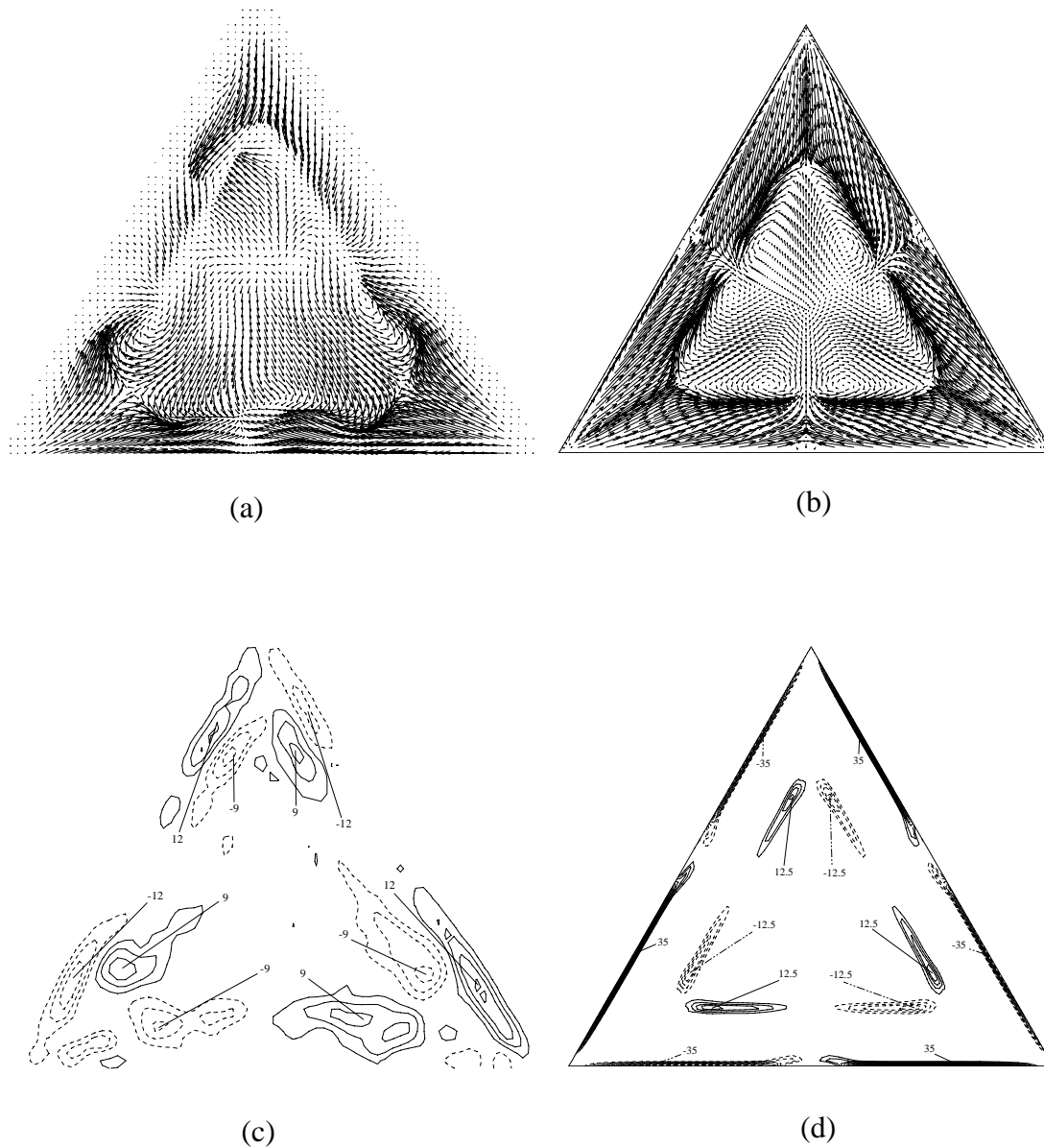
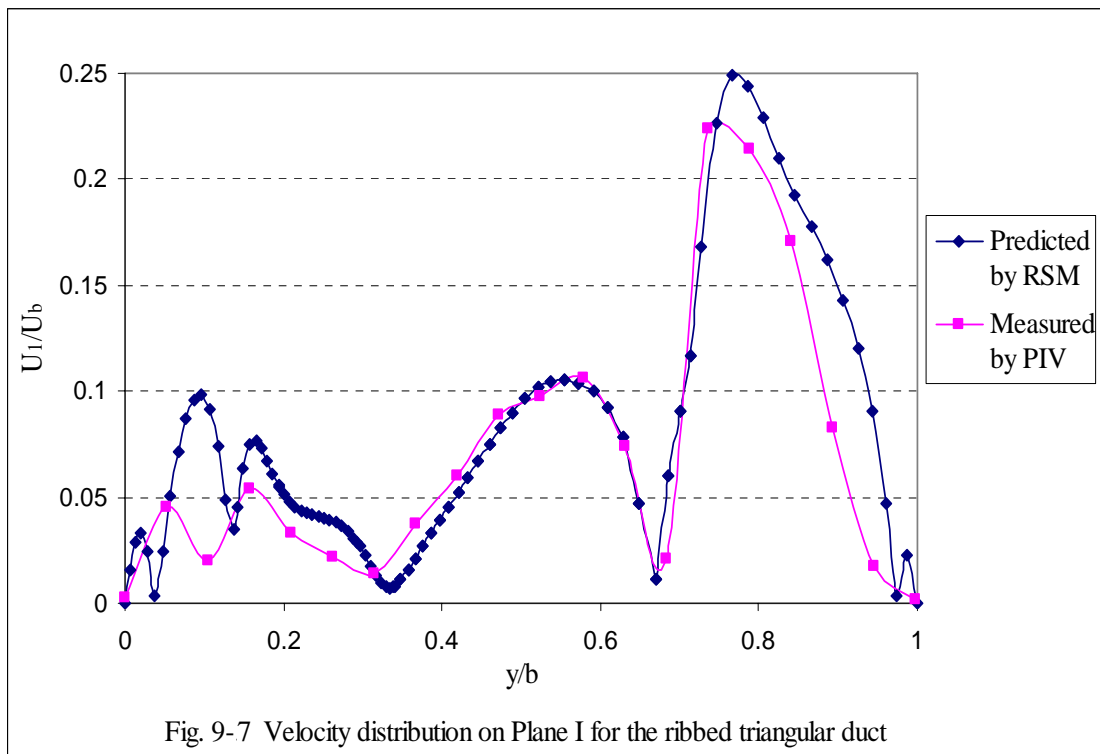


Fig. 9-6 Velocity profiles in Plane I of the ribbed triangular duct as, (a) measured by PIV in Chapter 6; (b) predicted by RSM in Chapter 8, and corresponding vorticity maps as, (c) measured by PIV in Chapter 6; (d) predicted by RSM in Chapter 8.



measured results, especially at the extremum points. An average deviation of 0.23% of the bulk velocity between the experimental and numerical results is observed.

9.3.2 Velocity Fields and Distributions in Plane II

9.3.2.1 Smooth Triangular Duct

The numerically predicted flow patterns in Plane II (XZ Plane) for the smooth triangular duct are presented in Fig. 9-8. Because of the symmetrical geometry of the triangular duct, the velocity vectors are observed to distribute evenly and symmetrically with the centerline of $x/a = 0.5$, though the magnitude of the velocity near the sides ($x/a = 0$ and 1) is much smaller than those in middle. It is due to the effects of the duct walls on the fluid flow. A good agreement with the

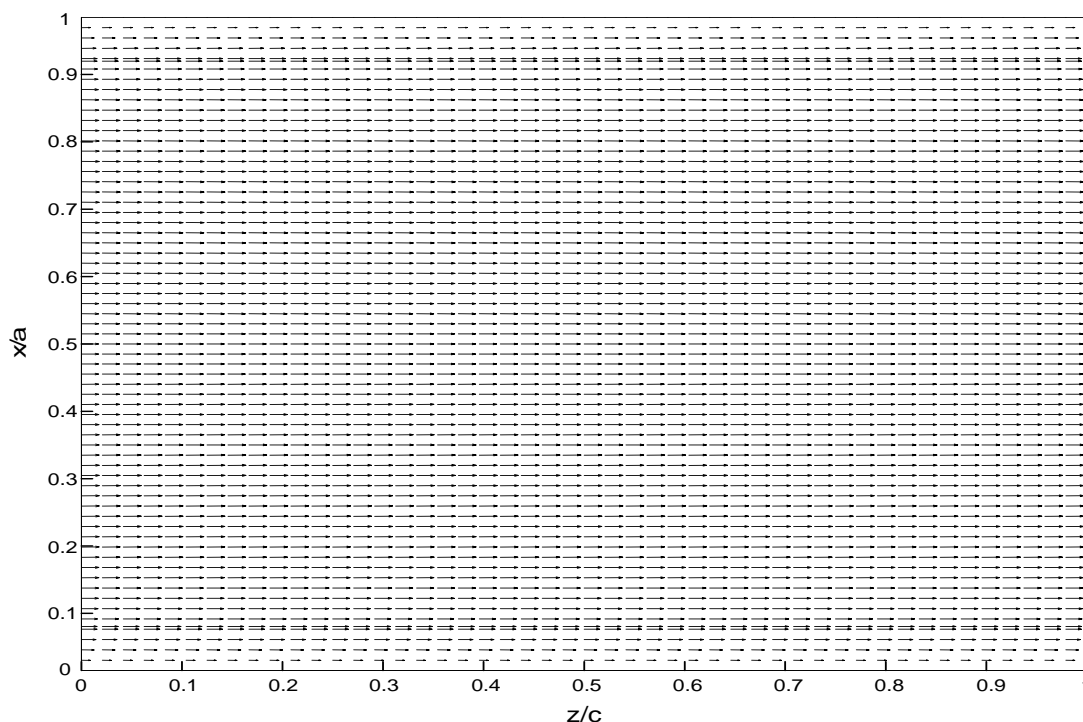
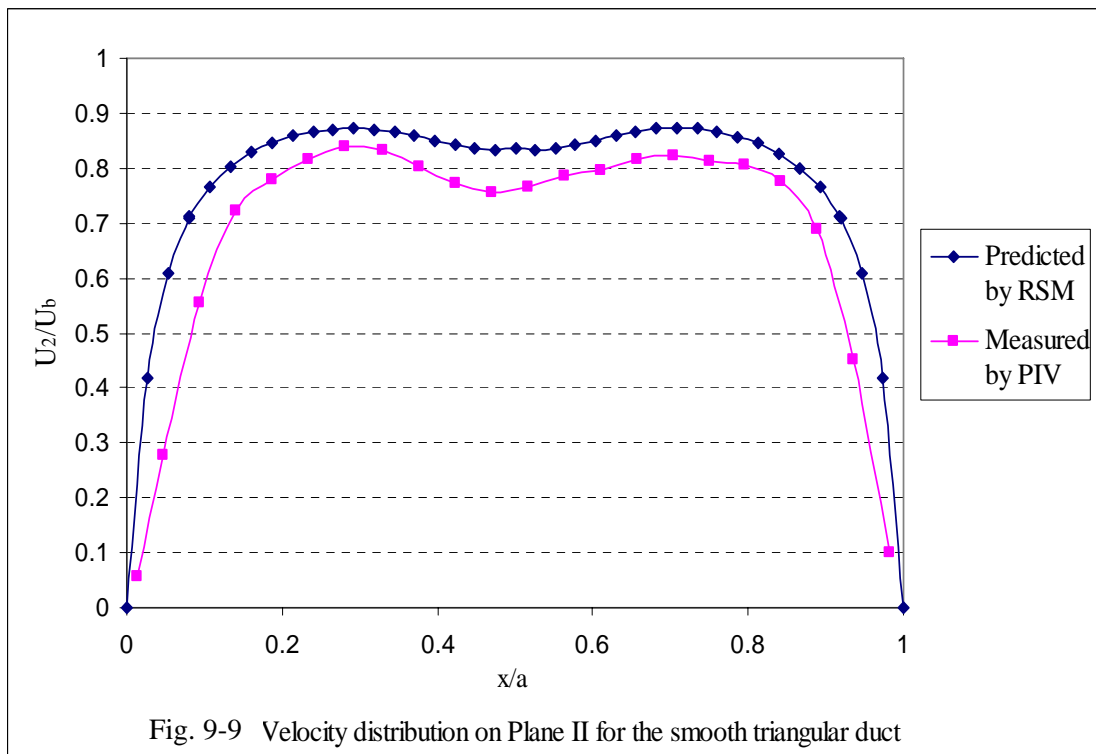


Fig. 9-8 Velocity profile in Plane II of the smooth triangular duct

measured results as presented in Fig. 6-7 is obtained for the flow patterns. To clearly observe the flow characteristics in the Plane *II*, the velocity distribution ($U_2 = \sqrt{u^2 + w^2}$) along its center line (i.e. Line **B**: $z/c = 0.5$, as shown in Fig. 9-3) is presented in Fig. 9-9. Symmetrical distribution of the velocity is observed again, however, the results are slightly over-predicted by using the RSM with an average deviation of 8.34% of the bulk velocity.

9.3.2.2 Ribbed Triangular Duct

The secondary flow fields in the Plane *II* of the ribbed triangular duct obtained from both experimental (i.e. Fig. 6-8 of Chapter 6) and numerical studies are shown in Fig. 9-10.



Two large vortex cells are predicted to exist symmetrically at the symmetry line of this plane (i.e. XZ Plane, Line **O**: $x/a = 0.5$), which are in good agreement with the results obtained in the experimental investigation. As explained in Chapter 6, the vortices are generated as a result of the difference in the non-zero normal Reynolds stresses ($\overline{v'v'}$), which is symmetrical about the symmetry Line **O**. The effects of rib-induced low-pressure zone behind the ribs also contribute to it. Compared to the flow patterns obtained from the smooth triangular duct as shown in Fig. 9-8, it is suggested that the three-dimensional flow structures are generated after the introduction of the attached turbulence-promoting ribs. In addition, it is observed that the vortices are fully developed at a distance of “ $3e$ ” (i.e. $1c$) away from the ribs.

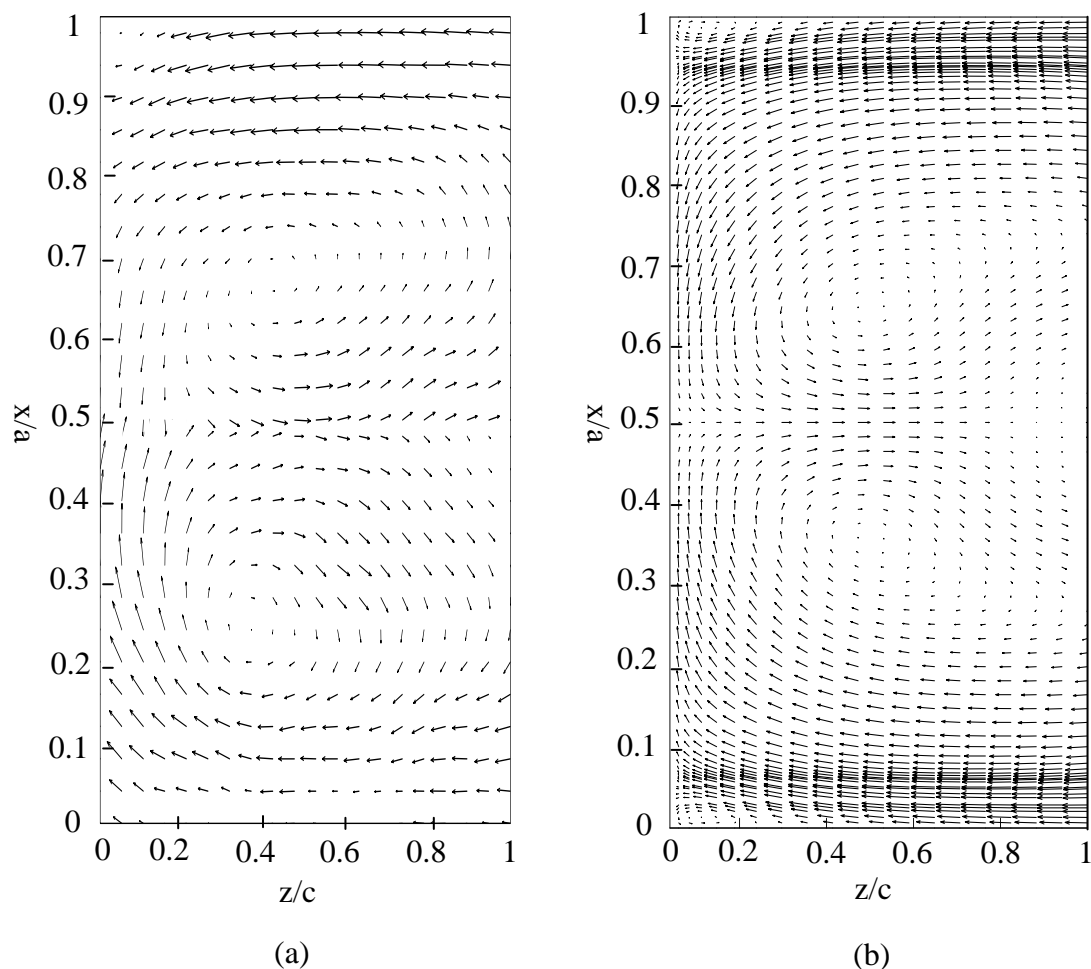
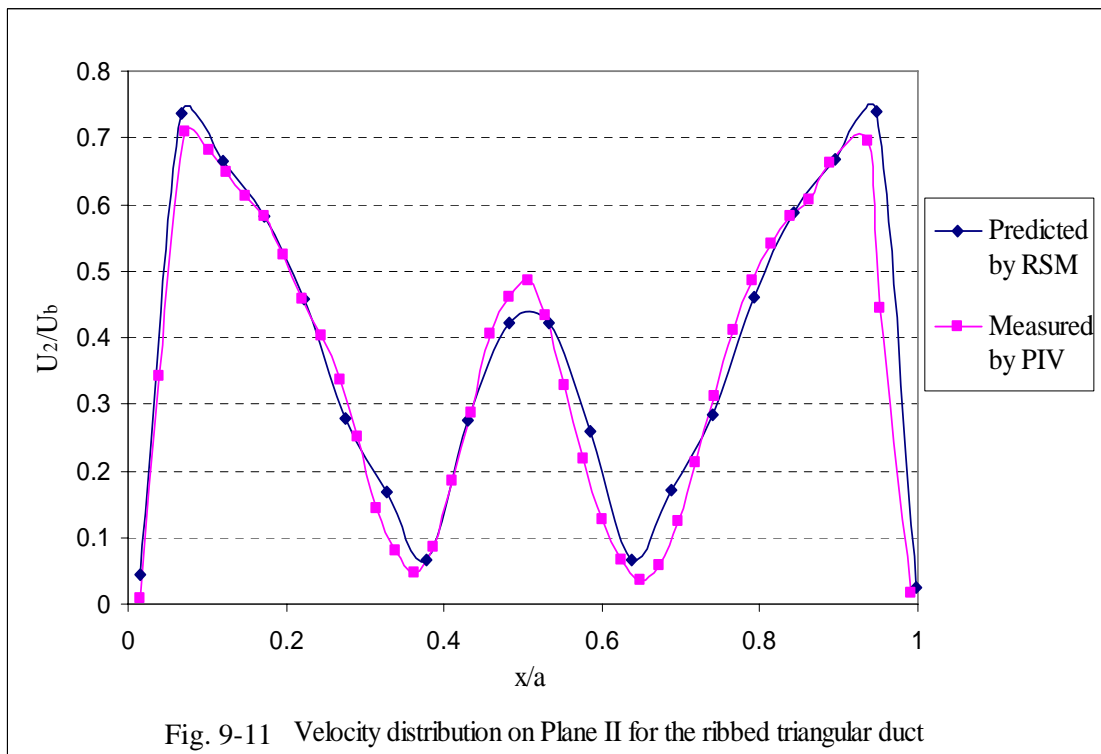


Fig. 9-10 Velocity profiles in Plane II of the ribbed triangular duct as, (a) measured by PIV; (b) predicted by RSM.

Considering the velocity distributions along the corresponding centerline of this plane (i.e. XZ Plane, Line **B**: $z/c = 0.5$), as shown in Fig. 9-11, it is found the symmetrical characteristic occurs again. However, the velocities in the middle of the plane are greatly lowered compared to those in the smooth triangular duct presented in Fig. 9-9. There are two minimum values observed at the center-locations of the two vortices. A deviation of 1.66% of the bulk velocity between results from these two methods is observed.



9.3.3 Velocity Fields and Distributions in Plane III

9.3.3.1 Smooth Triangular Duct

A rather linear flow pattern of the velocity fields in Plane III (YZ Plane) of the smooth triangular duct is detected, as shown in Fig. 9-12. Velocity vectors around the corners (i.e. $y/b = 1$) are much smaller than those near the bottom plate (i.e. $y/b = 0$). It can be concluded that the effect of the duct corner on the fluid flow is much more significant than that of the duct wall. Much larger velocity vectors are detected around the location of $y/b = 0.33$, which corresponds to the occurrence of the maximum normal Reynolds stress $\overline{w'w'}$. A reasonably good agreement is

achieved when the numerical predicted values are compared to those measured by the PIV technique as presented in Fig. 6-9 of Chapter 6.

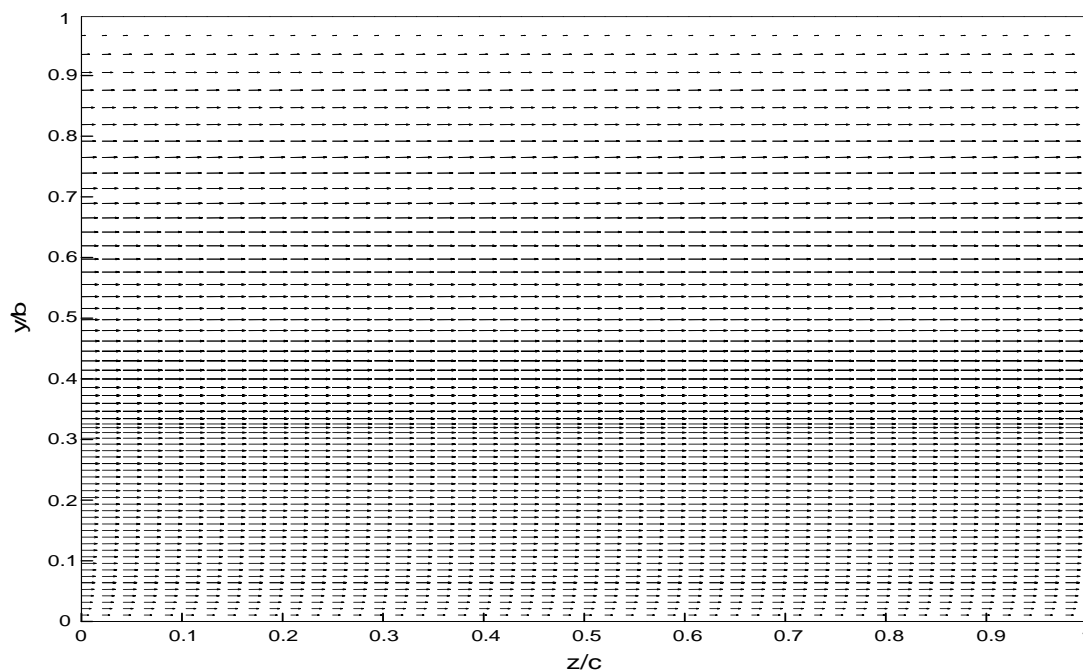


Fig. 9-12 Velocity profile in Plane III for the smooth triangular duct

9.3.3.2 Ribbed Triangular Duct

To facilitate a better observation of the flow patterns in Plane *III* (YZ Plane) during the PIV measurements being conducted, an enlarged region between two consecutive ribs with a width of $2c$ (i.e. $\sim 6e$) was investigated. The vertical plane *III* behind the ribs could be divided into two parts, which were enlarged and presented in Fig. 9-13: upper Part *1* with ' $2e$ ' in height and lower Part *2* with ' $1e$ ' in height, respectively. Compared to the experimentally measured results as presented in Fig. 6-11 of

Chapter 6, good agreements are obtained (“*upper part*” in the experimental study was referred to “*Part 2*” in the numerical simulation study here, whereas “*lower part*” in the experimental study was referred to as “*Part 1*”).

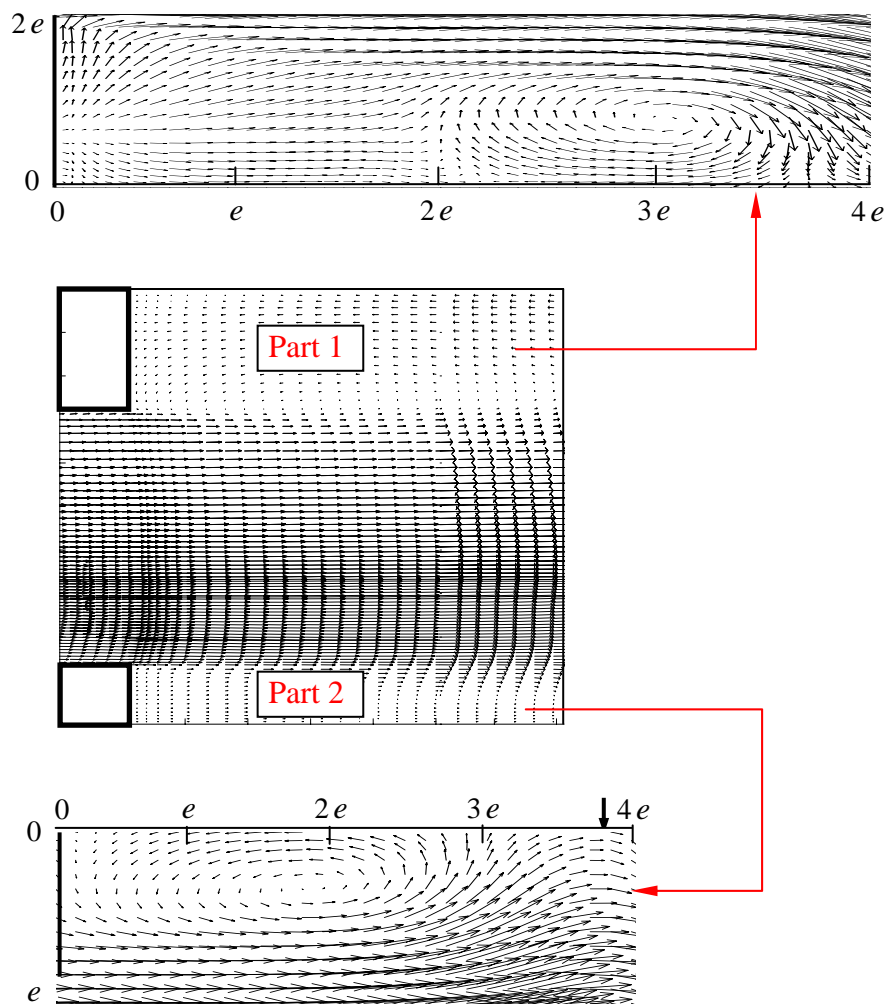


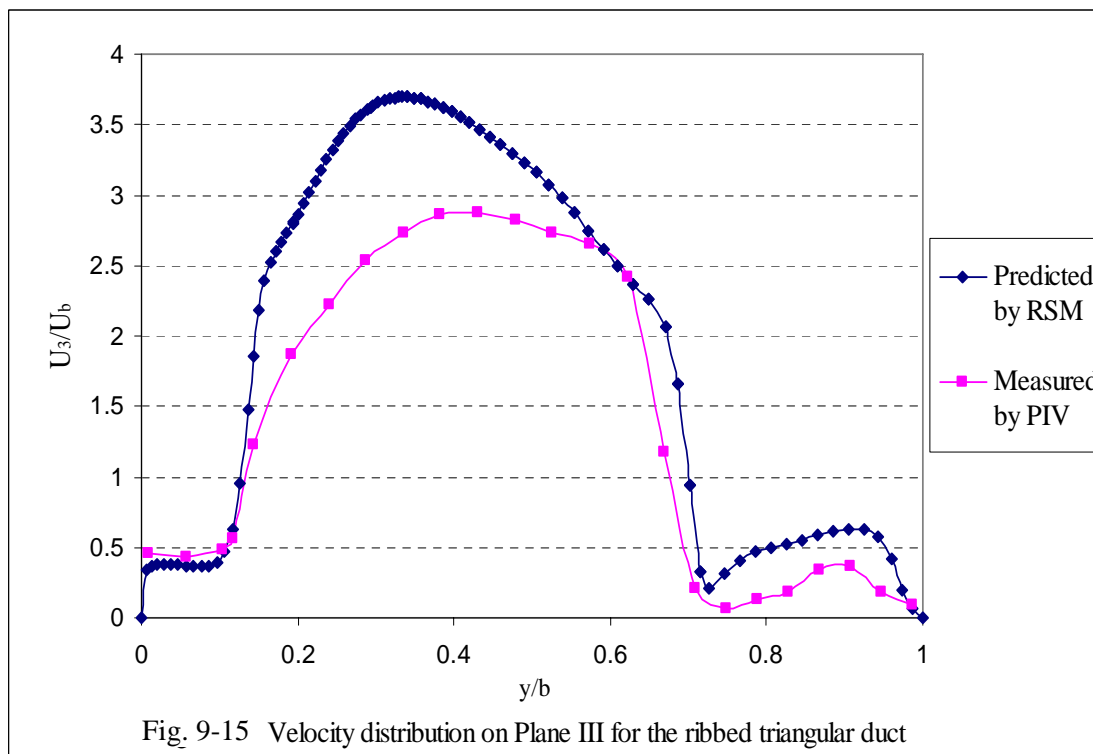
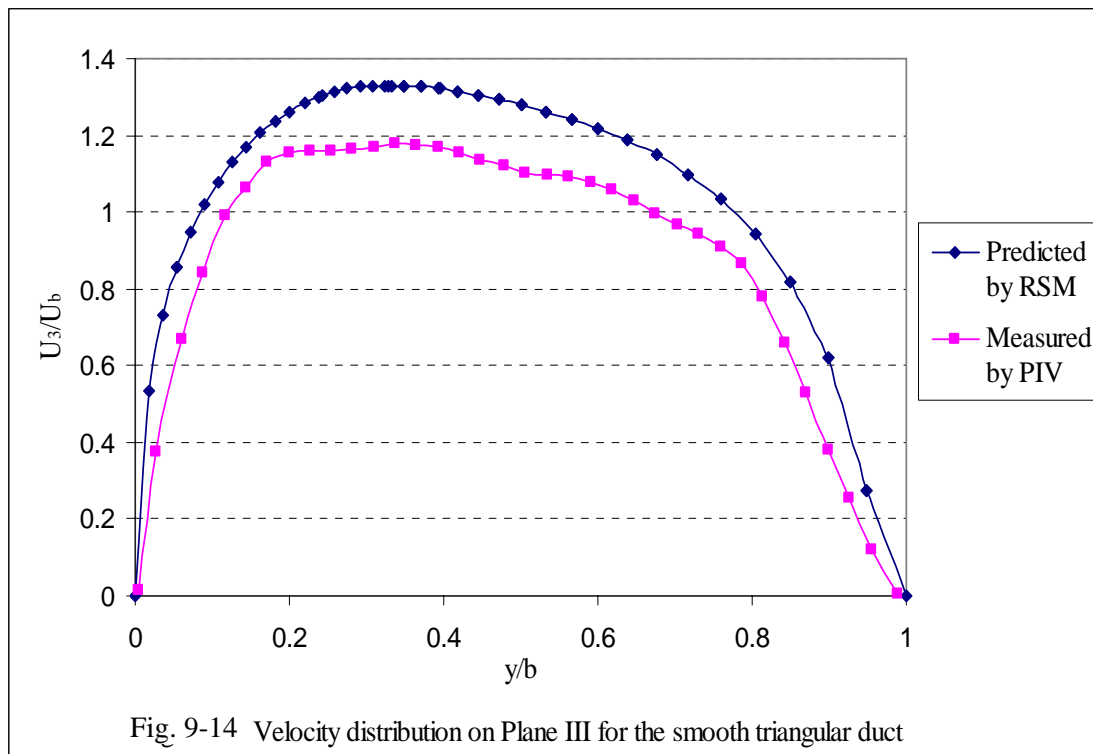
Fig. 9-13 Velocity profile in Plane III for the ribbed triangular duct

In fact, due to the sudden expansion of the flow field and the occurrence of the low-pressure region at the backside of the ribs, separation zones are developed behind the ribs. It is noted that the rib-induced high turbulence intensities and large velocity gradients in this region also contribute to such separations. Vortices are predicted to form behind the ribs. Through the secondary flow's detachments from the main flow downstream the ribs are well displayed in both Parts 1 and 2, the flow reattachment to the bottom surface is only observed for Part 2. Since in Part 2, the 'block' height is same as the 'rib' size, namely, e , so the 'block' spacing to 'block' height ratio was $S_r/e = 6.33$; while in Part 1, because of the different alignment, the 'block' height was double of the rib size, leading to a 'block' spacing to 'block' height ratio of $S_r/2e = 3.17$. As discussed in [Hishida, 1996], when the rib's spacing-to-height ratio was less than 5, a recirculating flow was formed in the cavity between two consecutive ribs and no flow reattachment could be achieved, which agreed well with the finding in Part 1. Moreover, in Part 2, the main flow is observed to reattach to the bottom floor ($y/b = 0$) at the location (shown by the solid arrow in Fig. 9-13) about "3~4 e " from the backside of the upstream rib as shown by the solid arrows in Fig. 9-13, which is consistent with the finding obtained through the experimental visualization. The vortex formed behind the rib is about 2/3 of the rib's height.

Compared to flow patterns obtained from the smooth triangular duct for the same plane III (as shown in the Fig. 9-12), it can be concluded that the rib-induced turbulences: detachment of the secondary flow and reattachment of the main flow, are accounted for the enhancement of the forced convective turbulent flow performance of the triangular duct.

Figures 9-14 and 9-15 show the velocity distributions ($U_3 = \sqrt{v^2 + w^2}$) along the line of Plane *III* (i.e. YZ Plane, Line **C**: $z/c = 0.5$) for the smooth and ribbed triangular ducts, respectively. The results predicted by using the RSM are slightly higher than those measured by the PIV technique. Deviations between results from the experimental and numerical methods are found to be 20.69% and 49.15% of the bulk velocity, respectively.

Furthermore, it is interesting to find that maximum values are obtained at the point ($y/b = 0.33$), which are corresponding to the minimum points as shown in Figs. 9-5 and 9-7. As explained previously, it is a result of the maximum normal Reynolds stress \overline{ww} occurred here, which strengthens the velocity component w , while weakens the other two velocity components u and v . Noticed that the magnitude of velocity $U_3 = \sqrt{v^2 + w^2}$ in the middle of Plane *III* of the ribbed triangular duct is much magnified compared to that of the smooth triangular duct, it is due to the sudden expansion of the flow area. For the near rib regions, an even distribution of the velocity is observed. Taking into consideration the distributions of $U_1 = \sqrt{u^2 + v^2}$ in Plane *I* and $U_2 = \sqrt{u^2 + w^2}$ in Plane *II*, which are lowered by the ribs, especially in the near-wall regions, it can be concluded that the rib-induced secondary flow plays an important role at the regions of around the ribs, in the corners and close to the wall, which however has little effects on the main flow. In other words, the additional ribs redistributed the kinetic energy of the turbulent flow, influenced the distributions of the velocity components, and finally affected the thermal and hydrodynamic performances of the triangular duct.



9.4 Summary

The turbulent flow in a horizontal triangular duct with or without internal ribbed surfaces was approached numerically with 3-D Reynolds Stress models. After analyses of the velocity fields as well as the velocity distributions in the three typical planes behind the ribs as shown in Fig. 9-3 were conducted, some conclusions are obtained as follows:

- Turbulence-generated secondary flows were found to occur in the near-wall regions, especially around the triangular duct's corners, via both experimental and numerical studies. Rather complicated flow patterns were induced, which were further disturbed by the additional ribs on the internal surfaces of the duct acting as turbulence promoters. Because of the disturbance provided by the ribs, three-dimensional flow motions were detected beyond the ribs.
- Vortices were developed beyond the ribs. It was due to the sudden expansion of the flow area, which led to the formation of a lower pressure region at the rib's downstream region. The main turbulent flow was also found to separate into two parts at this point: one part became the main stream of the downstream flow, while the other part was detached to form a recirculation zone right behind the rib. Moreover, because of the suppression on the flow from the duct's corners, vortices were also formed there.
- The rib-induced secondary flows, in the forms of recirculating flows and vortices around the ribs, were believed to contribute most to the improvement of the present turbulent flow, either in heat or mass transfer.
- The velocity fields predicted with the RSM were found to match reasonably well

with those measured using the PIV visualization technique. However, for the velocity distributions, the numerically predicted values were slightly higher than the experimental results. A largest deviation was observed in the near-wall regions. Perhaps, it is due to some basic deviations between the numerical and experimental studies. For example, some parameters were assumed constant in the numerical studies, but might not be the cases during the experimental measurements; some fluid and solid properties, which were difficult to measure experimentally, were also assumed with values for the facility of numerical approaching.

- Since the flow patterns around the triangular duct corners had not been clearly visualized due to the present PIV perspective error, further investigation in this micro region is recommended to conduct by applying a three-dimensional Stereo PIV system. It is hoped that this kind of error can be corrected. Besides, the assumptions applied in the simulations as mentioned above also need to be confirmed and improved correspondingly, based on the experimental results.

10 CONCLUSIONS AND SUGGESTIONS FOR FUTURE WORK

10.1 Conclusions

The present study focused on the investigations of forced convection and fluid friction characteristics of a steady-state turbulent flow in an equilateral triangular duct with ribbed or grooved internal surfaces. The whole project was successfully performed through the following five major stages:

1. Experimental investigation of a fully developed turbulent flow in a horizontal equilateral triangular duct with rib-roughened internal surfaces was conducted. Effects of Reynolds number, rib size and rib-to-rib spacing on its thermal and hydrodynamic performances were studied.
2. Experimental investigation of the fully developed turbulent flow in a similar triangular duct but fabricated with uniformly-spaced V-grooves on its internal surfaces was performed. Effects of Reynolds number, V-groove apex angle and groove-to-groove spacing on its thermal and hydrodynamic performances were studied.
3. Experimental visualization of the turbulent flow in a rib-roughened equilateral triangular duct was carried out, where the uniformly-spaced square ribs were applied as turbulence promoters. It was aimed to view the rib-induced secondary flow at the near-wall regions, which consequently affected the thermal

performance of the duct, thus a better understanding of the flow characteristics by attaching ribs to an equilateral triangular duct would be obtained.

4. Numerical simulation of a rib-roughened triangular duct was conducted via two-consecutive parts. The first part focused on the individual effects of the internal ribbed surfaces and the duct's sharp corners on its thermal and hydrodynamic performances. Effects of the Reynolds number on the flow patterns were also studied. The simulations were conducted via two relatively simple turbulence models.
5. The secondary part of the numerical simulation study of the rib-roughened triangular duct concerned with the development of a more complicated three-dimensional turbulence model, in which the conjugated effects of the duct's sharp corners and internal ribbed surfaces on the thermal and hydrodynamic performances of the turbulent flow in the triangular duct were investigated. Development of the secondary flow and the vortices formed around the ribs as well as in the near-wall regions were observed.

After performing the investigations as described in the above five stages, the following conclusions were obtained:

10.1.1 Experimental Measurement of Turbulent Flow in the Rib- or V-Groove-Roughened Triangular Duct

A horizontal air-cooled equilateral triangular duct, with a cross-sectional dimension of $76\text{mm} \times 76\text{mm} \times 76\text{mm}$ (i.e. corresponding to a hydraulic diameter of $D = 44\text{mm}$), was attached or machined with uniformly-spaced square ribs or V-grooves on its internal surfaces. For the ribbed triangular duct, different rib sizes ranged from 5mm

to 9mm (i.e. $0.1136 \leq e/D \leq 0.2045$) and rib-to-rib spacings ranged from 27mm to 110mm (i.e. $3.41 \leq S_r/e \leq 13.93$) were applied. For the V-grooved triangular duct, V-groove apex angles ranged from 45° to 150° and groove-to-groove spacings ranged from 24mm to 54mm (i.e. $0.54 \leq S_v/D \leq 1.23$) were applied. Flow visualization on the similar triangular duct assembly was also conducted by using the PIV technique.

- Application of the roughened internal surfaces, either ribs or V-grooves acting as the roughness elements, was able to improve the forced convection heat transfer between the turbulent flow and the triangular duct effectively, especially for the ribbed triangular duct. However, a higher axial pressure drop along the triangular duct was encountered simultaneously;
 - Ribbed surface had superiority over V-grooved surface not only from the heat transfer enhancement point for the triangular duct (a much better thermal performance was obtained by the ribbed surface with an equivalent pumping power requirement), but also from the practical application limitation point (since the depth of the V-grooves was restricted by the thickness of the plate to be roughened).
 - Optimum rib size and rib-to-rib spacing were obtained at 7.9mm (corresponding to $e/D = 0.1795$) and 57mm (corresponding to $S_r/e = 7.22$), respectively. With the use of the optimum rib arrangement, a best thermal performance of the triangular duct was achieved.
 - Non-dimensional expressions were developed for the determinations of the average Nusselt number and the average friction factor of the equilateral triangular duct attached with uniformly-spaced square ribs of different sizes and
-
-

spacings on its internal surfaces. The relationships were presented in terms of Reynolds number and geometry of the roughness element (i.e. relative rib height and rib-to-rib spacing) as below:

$Nu =$

$$0.0058 Re^{0.5924} \left(\frac{H}{D}\right)^{-2.7515} \left(\frac{S_r}{W}\right)^{1.8414} \exp\left\{-0.7772 \left(\ln\left(\frac{H}{D}\right)\right)^2\right\} \exp\left\{-0.4684 \left(\ln\left(\frac{S_r}{W}\right)\right)^2\right\}$$

$$f = 5.04 Re^{-0.2897} \left(\frac{H}{D}\right)^{1.6224} \left(\frac{S_r}{W}\right)^{1.7842} \exp\left\{-0.4407 \left(\ln\left(\frac{S_r}{W}\right)\right)^2\right\}$$

They were applicable in the range of hydraulic-diameter-based Reynolds number (Re) from 4,000 to 23,000, relative rib size (H/D) from 0.11 to 0.21, and relative rib-to-rib spacing (S_r/W) from 3.41 to 13.93. Here, $H = W = e = 5\text{mm}, 6\text{mm}, 7\text{mm}, 7.9\text{mm}, 9\text{mm}$, and $D = 44\text{mm}$.

- Similarly, non-dimensional relationships for the predictions of average Nusselt number and average friction factor in terms of Reynolds number, V-groove apex angle and groove-to-groove spacing were also developed from the experimental result as shown below:

$$Nu = 0.0485 Re^{0.7204} \left(\frac{S_v}{D}\right)^{-0.1232} \mathcal{G}^{-0.0414}$$

$$f = 0.144 Re^{-0.2809} \left(\frac{S_v}{D}\right)^{-0.3763} \mathcal{G}^{-0.1736}$$

The above two equations were valid when $\vartheta = \frac{\theta}{180}\pi$ and $45^\circ \leq \theta \leq 150^\circ$,

$$5,200 \leq Re \leq 35,500 \text{ and } 0.54 \leq \frac{S_v}{D} \leq 1.23.$$

10.1.2 Numerical Prediction of Turbulent Flow in the Ribbed Triangular Duct

For the numerical simulation studies, the Standard $k - \varepsilon$ Model and the Reynolds Stress Model (RSM) with the standard wall functions were adopted. The SIMPLE algorithm was used in the calculations to handle the pressure-velocity coupling. A finite-volume based code, FLUENT 6.0, was applied for the calculations.

- Development of the turbulence-generated secondary flows was observed in the regions around the rib surface and in the sharp corners of the triangular duct, respectively. The boundary layer of the rib-disturbed turbulent flow became thinner due to the enhanced local turbulence. Therefore, an enhancement of the thermal performance of the triangular duct was obtained.
- Three-dimensional flow patterns of the ribbed triangular duct were identified through both visualization and simulation methods. Vortices were found to develop at the near-wall and rib-surface regions. The rib-induced secondary flows at the near-wall regions of the duct as well as vortices around the rib surfaces were concluded to contribute significantly to the improvement of turbulent flow performance of the present system.
- There was no flow attachment detected for a rib's spacing-to-size ratio of $S_r/e = 3.17$ (i.e. < 4), while for a larger ratio of $S_r/e = 6.33$, the main flow attached to

the bottom surface at a distance of $3\sim 4e$ away from the back surface of the upstream rib.

- The distribution of local Nusselt number over the ribbed surface was investigated and discussed in detail. A decay of the heat transfer rate was detected along the streamwise direction over the ribbed surface. The turbulent flow was considered to be fully developed after flowing over the second rib.
 - The Standard $k - \varepsilon$ Model was able to give a better prediction of the turbulent flow in a two-dimensional ribbed channel than the RSM (the channel was formed by two parallel plates with uniformly-spaced square ribs attached on its bottom inner surface), especially at the downstream region of the rib, where an S-shape distribution of Nusselt number was successfully predicted by the Standard $k - \varepsilon$ Model, but not by the RSM. However, for the more complicated three-dimensional triangular duct with internal ribbed surfaces, the RSM was found to have superiority over the Standard $k - \varepsilon$ Model on the prediction of the turbulence-generated secondary flow.
 - Through simulating the axial and transverse cross-sections of the ribbed triangular duct separately with two relatively simple turbulence models: the former one was simulated by two parallel plates with the bottom plate attached with uniformly-spaced square ribs; whereas the latter one was simulated by an equilateral triangular duct with smooth internal surfaces, predictions agreeing closely with the experimental results were obtained. It was shown that for similar flow systems, the much more complicated and expensive three-dimensional model formed by a triangular duct with internal ribbed surface might be avoided to apply. In addition, it was found that the effect of the ribs on
-

the turbulent flow was much greater than that of the duct's sharp corners. Besides, the negative effect on the thermal performance of a triangular duct provided by its corner geometry would be diminished when the Reynolds number was sufficiently high.

- The velocity fields predicted by the RSM agreed well with those measured by using the PIV visualization technique. However, for the velocity distributions, the numerically predicted results were slightly higher than the experimental results.

10.2 Suggestions for Future Work

After performing a study on the forced convection and fluid friction of the turbulent flow in the triangular duct with internal ribbed or grooved surfaces, some tasks are suggested for future work:

1. Effect of the V-groove depth has not been identified in the present study, which may be a major focus work for further study in this area.
2. Since only the regions behind the ribs were visualized and analyzed in the present study, the flows upstream the ribs should also be investigated in the future work. In addition, the micro-regions close to the walls were not clearly viewed in the present study, further study need to be taken by a closer visualization of these regions to get more quantitative results, or perhaps, a three-dimensional Stereo PIV system should be applied for visualizing.
3. From the numerical study on the local distribution of Nusselt number over the ribbed surfaces, sharp variations around the rib's corners were commonly

obtained. It may be due to the use of relatively coarse mesh around these regions. Therefore, an even finer grid density should be adopted around the rib's corners, thus prediction of the Nusselt number distribution over the ribbed surface can be more accurate.

4. The numerical predicted results obtained by the three-dimensional RSM present higher velocity distributions than the experimental measured results. The ideal initial conditions such as uniform incoming air velocity, parameter constants as well as unvaried fluid and solid properties applied in the numerical simulations may differ from those encountered in the experimental measurements. Further work should be conducted to minimize the deviations between the numerical and experimental approaches.

PUBLICATIONS ARISING FROM THE THESIS

International Journals:

1. **D. D. Luo**, C. W. Leung and T. L. Chan, Optimum Rib Size to Enhance Forced Convection in a Horizontal Triangular Duct with Ribbed Internal Surfaces, *Heat and Mass Transfer*, 40: 893-900, 2004.
2. **D. D. Luo**, C. W. Leung and T. L. Chan, Forced Convection and Flow Friction Characteristics of Air-Cooled Horizontal Equilateral Triangular Ducts with Ribbed Internal Surfaces, *International Journal of Heat and Mass Transfer*, 47: 5439-5450, 2004.
3. **D. D. Luo**, C. W. Leung, T. L. Chan and W. O. Wong, Simulation of Turbulent Flow and Forced Convection in a Triangular Duct with Internal Ribbed Surfaces, *Numerical Heat Transfer, Part A*, 48: 447-459, 2005.
4. **D. D. Luo**, C. W. Leung, T. L. Chan and W. O. Wong, Flow and Forced-Convection Characteristics of Turbulent Flow through Parallel Plates with Periodic Transverse Ribs, *Numerical Heat Transfer, Part A*, 48: 43-58, 2005.
5. **D. D. Luo**, C. W. Leung and T. L. Chan, Thermal and Frictional Characteristics of Internally-Grooved Triangular Ducts, *Applied Thermal Engineering* (under review), 2006.
6. **D. D. Luo**, C. W. Leung, T. L. Chan and W. O. Wong, Flow Characteristics in a Triangular Duct with Internal Ribbed Surfaces, *Journal of Fluid Engineering – Transaction of ASME* (under review), 2006.

Conference Proceedings:

7. **D. D. Luo**, C. W. Leung and T. L. Chan, Optimum Rib-to-Rib Spacing to Enhance Forced Convection in the Triangular Duct with Ribbed Inner Surfaces, *ASME International Mechanical Engineering Congress and RD&D Expo., Washington, D. C., USA*, Paper no. IMECE2003-41744, 2003.
 8. **D. D. Luo**, C. W. Leung, T. L. Chan and W. O. Wong, Enhanced Turbulent Forced Convection of Triangular Duct with Internal Ribbed Surfaces, *7th APISCEU, Hong Kong*, Paper no. A4-308, 2004.
 9. **D. D. Luo**, C. W. Leung, T. L. Chan and W. O. Wong, PIV Study of Flow Characteristics in a Triangular Duct with Internal Ribbed Surfaces, *8th Flucome, Chengdu, China*, Paper No. 375, 2005.
 10. **D. D. Luo**, C. W. Leung, T. L. Chan and W. O. Wong, Numerical Study of Turbulent Flow in a Triangular Duct with Internal Ribbed Surfaces, *ITI Conference on Turbulence, Bad Zwischenahn, Germany*, Poster Paper 21, 2005.
-
-

References

Acharya S., Dutta S. and Myrum T. A., Heat Transfer in Turbulent Flow Past a Surface-Mounted Two-Dimensional Rib, *ASME Journal of Fluids Engineering*, 120: 724-734, 1998.

Acharya S., Dutta S., Myrum T. A. and Baker R. S., Periodically Developed Flow and Heat Transfer in a Ribbed Duct, *International Journal of Heat and Mass Transfer*, 36: 2069-2082, 1993.

Acharya S., Dutta S., Myrum T. A. and Baker R. S., Turbulent Flow Past a Surface-Mounted Two-Dimensional Rib, *ASME Journal of Fluids Engineering*, 116: 238-246, 1994.

Acharya S., Myrum T. A., Qiu X. and Sinha S., Developed and Periodically Developed Flow, Temperature and Heat Transfer in a Ribbed Duct, *International Journal of Heat and Mass Transfer*, 40: 461-479, 1996.

Ahn S. W., The Effects of Roughness Types on Friction Factors and Heat Transfer in Roughened Rectangular Duct, *International Community of Heat and Mass Transfer*, 28: 933-942, 2001.

Aliaga D. A., Lamb J. P. and Klein D. E., Convection Heat Transfer Distribution over Plates with Square Ribs from Infrared Thermography Measurements, *International Journal of Heat and Mass Transfer*, 37: 363-374, 1994.

Aly A. M. M., Trupp A. C. and Gerrard A. D., Measurements and Prediction of Fully Developed Turbulent Flow in an Equilateral Triangular Duct, *Journal of Fluid Mechanics*, 85(1): 57-83, 1978.

Baliga B. R. and Azrak R. R., Laminar Fully Developed Flow and Heat Transfer in Triangular Plate-Fin Ducts, *ASME Journal of Heat Transfer*, 108: 24-33, 1986.

Benedict R. P., Fundamentals of Temperature, Pressure and Flow Measurements, 2nd edition, New York, John Wiley & Sons, 1977.

Bonhoff B., Parneix S., Leusch J., Johnson B. V., Schabacker J. and Bolcs A., Experimental and Numerical Study of Developed Flow and Heat Transfer in Coolant Channels with 45° Ribs, *International Journal of Heat and Fluid Flow*, 20: 311-319, 1999.

Braaten M. E. and Patankar S. V., Analysis of Laminar Mixed Convection in Shrouded Arrays of Heated Rectangular Blocks, *Proceeding of the 22nd National Heat Transfer Conference and Exhibition*, 231-237, 1984.

Braga S. L. and Saboya F. E. M., Turbulent Heat Transfer and Pressure Drop in an Internally Finned Equilateral Triangular Duct, *Experimental Thermal and Fluid Science*, 12: 57-64, 1996.

Bredberg J., Peng S. H. and Davidson L., On the Wall Boundary Condition for Computing Turbulent Heat Transfer with $k - \omega$ Models, *Proceedings of the ASME Heat Transfer Division*, HTD-366-5: 243-250, 2000.

Chen S., Chan T. L., Leung C. W. and Yu B., Numerical Prediction of Laminar Forced Convection in Triangular Ducts with Unstructured Triangular Grid Method, *Numerical Heat Transfer, Part A*, 38: 209-224, 2000.

Demuren A. O., Calculation of Turbulence-Driven Secondary Motion in Ducts with Arbitrary Cross Section, *AIAA Journal*, 29(4), April, 1991.

Dittus F. W. and Boelter L. M. K., Heat Transfer in Automobile Radiators of the Tubular Type, *University of California Publications on Engineering*, Berkeley, CA, 2: 443, 1930.

Dutta S., Han J. C. and Zhang Y., Local Heat Transfer in a Rotating Two-pass Triangular Duct with Smooth Walls, *International Gas Turbine and Aeroengine Congress and Exposition*, The Hague, Netherlands, June 13-16, 1994.

Eggels J. G. M., Unger F., Weiss M. H., Westerweel J., Adrian R. J., Friedrich R. and Nieuwstadt F. T. M., Fully Developed Turbulent Pipe Flow: A Comparison between Direct Numerical Simulation and Experiment, *Journal of Fluid Mechanics*, 268: 175-209, 1994.

Emery A. F., Neighbors P. K. and Gessner F. B., The Numerical Prediction of Developing Turbulent Flow and Heat Transfer in a Square Duct, *ASME Journal of Heat Transfer*, 102: 51-57, 1980.

Fluent Inc. Product Documentation 6.0, 2001.

Gao X. and Sundén B., Heat Transfer and Pressure Drop Measurements in Rib-Roughened Rectangular Ducts, *Experimental Thermal Fluid Science*, 24: 25-34, 2001.

Gao X. and Sundén B., PIV Measurement of the Flow Field in Rectangular Ducts with 60° Parallel, Crossed and V-Shaped Ribs, *Experimental Thermal Fluid Science*, 28: 639-653, 2004.

Gatski T. B. and Speziale C. G., On Explicit Algebraic Stress Models for Complex Turbulent Flows, *Journal of Fluid Mechanics*, 254: 59-78, 1993.

Ghaddar N. K., Korczak K. Z. and Mikic B. B., Numerical Investigation of Incompressible Flow in Grooved Channels, Part 1, Stability and Self-Sustained Oscillations, *Journal of Fluid Mechanics*, 163: 99-127, 1986.

Ghaddar N. K., Magen M., Mikic B. B. and Patera A. T., Numerical Investigation of Incompressible Flow in Grooved Channels, Part 2, Resonance and Oscillatory Heat-Transfer Enhancement, *Journal of Fluid Mechanics*, 168: 544-567, 1986.

Greiner M., An Experimental Investigation of Resonant Heat Transfer Enhancement in Grooved Channels, *International Journal of Heat and Mass Transfer*, 34: 1383-1391, 1991.

Greiner M., Chen R. F. and Wirtz R. A., Passive Heat Transfer Enhancement from a Grooved Channel, *ASME/JSME Thermal Engineering Proceedings*, 3: 97-101, 1991.

Greiner M., Faulkner R. J., Van V. T., Tufo H. M. and Fischer P. F., Simulations of Three-Dimensional Flow and Augmented Heat Transfer in a Symmetrically Grooved Channel, *ASME Journal of Heat Transfer*, 122: 653-660, 2000.

Greiner M., Fischer P. F., Tufo H. M. and Wirtz R. A., Three-Dimensional Simulations of Enhanced Heat Transfer in a Flat Passage Downstream from a Grooved Channel, *ASME Journal of Heat Transfer*, 124: 169-175, 2002.

Han J. C. and Park J. S., Developing Heat Transfer in Rectangular Channels with Rib Turbulators, *International Journal of Heat and Mass Transfer*, 31: 183-195, 1988.

Han J. C. and Zhang Y. M., High Performance Heat Transfer Ducts with Parallel Broken and V-Shaped Broken Ribs, *International Journal of Heat and Mass Transfer*, 35: 513-523, 1992.

Han J. C., Glicksman L. R. and Rohsenow W. M., An Investigation of Heat Transfer and Friction for Rib-Roughened Surfaces, *International Journal of Heat and Mass Transfer*, 21: 1143-1156, 1978.

Han J. C., Heat Transfer and Friction in Channels with Two Opposite Rib-Roughened Walls, *ASME Journal of Heat Transfer*, 106: 774-781, 1984.

Haque M. A., Turner J. T., Hassan A. K. A. and Barrow H., An Observation on the Origin of Secondary Flow in Straight Noncircular Ducts, *Waerme- und Stoffuebertragung, Fluid Mechanics and Heat Transfer*, 17(2): 93-95, 1983.

Hirota M., Fujita H., Yokosawa H., Nakayama T. and Tanaka T., Developing Heat/Mass Transfer in Low-Aspect-Ratio Rectangular Channels with Ribbed Walls, *Heat Transfer, Proceeding of 11th IHTC*, 5: 363-368, 1998.

Hirota M., Yokosawa H. and Fujita H., Turbulent Kinetic Energy in Turbulent Flows through Square Ducts with Rib-Roughened Walls, *International Journal of Heat and Fluid Flow*, 13(1): 22-29, 1992.

Hishida M., Local Heat-Transfer Coefficient Distribution on a Ribbed Surface, *Journal of Enhanced Heat Transfer*, 3(3): 187-200, 1996.

Hitoshi S., Akiyama M. and Takahashi T., Numerical Analyses of Turbulence Structure in Rectangular Ducts with Rough and Smooth Walls Applicability of Simple Analysis Methods Using Algebraic Reynolds Stress Model, *Nippon Genshiryoku Gakkaishi/Journal of the Atomic Energy Society of Japan*, 40: 312-322, 1998.

Hong Y. M. and Hsieh S. S., Heat Transfer and Friction Factor Measurement in Ducts with Staggered and Inline Ribs, *ASME Journal of Heat Transfer*, 115: 58-65, 1993.

Hosni M. H., Coleman H. W. and Taylor R. P., Measurements and Calculations of Rough-Wall Heat Transfer in the Turbulent Boundary Layer, *International Journal of Heat and Mass Transfer*, 34: 1067-1082, 1991.

Huang P. C. and Vakai K., Analysis of Forced Convection Enhancement in a Channel Using Porous Blocks, *Journal of Thermophysics and Heat Transfer*, 8: 563-573, 1994.

Hwang J. J. and Cheng C. S., Impingement Cooling in Triangular Ducts Using an Array of Side-Entry Wall Jets, *International Journal of Heat and Mass Transfer*, 44(5): 1053-1063, 2001.

Iacovides H., Computation of Flow and Heat Transfer through Rotating Ribbed Passages, *Biennial Colloquium on Computational Fluid Dynamics, UMIST*, 3: 19-24, 1996.

Ince N. Z. and Launder B. E., On the Computation of Buoyancy-Driven Turbulent Flows in Rectangular Enclosures, *International Journal of Heat and Fluid Flow*, 10: 110-117, 1988.

Incropera F. P., Convection Heat Transfer in Electronic Equipment, *ASME Journal of Heat Transfer*, 110: 1097-1111, 1988.

Kang H. J., Wong T. T. and Leung C. W., Effects of Surface Roughness on Forced Convection and Friction in Triangular Duct, *Experimental Heat Transfer*, 11: 241-253, 1998.

Kays W. M. and Crawford M. E., Convective Heat and Mass Transfer, 3rd edition, McGraw-Hill Book Company, New York, 1993.

Kays W. M. and London A. L., Compact Heat Exchangers, 3rd edition, McGraw-Hill Book Company, New York, 1984.

Kim S. H. and Anand N. K., Laminar Heat-Transfer Between a Series of Parallel Plates with Surface-Mounted Discrete Heat Sources, *ASME Journal of Electronic Packaging*, 117: 52-62, 1995.

Kiml R., Mochizuki S. and Murata A., Effects of Rib Arrangements on Heat Transfer and Flow Behavior in a Rectangular Rib-Roughened Passage: Application

to Cooling of Gas Turbine Blade Trailing Edge, *ASME Journal of Heat Transfer*, 123: 675-681, 2001.

Kiwan S. and Al-Nimr M. A., Using Porous Fins for Heat Transfer Enhancement, *ASME Journal of Heat Transfer*, 123: 790-794, 2001.

Kwon H. J., Wu S. J. and Cho H. H., Effects of Discrete Rib-Turbulators on Heat/Mass Transfer Augmentation in a Rectangular Duct, *Transactions of KSME (B)*, 24: 744-756, 2000.

Lauder B. E. and Spalding D. B., The Numerical Computation of Turbulent Flows, *Computer Methods in Applied Mechanics and Engineering*, 3: 269-289, 1974.

Lauder B. E., Reece G. J. and Rodi W., Progress in the Development of a Reynolds Stress Turbulence Closure, *Journal of Fluid Mechanics*, 68(3): 537-566, 1975.

Lee C. K. and Abdel-Moneim S. A., Computational Analysis of Heat Transfer in Turbulent Flow Past a Horizontal Surface with Two-Dimensional Ribs, *International Community of Heat and Mass Transfer*, 28(2): 161-170, 2001.

Lehmann G. L. and Wirtz R. A., Convection from Surface-Mounted Repeated Ribs in a Channel Flow, *ASME*, Paper no. 84-WA/Ht-88, 1984.

Lehmann G. L. and Wirtz R. A., The Effect of Variations in Streamwise Spacing and Length on Convection from Surface-Mounted Rectangular Components, *Heat Transfer Electronic Equipment, ASME HTD*, 48: 39-47, 1985.

Leung C. W. and Kang H. J., Convective Heat Transfer from Simulated Air-Cooled Printed-Circuit Board Assembly on Horizontal or Vertical Orientation, *International Community of Heat and Mass Transfer*, 25(1): 67-80, 1998.

Leung C. W. and Kang H. J., Laminar Convection of Horizontal and Vertical Simulated Printed-Circuit Board Assemblies, *Experimental Heat Transfer*, 10: 39-49, 1997.

Leung C. W. and Probert S. D., Forced-Convective Internal Cooling of a Horizontal Equilateral-Triangle Cross-Sectional Duct, *Applied Energy*, 50: 313-321, 1995.

Leung C. W. and Probert S. D., Forced-Convective Turbulent Flows through Horizontal Ducts with Isosceles Triangular Internal Cross-Sections, *Applied Energy*, 57(1): 13-24, 1997.

Leung C. W., Chan T. L. and Chen S., Forced Convection and Friction in a Triangular Duct with Uniformly Spaced Square Ribs on Inner Surfaces, *Heat and Mass Transfer*, 37: 19-25, 2001.

Leung C. W., Chen S. and Chan T. L., Numerical Simulation of Laminar Forced Convection in an Air-Cooled Horizontal Printed Circuit Board Assembly, *Numerical Heat Transfer, Part A*, 37: 373-393, 2000.

Leung C. W., Chen S., Wong T. T. and Probert S. D., Forced Convection and Pressure Drop in a Horizontal Triangular-Sectional Duct with V-Grooved (i.e. orthogonal to the mean flow) Inner Surfaces, *Applied Energy*, 66: 199-211, 2000.

Leung C. W., Kang H. J. and Probert S. D., Horizontal Simulated Printed-Circuit Board Assembly in Fully-Developed Laminar-Flow Convection, *Applied Energy*, 56(1): 71-91, 1997.

Leung C. W., Wong T. T. and Kang H. J., Forced Convection of Turbulent Flow in Triangular Ducts with Different Angles and Surface Roughness, *Heat and Mass Transfer*, 34: 63-68, 1998.

Leung C. W., Wong T. T. and Probert S. D., Enhanced Forced-Convection from Ribbed or Machine-Roughened Inner Surfaces within Triangular Ducts, *Applied Energy*, 69: 87-99, 2001.

Liou T. M. and Chen C. C., Heat Transfer in a Rotating Two-Pass Smooth Passage with a 180° Rectangular Turn, *International Journal of Heat and Mass Transfer*, 42: 231-247, 1999.

Liou T. M. and Hwang J. J., Effect of Ridge Shapes on Turbulent Heat Transfer and Friction in a Rectangular Channel, *International Journal of Heat and Mass Transfer*, 36: 931-940, 1993.

Liou T. M., Wu Y. Y. and Chang Y., LDV Measurements of Periodic Fully Developed Main and Secondary Flow in a Channel with Rib-Disturbed Walls, *ASME Journal of Fluids Engineering*, 115: 109-114, 1993.

Lorenz S., Mukomilow D. and Leiner W., Distribution of the Heat Transfer Coefficient in a Channel with Periodic Transverse Grooves, *Experimental Thermal and Fluid Science*, 11(3): 234-242, 1995.

Masoud R. and Thomas B. G., Predicting Turbulent Convective Heat Transfer in Fully Developed Duct Flows, *International Journal of Heat and Fluid Flow*, 22: 381-392, 2001.

Montgomery D. C., Design and Analysis of Experiments, 5th edition, Chapter 2, New York: John Wiley, 2001.

Nikuradse J., V.D.I. Forschungsheft, 70, 1229, 1926.

Ohara T., Yamamoto T. and Fujita H., Evaporative Heat Transfer and Pressure Drop in a Rib-Roughened Flat Channel, *ASME/JSME Thermal Engineering Proceedings*, 4: 399-406, 1991.

Ooi A., Iaccarino G., Durbin P. A. and Behnia M., Reynolds Averaged Simulation of Flow and Heat Transfer in Ribbed Ducts, *International Journal of Heat and Fluid Flow*, 23: 750-757, 2002.

Ould-Amer Y., Chikh S., Bouhadef K. and Lauriat G., Forced Convection Cooling Enhancement by Use of Porous Materials, *International Journal of Heat and Fluid Flow*, 19: 251-258, 1998.

Peterson G. P. and Ortega A., Thermal Control of Electronic Equipment and Devices, *Advances in Heat Transfer*, 20: 181-314, 1990.

Podhorsky M. and Krips H., Heat Exchangers: A Practical Approach to Mechanical Construction, Design, and Calculations, Begell House, Inc., New York, 1998.

Ramesh K. Shah and Dušan P. Sekulić, Fundamentals of Heat Exchanger Design, John Wiley & Sons, Inc., Hoboken, New Jersey, 2003.

Rau G., Cakan M., Moeller D. and Arts T., The Effect of Periodic Ribs on the Local Aerodynamic and Heat Transfer Performance of a Straight Cooling Channel, *ASME Journal of Turbomachinery*, 120: 368-375, 1998.

Rau G., The Blockage Effect of Turbulators in a Rectilinear Cooling Channel, *VKI Lecture Series 1995-05, Brussels*, 1995.

Roetzel W. and Xuan Y., Dynamic Behaviour of Heat Exchangers, Vol. 3, WIT Press/Computational Mechanics Publications, Boston, Southampton, 1999.

Roger C. B., Flow Measurement Handbook, Cambridge University Press, American, 2000.

Rokni M. and Sundén B., Numerical Investigation of Turbulent Forced Convection in Ducts with Rectangular and Trapezoidal Cross-section Area by Using Different Turbulence Models, *Numerical Heat Transfer, Part A*, 30: 321-346, 1996.

Rokni M. and Sundén B., Turbulence Modeling Experience in Ducts with Forced Convection Flow, *Numerical Heat Transfer, Part A*, 35: 629-654, 1999.

Rokni M., A New Low-Reynolds Version of an Explicit Algebraic Stress Model for Turbulent Convective Heat Transfer in Ducts, *Numerical Heat Transfer, Part A*, 37: 331-363, 2000.

Rokni M., Olsson C. O. and Sundén B., Numerical and Experimental Investigation of Turbulent Flow in a Rectangular Duct, *International Journal of Numerical Methods in Fluids*, 28: 225-242, 1998.

Safasivam R., Manglik R. M. and Jog M. A., Fully Developed Forced Convection Through Trapezoidal and Hexagonal Ducts, *International Journal of Heat and Mass Transfer*, 42: 4321-4331, 1999.

Sahin A. Z., Irreversibilities in Various Duct Geometries with Constant Wall Heat Flux and Laminar Flow, *Energy*, 23: 465-473, 1998.

Sahin A. Z., Second Law Comparison for Optimum Shape of Duct Subjected to Constant Wall Temperature and Laminar Flow, *Heat and Mass Transfer*, 33: 425-430, 1998.

Saidi A. and **Sundén B.**, Numerical Simulation of Turbulent Convective Heat Transfer in Square Ribbed Ducts, *Numerical heat Transfer, Part A*, 38: 67-88, 2000.

Saini R. P. and **Saini J. S.**, Heat Transfer and Friction Factor Correlations for Artificially Roughened Ducts with Expanded Metal Mesh as the Roughness Element, *International Journal of Heat and Mass Transfer*, 40(4): 973-986, 1997.

Schabacker J., **Boelcs A.** and **Johnson V.**, PIV Investigation of the Flow Characteristics in an Internal Coolant Passage with 45° Rib Arrangement, *ASME*, Paper no. 99-GT-120, 1999.

Schabacker J., **Boelcs A.** and **Johnson V.**, PIV Investigation of the Flow Characteristics in an Internal Coolant Passage with Two Ducts Connected by a Sharp 180° Bend, *ASME*, Paper no. 98-GT-544, 1998.

Schlichting H., Boundary-Layer Theory, 7th edition, New York: McGraw-Hill, 1979.

Shah R. K. and **London A. L.**, Laminar Flow Forced Convection in Ducts, New York, Academic Press, 1978.

Shah R. K., Laminar-Flow Friction and Forced-Convection Heat-Transfer in Ducts of Arbitrary Geometry, *International Journal of Heat and Mass Transfer*, 18: 849-862, 1975.

Shiina Y., Experimental Observation of Flow Effects on Heat Transfer of Wired Turbulence Promoters at Low Reynolds Number, *3rd Symposium On Flow Visualization ISAS University of Tokyo*, 115-120, 1975.

Smits A. J. and **Lim T. T.**, Flow Visualization: Techniques and Examples, Chapter 6, 2000.

Son S. Y., **Kihm K. D.** and **Han J. C.**, PIV Measurements for Heat Transfer Characterization in Two-pass Channels with Smooth and 90° Ribbed Walls, *International Journal of Heat and Mass Transfer*, 45: 4809-4822, 2002.

Soo W. A. and **Kang P. S.**, Heat Transfer and Pressure Drop in the Roughened Equilateral Triangular Duct, *International Community of Heat and Mass Transfer*, 29: 479-488, 2002.

Sparrow E. M. and **Haji-Sheikh A.**, Laminar Heat-Transfer and Pressure Drop in Isosceles Triangular, Right Triangular and Circular Sector Ducts, *ASME Journal of Heat Transfer*, 87: 426-427, 1965.

Sparrow E. M. and Haji-Sheikh A., Flow and Heat Transfer in Ducts of Arbitrary Shape with Arbitrary Thermal Boundary Conditions, *ASME Journal of Heat Transfer*, 88: 351-358, 1966.

Sparrow E. M., Niethammer J. E. and Chaboki A., Heat Transfer and Pressure Drop Characteristics of Arrays of Rectangular Modules Encountered in Electronic Equipment, *International Journal of Heat and Mass Transfer*, 25: 961-973, 1982.

Speziale C. G., On Turbulent Secondary Flows in Pipes of Noncircular Cross-Section, *International Journal of Engineering Science*, 20: 863-872, 1982.

Sridhar S., Faghri M., Lessmann R. C. and Schmidt R., Heat Transfer Behaviour Including Thermal Wakes in Forced Air Cooling of Arrays of Rectangular Blocks, *ASME HTD*, 153: 15-25, 1990.

Sugiyama H., Akiyama M., Hirata M. and Ueno S., Numerical Analysis of Fully Developed Turbulent Flow in an Equilateral Triangular Duct by a Reynolds Stress Model, *Transactions of JSME, Part B*, 57(54): 2943-2949, 1991.

Sugiyama H., Akiyama M., Hitomi D. and Shinohara Y., Numerical Analysis of Turbulent Flow Developing in a 30/60 Degree Right Triangular Duct, *Transactions of JSME, Part B*, 63(607): 78-85, 1997.

Tam W. C., Leung C. W. and Probert S. D., Forced Convection Air-Cooling of Simulated Printed-Circuit Boards, *Applied Energy*, 46: 197-214, 1993.

Uzun I. and Ünsal M., Numerical Study of Laminar Heat Convection in Ducts of Irregular Cross-Sections, *International Communications in Heat and Mass Transfer*, 24: 835-848, 1997.

Vakai K. and Kim S. J., Analysis of Surface Enhancement by a Porous Substrate, *ASME Journal of Heat Transfer*, 112: 700-705, 1990.

Westerweel J., Digital Particle Image Velocimetry – Theory and Application, Delft: Delft University Press, 1993.

Westerweel J., Draad A. A., Van Der Hoeven J. G. Th. and Van Oord J., Measurement of Fully-Developed Pipe Flow with Digital Particle Image Velocimetry, *Experiments in Fluids*, 20: 165-177, 1996.

White F. M., Fluid Mechanics, 3rd edition, McGraw-Hill, New York, 1994.

Whittaker E. T. and Robinson G., The Method of Least Squares, Chapter 9 in The Calculus of Observations: A Treatise on Numerical Mathematics, 4th edition, New York: Dover, 1967.

Willert C. E. and Gharib M., Digital Particle Image Velocimetry, *Experiments in Fluids*, 10: 181-193, 1991.

Wilson N. W. and Medwell J. O., An Analysis of Heat Transfer for Fully Developed Turbulent Flow in Concentric Annuli, *ASME Journal of Heat Transfer*, 43-50, 1968.

Wong T. T. and Leung C. W., Forced-Convection Augmentation of Turbulent Flow in a Triangular Duct with Artificially Roughened Internal Surfaces, *Experimental Heat Transfer*, 15: 89-106, 2002.

Wong T. T., Leung C. W., Li Z. Y. and Tao W. Q., Turbulent Convection of Air-Cooled Rectangular Duct with Surface-Mounted Cross-Ribs, *International Journal of Heat and Mass Transfer*, 46: 4629-4638, 2003.

Xin R. C., Dong Z. F., Ebdian M. A. and Tao W. Q., Analytical and Numerical Solutions of Forced Convection in Ducts with a Boundary Condition of the Third Kind, *1994 International Mechanical Engineering Congress & Exhibition*, Chicago, Illinois, Paper No. 94-WA/HT-25, 1994.

Yang G., Ebdian M. A. and Campo A., A Numerical Study of Convective and Radiative Transfer in Ducts of Rectangular and Equilateral Cross Sections, *International Journal of Heat and Mass Transfer*, 34: 1319-1322, 1991.

Yilmaz T. and Cihan E., General Equation for Heat Transfer for Laminar Flow in Ducts of Arbitrary Cross-Sections, *International Journal of Heat and Mass Transfer*, 36(13): 3265-3270, 1993.

Yokosawa H., Fujita H., Hirota M. and Iwata S., Measurements of Turbulent Flow in a Square Duct with Roughened Walls on Two Opposite Sides, *International Journal of Heat and Fluid Flow*, 10(2): 125-130, 1989.

Young T. J. and Vafai K., Convective Cooling of a Heated Obstacle in a Channel, *International Journal of Heat and Mass Transfer*, 41: 3131-3148, 1998.

Young T. J. and Vafai K., Convective Flow and Heat Transfer in a Channel Containing Multiple Heated Obstacles, *International Journal of Heat and Mass Transfer*, 41: 3279-3298, 1998.

Zhang H. Y., Ebdian M. A., and Campo A., Computation of Heat and Fluid Flow in Ducts of Arbitrary Cross Section, *Numerical Heat Transfer, Part A*, 17: 231-248, 1990.

Zhang Y. M., Gu W. Z. and Han J. C., Heat Transfer and Friction in Rectangular Channels with Ribbed or Rib-Bed-Grooved Walls, *ASME Journal of Heat Transfer*, 116: 58-65, 1994.

APPENDIX I

Error Analysis and Estimation

1. Introduction

Errors and uncertainties are not avoidable in all measurements, no matter how well the experiments are conducted and how hard we might try to minimize them. However, the accuracy of a measurement determines the reliability of a conclusion that we draw from the data. It also reflects how ‘good’ the experiment information is.

Estimation of the accuracy is known technically as the uncertainty of measurement. Uncertainty is also an estimate of experiment error. It is important and necessary to carry out an analysis of the experimental uncertainties.

A method of uncertainty estimation in experimental results had been presented by Montgomery [2001].

2. Basic Definition of Error

Error is the difference between the measured value and true value, and we have

$$x = x_{measured} \pm \delta x$$

Where, x is the best estimate of the measured value, $x_{measured}$ is the value obtained by correction (centering) of the measured value of x , and δx is the error of x .

3. Types of Errors

The measuring device, the procedure of how you measure, and the observed quantity itself, all can bring in errors. Generally, there are basically two types of errors:

Systematic error	Systematic error is the fixed component of the total error. It is reproducible and hard to be analyzed by statistical methods. It is often due to a problem that persists throughout the entire experiment. Hence, the data induced is either too high or too low, off in the same direction.
------------------	---

Random error	In contrast to systematic error, random error is unbiased, which means it is equal probability that an individual measurement is too high or too low. It is due to the experimenter's inability to take the measurement to get exactly the same value in exactly the same way. Random error means that several measurements of a quantity will not always come out the same but will spread around a mean value, which is much closer to the 'real' value than any individual measurement. Random error can be minimized by statistical methods.
--------------	--

4. Sources of Errors

In the present study, errors come from different aspects. Considering the priority of errors, several effective points are selected, including:

Sources	Descriptions
Test rig design	Heat flux may not be distributed uniformly along the duct walls; Error in the duct wall temperature measurements due to the misalignment of thermocouples when installed on the duct walls, and also the spacing and resistance between the thermocouples and duct walls; Error in the inlet and outlet air temperature measurements; Error due to flow rate and pressure measurements, which is due to turbulent effect; Error in the component connections, which is caused by air leakage; Flow may not be fully developed over the whole duct system.
Manufacturing process and tooling	The cross sectional area of the duct is probably not constant over the whole axial length of the duct, since the tolerances are unavoidable in the manufacturing process; The duct dimension variation may occur when the heat is applied to the duct walls; The ribs/grooves are not manufactured uniformly or the spacing between two adjacent objectives is not constant in each experiment.
Instruments	Thermocouples; Manometers; Wattmeters; Power supply; Calibrators.
Heat loss	Conduction from the duct wall surface to the plywood and from plywood to fiber glass and convection from fiber glass to ambient; Conduction from the cross section of the test duct to the duct connectors;

	Radiation loss at both ends of the test duct to ambient.
Handling data	Round-off error exists in data calculation; The standard error in curve-fitting process.
Environmental effects	Operating systems nearby such as diesel and petrol engines, which can cause vibration; Large fans overhead, which can affect the condition of atmosphere in the room; People walking around.

5. Estimating of Uncertainty

➤ Procedures to determine the overall errors:

- To find out the sample standard deviation of the finding values:

$$S = \sqrt{\frac{\sum (x_i - \bar{x})^2}{N - 1}}$$

- To find the constant of t -distribution from the T -chart (only applied in less samples, i.e. $n < 30$) and 95% confidence interval;
- To find out the systematic error:

Systematic error (bias error) = mean of the measured value - true value

- The random error (precision error) is defined as:

$$\text{Precision error} = \frac{ts}{\sqrt{n}}$$

- Then to calculate the error in each instruments or components shown as:

$$U_x = \sqrt{U_{bi}^2 + U_{ran}^2}$$

Where, U_{bi} is Bias error, U_{ran} is Random error, and U_x is Total error.

➤ Overall % errors

- Let R be a given function of the independent variables $x_1, x_2, x_3, \dots, x_n$.
- Thus, $R = R(x_1, x_2, x_3, \dots, x_n)$
- Let U_R be the uncertainty in the result and U_1, U_2, \dots, U_n be the uncertainties in the independent variables which are all given with the same odds, the uncertainty in the result having these odds is given as:

$$\frac{U_R}{R} = \left[\left(\frac{\partial R}{\partial x_1} \frac{R_1}{R} \right)^2 + \left(\frac{\partial R}{\partial x_2} \frac{R_2}{R} \right)^2 + \dots + \left(\frac{\partial R}{\partial x_n} \frac{R_n}{R} \right)^2 \right]^{\frac{1}{2}}$$

6. Uncertainties in Each Component

Details about the uncertainties in each component are listed below:

Component	Uncertainties
Temperature measurement	Random and precision errors in thermocouple calibrations; Calibrator error which can be obtained from the product specification; Error in digital thermometer, which also can be obtained from product specification.
Heat input measurement	Random and precision errors in Wattmeter calibrations; Random and precision errors in heater; Error in digital multi-meter calibrator.
Airflow rate measurement	Random and precision errors in manometer calibrations; Error in pitot tube; Error in microtector; Error in blower.
Pressure drop measurement	Random and precision errors in manometer calibrations; Error in calibrator; Error in blower.

For example, the uncertainties in each individual component can be calculated as follow:

$$U_{thermocouple} = \sqrt{u_{Ti}^2 + U_{thermocouple_calibrator}^2 + U_{Digital_thermometer}^2}$$

$$U_W = \sqrt{U_W^2 + U_{digital_multimeter}^2}$$

$$U_E = \sqrt{U_W^2 + U_{P1}^2}$$

$$U_{man1} = \sqrt{U_{microtector}^2 + U_{man2}^2 + U_{P2}^2}$$

$$U_{man2} = \sqrt{U_{microtector}^2 + U_{man1}^2 + U_{P2}^2 + U_{Pitot_tube}^2}$$

Ten sets of data are obtained from each experiment.

7. Least-Square Method

The common method of fitting a set of experimental results with a mathematical expression is Least-Square method. Sparrow and Haji-Sheikh [1966] were the first investigators to adopt this method to a forced convective flow in arbitrary ducts. The method expresses a relationship between variables in the form of a mathematical formula. The resulting regression equation is in a convenient form for extrapolation, and the results obtained are definite and independent of subjective estimate. A detailed description can be found in [Whittaker et al. 1967].

A. Equation Deduction

For a linear equation,

$$y = mx + c$$

Suppose that when x had the value x_i , y is observed to have the value y_i . If the quantity $mx_i + c$ is calculated by using some pairs of values for ‘ m ’ and ‘ c ’, then the difference between this value and the observation is:

$$\Delta y_i = (mx_i + c) - y_i$$

It can apply the Least-Square method by squaring this number and those obtained for all the values of ‘ i ’, summing these squares and adjusting ‘ m ’ and ‘ c ’ until this sum is a minimum. This last operation is done with the aid of partial differentiation of the necessary conditions for relative minimum:

$$\Delta y_i^2 = \sum y_i^2$$

$$\frac{\partial \sum y_i^2}{\partial m} = 0, \quad \frac{\partial \sum y_i^2}{\partial c} = 0$$

Taking the indicated derivatives and solving for ‘ m ’ and ‘ c ’ leads to:

$$m = \frac{n \sum x_i y_i - \sum x_i \sum y_i}{n \sum x_i^2 - (\sum x_i)^2}, \quad c = \frac{\sum x_i^2 \sum y_i - \sum x_i \sum x_i y_i}{n \sum x_i^2 - (\sum x_i)^2}$$

The new equation becomes:

$$\bar{y} = m\bar{x} + c$$

B. Correlation Coefficient

A measure of the 'goodness' of a regression line for estimation purpose is the Correlation Coefficient (r) (i.e. for the perfect case, $r=1$). The determination of r is as following:

$$\sigma_y = \left[\frac{\sum_{i=1}^n (y_i - y_m)^2}{n-1} \right]^{\frac{1}{2}}$$

$$\sigma_{y,x} = \left[\frac{\sum_{i=1}^n (y_i - y_{ic})^2}{n-2} \right]^{\frac{1}{2}}$$

$$r = \left[1 - \frac{\sigma_{y,x}^2}{\sigma_y^2} \right]^{\frac{1}{2}}$$

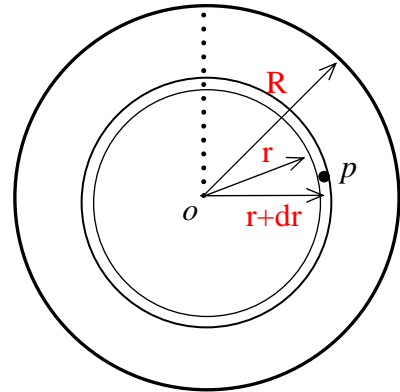
Where, y_i is the actual values of y , y_m is the mean value of y , and $y_{ic} = mx_i + c$.

In view of Correlation Coefficient, the values are all close to unity so that the goodness of fit for the regression lines obtained from the experimental results is acceptable for estimation purpose.

APPENDIX II

Determination of Mass Flow Rate

As stated in Chapter 3, the mass flow rate (\dot{m}) of the airflow through the circular pipe needs to be determined. A sketch map of the circular pipe is shown at the right.



Suppose a flow with a density of (ρ) through the pipe with a radius of (R) at the location p , which is of a distance (r) to the center o , has a velocity of (U).

Certainly, on the one hand, U varies with r , which can be expressed as:

$$U = f(r) \quad \dots\dots (1)$$

On the other hand, the mass flow rate (\dot{m}) can be determined from:

$$\dot{m} = \int_0^R \rho \cdot (2 \cdot \pi \cdot r \cdot dr) \cdot U$$

$$\dot{m} = \int_0^R 2\pi\rho \cdot f(r) \cdot r \cdot dr \quad \dots\dots (2)$$

Here, the density of the airflow (ρ), which is assumed constant at the whole cross sectional plane, can be estimated with the aid of environment conditions, such as air temperature and ambient pressure.

As for the air velocity ($U = f(r)$), it is determined from the pressure measurements (P_i) of fourteen points (r_i), which are at an interval of (Δr_i) along the radius from the center point o (as shown in the sketch map):

$$U_i = \sqrt{\frac{2P_i}{\rho}}, \quad (i=1, 2, \dots, 14) \quad \dots\dots (3)$$

Thus, the mass flow rate (\dot{m}) expressed in Equation (2) can be rewritten as:

$$\dot{m} = \sum_{i=1}^{14} 2\pi\rho \cdot \sqrt{\frac{2P_i}{\rho}} \cdot r_i \cdot \Delta r_i \quad \dots\dots (4)$$

APPENDIX III

Instruments Used in Experiments

1. DIGITAL MULTI-METER¹

Model: CE-DT830B

Features:

- Size: 2.9"W x 5"L x 1"D
- Power: 9VDC Battery (Included)
- Input Impedance: 1M ohm
- DC Volts: 200mV, 2V, 20V, 200V, 1000V
- AC Volts: 200V, 750V
- Accuracy: DC 1/2%, AC 1.2%
- Resolution: 0.1mV
- DC Current: 200 μ A, 2mA, 20mA, 200mA, 10A
- Accuracy: 1.2%rdg +2 digits
- Resolution: .1 μ A
- Resistance: 200 ohm, 2K ohm, 20K ohm, 200K ohm, 2M ohm
- Accuracy: 1.2%rdg + 2 digits
- Resolution: 0.1 ohms



2. MICROTECTOR® PORTABLE ELECTRONIC POINT GAGE²

Model: 1430

Features:

- Range: 0-2'' w.c. (water column)
- Accuracy: $\pm 0.00025''$ w.c.
- Principle of operation:



¹ Hobbytron.com

² Dwyer Instruments, Inc.

A pressure to be measured is applied to the manometer fluid which is displaced in each leg of the manometer by an amount equal to $\frac{1}{2}$ of the applied pressure. A micrometer mounted-point is then lowered until it contacts the manometer gage fluid. The instant of contact is detected by completion of a low-power A.C. circuit. Current for this circuit is supplied by a 1/5 volt penlight cell feeding two semiconductor amplifiers which act as a free-running multivibrator operating at a frequency of approximately two kilohertz. Completion of the A.C. circuit activates a bridge rectifier which provides the signal for indication on a sensitive D.C. microammeter (0 to 50 microamps).

On indication of contact, the operator stops lowering the point and reads the micrometer which indicates one half of the applied pressure. By interpolating eight divisions (each being 0.000125" w.c.) between 0.001 micrometer graduations, a total accuracy of 0.00025 can easily be achieved. The micrometer complies with Federal Specification GGG-C-105A and is traceable to a master at the NIST.

3. DIGITAL WATT METER³

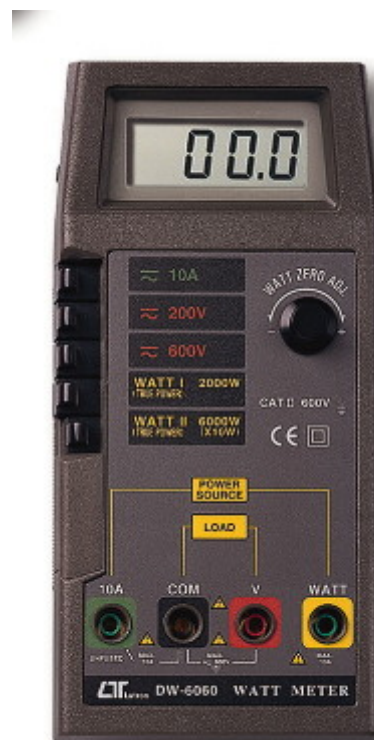
Model: DW-6060

1. Features

The DIGITAL WATT METER gives a direct reading of Watt value on 3 $\frac{1}{2}$ digits LCD display, five range and functions give precision reading to the ACV, ACA, DCV, DCA and WATT. It can be requiring to accurate current, voltage, and true power measurement.

2. Specifications:

- Polarity: Bi-polar by automatic Switching, “-” indicates reverse polarity
- Zero Adjust: (Watt) External adjustment for zero of the display, limited to +30 to -30 digits. (ACV/DCV, ACA/DCA) Automatic adjustment
- Over-Input: Indication of “1” or “-1”
- Operating Temp.: 0°C to 50°C (32°F to 122°F)
- Operating Humidity: Less than 80% RH
- Power Consumption: Approx. DC 6mA



³ Lutron, PEDAК® MEETTECHNIEK

Electrical Specifications ($23 \pm 5^{\circ}\text{C}$)			
AC WATT (true power)			
Range	Accuracy	Resolution	Overload Circuit Protection
2000 W	$\pm (1\%+1d)$	1 W	ACV: 600 ACV ACA: 10 ACA
6000 W	$\pm (1\%+1d)$	10 W	
<i>Remark:</i>			
<ul style="list-style-type: none"> ❖ Input Voltage: 0 to 600 ACA ❖ Input Current: 0-10 ACA ❖ Frequency Characteristic: 45 Hz-65 Hz ❖ Accuracy Spec. Tested on Input Voltage > 60 ACA (60 Hz) 			
AC/DC VOLTAGE			
Range	Accuracy	Resolution	Overload Circuit Protection
200 V	$\pm (0.8\%+1d)$	0.1 V	ACV: 600 ACV DCV: 600 DCV
600 V	$\pm (0.8\%+1d)$	1 V	
<i>Remark:</i>			
<ul style="list-style-type: none"> ❖ Frequency Characteristic: 45 Hz-65 Hz ❖ Converter Response: Average responding, calibrated to display RMS value of sine wave ❖ Input Impedance: 1 Mega ohm 			
AC/DC CURRENT			
Range	Accuracy	Resolution	Max. Input Current
10 A	$\pm (1\%+1d)$	10 mA	10 A
<i>Remark:</i>			
<ul style="list-style-type: none"> ❖ Voltage Drop (in case of full scale): 200 AC/DC mV ❖ Frequency Characteristic: 45 Hz-65 Hz ❖ Converter Response: Average responding, calibrated to display RMS value of sine wave 			

4. VARIABLE-VOLTAGE TRANSFORMER⁴

Model: TDGC Regulating Transformer

Features:

- Rated Capacity: 2kVA
- Phase Number: 1
- Rated Frequency: 50/60 Hz
- Rated Input Voltage: 220/110 V
- Rated Output Voltage: 0~250 V
- Rated Output Current: 8/3.2 A



5. CENTRIFUGAL BLOWER/MINI SIROCCO FAN⁵



Centrifugal Blower	
Type: TECO BSTZ-U1AA	Speed/RPM: 2910/3405 min ⁻¹
Voltage: 115/230 V	Output: 550 W
Frequency: 50/60 Hz	Phase: 1 Dia.
Capacitor: 250 VAC/ μ F	Poles: 2 P
Frame: 80	Net Weight: 10 Kg
Mini Sirocco Fan	
Type: JSD-55	
Caph.: 12/14 C.M.M.	Static Pressure: 50/52 mm/Aq

⁴ TDGC

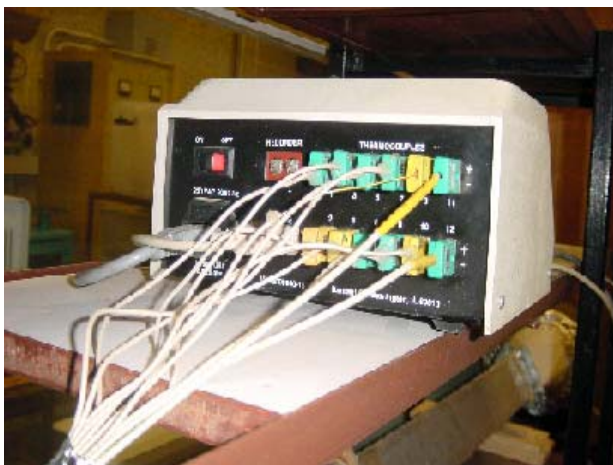
⁵ Jouning Blower Co.

6. DIGITAL THERMOMETER⁶

Model: 92800-15, Digi-Sense Scanning Thermocouple Thermometer

Features:

- 12 channels and RS-232
- 230 V and 50/60 Hz
- 1/16A FUSE (5×20mm)
- Resolution: 0.01°C



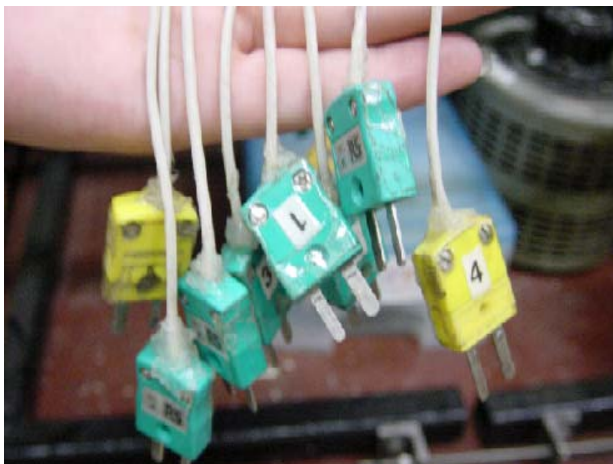
⁶ Cole Parmer, Barnant Co.

7. THERMOCOUPLE⁷

Type: *K*

Features:

- Material: Nickel-10% chromium (+) vs. nickel-5% aluminum and silicon (-)
- Temperature range of 0° to 400°C
- Oxidation resistance
- Bead diameter: 0.25mm/1.5mm
- Resolution: 0.1°C
- Accuracy: $\pm 0.5^\circ\text{C}$



⁷ <http://www.watlow.com/reference/refdata/0310.cfm>

8. MANOMETER⁸

I. Short Tube Mk 4 & 5 AIRFLOW TESTING SET



Instructions: The manometer may be used in a number of alternative positions. To move from one position to another, spring supporting tube slightly forward, and move into the required location. Level panel by two screws provided. After locating limb reset zero by rotating knob on panel. Do not force beyond limit of travel.

Tube Position	Range			Scale Multiplier	Precision
	kN/m ²	in.	cm.		
Vertical	0-2.5	0-10	0-25	1	0.01
Top Inclined	0-0.5	0-2	0-5	0.2	0.01
Middle Inclined	0-0.25	0-1	0-2.5	0.1	0.01
Bottom Inclined	0-0.125	0-0.5	0-1.25	0.05	0.01

II. Type 6 AIRFLOW TESTING SET

Manometer Arm Position	Range			Scale Multiplier	Precision
	kpa	ins	m.m.		
Vertical	0-2	0-8	0-200	1	0.02
Inclined	0-0.2	0-0.8	0-20	0.1	0.02

⁸ Airflow Development LTD.



9. BAROMETER⁹

Model: BA888 (6 Line Barometer Weather Station)

Features:

- Thermometer (range: -5°C to +55°C, +23°F to 131°F; resolution: 0.5°C, 0.9°F)
- Hygrometer (range: 25% to 95% RH/relative humidity; resolution: 1% RH)
- Barometer (range: 794mb/hPa to 1050mb/hPa, 23.45 inHg to 31.01 inHg; resolution: 1mb, 0.03 inHg)
- Altitude compensation (0-3500m)
- Graphical weather forecast
- Development of atmospheric pressure of the preceding 24 hours
- Optional hourly check of this development
- Clock, Alarm & date



⁹ Oregon Scientific

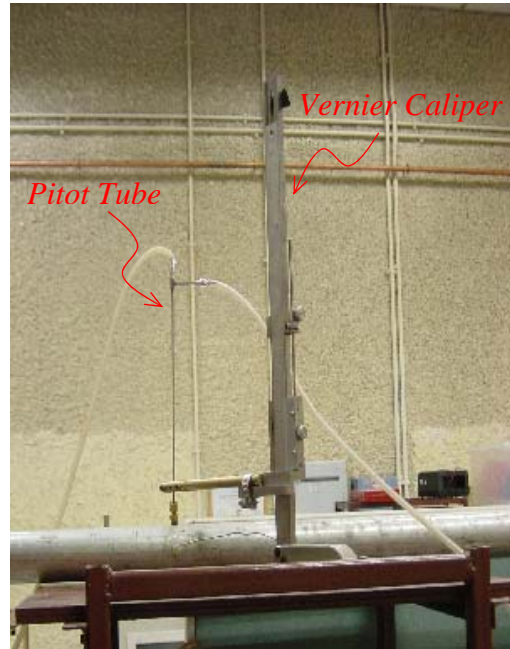
10.PITOT TUBE & VERNIER CALIPER (514-103)

I. Pitot Tube

The Pitot tube allows the direct measurement of dynamic pressure hence the calculation of flow velocity in ducts.

II. Vernier Caliper

- Range: 0-300mm (0-12 in)
- Resolution: 0.02mm
- Precision: $\pm 0.04\text{mm}$



11.FLOW METER/ANEMOMETER¹⁰

Model: 8908

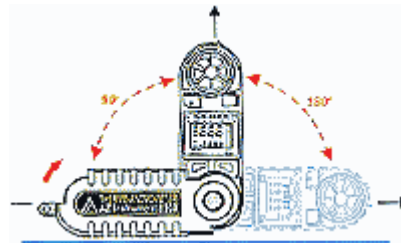
1. Features:

- Pocket-knife design makes it convenient and portable
- Precision measurement and easy to use
- Temp / windchill: Average updates every second
- Windspeed: Moving 2-sec average with Maximum 2-second gust
- Measurement units: knots, mph, kph, ft / min, m/ sec, beaufort
- Sealed precision thermistor water resistant and shock proof housing
- Detented at 180° for fully opened
- Detented at 90° for tripod mountable
- Safety wrist strap included
- Replaceable lithium battery
- Replaceable impeller (33(Dia.) × 16(T) mm)



2. Specifications:

▲	Min/Max Windspeed:	0.5 ~ 44.7 MPH 60 ~ 3937 FT/M
▲	Relative Humidity range:	0 ~100%
▲	One Button Data Hold	
▲	Records maximum readings	
▲	°C/°F unit switchable	
▲	Auto power off:	Approx. 20 min.
▲	Operating temperature:	-15 ~ 50 °C
▲	Average readings:	5 / 10 / 13 second averages
▲	Dimension:	235 × 45 × 25 mm for 180° full opened; 140 × 45 × 25 mm for folded.



Unit		Range	Resolution
m/s	meter per second	1.1~20.0	0.1
Ft /Min	Feet per minute	60~3937	2
KNT	Knot	0.4~38.8	0.1
KMH	Kilometer per hour	0.8~72.0	0.1
MPH	Mile per hour	0.5~44.7	0.1
BF	Beaufort	1~8	1

¹⁰ AZ Instrument